Technische Universität München
TUM School of Natural Sciences

Structural and Electrolyte Effects in Cathodic Reactions at Pt-based Electrocatalysts

Kun-Ting Song

Vollständiger Abdruck der von der TUM School of Natural Sciences der Technischen Universität München zur Erlangung des akademischen Grades eines

Doktors der Naturwissenschaften (Dr. rer. nat.)

genehmigten Dissertation.

Vorsitz:	Prof. Dr. Nora Brambilla
Prüfer der Dissertation:	1. Prof. Dr. Aliaksandr S. Bandarenka 2. Prof. Dr. Timo Jacob

Die Dissertation wurde am 25.07.2024 bei der Technischen Universität München eingereicht und durch die TUM School of Natural Sciences am 07.10.2024 angenommen.

This thesis builds upon the following published (or in preparation) manuscripts and attended conferences:

Publications:

1. Song, K.-T.; Zagalskaya, A.; Schott, C. M.; Schneider, P. M.; Garlyyev, B.; Alexandrov, V.; Bandarenka, A. S. Influence of Alkali Metal Cations on the Oxygen Reduction Activity of Pt_5Y and Pt_5Gd Alloys. *J. Phys. Chem. C* **2024**, *128* (12), 4969–4977.

2. Song, K.-T.;† Schneider, P. M.;† Grabovac I.; Garlyyev B.; Watzele S. A.; Bandarenka, A. S. Influence of the Electrolyte pH on the Double Layer Capacitance of Polycrystalline Pt and Au Electrodes in Acidic Solutions (paper in preparation)

3. Song, K.-T.;† Schott, C. M.;† Schneider, P. M.; Watzele, S. A.; Kluge, R. M.; Gubanova, E. L.; Bandarenka, A. S. Combining Impedance and Hydrodynamic Methods in Electrocatalysis. Characterization of Pt(pc), Pt_5Gd, and Nanostructured Pd for the Hydrogen Evolution Reaction. *J. Phys. Energy* **2023**, *5* (1), 014016.

4. Schott, C.; Schneider, P.; Song, K.-T.; Yu, H.; Götz, R.; Haimerl, F.; Gubanova, E.; Zhou, J.; Schmidt, T.; Zhang, Q.; Alexandrov, V.; Bandarenka, A. S. How to Assess and Predict Electrical Double Layer Properties: Implications for Electrocatalysis. *Chem. Rev.* **2024**, DOI: 10.1021/acs.chemrev.3c00806. (paper accepted)

5. Ma, X.; Schröck, L.; Gao, G.; Ai, Q.; Zarrabeitia, M.; Liang, C.; Hussain, M. Z.; Khare, R.; Song, K.-T.; Zheng, D. J.; Koch, M.; Stephens, I. E. L.; Hou, S.; Shao-Horn, Y.; Warnan, J.; Bandarenka, A. S.; Fischer, R. A. Tuning the Reconstruction of Metal–Organic Frameworks during the Oxygen Evolution Reaction. *ACS Catal*. **2024**, *14* (1), 15916–15926.

6. Hou, S.; Xu, L.; Mukherjee, S.; Zhou, J.; Song, K.-T.; Zhou, Z.; Zhang, S.; Ma, X.; Warnan, J.; Bandarenka, A. S.; Fischer, R. A. Impact of Organic Anions on Metal

Hydroxide Oxygen Evolution Catalysts. *ACS Catal.* **2024**, *14* (1), 12074–12081.

7. Sarpey, T. K.; Himmelreich, A. V.; Song, K.-T.; Gubanova, E. L.; Bandarenka, A. S. The Electrocatalytic Activity of Au Electrodes Changes Significantly in Various Na^+/K^+ Supporting Electrolyte Mixtures. *Small Sci.* **2024**, *4* (7), 2400042.

8. Schott, C. M.; Schneider, P. M.; Sadraoui, K.; Song, K.-T.; Garlyyev, B.; Watzele, S. A.; Michalička, J.; Macak, J. M.; Viola, A.; Maillard, F.; et al.. Top-down Surfactant-Free Synthesis of Supported Palladium-Nanostructured Catalysts. *Small Sci.* **2024**, *4* (3), 2300241.

9. Yu, H.; Schott, C.; Schmidt, T.; Schneider, P. M.; Song, K.-T.; Zhang, Q.; Capogrosso, A.; Deville, L.; Gubanova, E.; Bandarenka, A. S. Investigation of Active Electrocatalytic Centers under Reaction Conditions Using Operando Microscopies. *Curr. Opin. Electrochem.* **2023**, *42*, 101386.

10. Taji, Y.; Zagalskaya, A.; Evazzade, I.; Watzele, S.; Song, K.-T.; Xue, S.; Schott, C.; Garlyyev, B.; Alexandrov, V.; Gubanova, E.; Bandarenka, A. S. Alkali Metal Cations Change the Hydrogen Evolution Reaction Mechanisms at Pt Electrodes in Alkaline Media. *Nano Mater. Sci.* **2022**. https://doi.org/10.1016/j.nanoms.2022.09.003.

† Authors contributed equally to the publications.

Conference contributions:

1. e-conversion Conference, Tutzing, Germany, 15th - 18th October 2023, *Influence of the Electrolyte pH on the Electrical Double Layer of Pt-Electrodes in Acidic Solutions. (Poster)*

2. 74th Annual Meeting of the International Society of Electrochemistry, Lyon, France, 3rd - 8th September 2023, *Combining Impedance and Hydrodynamic Methods in Electrocatalysis. Characterization of Pt(pc), Pt_5Gd for the Hydrogen Evolution Reaction. (Poster)*

3. e-conversion Conference, Venice, Italy, 4th - 7th October 2022, *Combining Impedance and Hydrodynamic Methods in Electrocatalysis. Characterization of Pt(pc), Pt_5Gd for the Hydrogen Evolution Reaction. (Poster)*

4. 12th Energy Colloquium of the Munich Institute of Integrated Materials, Energy and Process Engineering, Munich, Germany, 28th July 2022. *(Attendance)*

5. 32nd Topical Meeting of the International Society of Electrochemistry, Stockholm, Sweden, 19th - 22nd June 2022, *Influence of Alkali Metal Cations on the Oxygen Reduction Reaction Activity of Pt(pc), Pt_5Y, and Pt_5Gd Alloys. (Poster)*

6. e-conversion Conference, Munich, Germany, 15th - 16th September 2021, *Influence of Alkali Metal Cations on the Oxygen Reduction Reaction Activity of Pt_5Y and Pt_5Gd Alloys. (Poster)*

7. 11th Energy Colloquium of the Munich School of Engineering 2021, Munich, 28th - 29th July 2021. *(Attendance)*

Abstract

Enhancing the efficiency of electrocatalysts is essential for developing a sustainable hydrogen economy. Pt-based electrocatalysts are the key cathode materials for the hydrogen evolution reaction (HER) and the oxygen reduction reaction (ORR) taking place in electrolyzers and fuel cells. However, the too-strong binding energies of Pt with reaction intermediates and the scarcity of raw materials cause bottlenecks in its applications in heterogeneous electrocatalysis. It is known that the effects of the surface structure of catalysts and the electrolyte compositions play an essential role in the rational design of electrocatalysts. This thesis investigates both contributions concerning the ORR and HER at Pt-based surfaces and develops new approaches for more informative characterization of those systems. This work first discusses the combined techniques of electrochemical impedance spectroscopy and the rotating disc electrode to investigate the HER mechanisms under controlled hydrodynamic configurations for the module systems consisting of polycrystalline Pt (Pt(pc)) and Pt_5Gd in acidic and alkaline media. The electrical equivalent circuit has been established to differentiate the Volmer-Heyrovsky and Volmer-Tafel mechanisms of HER. In acidic media, both the reaction kinetics and diffusion influence the HER, and the contribution of both reaction pathways is independent of the electrode rotation rate. In contrast, the HER in alkaline media is more kinetically limited and prefers the Volmer-Heyrovsky mechanism at lower rotation rates. Secondly, the influence of alkali metal cations on the ORR activities for Pt_5Gd and Pt_5Y has been studied. Due to the strain effect, the Pt alloys have faster reaction kinetics, and the ORR performance increases linearly with the increasing hydration energy of alkali cations in the order of $Li^+ > Na^+ > K^+ > Rb^+ > Cs^+$. However, Pt(pc) shows the reverse trend in alkaline solutions. The density functional theory calculations support the experimental results of the opposite trends of ORR activities between Pt alloys and Pt electrodes. Those

findings show that the non-covalent interactions between the hydrated solvation shells and reaction intermediates and the induced strain at the surface synergistically alter the activity, which can provide further guidelines for developing better energy devices.

Kurzfassung

Die Effizienzsteigerung von Elektrokatalysatoren ist entscheidend für die Entwicklung einer nachhaltigen Wasserstoffwirtschaft. Pt-basierte Elektrokatalysatoren sind die Schlüsselmaterialien für die Kathode bei der Wasserstoffentwicklungsreaktion (HER) und der Sauerstoffreduktionsreaktion (ORR), die in Elektrolyseuren und Brennstoffzellen stattfinden. Allerdings stellen die zu starken Bindungsenergien von Pt mit Reaktionszwischenprodukten und die Knappheit der Rohstoffe Einschränkungen der Anwendungen in der heterogenen Elektrokatalyse dar. Es ist bekannt, dass die Effekte der Oberflächenstruktur von Katalysatoren und die Zusammensetzung des Elektrolyten eine wesentliche Rolle bei der rationalen Gestaltung von Elektrokatalysatoren spielen. Diese Dissertation untersucht beide Beiträge hinsichtlich der ORR und HER an Pt-basierten Oberflächen und entwickelt neue Ansätze für eine informativere Charakterisierung dieser Systeme. Diese Arbeit diskutiert zunächst kombinierten Techniken der elektrochemischen Impedanzspektroskopie und der rotierenden Scheibenelektrode, um die HER Mechanismen unter kontrollierten hydrodynamischen Konfigurationen für die Modulsysteme bestehend aus polykristallinem Pt (Pt(pc)) und Pt_5Gd in sauren und alkalischen Medien zu untersuchen. Der elektrische Ersatzschaltkreis wurde festgelegt, um zwischen Volmer-Heyrovsky und Volmer-Tafel Mechanismen der HER zu differenzieren. In sauren Medien beeinflussen sowohl die Reaktionskinetik als auch die Diffusion die HER, und der Beitrag beider Reaktionswege ist unabhängig von der Rotationsgeschwindigkeit der Elektrode. Im Gegensatz dazu ist die HER in alkalischen Medien stärker kinetisch limitiert und bevorzugt den Volmer-Heyrovsky Mechanismus bei niedrigeren Rotationsgeschwindigkeiten. Des Weiteren wurde der Einfluss von Alkalimetallkationen auf die ORR Aktivitäten für Pt_5Gd und Pt_5Y untersucht. Aufgrund des Verformungseffekts weisen die Pt Legierungen schnellere Reaktionskinetiken auf,

und die ORR Leistung steigt linear mit zunehmender Hydratationsenergie der Alkalikationen in der Reihenfolge $Li^+ > Na^+ > K^+ > Rb^+ > Cs^+$. Pt(pc) zeigt hingegen den umgekehrten Trend in alkalischen Lösungen. Die Berechnungen der Dichtefunktionaltheorie unterstützen die experimentellen Ergebnisse der entgegengesetzten Trends der ORR Aktivitäten zwischen Pt Legierungen und Pt Elektroden. Diese Erkenntnisse zeigen, dass die nicht-kovalenten Wechselwirkungen zwischen den hydratisierten Solvatisierungshüllen und den Reaktionszwischenprodukten sowie die induzierte Oberflächenverformung synergistisch die Aktivität verändern, was weitere Richtlinien für die Entwicklung besserer Energiesysteme bieten kann.

Acknowledgment

I sincerely would like to express my gratitude to all those who have supported and encouraged me during the grateful journey. Without their help, I wouldn't have been able to accomplish this research work. Therefore, I would like to thank…

… **Prof. Aliaksandr Bandarenka** for providing me with the opportunity to join his group since my Master's thesis and throughout the continual PhD program. His wealth of professional experience and deep knowledge have played an essential role in enhancing my ability to engage in scientific research effectively. I am genuinely grateful for the fruitful discussions and scientific inspiration he shared with me.

… **Prof. Timo Jacob** from Ulm University for being the second examiner and dedicating time to this work.

… **Prof. Ifan Stephens** and **Prof. Tanja Kallio** for offering me the opportunity to participate in the exchange research programs within their groups at Imperial College London and Aalto University, respectively. These experiences broadened my knowledge and helped me explore diverse cultures.

… **Prof. Vitaly Alexandrov** and **Dr. Alexandra Zagalskaya** from the University of Nebraska-Lincoln (UNL) for their invaluable contributions to the theoretical calculations that supported our experimental findings. Their expertise and collaboration have greatly enhanced the strength and depth of our research work.

…our previous colleagues, **Dr. Batyr Garlyyev**, **Dr. Sebastian Watzele**, **Dr. Regina Kluge**, **Dr. Xing Ding**, **Dr. Leon Katzenmeier**, **Dr. Richard Haid**, **Dr. Shujin Hou**, **Dr. Theophilus Sarpey** and **Dr. Xaver Lamprecht** for kindly helping my initial experimental work and solving the practical laboratory issues.

… **Siegfried Schreier** for his profession of solving technical problems and supporting

experimental setups.

… particularly my colleagues, **Dr. Elena Gubanova**, **Peter Schneider**, **Göktug Yesilbas**, **Christian Schott**, **Xiaoxin Ma**, **Rainer Götz**, **Thorsten Schmidt**, **Raphael Streng**, **Lewin Deville**, **Qingdian Liao**, and **Haiting Yu**, for their kindness and patience in daily working and hanging out together as well as many contributions to my scientific publications. I am grateful for the memorable moments we have shared and the meaningful connections we have formed professionally and personally. Many thanks to **Ivo Grabovac** for the excellent support in preparing the manuscript based on his bachelor's project.

… other previous and present ECS group and external members, **Dr. Rohit Gaddam**, **Johannes Sterzinger**, **Huiyu Gai**, **Jian Zhou**, **Da Lei**, and others, for providing a great working environment.

… all my dear friends, both within and outside Munich, for our wonderful off-work experiences and activities. I am truly grateful for your encouragement and companionship in overcoming all difficulties on this journey.

…my dear parents and my dear families for all mental and physical help my whole life. I appreciate their boundless patience, unconditional love, and tireless efforts, which have been a constant source of strength and inspiration for me.

Contents

1. Introduction

1.1. Basics of Hydrogen Economy: Potential and Challenges

Although the industrial revolution since the 18th century, continuous urbanization, and the manufacturing economy brought many advantages to global society, the accompanying issues of using fossil fuels as the main energy sources and the increasing energy demand have caused global environmental issues (e.g., global warming[1,2] as well as air and water pollution[3,4]) and the energy insecurity of limited resources of fossil fuels.[5] Governments and scientists worldwide have collaborated to develop and implement actions to reduce environmental damage. In 2005, the Paris Agreement set the goal of limiting the global average temperature increase to 1.5°C.[6,7] This involves reducing carbon dioxide (CO_2) and other greenhouse gas emissions in the atmosphere and decarbonizing the energy supply to promote sustainable development. According to the Intergovernmental Panel on Climate Change (IPCC), it is expected to reach the status of a fully decarbonized or even carbon-negative economy by 2100.[8,9]

To tackle this challenge, the concept of the future hydrogen economy was first proposed by John Bockris at General Motors Technical Center in the 1970s.[10,11,12,13] It is suggested that hydrogen replaces fossil fuels as the primary energy resource for industrial manufacturing, transportation, and the economy to achieve the zero-emission goal. Molecular hydrogen (H_2) is regarded as an ideal energy resource because of its higher gravimetric energy density (120 MJ/kg) compared to fossil fuels, including liquefied natural gas (54.4 MJ/kg), automotive gasoline (46.4 MJ/kg) and diesel (45.6 MJ/kg), etc.[14,15] Hydrogen is one of the earth's lightest and most abundant and widespread elements, and it is stored in different forms, such as water (H_2O),

hydrocarbons, and other organic substances.[16,17,18,19]. With these advantages, it has a high potential of being one of the main energy sources. However, the main challenge in industrial manufacture is producing and extracting pure H_2 environmentally friendly from these compounds. According to recent reports, the current global hydrogen production is mainly from natural gas (about 50%), refinery/chemical industry off-gases (about 30%), and coal gasification (about 18%). Still, only approximately 4% is generated from water splitting.[20,21] The production cost of grey hydrogen, primarily derived from steam methane reforming, is estimated at 0.6-1.9 $/kg. In contrast, as of 2020, green hydrogen produced through electrolysis costs significantly higher, ranging between 3.7 and 6.1 $/kg, making it unprofitable for industrial use.[22]

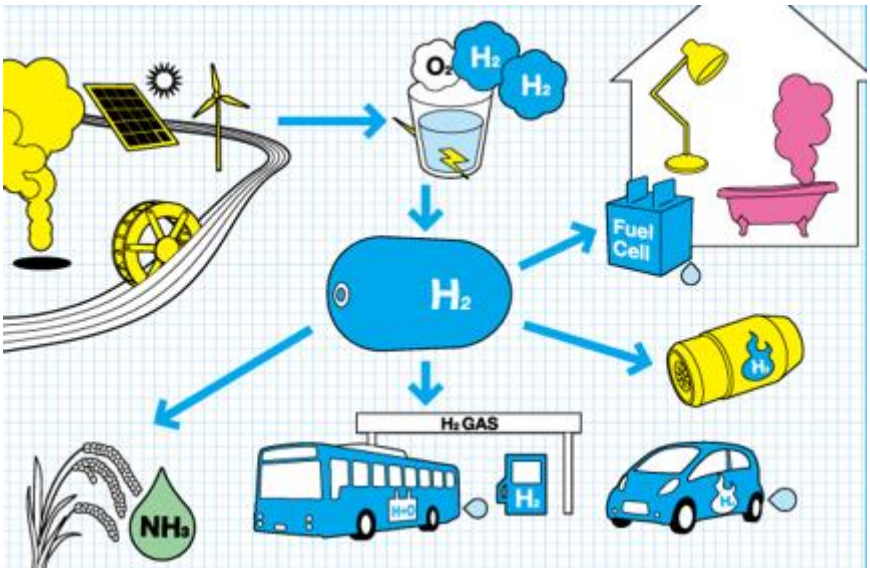

Figure 1.1. The diagram illustrating the concept of a hydrogen economy with the so-called "green" hydrogen, which is produced from renewable energy sources, such as solar, geothermal, wind, etc. The hydrogen from electrolysis is stored and then utilized to produce synthetic natural gases, generate power, and transport via fuel cells and other energy-conversion devices. Reprinted from reference [23].

The so-called "green" hydrogen production method to supply the increasing demand for hydrogen must be improved to make it a feasible carbon-free alternative to conventional hydrogen generation.[24,25,26] As conceived in **Figure 1.1**, in a low-carbon

economy, renewable hydrogen is generated from clean, sustainable, and renewable energy sources, such as solar, wind, hydropower, geothermal, etc. The hydrogen gas produced via water electrolysis is then stored in solid, liquid, and gaseous forms for future use. The stored hydrogen can be used in the industrial manufacture of raw materials and chemicals or consumed as a fuel for daily power generation and transportation via fuel cells. The released by-products, water, and heat are pollution-free and can be recycled and used in other applications.[23]

According to reports, the transportation sector contributes approximately 20% of total CO_2 emissions (overall 36.7 billion tons of CO_2 in 2016), with road transport accounting for roughly 75% within this sector.[27] Within the scope of zero-emission transportation, the European Parliament set the goal to eliminate 40% of CO_2 from vehicles by 2030.[28] Various types of alternative technologies are being pursued to replace conventional fossil fuel vehicles (e.g., Battery Electric Vehicles (BEVs), Plug-in Hybrid Electric Vehicles (PHEVs), and Hydrogen Fuel Cell Vehicles (FCVs)).[29,30,31,32,33,34] The global electric market share increased remarkably from about 0.27% to 13.0% from 2013 to 2021.[35] Many car companies currently prioritize BEVs, mainly with lithium-ion batteries, due to their high efficiency, lower operating costs, and government support. However, the challenges, such as a restricted range, longer charging/discharging periods, and insufficient charging infrastructure, need further improvements.[36,37] In contrast, certain companies, such as Toyota,[38] Honda,[39] Hyundai,[40] BMW,[41] etc., continuously invest in the development of commercial FCVs, driven by the competitive advantages including quicker refueling time, longer driving range, and higher energy efficiency (40-60%) than traditional combustion engines (30-40%). However, the main problem is the high cost of fuel cell manufacturing and maintenance (e.g., precious catalysts and expensive membranes), which limits widespread commercialization.[42,43,44] Other technical and strategic drawbacks (e.g., the

insufficient hydrogen supply infrastructures and poor reliability, safety issues, slow cold start, and poor energy management systems) also need to be overcome.[45,46] From 2023, two commercial FCVs are available, including Toyota's Mirai[38] and Hyundai's Nexo.[40,47] Indeed, each technology contains its own set of strengths and challenges related to infrastructure, cost, and technology development towards different transportation categories, from personal to public applications. As Zipse, Chairman of the Board of Management of BMW, highlighted the concept,[41] "We should harness the potential of hydrogen to accelerate the transformation of the mobility sector as well. Hydrogen is the missing puzzle piece for emission-free mobility; after all, no single technology will be enough to enable carbon-neutral mobility worldwide." Specifically, in terms of long-distance transport (e.g., shipping, buses, and trucks), the significance of hydrogen-based fuels as alternative energy sources becomes pronounced and cost-competitive since hydrogen tanks' mass and volume demands only increase slightly compared to the sharp increase of BEVs.[48] For example, it is expected that the global hydrogen bus and aircraft markets will grow to about $49.2 and $1.7 billion, respectively, by 2030.[49,50] Therefore, the goals of utilizing "green" hydrogen and increasing the conversion performance of fuel cells and electrolyzers still need much effort in terms of cost, reliability, and durability. Rational design approaches for efficient energy conversion device electrocatalysts are crucial for developing a sustainable economy.

1.2. Important Impacts Controlling Electrocatalytic Performance

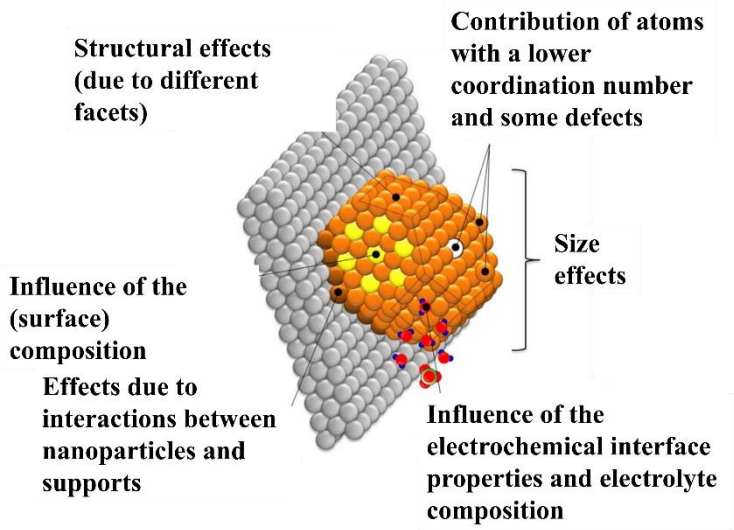

Figure 1.2. The schematic of the essential factors and parameters affecting the electrocatalytic performance in real-world high surface-area nanostructured electrocatalysts. Adapted with permission from reference [51]. Copyright © 2013 Elsevier Inc.

As mentioned above, electrocatalysis is essential for the functionality of energy conversion devices like fuel cells and electrolyzers, enabling efficient redox reactions to occur at the electrode/electrolyte interfaces. **Figure 1.2** schematically illustrates several parameters and factors to modify the reaction conditions and enhance the electrocatalytic performance towards activity, selectivity, and stability. Here, the primary focus is on the structural and electronic effects of electrode surfaces and the influence of electrolyte composition.[51,52,53,54,55] In real-world electrochemical cells, the active reaction sites are found on nanostructured electrocatalysts, which are contacted with high surface-area carbon supports for electrical conductivity.[56,57,58] The structural sensitivity of electrocatalysts is attributed to catalyst surfaces that contain varying crystal orientations, defects, atoms with different coordination numbers, and nanoparticle sizes and shapes, thereby influencing the overall electrocatalytic

performance.[59,60,61,62,63,64,65,66,67] Furthermore, the electronic effect influences the electronic status of the specific sites at the surface. Optimization strategies focus on the surface composition, which includes, for example, bimetallic alloys altering the binding energies of the reaction intermediates.[68,69,70,71,72,73] Other approaches involve computational methods such as density functional theory (DFT) calculations with particular descriptors to predict and search optimal electrocatalysts.[74,75,76,77,78,79,80]

Besides the influence of electrode surface structure and composition, the effect of electrolyte components plays a crucial role in shaping reaction environments, including the pH value, the concentration, and the nature of cations and anions in electrolytes.[81,82,83] The electrochemical electrode/electrolyte interfaces are complex and dynamically interact between the catalyst surfaces, reactants, intermediates, products, and electrolyte components.[51] To sort out the puzzle of electrocatalytic systems, one of the primary objectives of this thesis is to systematically analyze and clarify these effects to understand their influences on electrocatalytic performance concerning Pt-based electrodes and two cathodic reactions, namely the hydrogen evolution reaction (HER) and oxygen reduction reaction (ORR).

1.3. Motivation and Aim of This Work

In this thesis, we investigate model systems mainly focusing on how the electrolyte composition and the surface structure of Pt-based catalysts influence the HER and ORR, which are crucially essential for industrial water electrolyzers and fuel cells, respectively. Several unsolved questions regarding both reactions are highlighted in the following paragraphs.

Firstly, the hydrogen reactions are known as the simpler and faster reactions compared to the complex and multi-electron transfer processes involved in the oxygen reactions. Previous studies have examined the contribution of Volmer-Heyrovsky and Volmer-Tafel reaction pathways to the overall HER in acidic environments using electrochemical impedance spectroscopy (EIS) on Pt microelectrodes, which offer controlled mass transport at stationary electrodes and minimal ohmic drops due to their relatively small surface areas.[84,85] However, the relative contributions of each reaction pathway and the physicochemical parameters (e.g., reaction kinetic constants, parameters characterizing specific adsorption, mass transports, etc.) are still unclear under certain potential and hydrodynamic conditions.

Because of the different reaction pathways of HER in acidic and alkaline media, we utilized a combined approach of the rotating disc electrode (RDE) and EIS to address both essential environments commonly used in lab research and industrial applications. We utilized the polycrystalline Pt (Pt(pc)) and Pt_5Gd disc electrodes under controlled hydrodynamic configurations. Additionally, we explored a more complex system involving nanostructure electrocatalysts to validate the impedance model towards HER mechanisms further.

Secondly, the complex reaction pathways of ORR, with its sluggish reaction kinetics and high overpotentials, consequently increase the costs of electrocatalysts with high

mass loading and limit the development of fuel cells. In addition to the factors and strategies outlined in **Section 1.2** aimed at enhancing ORR performance (e.g., structural and electronic influences on electrocatalyst electrodes and electrolyte compositions), studies have highlighted the substantial impact of electrolyte cations and anions on ORR activities for various single-crystal electrodes and Pt/C electrocatalysts.[81,86,87,88,89,90] However, the comprehensive exploration of electrolyte effects on the ORR performance of Pt-based alloys remains insufficient.

Therefore, we investigated the influence of alkali metal cations as spectators on the ORR activities for active Pt_5Gd and Pt_5Y as model systems of Pt alloys due to their relatively high ORR stability and compared the results with the reference Pt(pc) electrode. DFT calculations further examined the experimental findings to associate the correlation between surface strain and the alkali cation effects to find the optimal theoretical overpotential towards ORR.

The basic theory and the important electrocatalytic reactions will be presented in **Chapter 2** to outline the whole investigation in the following chapters. The experimental details of different setups and techniques will be briefly introduced in **Chapter 3**, while the experimental and computational results will be discussed and summarized in **Chapter 4** and **Chapter 5**.

.

2. Basics of Electrocatalysis for Energy Conversion

2.1. Electrocatalysts

2.1.1. Role of Electrocatalysts in Reactions

In general, a catalyst is a substance that helps to increase a chemical reaction rate without being consumed or without being a part of the products. This concept was first formulated by Wilhelm Ostwald, who was awarded the Nobel Prize in 1909.[91] Electrocatalysis deals with redox reactions taking place at the electrified interfaces between electronically conducting electrodes and ionically conducting electrolytes.[92]

Figure 2.1 depicts an example of the energy diagram of two reaction pathways involving catalyst participation and the other without. Regardless of whether the reaction is exothermic or endothermic, in the absence of a catalyst (represented by the blue curve), the reactants must overcome the activation energy (E_a) barrier to reach the transition state and form products. Compared with catalyst involvement (denoted by the red curve), the overall E_a notably decreases and accelerates the reaction rate. Moreover, the catalyst may lower the reaction barrier and alter the reaction pathway on its surface by forming intermediates between the reactants and products, each associated with corresponding reduced activation energies (noted as E_{a1} and E_{a2}). It is worth noting that despite the participation of catalysts, the thermodynamic change of Gibbs free energy (ΔG) between reactants and products remains unchanged and independent of the catalyst.[93]

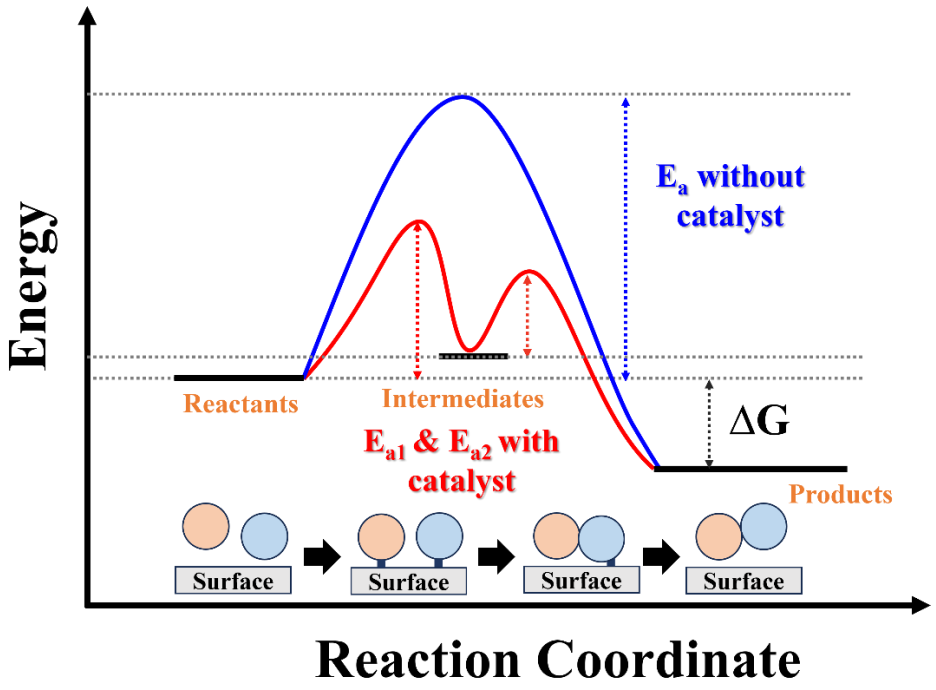

Figure 2.1. A schematic energy diagram of non-catalytic and catalytic reaction pathways from reactants (intermediates) to products. The activation energy (E_a, blue) without a catalyst is much higher than in the case with a catalyst to form the intermediates (E_{a1} and E_{a2}, red). The energy change between the reactants and products is defined as ΔG and is thermodynamically the same for both cases. Adapted with permission from reference [94].

Figure 2.1 conceptualizes how catalysts influence activation energy and reaction pathways to promote reaction rates. However, the actual influence of catalysis is more complex. Various catalysts exhibit different activity, stability, and selectivity properties essential for different reactions. The activity usually indicates the ability of a catalyst to increase the reaction rate. Besides the two standard parameters of exchange current density,[95,96] and overpotential[97,98] to benchmark the electrocatalytic activity, the turnover frequency[99,100,101] determines the intrinsic activity by illustrating the amount of product formation per unit of time per catalytic site.[102] In addition, stability highlights the impact of deactivation issues on the catalyst's lifetime at a specific activity level.[103] Selectivity refers to the ability of the catalyst to promote preferentially one of the possible reactions to obtain the maximum yield of the desired products.[104]

2.1.2. Active Sites, Sabatier Principle, and Scaling Relations

The concept of active sites plays a vital role in interpreting the reactions on solid catalysts. Two primary schools of thought illustrate active sites from different perspectives. Irvine Langmuir, in 1922, proposed a simplified theoretical consideration stating that the reactions occur with homogenous adsorbates on plane surfaces like a checkboard in two dimensions, in which the active sites are located at certain facets.[105,106] In comparison, in 1925, the school of thought from Hugh Stott Taylor considered the reactions taking place with higher complexity in a three-dimensional perspective, which differs from Langmuir's equivalent adsorption sites. Taylor stated that a catalytic reaction does not occur homogeneously over the catalyst surface but only at certain active sites or spots with specific conditions defined by their crystalline structure, composition, and defects.[105,107,108]

Furthermore, one of the direct approaches to assessing electrocatalytic performance is based on the activity of catalysts, as described previously. Paul Sabatier proposed the first conceptual statement in 1911,[109,110] that qualitatively explained the heterogenous catalytic performance. To obtain the highest catalytic activity, the principle involves the interactions between the catalyst surface and reaction intermediates as being "just right". If the interaction is too strong, the reaction is limited by the desorption of species from the surface. On the other hand, if the interaction is too weak, the reaction does not occur as it is difficult to activate the reactants. The Sabatier principle led to the so-called volcano plot approach, introduced by Balandin in 1969, among others.[111] This type of plot establishes a relationship between the activity (i.e., the reaction kinetics) and a particular descriptor, which can be enthalpies of adsorption of intermediates or other parameters.[111, 112] At that time, however, determining experimentally accessible physical quantities as descriptors remained challenging and needed further exploration to be supported by theoretical studies.[113]

The problems have been partly addressed by developing theoretical and computational approaches. For instance, Nørskov et al. elaborated on using the intermediate's binding energy as a descriptor on simulated surfaces by DFT calculations,[74,75,76,77] which quantitatively predicts the catalyst activity and, in many cases, selectivity.

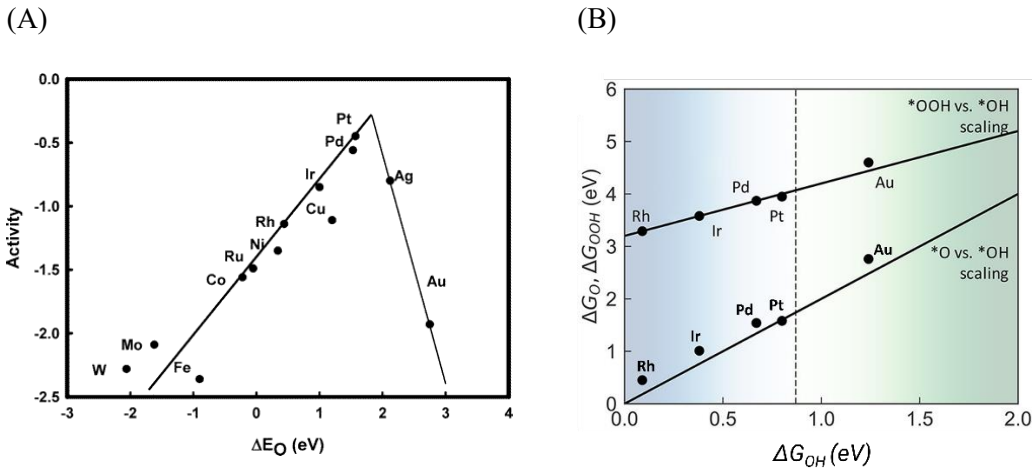

Figure 2.2. (A) The ORR volcano plot linking the activity and the *O binding energy obtained by DFT calculations. Reprinted with permission from reference [74]. Copyright © 2004, American Chemical Society (B) The scaling relations in the case of the ORR involving the chemisorption energies of *O and *OOH with *OH as the descriptors for (111) surfaces of different metals. Adapted with permission from reference [75]. Copyright © 2018, American Chemical Society.

For instance, **Figure 2.2A** shows the ORR volcano plot with the activity trend as a function of the theoretical binding energy of *O intermediate (ΔE_O).[74] According to the Sabatier principle, the lower ORR activities exist at the two sides of the volcano plot, in which the catalysts have either too strong or too weak binding. Pt behaves as a relatively good ORR catalyst compared to other metals and is located close to the optimal binding to the oxygen species.

However, the catalytic reaction mechanisms often involve multiple steps with different intermediates. The frequently observed mathematical relationships, known as the scaling relations, demonstrate the linear correlations between the binding energies of

adsorbed intermediates with various catalysts. For example, **Figure 2.2B** shows the scaling relations for the ORR with the chemisorption energies of *OOH and *O as a function of the chemisorption energy of *OH for several metals with (111) surfaces. The linear relationships are attributed to the similar binding conditions of all adsorbed species with the same atom (e.g., an O atom for ORR intermediates) on the surfaces.[75] By utilizing scaling relations, the prediction of the activity of catalysts in multistage chemical reactions can be simplified and expressed as a function of a single key intermediate adsorption energy for the volcano plots. Nevertheless, the strong correlations between the binding energies of intermediates hinder the optimization of each intermediate step independently to obtain a lower overpotential. Therefore, to "break" the scaling relations, several approaches are highlighted to developing three-dimensional active catalysts and multifunctional active sites to optimize each intermediate step and provide additional promotors, functional ligands, and electrolyte compositions.[75,114]

2.2. Properties of Solid/Liquid Interfaces

2.2.1. Electrical Double Layer

The electrical double layer (EDL) is one of the essential parts of electrochemical systems because all the interfacial electrochemical processes occur within this region.[115,116,117] The formation of the EDL stems from the electrostatic forces at the interfacial region, where the electroneutrality is maintained between the polarized electrode and the ionic conducting solution. When no faradaic reaction occurs, this interface exhibits capacitor-like behavior (double-layer capacitance, C_{dl}). Historically, the first model of the EDL was proposed by Hermann von Helmholtz in 1853.[118] In this so-called Helmholtz model, the charge is linearly proportional to the applied voltage on the electrode without considering the thermal motion of ions (and other specific ionic interactions). The model was improved by Louis Georges Gouy and David Leonard Chapman in 1910 and 1913, respectively.[119,120] The Gouy-Chapman model proposes the diffuse layer model by considering the thermal motions of ions in the electrolyte. The distribution of charged ions considered as point charges follows the Maxwell-Boltzmann statistics, decreasing exponentially from the polarized electrode surface. A further modified model was suggested by Otto Stern in 1924,[121] who combined the Helmholtz and Gouy-Chapman models with the consideration of the thermal motions and the size of ions in the electrolyte. The contemporary comprehensive model of the EDL was presented by David C. Grahame in 1947. He refined and adapted the Stern model by dividing the Helmholtz layer into the inner and outer Helmholtz planes (**Figure 2.3**).[122]

Figure 2.3 illustrates the classical EDL model, primarily based on Grahame's model, with a potential ($Ø_{Me}$) applied at the metal electrode with a negative charge. The rigid Helmholtz and diffuse layers in the electrolyte balance the electrode charge and

maintain system electroneutrality. Besides, the Helmholtz layer consists of the inner Helmholtz plane (IHP), mainly with specifically adsorbed anions and water diploes as the solvent aligning along the electrode surface, and the outer Helmholtz plane (OHP), primarily with non-specific adsorption of solvated ions.

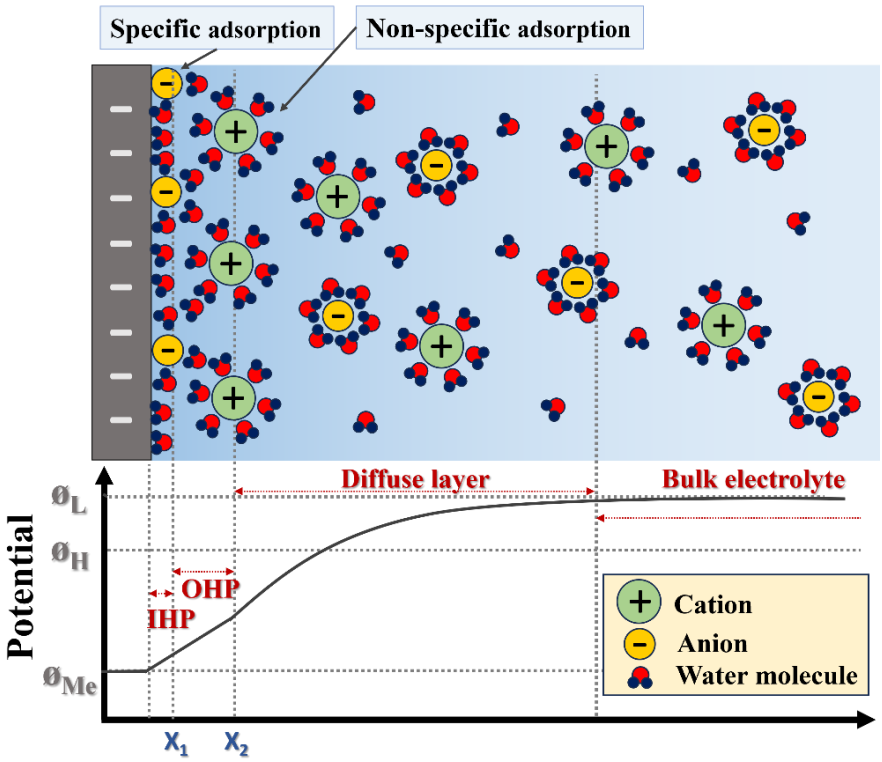

Figure 2.3. A model of the EDL at the electrode/electrolyte interface. Opposite of the negatively charged electrode (with potential $Ø_{Me}$), the EDL structure includes the Helmholtz and diffuse layers. Here, the potential increases linearly to $Ø_H$ within the Helmholtz layer, transitioning to an exponential rise towards $Ø_L$ within the diffuse layer. The Helmholtz layer is further subdivided into the IHP, which includes specifically adsorbed ions and water dipoles, and the OHP, which features hydration shells, extending to distances X_1 and X_2, respectively. Adapted with permission from reference [123].

Within the EDL region, the potential increases linearly from $Ø_{Me}$ to $Ø_H$ in the Helmholtz layer and exponentially from $Ø_H$ to a nearly constant value of $Ø_L$ in the diffuse layer of the bulk electrolyte. The corresponding EDL's thickness and the C_{dl} value are typically in the range of nanometers and microfarad per square centimeter, respectively.[124,125,126] However, the parameters associated with the EDL structure are influenced by various

factors, such as temperature and the properties of the electrode surface and electrolyte at the interface.[127,128] Therefore, further research is required to comprehend the correlations between these factors and the performance of various electrochemical systems.

2.2.2. Electrochemical Potential and Nernst Equation

Electrochemical potential considers both chemical and electrical energies in the electrochemical systems and is introduced by the following **Equation 2.1**.[129,130]

$$\overline{\mu_i} = \mu_i + Z_i \mathrm{F}\varphi \qquad \textbf{Equation 2.1}$$

The electrochemical potential ($\overline{\mu_i}$) of a species i is the combination of the chemical potential (μ_i) and the electrical work in terms of Z_iFφ, where Z_i is the charge on a species i per mole, F is the Faraday constant, and φ is the absolute electrostatic potential of the exact phase.

For redox reactions at the electrode/electrolyte interface, the net reaction rate and the change in electrochemical potential become zero when electrochemical equilibrium is reached. Consequently, the Galvani potential difference ($\Delta\varphi$) between the metal electrode (φ_{Me}) and electrolyte solution (φ_{Sol}) can be described by the Nernst equation (see **Equation 2.2**):

$$\Delta\varphi = \varphi_{Me} - \varphi_{Sol} = \varphi_{00} + \frac{RT}{nF} ln \frac{a_{ox}}{a_{red}} \qquad \textbf{Equation 2.2}$$

where R is the ideal gas constant, T is the temperature in Kelvin, n is the number of electrons transferred, F is the Faraday constant, and a_{ox} and a_{red} are the chemical activities of the oxidized and reduced species at the interfaces, respectively.

Since the absolute value of a Galvani potential is not directly measurable, the standard

potential (φ_{00}) is defined as a reference potential. One of the typical reference potentials is defined using the standard hydrogen electrode (SHE), in which 0 V vs SHE is based on the potential of the hydrogen reaction on a Pt electrode under a standard condition of 1 bar and 1 M of each gas and reactant (e.g., H_2 and proton, H^+) at 298.15 K.[131] Another standard reference potential is defined via the reversible hydrogen electrode (RHE), which considers the pH dependence in electrolytes. The correlation between the potential in the SHE scale (denoted as E_{SHE}) and that of the RHE scale (denoted as E_{RHE}) is described by the equation:

$$E_{SHE}(V) = E_{RHE} + 0.059(V) * pH \qquad \textbf{Equation 2.3}$$

2.2.3. Reaction Kinetics and Overpotentials

In an electrochemical system, non-Faradaic processes involve charged ions undergoing rearrangements at the electrode surface, resembling a capacitor within the EDL region, as mentioned earlier. In contrast, if Faradaic reactions occur at the electrode/electrolyte interface, the current is observed in an external circuit (**Figure 2.4**). For instance, the reactants initially diffuse to the interfacial region from the bulk electrolyte and adsorb at the electrode surface. Subsequently, the charge transfer occurs through the oxidation or reduction of the reactants, resulting in anodic or cathodic currents, respectively. Finally, the resulting products desorb from the surface and diffuse into the bulk electrolyte. The slowest step among the series of reaction steps restricts the overall reaction rate and is defined as the rate-limiting step.

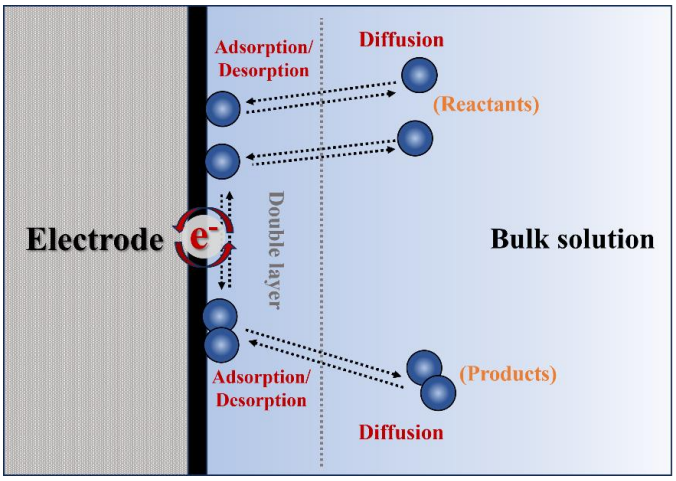

Figure 2.4. The schematics of electrocatalytic reactions at an electrode/electrolyte interface with the diffusion, adsorption/desorption, and charge transfer processes. Adapted with permission from reference [132]. Copyright © 2022, Springer Nature.

In a simple case of the following redox reaction (see **Equation 2.4**) with a one-step and one-electron process at the electrode/electrolyte interface

$$Ox + e^- \underset{k_{Ox}}{\overset{k_{Red}}{\rightleftharpoons}} Red \qquad \textbf{Equation 2.4}$$

the rate constants, k_{Red} and k_{Ox}, relate to the reaction rate of the reduction and oxidation processes, respectively, which demonstrate the probability of the reactions taking place. As illustrated in **Figure 2.1**, the charge transfer reaction must successfully overcome the activation barrier to convert reactants into desired products. The relationship can be expressed using the Arrhenius equation, as shown in **Equation 2.5**:

$$k = Ae^{-E_a/RT} \qquad \textbf{Equation 2.5}$$

Here, k and E_a are the aforementioned rate constant and activation energy, respectively. A is the pre-exponential factor, R is the ideal gas constant, and T is temperature. Furthermore, the current density (j) is a function of k, and the species concentration (C_{sur}) at the electrode surface (**Equation 2.6**), with n and F representing the number of electrons transferred and the Faraday constant, respectively.

$$j = nFkC_{sur} \qquad \textbf{Equation 2.6}$$

As the charge transfer occurs at the electrode, the total current density (j_{tot}), recognized as the net reaction current, is a combination of the cathodic and anodic current densities (j_{red} and j_{ox}), as depicted in **Figure 2.5A** and **Equation 2.7**. At the standard free energy state of activation, the change in electrode potential shifts the energy profiles and leads to the Faradaic current following the so-called Butler-Volmer equation, which demonstrates the relation between the current density and electrode potential under non-equilibrium conditions (**Equation 2.8**, **Equation 2.9**, and **Equation 2.10**). The value of exchange current density (j_0) can be obtained via the extrapolation of the current in the Tafel plots, as shown in **Figure 2.5B**, which is essential to evaluate the reaction kinetics at electrode surfaces.

$$j_{tot} = j_{red} + j_{ox} \qquad \textbf{Equation 2.7}$$

$$j_{tot} = j_0 \{\exp\left[\frac{(1-\alpha)nF\eta}{RT}\right] - \exp\left[\frac{-\alpha nF\eta}{RT}\right]\} \qquad \textbf{Equation 2.8}$$

$$\eta = E - E_{eq} \qquad \textbf{Equation 2.9}$$

$$j_0 = nFk^0 C_{ox}^{*(1-\alpha)} C_{red}^{*\alpha} \qquad \textbf{Equation 2.10}$$

Here, n is the number of electrons transferred (i.e., $n = 1$ for a one-electron transfer), F is the Faraday constant, α is the symmetry factor, E and E_{eq} are the applied potential and the equilibrium potential, k^0 the standard rate constant, and C_{ox}^* and C_{red}^* are the bulk concentrations of electroactive species being oxidized or reduced, respectively. The overpotential (η) is defined as the difference between the applied potential at the electrode and the equilibrium potential, as shown in **Equation 2.9**. As the reaction reaches the equilibrium condition ($E = E_{eq}$ and $\eta = 0$), the net current is zero ($j_{tot} = 0$) and $j_0 = j_{ox} = -j_{red}$. Further elaboration on the entire procedure and equation

derivation can be found in textbooks.[130,133]

(A) (B)

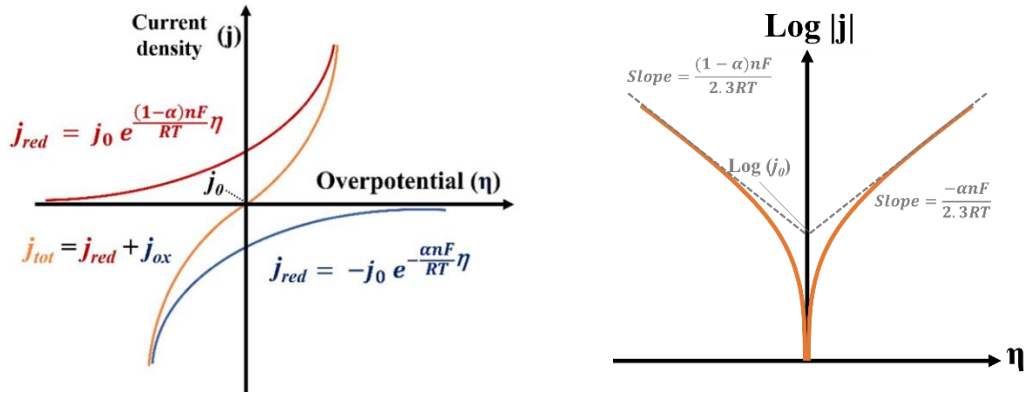

Figure 2.5. (A) The current density-overpotential profile based on the Butler-Volmer equation with j_{tot} consisting of j_{red} and j_{ox}. (B) The Tafel plot with the determination of j_0 and Tafel slopes for the reaction kinetics.

In fact, the Butler-Volmer equation only describes the half-cell reactions taking place in energy conversion devices. **Figure 2.6A** depicts the polarization curves of complete cells for water electrolyzers and hydrogen fuel cells, illustrating the hydrogen and oxygen redox reactions at equilibrium potentials of 0 V and 1.23 V, respectively. For example, overpotentials above the thermodynamic equilibrium potentials must be applied to produce H_2 and molecular oxygen (O_2) in water electrolyzers under equal current densities on both anode and cathode sides. Similarly, the fuel cell voltage controls the current density of the reversed reactions. It is noted that the total reaction rate of both water electrolyzers and hydrogen fuel cells is mainly limited by the oxygen reactions due to their poor reaction kinetics compared to the hydrogen reactions.

Figure 2.6B illustrates the three primary losses in the voltage-current (density) profile of a proton-exchange membrane fuel cell (PEMFC). As mentioned earlier, close to the thermodynamic ideal voltage (E_0), the activation energy dominates the reaction kinetics at the electrocatalyst surface. As the current density further increases, the ohmic losses, primarily due to the resistance of the membrane electrode assembly (MEA) and the

electronic contacts of each component, cause the potential to decrease linearly with increasing current density. Finally, the cell voltage drops significantly when the diffusion limitations are reached. This is attributed to the slow mass transport of reactants through the gas diffusion layer (GDL) and MEA, resulting in a concentration gradient towards the highly reactive electrode surfaces.[134,135]

(A) (B)

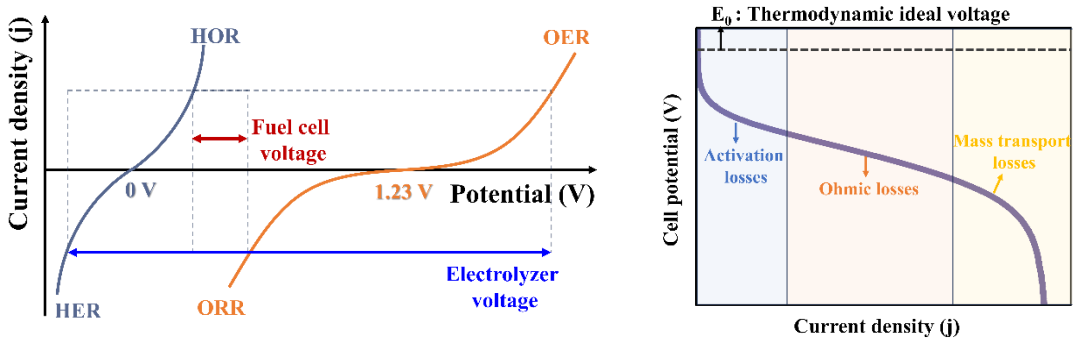

Figure 2.6. (A) A schematic of polarization curves for the water electrolyzer and hydrogen fuel cell. Adapted with permission from reference [136]. Copyright © 2016, Springer Science Business Media New York. (B) The current density-voltage profile of a complete fuel cell with the different types of losses. Adapted with permission from reference [137].

2.3. Typical Electrocatalytic Reactions in Fuel Cells and Electrolyzers

Energy conversion devices, such as water electrolyzers and fuel cells, are pivotal in converting electric energy into chemical energy and vice versa. This section will briefly introduce the fundamental working principles, typical reactions, reaction mechanisms, and state-of-the-art electrocatalysts for these devices in acidic and alkaline media.

Figure 2.7A shows the basic operating principle of the proton-exchange membrane (PEM) water electrolyzers. When an external bias is applied through the external circuit, hydrogen ions (e.g., H^+ and hydronium, H_3O^+) undergo reduction at the cathode during the HER, while water molecules are oxidized at the anode during the oxygen evolution reaction (OER), as shown in **Equation 2.11**, **Equation 2.12**, and **Equation 2.13**.

Overall reaction	$2H_2O \rightarrow 2H_2 + O_2$	**Equation 2.11**
HER (cathode)	$4H^+ + 4e^- \rightarrow 2H_2$	**Equation 2.12**
OER (anode)	$2H_2O \rightarrow O_2 + 4H^+ + 4e^-$	**Equation 2.13**

On the other hand, a PEMFC demonstrates the reverse reactions, as shown in **Figure 2.7B**. H_2 fuel is oxidized at the anode via the hydrogen oxidation reaction (HOR), and O_2 is reduced at the cathode via the ORR to produce electricity (see **Equation 2.14**, **Equation 2.15**, and **Equation 2.16**).

Overall reaction	$2H_2 + O_2 \rightarrow 2H_2O$	**Equation 2.14**
ORR (cathode)	$O_2 + 4H^+ + 4e^- \rightarrow 2H_2O$	**Equation 2.15**
HOR (anode)	$2H_2 \rightarrow 4H^+ + 4e^-$	**Equation 2.16**

In water electrolyzers and fuel cells, electron flow moves from the anode to the cathode.

However, the positive and negative electrolyte ions, such as H^+ and hydroxide (OH^-), move in opposite directions through the membrane to maintain the electroneutrality of the device. This results in different reaction pathways in acidic and alkaline environments.[138,139,140]

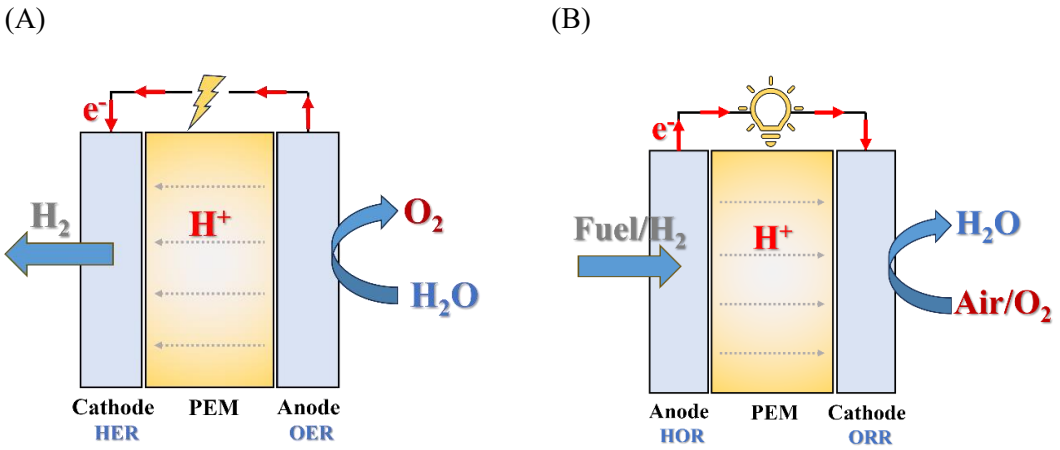

Figure 2.7. The schematic of a PEM (A) water electrolyzer and (B) fuel cell. During the electrolysis process, H_2 and O_2 gases are produced at the cathode through the HER and the anode through the OER. In contrast, a fuel cell operates in the opposite reaction direction to generate electricity. For a fuel cell in acidic media, H_2 serves as a fuel and undergoes oxidation at the anode via the HOR, while O_2 from air is reduced at the cathode through the ORR. H^+ travels through the PEM from the anode to the cathode in acidic solutions to maintain electroneutrality and balance the electron flow in an external circuit.

2.3.1. Hydrogen Evolution Reaction

The HER occurring at the cathode during water electrolysis is a simple two-electron electrochemical process.[141] The whole HER process involves three elementary steps. In acidic media, the first step involves proton reduction via electron transfer and subsequent adsorption on the free active sites of the electrocatalyst, known as the Volmer step (**Equation 2.17**). Here, the adsorbed hydrogen atom is noted as $^*H$. Following the Volmer step, the HER follows two different pathways in the second step.

The Heyrovsky step (**Equation 2.18**) illustrates the reduction of the second proton at the same $^*H$ site, resulting in the formation of H_2. Alternatively, the Tafel step (**Equation 2.19**) describes a mechanism where two $^*H$ species from separate active sites combine directly to produce H_2 at the electrode surface.

Volmer step	$H^+ + e^- \rightarrow {}^*H$	**Equation 2.17**
Heyrovsky step	${}^*H + H^+ + e^- \rightarrow H_2$	**Equation 2.18**
Tafel step	$2{}^*H \rightarrow H_2$	**Equation 2.19**

In contrast, the HER in alkaline media involves water dissociation to form $^*H$ and OH^- of the Volmer and Heyrovsky steps (**Equation 2.20** and **Equation 2.21**), while the Tafel step (**Equation 2.22**) remains the same as in acidic media.[142,143]

Volmer step	$H_2O + e^- \rightarrow {}^*H + OH^-$	**Equation 2.20**
Heyrovsky step	$H_2O + {}^*H + e^- \rightarrow H_2 + OH^-$	**Equation 2.21**
Tafel step	$2{}^*H \rightarrow H_2$	**Equation 2.22**

As a result, the HER pathway can follow either the Volmer-Heyrovsky or the Volmer-Tafel mechanism in acidic and alkaline solutions. A detailed exploration of HER kinetics, adsorption, and mass transport characteristics via the combined RDE-EIS approach will be discussed in **Section 4.2**. Furthermore, the binding strength of $^*H$ is a crucial factor affecting HER kinetics. **Figure 2.8A** displays a volcano plot representing HER activity, with the logarithm of j_o plotted against the chemisorption energy of $^*H$ on the metal electrodes (E_{ME-H}) as the descriptor.[144,145] According to the Sabatier principle, the optimal interaction between the intermediate (e.g., $^*H$) and the metal catalysts should be precisely balanced. Platinum-group metals like Pt, Rh, and Ir, positioned at the peak of the volcano plot, present promising HER performances. However, they tend to exhibit slightly stronger hydrogen bond strengths. Conversely,

electrocatalysts situated on the left side of the plot, such as Au and Ag, display lower j_0 values due to comparatively weaker hydrogen binding.

(A) (B)

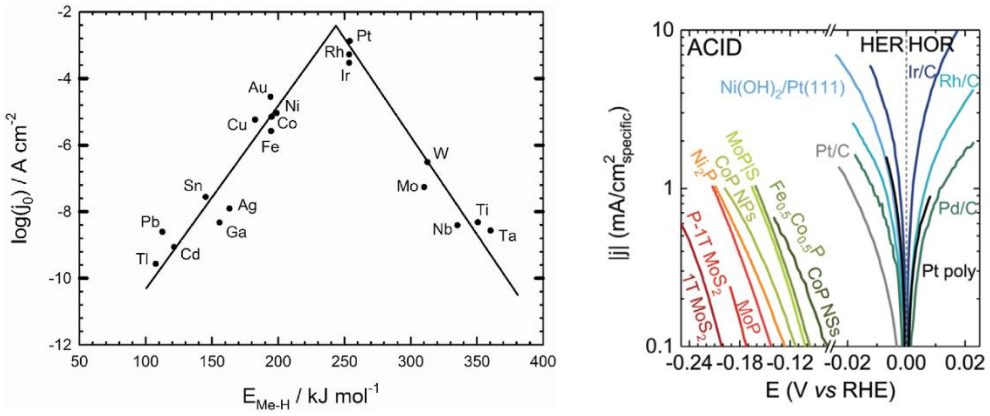

Figure 2.8. (A) The volcano plot for the HER with the relationship between the logarithm of j_0 and the E_{ME-H}. Reprinted with permission from reference [144]. (B) The state-of-the-art electrocatalysts with mass activity for HER/HOR in acid. Reprinted with permission from reference [146]. Copyright © 2019 WILEY-VCH Verlag GmbH & Co. KGaA, Weinheim.

Figure 2.8B illustrates the state-of-the-art electrocatalysts for HER in acid electrolytes,[146] in which the noble metal catalysts with superior HER activities follow the predicted volcano plot (**Figure 2.8A**). However, their restricted sources and high costs bring efforts to explore alternative promising materials, such as nonprecious electrocatalysts like MoS_2 and transition metal phosphides like CoP and Ni_2P.[146,147,148,149] Another promising approach involves optimizing the electrolyte compositions. Studies have reported that cation effects in alkaline media can influence the HER activity for Pt electrodes in the following order: LiOH > NaOH > KOH > RbOH > CsOH.[150,151]

2.3.2. Hydrogen Oxidation Reaction

The HOR illustrates the reverse reaction pathways of HER with the same elementary steps, as shown in **Equation 2.16**. The correlation between hydrogen bond strength and reaction kinetics resembles the HER volcano plot depicted in **Figure 2.8A**. Pt/C catalysts are currently the state-of-the-art anode materials for fuel cells. Its high reaction rate allows for an ultralow Pt mass loading (0.05 mg_{Pt}/cm^2) with an overpotential of less than 3 mV in PEMFCs.[152,153,154] However, even when using reformed H_2 fuel with only trace amounts of carbon monoxide (CO), PEMFCs suffer from CO poisoning of the Pt electrocatalyst of the anode.[155] Therefore, alternative anode materials with higher CO tolerance, such as Pt alloys like Pt-Ru, Pt-Mo, and Pt_3Sn, are reported.[156,157,158,159,160] The other candidates are non-precious catalysts like Ni-based alloys in hydroxide exchange membrane fuel cells (HEMFCs). Nevertheless, the reaction kinetics in alkaline electrolytes are 2-3 orders of magnitude slower than in acidic media.[161,162] Therefore, higher mass loading of catalysts is necessary to reach the same power output level as the counterpart in acid.

2.3.3. Oxygen Reduction Reaction

The ORR at the cathode, shown in **Equation 2.15**, is critical to the operation of PEMFCs. Due to the highly complex electron transfer process, the activation losses within the low overpotential region are primarily attributed to the ORR, as shown in **Figure 2.6**. As a result, the current mass loading of Pt in PEMFCs is approximately 0.4 mg cm^{-2} at the cathode,[153,163,298] making the ORR a significant bottleneck for commercial product development. **Figure 2.9A** illustrates the possible ORR pathways in acidic solutions.[164] The four-electron pathway is preferred in fuel cell systems and

can be further described using dissociative and associative mechanisms. Initially, O_2 molecules are adsorbed onto the electrode surface. In the dissociative mechanism, the O-O bonds break to form *O intermediates, which are then reduced to *OH and finally to H_2O molecules. In the associative mechanism, $*O_2$ is first converted to *OOH, generating the same *O and *OH intermediates, finally forming H_2O. Based on theoretical DFT calculations, the dissociative mechanism dominates at lower overpotentials, while the associative mechanism is more dominant at higher overpotentials.[74,164] In contrast, the two-electron pathway involves the formation of hydrogen peroxide as an intermediate ($*H_2O_2$) or H_2O_2 as a by-product. This pathway is challenging because H_2O_2 is difficult to reduce completely, and some decompose to O_2. Therefore, the peroxide pathway is unfavorable in fuel cells due to the lowered current and the possibility of corrosion of active electrocatalysts.[164,165] However, in terms of selectivity, it could be advantageous to produce H_2O_2, which is essential for many industrial applications.[166]

The ORR mechanism in alkaline media involves H_2O molecules as the reactant, unlike in acidic media, where H_2O is the product. **Figure 2.9B** schematically demonstrates the EDL structure during the ORR in an alkaline environment and suggests two possible reaction pathways.[167,313] First, the four-electron pathway in alkaline media occurs in the inner-sphere region by following a series of reactions (**Equation 2.23**).

Four-electron pathway

$$O_2 \rightarrow {}^*O_2 \qquad \textbf{Equation 2.23}$$

$$^*O_2 + H_2O + 2e^- \rightarrow {}^*OOH + OH^-$$

$$^*OOH + H_2O + 2e^- \rightarrow 3OH^-$$

The second mechanism appears within the outer-sphere region, where the solvated O_2 weakly interacts with the adsorbed hydroxyl species to undergo the two-electron

pathway with the formation of HOO^- as a product (**Equation 2.24**), compared to OH^- in the four-electron pathway (**Equation 2.23**). The desorption of the final product anion can be detected by using a rotating ring-disc electrode (RRDE) configuration.[167,313]

Two-electron pathway

$$M - OH + [O_2 \cdot (H_2O)_n]_{aq} + e^- \rightarrow M - OH + {}^*(HO_2) + OH^- + (H_2O)_{n-1} \quad \textbf{Equation 2.24}$$

$${}^*(HO_2) + e^- \rightarrow {}^*(HO_2^-)$$

$$(HO_2^-)^* \rightarrow (HO_2^-)_{aq}$$

(A) (B)

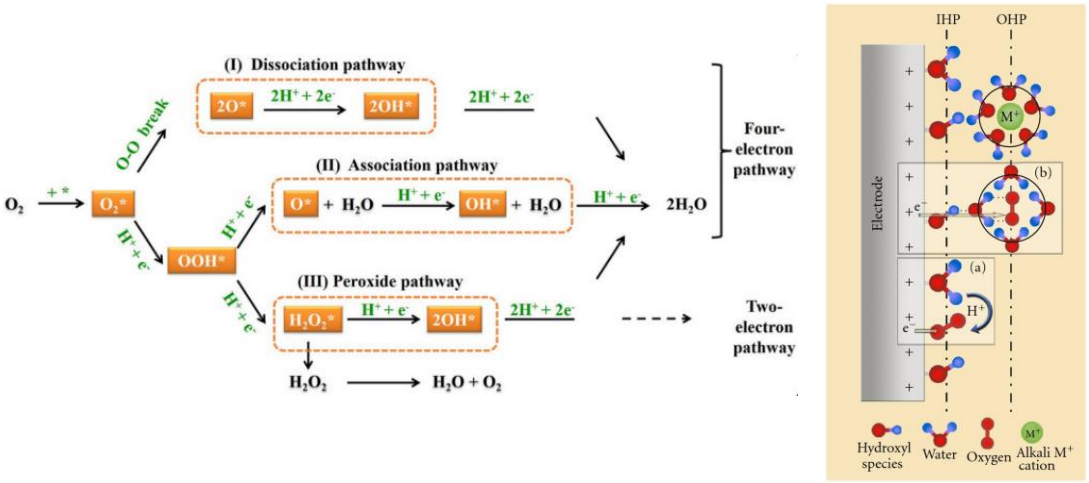

Figure 2.9. (A) The ORR mechanisms in an acidic environment (i.e., PEMFC) with the four-electron and two-electron pathways. Reprinted with permission from reference [164]. (B) A schematic of the interfacial double-layer structure during the ORR in alkaline media. Reprinted with permission from reference [167]. Copyright © 2012 Nagappan Ramaswamy and Sanjeev Mukerjee.

According to the ORR volcano plot of single-metal electrocatalysts in **Figure 2.2A**, Pt is located close to the peak, demonstrating the balanced binding energy with the intermediates. However, optimizing the binding conditions of single intermediates is limited by the scaling relations, making overcoming the overpotential challenging.

Theoretically, the optimal state of the ORR volcano plot is identified where the binding energy of *O is approximately 0.2 eV lower than that of pure Pt through DFT calculations.[78,304] Additionally, the formation of Pt oxides on the electrode surface under specific potential regions affects the reaction mechanisms with the involvement of different intermediates and alters the electrocatalytic activity, stability, and selectivity. The phenomenon takes an essential understanding of how reaction conditions change and requires further precise experimental and theoretical investigation.[168,169,170,171,172]

Considering the structure-sensitivity of extended Pt surfaces and nanoparticles, **Figure 2.10A** shows the relationship between the generalized coordination number ($\overline{CN}$) of the Pt(111) surface as a descriptor and the corresponding activities (or overpotentials). The $\overline{CN}$ considers the variation among the neighbors of an atom i with n_i first nearest neighbors in the following **Equation 2.25**:[173,174]

$$\overline{CN}(i) = \sum_{j=1}^{n_i} \frac{cn(j)}{cn_{max}} \qquad \textbf{Equation 2.25}$$

Here, $cn(j)$ are the conventional coordination numbers of the first nearest neighbors and cn_{max} is the maximum coordination as found in the bulk. On the terrace site of Pt(111) surface, the corresponding $\overline{CN}$ is equal to 7.5 with 0.15 V of overpotential. It is found that the surface atoms on concave sites with $\overline{CN}$ > 7.5 (blue) are more active towards the ideal peak position in the corresponding volcano plot. However, atoms on convex sites with $\overline{CN}$ < 7.5 (red) are less active.

Besides geometric structuring, efforts are reported to optimize the ORR activity and durability by alloying it with 3d transition metals (e.g., Fe, Co, Ni, and Cu) and lanthanide materials (e.g., La, Ce, and Gd).[68,175,176,177,301,178] **Figure 2.10B** shows the "double volcano" plot for polycrystalline and nanostructured Pt alloys, illustrating the relative ORR activities at 0.9 V vs. RHE with respect to the atomic radius of solute

atoms. For instance, Pt_xCu and Pt_xY alloys exhibit approximately six times higher activities than pure Pt. The formation of bimetallic alloys modifies the electronic structure of the catalyst active sites through the so-called strain and ligand effects.[179,180,181,182]

(A) (B)

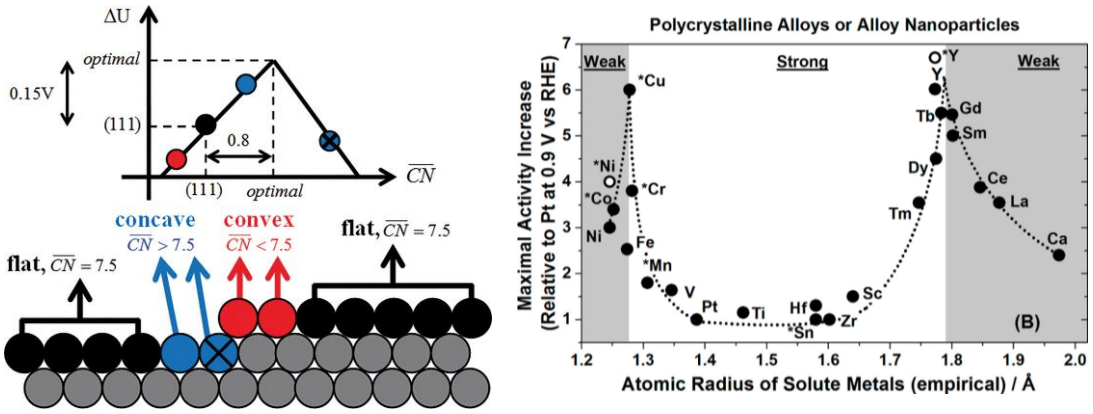

Figure 2.10. (A) A summary of the relations between the site geometry on a Pt (111) surface and the corresponding ORR activities. Reprinted with permission from reference [174]. (B) The reported maximum ORR activities of Pt alloys (including polycrystalline and nanostructured electrocatalysts) compared to reference Pt at 0.9 V vs. RHE as a function of the atomic radius of solute metals. Reprinted with permission from reference [179]. Copyright © 2016, American Chemical Society.

The strain effect arises from the difference in lattice parameters between the atoms in the surface layers and those in the bulk, introducing either compressive or tensile strain on the electrode surface. The ligand effect appears due to heterometallic bonding interactions of surface atoms with dissimilar neighboring atoms. Due to their close relation, it is difficult to decouple the influence of the strain and ligand effects on chemical properties. However, the ligand effect can be disregarded under certain conditions with more than three atomic layers away from the surface.[68,179,301]

In addition, electrolyte composition, such as cation effects, profoundly impacts ORR performance. For example, the ORR activity of Pt(111) electrodes in alkaline media

follows an opposite trend to that of HER, increasing activity as the cation hydration energy decreases. The effect of alkali cations on ORR performance for Pt alloys with different surface strains is further explored in **Section 4.3**.

2.3.4. Oxygen Evolution Reaction

The overall OER at the anode during water splitting involves complex four-electron transfer pathways, as shown in **Equation 2.13**. This results in slower reaction kinetics and higher overpotentials compared to the HER at the cathode for the same current density. Similarly to the other reactions discussed above, the electrolyte's pH also influences the OER. **Figure 2.11A** shows the possible reaction mechanisms for OER in both acidic (blue line) and alkaline (red line) solutions, highlighting the black route, which involves several reaction intermediates (*OH, *O, and *OOH) leading to the formation of O_2. Alternatively, the green route excludes the formation of an *OOH intermediate and involves the direct combination of two *O to form O_2.[183] The binding energy of these intermediates determines the overall reaction performance, as depicted in the OER volcano plot in **Figure 2.11B**.[184]

Different from the other electrolyzer and fuel cell reactions, Pt-based electrocatalysts do not exhibit the highest OER activity. This is because the OER occurs at high potentials far from its thermodynamic equilibrium potential of 1.23 V vs. RHE, leading to the formation of thick Pt oxide layers on the surface. These oxides have poor electronic conductivity and differ from the Pt surface formed during the ORR, reducing the OER activity.[185,186] In contrast, many other oxides offer better binding conditions for the OER reaction intermediates with smaller overpotentials, as shown in **Figure 2.11B**.

For instance, iridium oxide (IrO_2) is recognized as an effective OER electrocatalyst

among noble metal oxides. However, due to the high cost and limited availability of noble metals and the limited stability in alkaline media caused by anodic dissolution at higher oxidation potentials,[98,187,188] alternative materials are being explored. First-row transition metal-based (e.g., Fe, Co, and Ni) oxides, perovskite oxides, and FeCoW oxyhydroxides demonstrate promising OER performance.[98,189,190,191]

(A) (B)

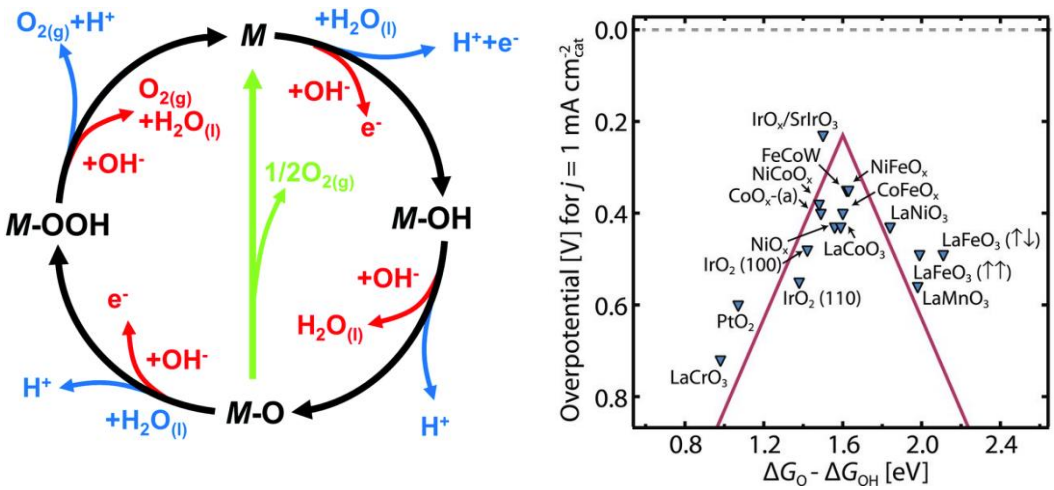

Figure 2.11. (A) The reaction pathways of OER in acidic (blue) and alkaline (red) media. The black line involves the participation of *OOH, while the green line shows the direct combination of *O intermediates in the OER mechanisms. Reprinted with permission from reference [183]. (B) The OER volcano plot for the metal-oxide electrocatalysts with experimental and theoretical findings. Reprinted with permission from reference [184].

3. Experimental

3.1. Surface Characterization

3.1.1. X-ray Diffraction

X-ray diffraction (XRD) is a non-contact and non-destructive technique that provides robust information about chemical characterization and crystalline phases in materials.[192,193] As shown in **Figure 3.1**, the basic working principle of XRD follows Bragg's law,[194,195,196] which explains the relationship between the incident and reflecting angles of the crystal surface with the following **Equation 3.1**:

$$n'\lambda = 2d_{hkl}sin\theta \qquad \textbf{Equation 3.1}$$

where n' is an integer, λ is the wavelength of the X-ray, d_{hkl} is the space between two crystal layers in certain lattice planes (hkl), and θ is the diffraction angles of impinging and reflecting X-ray photons, respectively.

In this work, XRD measurements of Pt(pc), Pt_5Gd, and Pt_5Y electrodes were characterized using PANalytical X'Pert Pro equipment (Malvern Panalytical GmbH, Germany), which includes a Cu-Ka source (λ = 1.5406 Å) and a Ni-based filter. The samples were measured with a scanning range (2θ) from 5° to 90° and with a scan rate of about 0.78° min^{-1}. The XRD patterns were further fitted using the corresponding powder diffraction file (PDF) cards, in which the Pt-Pt distance in a specific axis can be estimated based on **Equation 3.1** for the Pt(pc) and Pt alloys. The relative surface strain can be further calculated due to the lattice mismatch between the bulk crystal and the Pt surface.

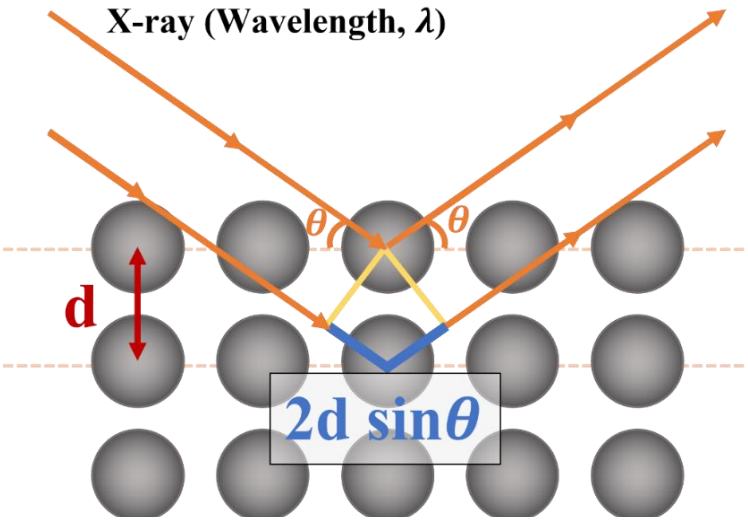

Figure 3.1. A schematic of XRD on a bulk crystal with the X-ray's incident and reflecting angles (θ) during constructive interference. The total phase difference, represented as 2dsinθ, occurs on the lattice planes, each spaced at a distance denoted as d.

3.1.2. X-ray Photoelectron Spectroscopy

In this work, X-ray photoelectron spectroscopy (XPS) was used to analyze the material surfaces' elemental composition and chemical bonding states.[197,198,199] **Figure 3.2** illustrates the working principle of XPS based on the photoelectric effect. The binding energy of the ejected electrons, known as photoelectrons, can be estimated by the measured kinetic energy with **Equation 3.2**:[200,201]

$$E_b = hv - E_k \qquad \textbf{Equation 3.2}$$

where E_b is the binding energy, h is Planck's constant, v is the frequency of exciting X-rays, and E_k is the kinetic energy, respectively. Each surface element's chemical and bonding condition is then derived from the XPS spectrum via the peak shifts.

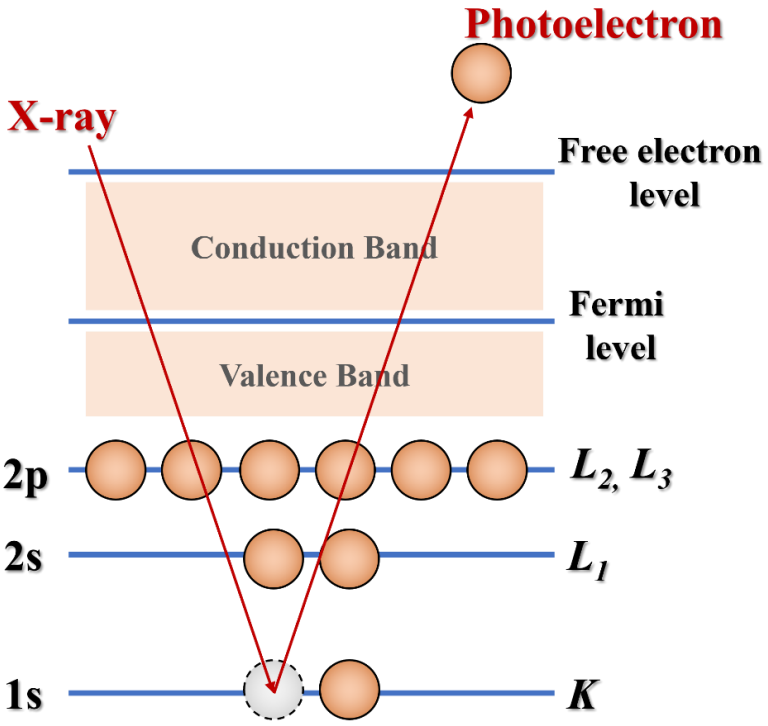

Figure 3.2. A schematic demonstration of the working principle of XPS based on the photoelectric effect. Adapted with permission from reference [200]. Copyright © 2019 Canadian Society for Chemical Engineering.

Thermo Scientific K-Alpha$^+$ was used in this work to investigate the surface composition of Pt-based alloys after electrochemical measurements, and the XPS spectra were fitted by the CasaXPS software. The molar concentration (x_i) of all elements of the electrode surface can be calculated by the following **Equation 3.3**:[202,203]

$$x_i = \frac{A_i/S_i}{\sum_{j=1}^{n}(A_j/S_j)} \qquad \textbf{Equation 3.3}$$

where A_i is the area under the corresponding core-level peak, s_i is the relative sensitivity factor (RSF), and n is the number of elements, respectively.

3.2. Electrochemical Measurements

3.2.1. Cyclic Voltammetry

Cyclic voltammetry is a common and robust technique used to study redox processes of molecular species[204,205,206] and to estimate the C_{dl}[207,208,209] at electrode/electrolyte interfaces. This analytical method provides the "fingerprint" of each material and electrolyte composition by recording the cyclic voltammogram (CV).

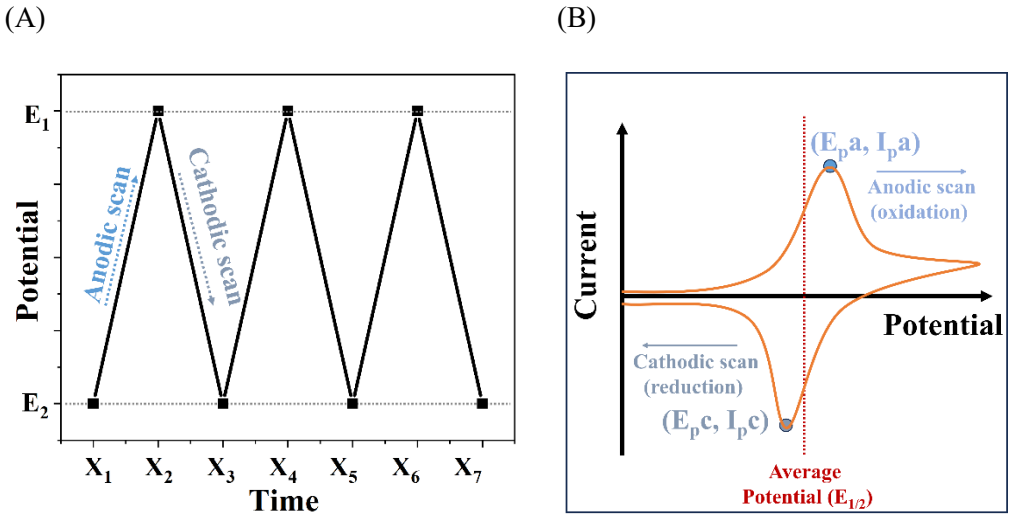

Figure 3.3. (A) A typical voltage-time profile with the applied potential varying linearly with selected potential from E_1 to E_2 over time with the noted anodic and cathodic scan sweep. (B) A CV profile with the applied potential and current response in an anodic (oxidizing) and a cathodic (reducing) scan.

Figure 3.3A shows the measuring procedure in cyclic voltammetry, in which the potential is varied linearly and periodically within the selected region between E_1 and E_2 with a constant scan rate (mV s^{-1}) over time. The scanning direction comprises the anodic and cathodic scans corresponding to the increasing and decreasing potential change. A CV shows the resulting current within an applied potential range, as shown in **Figure 3.3B**.

(A) (B)

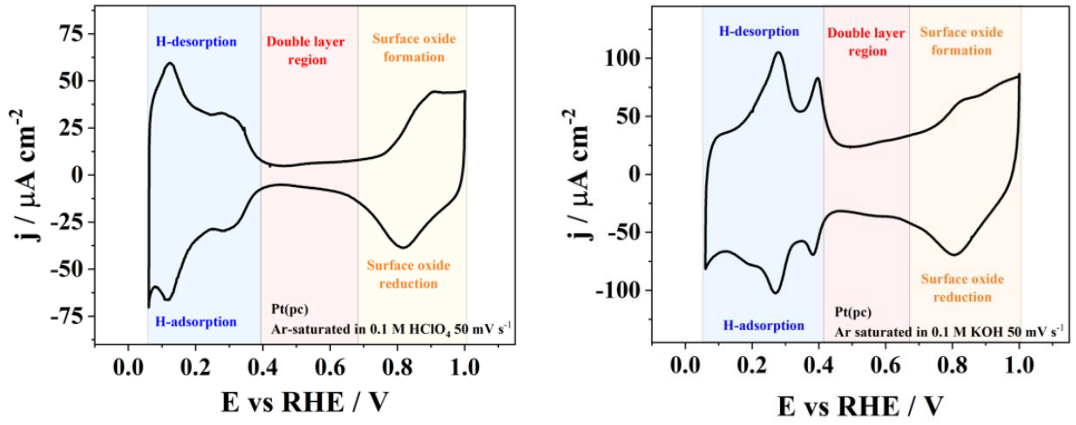

Figure 3.4. Typical CVs of Pt electrode measured in Ar-saturated 0.1 M (A) $HClO_4$ and (B) KOH solutions, respectively, including the marked hydrogen adsorption/desorption (blue), double layer (red), and surface oxide formation/reduction (yellow) regions. Adapted with permission from reference [294] (own work).

Figures 3.4A and **3.4B** show the typical CVs of the Pt(pc) electrode measured in Ar-saturated 0.1 M $HClO_4$ and KOH solutions in a three-electrode system. The marked potential regions, hydrogen absorption/desorption (blue), double layer (red), and oxide formation/reduction (yellow), demonstrate different electrochemical conditions on the catalyst surface. As the potential rises from above 0 to about 0.4 V vs. RHE, the underpotentially deposited (UPD) hydrogen undergoes desorption, and protons are released from the Pt surface. This desorption is accompanied by a charge transfer, offering one method to estimate the electrochemical active surface area (ECSA)[210,211,212] by integrating the adsorbed/desorbed proton charges. Within the potential range between around 0.4 V and 0.6 V vs. RHE, the estimated current from the selected scan rate is contributed by the charging/discharging of the EDL capacitance, which is briefly introduced in **Section 2.2.1**. As the potential continuously increases up to the theoretical equilibrium potential of ORR/OER at 1.23 V vs. RHE, the surface is oxidized by forming an oxide layer. On the other hand, at the cathodic scan (negative current), the processes reversely take place on the electrode surfaces.

3.2.2. Electrochemical Impedance Spectroscopy

EIS[213,214,215,216,217,218] is regarded as one of the most informative, non-destructive, and sensitive electrochemical techniques to study the reaction processes as well as the interfacial phenomenon for different types of current energy conversion and storage devices.[219,220,221,222,223,224] **Figure 3.5** illustrates the schematic concept of the EIS study on electrochemical solid/liquid interfaces. An EIS spectrum is obtained by applying a probing alternating current (AC) signal to a measuring system, regarded as a black box, and recording the system response. A physical model, represented by an electrical equivalent circuit (EEC), is often built to fit the obtained EIS spectra, extract information on the interfacial properties, and elaborate on the mechanistic insights of the studying systems.[225]

This work uses potentiostatic electrochemical impedance spectroscopy (PEIS), in which the potential is applied and the current is measured. The reverse measurement is called galvanostatic electrochemical impedance spectroscopy (GEIS), in which the current is controlled, and the potential is measured. In PEIS, the impedance can be represented by following **Equation 3.4**:

$$Z(\omega) = \frac{E(t)}{I(t)} = \frac{E_0 sin(\omega t)}{I_0 \sin(\omega t + \acute{\varphi})} = Re\big(Z(\omega)\big) + iIm\big(Z(\omega)\big) \qquad \textbf{Equation 3.4}$$

where $E(t) = E_0 sin(\omega t)$ is the applied sinusoidal potential as a function of time (t) with an amplitude (E_0) and a frequency (ω), and $I(t) = I_0 \sin(\omega t + \varphi)$ is the resulting sinusoidal current over time with an amplitude (I_0) and a phase shift ($\acute{\varphi}$), respectively.

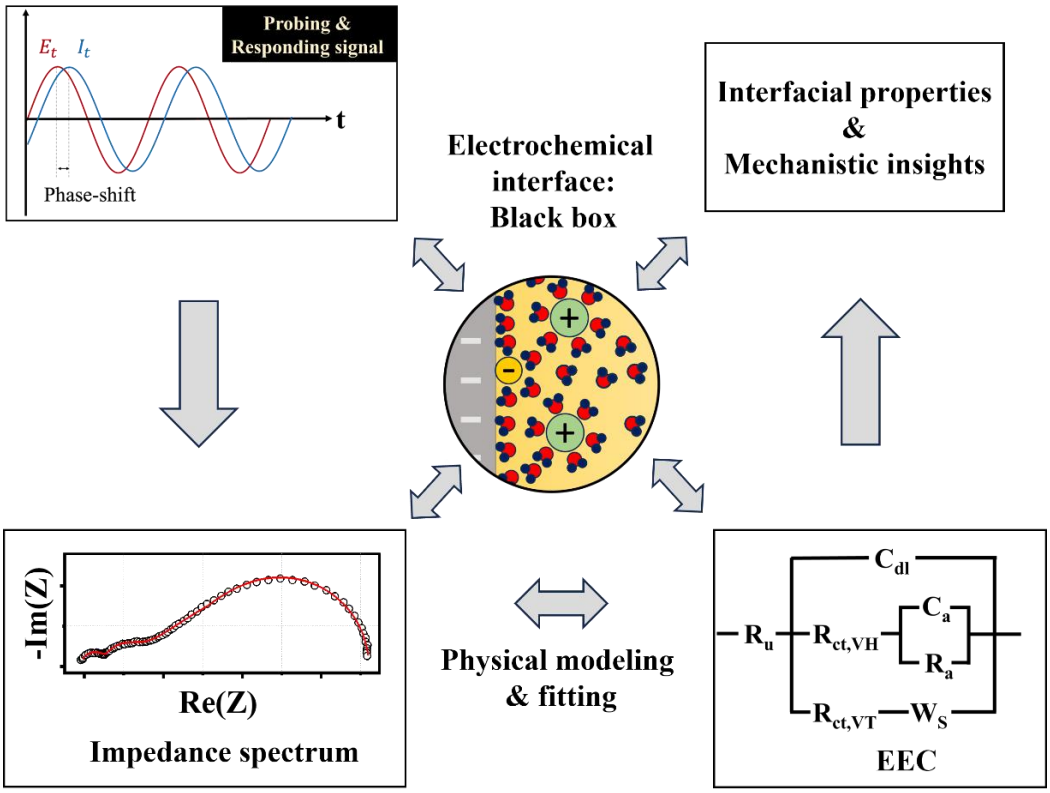

Figure 3.5. The schematic overview of an EIS analysis for an electrochemical interface. The potentiostat applies and records the probing and responding AC signals with a phase shift to the studied system. The subsequent impedance spectrum is then fitted using a physical model via an EEC to differentiate each interfacial parameter and demonstrate the mechanistic insights. Adapted with permission from reference [225].

Figures 3.6A and **3.6B** demonstrate two typical types of EIS data representation, including the Nyquist and Bode plots, respectively. The Nyquist plot includes a real part (ReZ) and an imaginary part (ImZ) of the impedance, with frequencies arranged from high to low values. The Bode plots represent the absolute value of impedance (|Z|) and the phase shift as a function of frequency.[226]

It is noted that a valid EIS measurement with a finite frequency range needs to fulfill the necessary conditions of causality, stability, and linearity.[213,227,228,229] Here, the criterion of causality is that the responding output signal must be only attributed to the perturbation of the input signal. Stability requires that the system should not change

significantly over time and return to the initial state once the external signal is removed. Linearity involves applying probing signals with small amplitudes (typically a few millivolts) to reach the quasi-linear condition since the electrochemical systems are usually highly nonlinear.

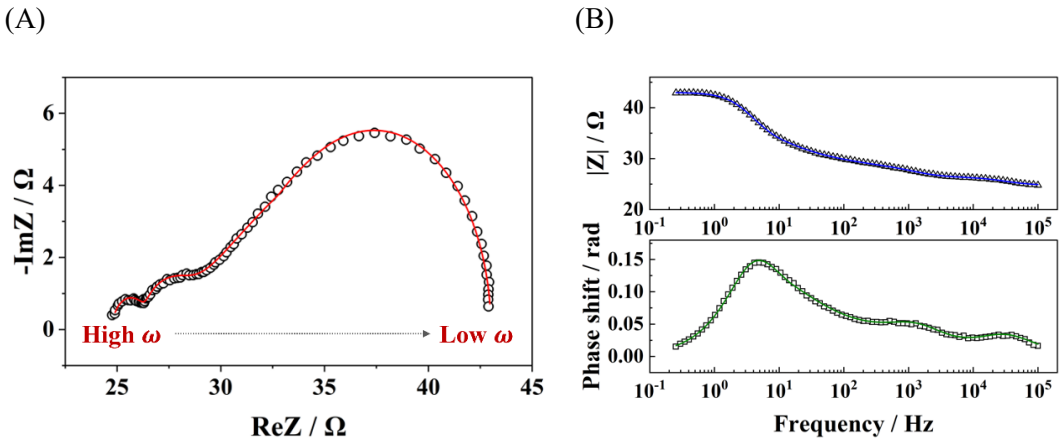

Figure 3.6. A typical (A) Nyquist plot and (B) Bode plots with the absolute value of impedance and the phase shift shown over selected frequencies. The EIS spectra were taken with an RDE setup using a Pt electrode under HER conditions. Adapted with permission from reference [276] (own work).

The Kramers-Kronig (KK) transformation algorithms provide a checking approach for evaluating the validity of impedance data[230,231,232,233,234,235,236,237] by mathematically calculating the real part from the imaginary part of the impedance and vice versa. In other words, the application of the KK relations in an electrochemical system is free of any physical models and assumptions. It can ensure impedance spectra satisfy the required conditions before the subsequent fitting and analysis via an EEC model.

As mentioned before, the physical impedance models can be expressed via EECs or mathematical equations, which contain the physicochemical parameters to model the electrochemical processes at the electrode/electrolyte interfaces. According to the Dolin-Ershler-Randles approximation,[213, 238 , 239 , 240] the electrochemical reactions consist of at least three main parts contributing to the EIS response of the

electrode/electrolyte interfaces. These components include the capacitive contributions from the interfacial impedance (the impedance of EDL or the interface itself), the charge transfer (Faradaic) reactions, and the electrolyte resistance. Notably, the first two parts are connected (exist) in parallel.

Here, several common elements in the EECs are described in **Table 3.1**, along with the symbols and the corresponding impedances.

Table 3.1. The common elements in the EEC models to fit impedance dada.

Elements	Symbol	Impedance
Resistor	R	$R = Z$
Inductor	L	$Z = j\omega L$
Capacitor	C	$Z = 1/j\omega C$

A resistor (R) is independent of frequency (ω) and contributes to the real part of the impedance. It describes the resistances of a liquid electrolyte, the charge transfer resistances, and the resistances of adsorption. The impedance of an inductor (L) is directly proportional to the frequency with the phase shift leading to a straight line in the Nyquist plots and the positive values of ImZ. In addition, a capacitor (C) demonstrates the opposite trend of an inductor and shows a straight line and the negative values of ImZ. It is used to model the EDL's response and the adsorption pseudocapacitance. In the practical situation, the constant phase element (CPE) is also used to replace the pure capacitor in the modeling of the EDL remarked as the following **Equation 3.5**:

$$Z_{dl} = Z_{CPE} = 1/(C'_{dl}(j\omega)^n) \qquad \textbf{Equation 3.5}$$

where the n value is the exponent of the CPE and C'_{dl} is the parameter that is proportional to the capacitance of the EDL (i.e., C_{dl}). If $n = 1$, Z_{CPE} is considered as a

pure ideal capacitor. However, if $n = 0$, it is regarded as a pure resistor. Subsequently, the C_{dl} is approximately close to C'_{dl}, if n is very close to 1. Moreover, if the constant phase shift is equal to 45°, the electrochemical system is related to the diffusional Warburg impedance (W). Under the semi-infinite diffusion condition, the Warburg element is used to describe the linear diffusional behavior, where the thickness of the diffusion layer is assumed to be infinite, as described by the following **Equation 3.6**:

$$Z_w = \frac{A_W}{\sqrt{\omega}} + \frac{A_W}{j\sqrt{\omega}} \qquad \textbf{Equation 3.6}$$

where the Warburg coefficient (A_W) is regarded as the coefficient dependent on the surface concentration of the electroactive species from the electrolyte side. In comparison, if the thickness of the diffusion layer is defined to a finite length, it is considered in the framework of the transmissive boundary and reflective boundary conditions, which are represented by the Warburg short (W_s) and the Warburg open (W_o) elements, respectively. Their corresponding impedances, Z_{Ws} and Z_{Wo}, are expressed by the following **Equation 3.7** and **Equation 3.8**.

$$Z_{Ws} = \frac{A_W}{\sqrt{j\omega}} \tanh(B\sqrt{j\omega}) \qquad \textbf{Equation 3.7}$$

$$Z_{Wo} = \frac{A_W}{\sqrt{j\omega}} \coth(B\sqrt{j\omega}) \qquad \textbf{Equation 3.8}$$

A detailed description of each element in the proposed EEC model for the HER mechanisms with the RDE setup is discussed in **Section 4.2**. In this work, the EIS data were first checked with the KK tests and then fitted and analyzed with EIS Data Analysis 1.3 software.

3.2.3. Electrochemical Active Surface Area

ECSA is an important parameter to calculate the specific activities of electrocatalysts with different types of material, structure, morphology, geometry, etc., as well as to investigate the degradation/aging of the electrodes in fuel cells and electrolyzers.[211,241,242,243,244,245,246] The evaluation of ECSA by the electrochemical methods for Pt and Pt-based electrocatalysts includes integration of the charge of oxidation peaks corresponding to monolayers of adsorbed species, such as underpotentially deposited hydrogen (H_{UPD}) and some metals and adsorbed CO molecules.[212,247,248]

This study uses copper underpotential deposition (Cu_{UPD}) and its subsequent stripping to distinguish the contributions between Pt and the secondary element in alloys, compared to conventional methods like H_{UPD} and CO stripping.[146,249,250] This approach allows for a more precise estimation of the ECSA for Pt_5Gd and Pt_5Y electrodes after operating electrochemical measurements because Cu forms a pseudomorphic overlayer, where one Cu atom goes to one Pt atom at the surface. The experimental procedures were based on the references.[251,252] The surface area is calculated based on the assumption that the stripping Cu_{UPD} on each surface atom is oxidized and then desorbed from the surface, as described in the following **Equation 3.9**.

$$Cu_{UPD} \rightarrow Cu^{2+} + 2e^{-} \qquad \textbf{Equation 3.9}$$

Before conducting Cu_{UPD} measurements, the electrode surface was cycled for the electrochemical cleaning. The voltammogram was then recorded in the potential range 0.06 V to 1.0 V vs. RHE in 0.1 M Ar-saturated $HClO_4$ solution at a scan rate of 20 mV s^{-1}. Subsequently, the electrode was immersed in an Ar-saturated solution with a mixture of 0.1 M $HClO_4$ and 2 mM Cu^{2+}, by utilizing the hanging meniscus configuration to avoid excessively immersed surface. The measured electrode was

polarized at 1.0 V vs. RHE for 160 seconds to eliminate any residual Cu and subsequently at 0.3 V vs. RHE for 100 seconds to form a Cu_{UPD} monolayer without any deposition of bulk Cu on the surface. The first cycle of CV was then recorded within the potential range between 0.3 V and 1.0 V vs. RHE under the same scan rate, as demonstrated in **Figure 3.7**. The ECSA was calculated by **Equation 3.10**:

$$ECSA = \frac{Q}{\theta \times Q_{ML}} \qquad \textbf{Equation 3.10}$$

where Q is the measured charge from the oxidation of the adsorbed Cu atoms (the integration of the red dotted area in **Figure 3.7**), θ is the coverage ratio, and Q_{ML} is the charge density related to a Cu monolayer formation on the surface (420 µC cm^{-2}), respectively. The value of θ is assumed to be equal to 1 due to sufficient polarization time to form a Cu monolayer on the surface.

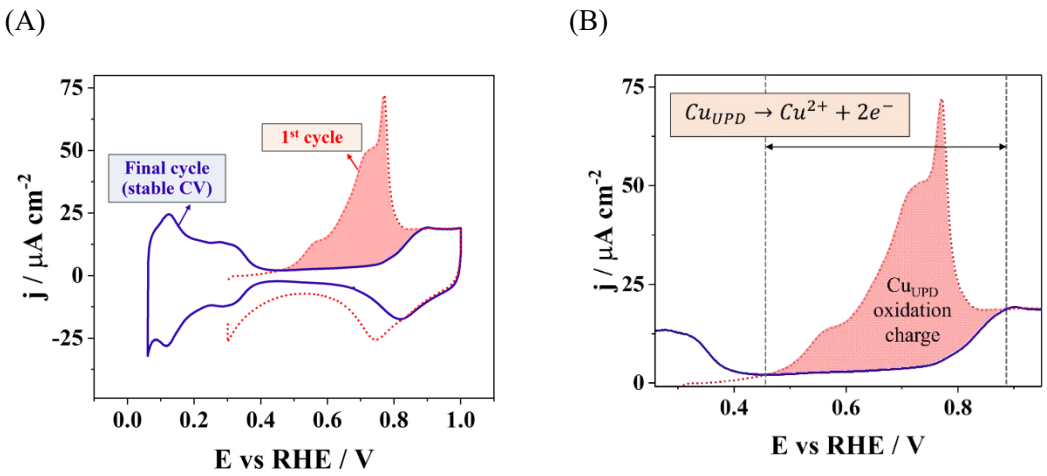

Figure 3.7. The example of the Cu_{UPD} measurement for Pt(pc) electrode. (A) The profile shows the stable CV (purple) and the 1st cycle of CV (red), recorded in Ar-saturated 0.1 M $HClO_4$ and a mixture of 0.1 M $HClO_4$ and 2 mM Cu^{2+} solutions, respectively, at a scan rate of 20 mV s^{-1}. (B) The evaluation of integrating Cu_{UPD} oxidation charge within the red dotted area. Adapted with permission from reference [294] (own work).

3.2.4. Calibration of Reference Electrodes

In this work, the reported potential is presented in the RHE scale, which is commonly used to evaluate and compare the electrocatalytic performance of the electrochemical measurements in a three-electrode system.[131,253] The conventional approach to convert the potential to the RHE scale is based on the Nernst equation. For example, the potential with a mercury-mercurous sulfate (MMS) electrode as a reference electrode (RE) is converted to the RHE scale by the following **Equation 3.11**:[176]

$$E_{RHE}(V) = E_{MMS} + 0.66V + 0.059V * pH \qquad \textbf{Equation 3.11}$$

However, this method may not consider the undefined potential shifts, like a liquid junction potential[254,255,256] appearing between the conducting electrolyte and the inert electrolyte of RE, and cause errors in estimating the activities of measured electrocatalysts. To more accurately report the measured potential vs RHE, it is necessary to calibrate the REs in the different acidic and alkaline solutions using the following procedure. **Figure 3.8** shows the calibration examples of 0.1 M $HClO_4$ and KOH electrolytes with an MMS electrode as a RE. The electrolyte was firstly purged with H_2 for about 30 minutes to obtain the H_2-saturated condition. The CV was then recorded with a scan rate of 10 mV s^{-1} at 1600 revolutions per minute (rpm) within the intersection potentials close to zero current to achieve the average potential for the measured acidic and alkaline electrolytes. The detailed calibration results for each acidic and alkaline medium, measured with two types of REs, including a MMS electrode and a mercury-mercuric oxide (MMO) electrode, are listed in **Table 3.2**. It is observed that there is approximately 30 mV of potential difference between the theoretical and experimental results for each calibration of 0.1 M alkaline solution with an MMS electrode, where the pH value is assumed to be 13. The results helped to report the CVs and the electrocatalytic activities with the potential in the RHE scale more

accurately for each measured solution.

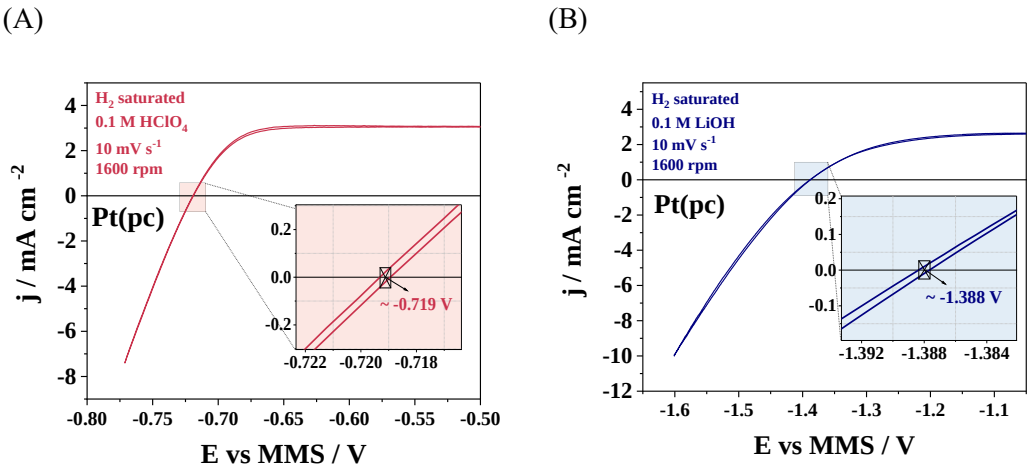

Figure 3.8. The examples of calibration of MMS as a RE in 0.1 M (A) $HClO_4$ and (B) KOH solutions with a scan rate of 10 mV s^{-1} at 1600 rpm. The typical HER/HOR polarization curves were recorded in H_2-saturated condition to define the intersection potential at zero current (the inset figures) for the measured RE. Adapted with permission from reference [294] (own work).

Table 3.2. The calibration results of MMS and MMO as the REs in each electrolyte. The table is adapted with permission from reference [294].

Electrolyte	Average interception potential	Reference electrode
0.1 M $HClO_4$	~ -719 mV	MMS
0.1 M LiOH	~ -1388 mV	MMS
0.1 M NaOH	~ -1392 mV	MMS
0.1 M KOH	~ -1393 mV	MMS
0.1 M RbOH	~ -1395 mV	MMS
0.1 M CsOH	~-1395 mV	MMS
0.1 M KOH	~ -906 mV	MMO

Besides, it is noted that achieving the H_2-saturated condition is necessary to ensure the accurate potential calibration of REs. For instance, **Figures 3.9A** and **3.9B** show the potential differences between the H_2- and Ar-saturated 0.1 M $HClO_4$ and LiOH electrolytes for Pt(pc) with an MMS electrode as a RE. The potential exhibits about 45 mV deviation for both solutions, which is attributed to the different saturated conditions that shift the Nernstian potential. Under the Ar-saturated condition, the reaction favorably produces H_2 gas to achieve equilibrium, resulting in a higher current density of HER compared to that under the H_2-saturated condition within lower overpotential regions in both acidic and alkaline media.

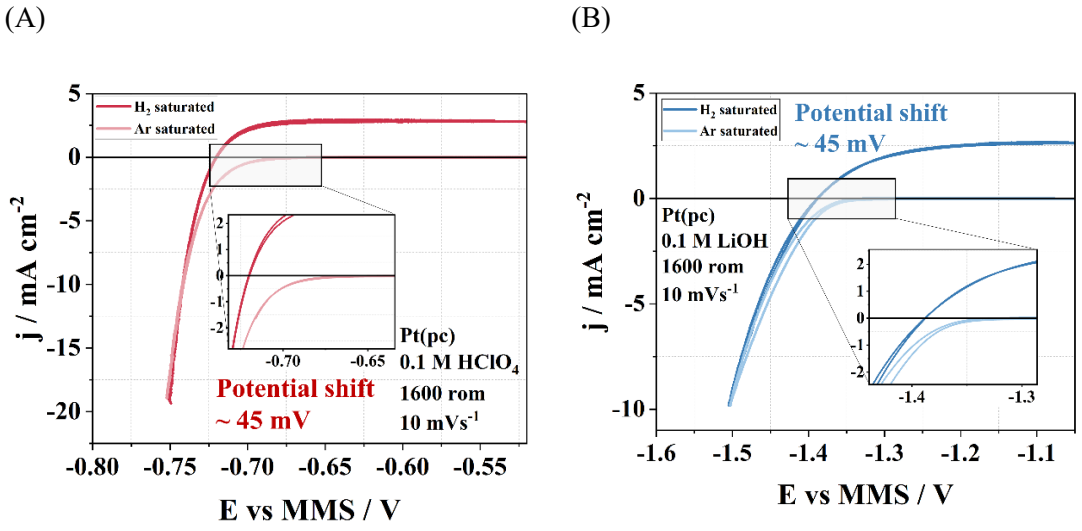

Figure 3.9. The iR-corrected HER/HOR polarization curves in H_2- and Ar-saturated (A) 0.1 M $HClO_4$ and (B) 0.1 M LiOH electrolytes in the potential scale of MMS electrodes at 1600 rpm with a scan rate of 10 mV s^{-1}. Adapted with permission from reference [294] (own work).

3.3. Experimental Setup and Measurement Details

3.3.1. Three-Electrode Cell

The three-electrode cells were used in this work to conduct the electrochemical measurements, as shown in **Figure 3.10A**. The cell consisted of the working electrode (WE), the counter electrode (CE), and the RE, which were connected to the RDE setup and further to the VSP-300 potentiostat (Bio-Logic, France). For a typical cyclic voltammetry or a PEIS measurement, the potential was controlled between the WE and the RE, and the current was measured between the working and counter electrodes via the potentiostat, respectively. The cell also includes the gas inlet and the gas outlet to manage the measuring gas environments.

(A) (B)

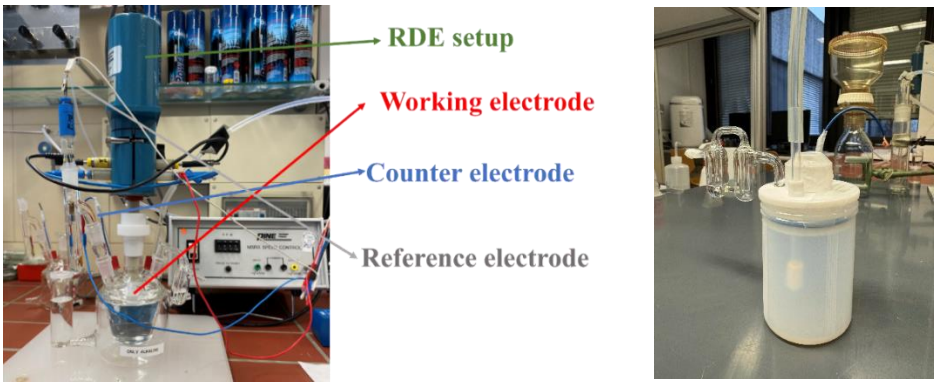

Figure 3.10. (A) The setup for the electrochemical measurements, which includes the RDE setup (green) and the three-electrode cell (DURAN® borosilicate glass) connected with the working electrode (red), counter electrode (blue), and reference electrode (gray), respectively. The gas inlet and the gas outlet of the cell controlled the gas environments during measuring. (B) The self-constructed perfluoroalkoxy (PFA) electrochemical cell with the same construction as a classical glass cell.

Moreover, to ensure that the glass cell used for electrochemical measurements in alkaline solutions does not introduce any undesired contamination issues to impact the

electrocatalytic performance due to the glass itself,[257,258,259,260,261] all measurements were performed in short-term periods in diluted alkaline solutions. **Figure 3.10B** shows the self-constructed perfluoroalkoxy (PFA) electrochemical cell, which was used for the comparison with the typical glass cell (DURAN® borosilicate glass).

3.3.2. Rotating Disc Electrode

The RDE setup is one of the common hydrodynamic techniques and is exploited to analyze the kinetics of the interfacial reactions and benchmark the reaction activities under different mass-transport conditions.[262,263,264,265,266,267] **Figure 3.11** shows the schematic RDE and the experimental RDE as a WE, which contains a measuring crystal inserted into an insulating holder, like Teflon. The holder maintains a consistent exposed surface area and prevents any leakages as the electrode immerses into the electrolyte. While the disc rotates at a given rate in a liquid electrolyte, it constantly provides a convective flow of reactant species coming from the bulk to the electrode surface and then flushing out horizontally along the electrode surface with the indicating directions of the blue arrows due to the centrifugal force.[268]

As the RDE provides constant mass diffusion conditions, the kinetics of electrocatalysts can be estimated according to the Koutecký-Levich equation:

$$\frac{1}{j_m} = \frac{1}{j_{kin}} + \frac{1}{j_{lim}} \qquad \textbf{Equation 3.12}$$

where j_m is the measured current density, j_{kin} is the kinetic current density, and j_{lim} is the limiting current density during measurements, respectively.

Besides, the diffusion-convection j_{lim} is dependent on the rotation speed and is defined as:

$$j_{lim} = 0.201nFD^{2/3}\,v^{-1/6}\,\omega^{1/2}C \qquad \textbf{Equation 3.13}$$

where n is the number of electrons during electron transfer, F is the Faraday constant, D is the diffusion coefficient of the reactant, v is the kinetic viscosity of the solution, ω is the rotation speed with a unit of rpm, and C is the bulk concentration of the solution, respectively.

(A) (B)

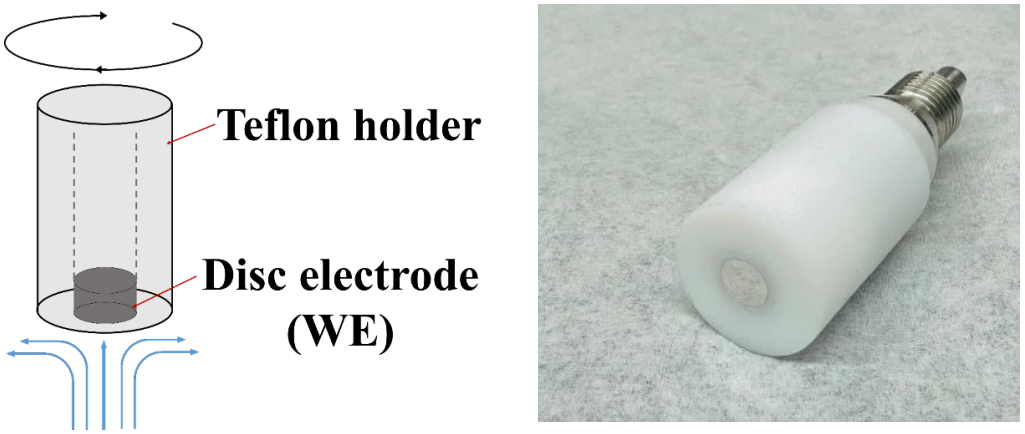

Figure 3.11. (A) The schematic RDE and (B) the experimental RDE include a disc crystal as a WE and a Teflon holder (non-conducting material). During rotation, the RDE provides a constant flux toward the electrode surface.

It is noted that **Equation 3.13** only applies to calculating the j_{kin} when the reaction is under irreversible processes such as the ORR. However, hydrogen reactions are regarded as reversible processes, and the way to extract the j_{kin} is revised to the following equations:[281]

$$\frac{1}{j_m} = \frac{1}{j_{kin}} + \frac{1}{j_d} \qquad \textbf{Equation 3.14}$$

$$j_d = j_{lim}\left(1 - \exp\left(-\frac{2F\eta}{RT}\right)\right) \qquad \textbf{Equation 3.15}$$

where j_m, j_{kin}, and j_{lim} are the measured, kinetic, and limiting current density, j_d is the

diffusion current density, F is the Faraday constant, η is the overpotential, R is the ideal gas constant, and T is the temperature in Kelvin, respectively.

Furthermore, before calculating the j_{kin} for each measurement, the reported potential ($E_{iR-corrected}$) was done by the applied potential (E_m) corrected with the iR compensation in **Equation 3.16**:

$$E_{iR-corrected} = E_m - j_m R_u \qquad \textbf{Equation 3.16}$$

where the uncompensated ohmic resistance (R_u), mainly from the electrolyte resistance, was done by the staircase PEIS measurement. A shunt capacitor was connected between the RE and the CE to suppress the measurement artifacts from the high-frequency range, as stated in the reference.[269]

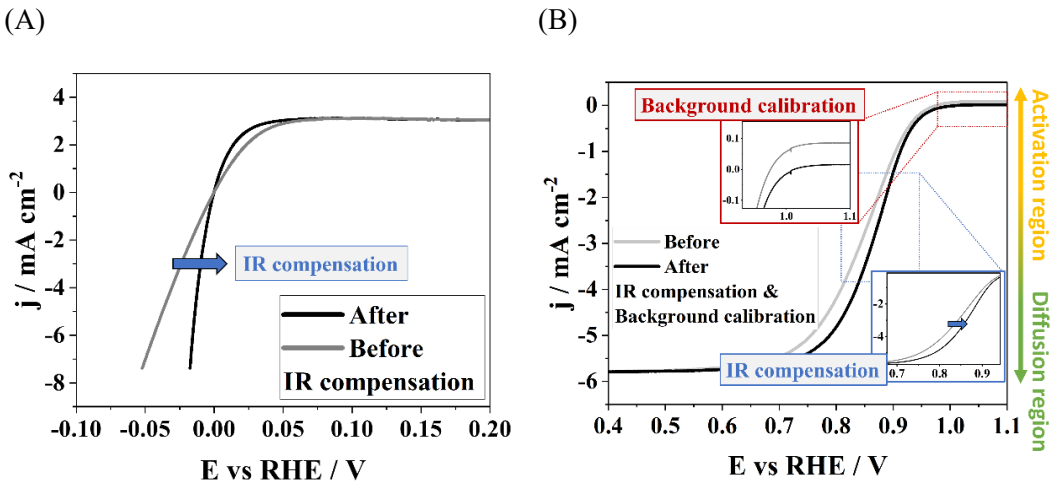

Figure 3.12. The examples of (A) the HER/HOR and (B) ORR the polarization curves recording in anodic scan for Pt(pc) electrode measured in O_2- and H_2-saturated 0.1 M $HClO_4$ at 1600 rpm with the conditions of before and after the iR compensation. The background calibration of ORR polarization curves was corrected from the CV measuring in an Ar-saturated condition. The lower and higher ORR current densities mainly correspond to the regions of the electrocatalytic activation and the mass diffusion of electrolytes, respectively.

Figures 3.12A and **3.12B** show examples of the HER/HOR and the ORR polarization curves in 0.1 M H_2- and O_2-saturated $HClO_4$, where the curves were corrected by the iR compensation in **Equation 3.16**. The ORR polarization curve was further calibrated by the CV background recording in an Ar-saturated condition to estimate ORR kinetics more accurately for the measured electrodes. To be more specific, during the ORR, as the potential is close to its so-called unset potential, in which the cathodic current density starts turning above the set value, the reactions at the surface are dominated by the kinetic activation energy of the electrocatalysts following the Butler-Volmer equation mentioned in **Section 2.2.3**. As the potential decreases, in which the overpotential increases, the current density reaches the j_{lim} and the reactions are mainly influenced by mass diffusion.

3.3.3. Preparation of Materials and Electrolytes

Detailed information on measuring electrodes in this work is listed in **Table 3.3**. The electrolytes for the electrochemical measurements were prepared from chemicals of extremely high quality, as listed in **Table 3.4**.

Table 3.3. The disc electrodes for electrochemical measurements.

Electrode	Surface dimension	Company
Pt(pc)	About 5 mm in diameter	MaTeck, Germany
Pt_5Gd alloy	About 5 mm in diameter	MaTeck, Germany
Pt_5Y alloy	About 5 mm in diameter	MaTeck, Germany

Table 3.4. The chemicals used to prepare the measuring electrolytes and cleaning processes.

Chemical	Quality	Company
Lithium hydroxide (LiOH)	99.995% (metals basis)	Thermo Fisher Scientific, USA
Sodium hydroxide (NaOH)	99.99% (metals basis)	Thermo Fisher Scientific, USA
Potassium hydroxide (KOH)	99.98% (metals basis)	Alfa Aesar, USA
Rubidium hydroxide (RbOH)	solution, 50 wt. % in H_2O, 99.9% trace metals basis	Sigma-Aldrich, USA
Cesium hydroxide (CsOH)	solution, 50 wt. % in H_2O, 99.9% trace metals basis	Sigma-Aldrich, USA
Perchloric acid ($HClO_4$)	70% $HClO_4$, Suprapur, and extra pure	Merck (Suprapur) and Acros (extra pure), Germany
Water (H_2O)	Ultrapure, 18.2 MΩ cm	Merck Millipore, Germany
Copper (II) oxide (CuO)	99.999% (trace metals basis)	Sigma-Aldrich, USA
Sulfuric acid (H_2SO_4)	96% H_2SO_4, p.a., ISO	Carl Roth, Germany
Hydrogen Peroxide (H_2O_2)	30% H_2O_2, p.a., ISO	Carl Roth, Germany

To avoid any possible contaminations, the electrochemical cells were cleaned with the so-called "Piranha solution",[270,271,272] a 3:1 mixture of Sulfuric acid and Hydrogen

Peroxide, and then rinsed with hot ultrapure water several times to remove the residual contaminations. Additionally, the measured electrodes were cleaned further using the electrochemical method. This procedure involved multiple cyclic voltammetry cycles with the potential to reach the HER and OER regions until a stable CV was obtained before the actual electrochemical measurements.

4. Results and Discussion

4.1. Electrode Characterizations

In this work, Pt(pc), Pt_5Gd, and Pt_5Y disc electrodes are utilized as a model system to investigate the electrochemical properties of the HER and ORR under different electrode/electrolyte interfacial conditions. Before discussing electrochemical results, the material characterizations, including the analysis of XRD, XPS, and ECSA, are illustrated in this section, respectively.

4.1.1. XRD Analysis for the Pt and Pt Alloys

Figures 4.1A-C show the XRD patterns of the Pt, Pt_5Gd, and Pt_5Y disc electrodes after the electrochemical measurements, in which the diffraction peaks are fitted according to the literature data,[68,251,301] as shown in **Table 4.1**. The measured crystals show polycrystalline structures. However, due to the presence of various secondary elements (e.g. Gd and Y) in the Pt alloys, the crystalline structures of both Pt_5Gd and Pt_5Y electrodes are more complex than that of pure Pt, which has a simple Cu structure with a lattice parameter a of about 3.92 Å. The crystallographic type of Pt_5Gd and Pt_5Y correspond to a Cu_5Ca and $AuBe_5$ structure and the corresponding lattice parameter a are about 5.29 Å and 7.49 Å, respectively. While it is reported that Pt_5Gd can also adopt an $AuBe_5$ structure with the multiplication of the c axis, the lattice parameter a is relatively constant in both structures.[68,301] Therefore, the corresponding surface strains from the lattice mismatch are based on the difference between the lattice parameter a of the Pt overlayer and the underlying bulk alloy after the so-called acid leaching process (see **Figure 4.1D**). Here, we assume the Pt overlayer has the same crystalline structure as the Pt(pc). As the Pt overlayer has a smaller lattice parameter than that of

the bulk, the induced compressive strains affect the electronic and chemical properties of the electrode surfaces and significantly influence the electrocatalytic performances.

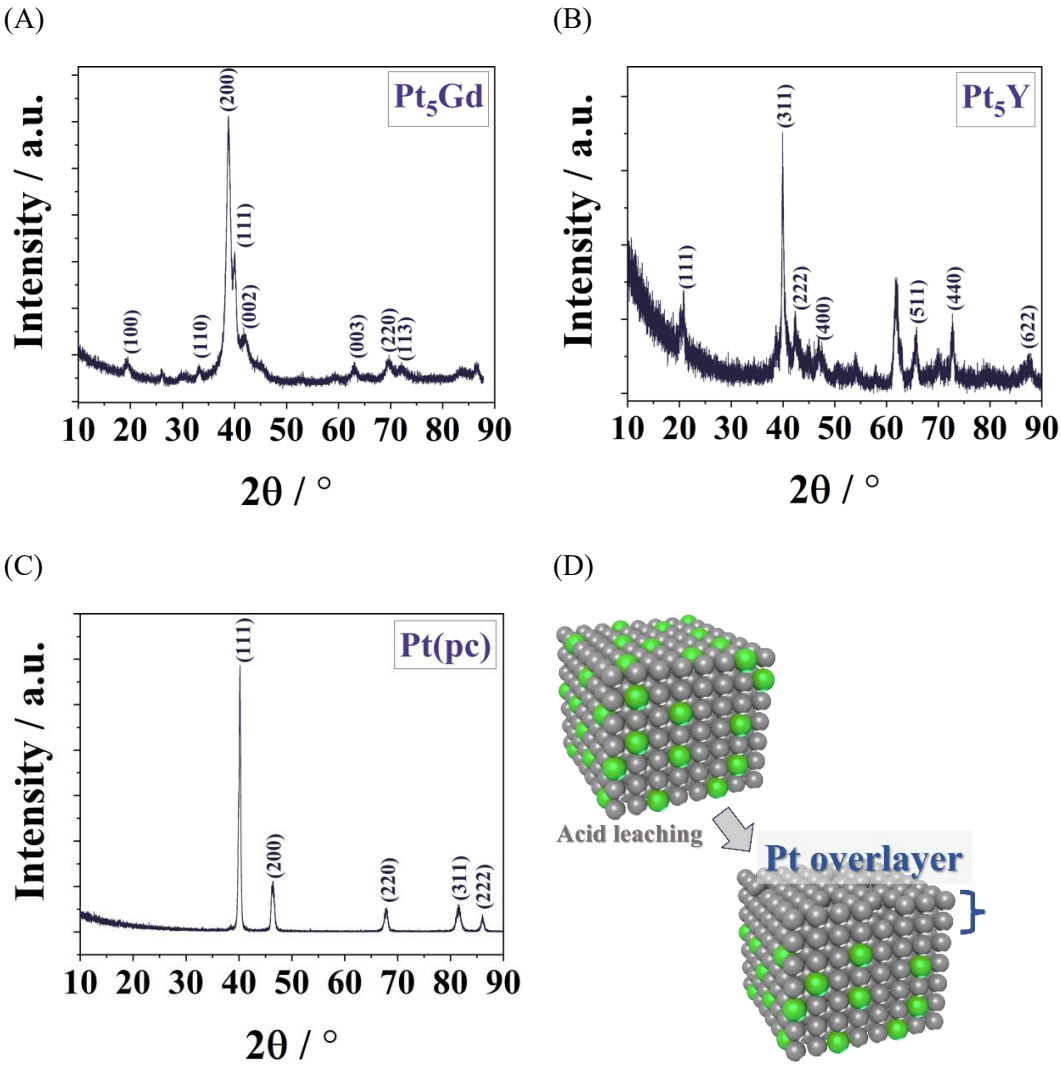

Figure 4.1. The XRD patterns of (A) Pt_5Gd, (B) Pt_5Y, and (C) Pt(pc) electrodes with labeled peaks correspond to the literature [68,251,301]. It is worth noting that all spectra were recorded after electrochemical measurements. Adapted with permission from reference [294] (own work). (D) The schematic of the formation of the Pt overlayer after the acid leaching process for Pt bulk alloys. The atoms of a secondary element (e.g., Gd and Y) are marked in green, and the Pt atoms are marked in grey.

Table 4.1. The XRD fitting results of disc electrodes with the corresponding literature. The table is adapted with permission from reference [294].

Crystal electrode	Crystallographic prototypes	Lattice parameter a [Å]	Corresponding literature
Pt_5Gd	Cu_5Ca	~5.29	[68,301]
Pt_5Y	$AuBe_5$	~7.49	[251]
Pt	Cu	~3.92	[251,301]

4.1.2. XPS Analysis for the Pt Alloys

Figure 4.2 demonstrates the XPS spectra and the fittings of the Pt_5Gd and Pt_5Y electrodes. The intensity peaks of Pt 4f, Gd 4d, and Y 3d and their corresponding binding energies are analyzed after the electrochemical measurements in acid media. The surface composition of Pt_5Gd and Pt_5Y is calculated by **Equation 3.3**. Based on the fitting results, approximately 6.2 % of Gd and 4.2 % of Y are detected on the electrode surfaces, respectively. This indicates that the complete dealloying Pt overlayer is formed for both Pt alloys after the acid-leaching process.

Besides, it is noted that the detection of a small number of atoms of a secondary element is attributed to the possible reasons that the penetrating thickness of incident X-ray beams involves not only the Pt overlayer but also part of the bulk alloys. The more precise thickness of the Pt overlayer is reported in the literature[301] by utilizing the non-destructive angle-resolved X-ray photoelectron spectroscopy (AR-XPS), which can extract the in-depth surface composition information and arbitrarily demonstrate three

monolayers of pure Pt overlayer (i.e., about 10 Å depth from the surface) for Pt_5Gd electrode.

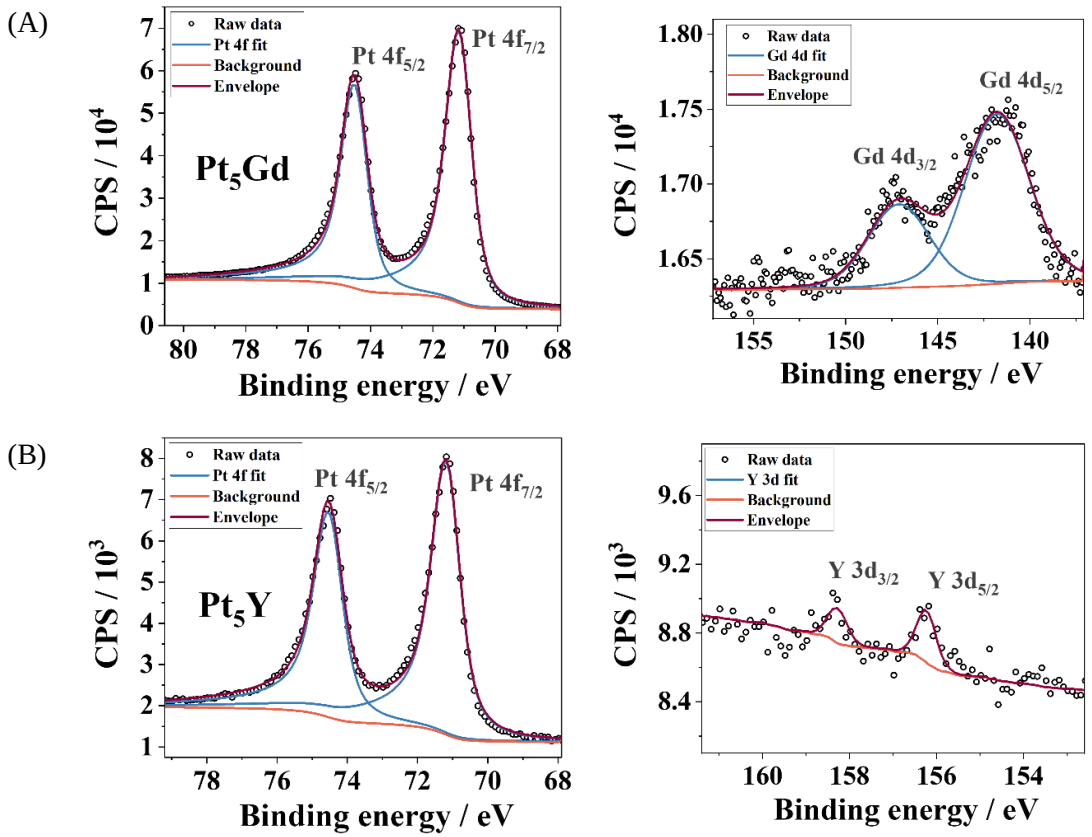

Figure 4.2. The XPS spectra with the fitting results of (A) Pt_5Gd and (B) Pt_5Y electrodes after the electrochemical measurements. Adapted with permission from reference [294] (own work).

4.1.3. ECSA Evaluation for the Pt and Pt Alloys

To further confirm the formation of the Pt overlayer on the bulk alloys, the ECSAs of measured electrodes are conducted by the Cu_{UPD} measurements, in which the detailed experimental procedure is illustrated in **Section 3.2.3**. **Figures 4.3A-C** show the stable CVs (black) of Pt_5Gd, Pt_5Y, and Pt(pc) electrodes, respectively, in Ar-saturated 0.1 M $HClO_4$ with a scan rate of 20 mV s^{-1}. It is noted that a stable CV is required to

ensure the completion of dealloying and the cleaning processes for the electrode surface.[301]

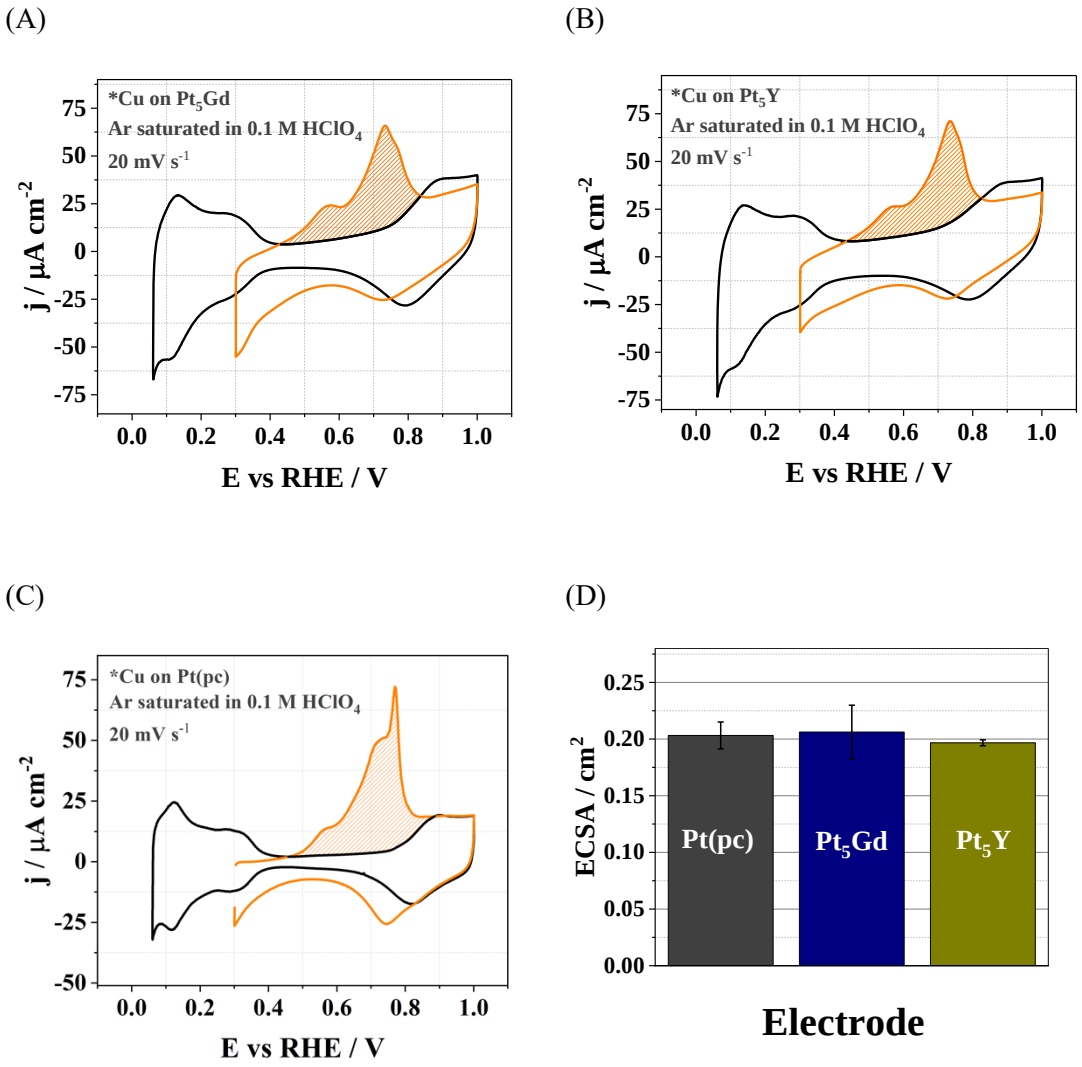

Figure 4.3. The Cu_{UPD} measurements for (A) Pt_5Gd, (B) Pt_5Y, and (C) Pt(pc) electrodes. The profile shows the stable CV (black) and the 1st cycle of CV (orange) for the Cu stripping, conducted in Ar-saturated 0.1 M $HClO_4$ and a mixture of 0.1 M $HClO_4$ and 2 mM Cu^{2+} solutions, respectively, at a scan rate of 20 mV s^{-1}. The calculated ECSA is noted in the slashed orange area for each electrode. (D) The bar chart represents the recorded ECSAs of the measured electrodes determined by Cu underpotential deposition/monolayer stripping. Adapted with permission from reference [294] (own work).

To that aim, **Figures 4.4A** and **4.4B** show the long-term cyclic voltammetry for the Pt_5Gd and Pt_5Y electrodes in Ar-saturated $HClO_4$ with a scan rate of 50 mV s^{-1}, respectively. The current density of CVs gradually increases with the increased number of cycles until it reaches its steady condition at the 64th cycle after surface dealloying and reconstructing. The representing H_{UPD} peaks for Pt, mainly attributed to (110) and (100) facets,[273,274,275] and the oxide formation/reduction peaks become more obvious during the cycling procedure, and this indicates that the Pt overlayer is developed with the secondary atom leaching out from the alloy surface.

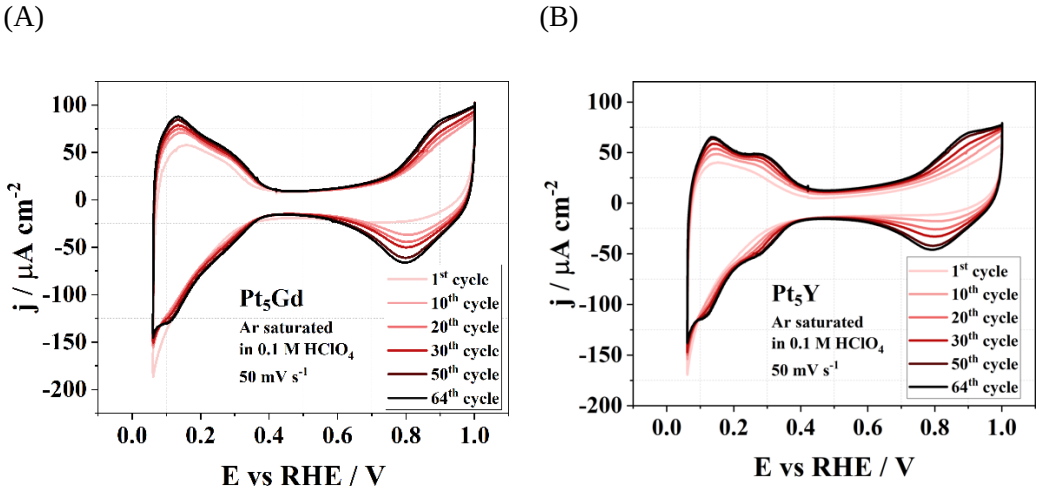

Figure 4.4. The CVs for (A) Pt_5Gd and (B) Pt_5Y electrodes in Ar-saturated 0.1 M $HClO_4$ with a scan rate of 50 mV s^{-1} during long-term cycling.

In addition, the Cu_{UPD} measurement is subsequently conducted in a mixture solution of 0.1 M $HClO_4$ and 2 mM Cu^{2+}. The recorded CV (orange) shows the Cu stripping process at the surface (see **Equation 3.9**) and the corresponding ECSAs based on the integration of Cu_{UPD} charge can be estimated according to **Equation 3.10**.

Figure 4.3D shows the average ECSAs of Pt(pc), Pt_5Gd, and Pt_5Y electrodes. Each electrode shows a similar ECSA, which closely matches its geometric surface area of approximately 0.2 cm^2 (for a disc electrode with a diameter of about 5 mm). This further indicates that the complete Pt overlayer on Pt bulk alloys is formed after the

acid-leaching process. Since the average ECSAs are comparable to the geometrical surface areas for the measured electrodes, all recorded current densities in this work are obtained from normalizing the currents by the geometrical surface area.

4.2. Combining Impedance and Hydrodynamic Approaches in Electrocatalysis. Characterization of Pt(pc), Pt_5Gd, and Nanostructured Pd/C for the HER

As mentioned earlier, hydrogen reactions are highly studied in electrochemistry and are extremely important for developing highly efficient energy conversion devices. The RDE hydrodynamic approach is widely used to study the activity and stability of different electrochemical reactions, as it offers precise control over the mass transport of electroactive species. Combining cyclic voltammetry with RDE is a standard characterization protocol in electrocatalysis. In contrast, the EIS is one of the most informative electrochemical methods, which can provide more detailed insights into reaction processes occurring simultaneously at the electrode/electrolyte interfaces. In this section, we conducted the combined EIS-RDE method and explored the mechanistic study of HER for Pt(pc) and Pt_5Gd disc electrodes in acidic and alkaline solutions as the model system. The EEC model was utilized to elucidate EIS spectra and extract the critical interfacial parameters during the HER under different rotation conditions. Each parameter in the EEC model and the relative contribution of Volmer-Heyrovsky and Volmer-Tafel reaction pathways were discussed, along with the influence of rotation rates. Furthermore, the more complex system, like nanostructured Pd/C catalysts, has also been investigated.

The main part of this section is based on the publication with the agreement of the listed co-authors:

Song, K.-T.; Schott, C. M.; Schneider, P. M.; Watzele, S. A.; Kluge, R. M.; Gubanova, E. L.; Bandarenka, A. S. Combining Impedance and Hydrodynamic Methods in Electrocatalysis. Characterization of Pt(pc), Pt_5Gd, and Nanostructured Pd for the Hydrogen Evolution Reaction. J. Phys. Energy **2023**, 5 (1), 014016[276]

4.2.1. Elucidation of Electrical Equivalent Circuit

The development of the EEC model is based on the previous work focusing on a Pt(pc) microelectrode under HER reaction conditions with different pH values and overpotentials.[84,85] As mentioned in **Section 2.3.1**, the overall HER can be divided into three elementary steps. The first step is the Volmer reaction, followed by the Heyrovsky, or the Tafel steps. The complete HER pathways are illustrated as the Volmer-Heyrovsky and Volmer-Tafel reaction pathways. The initial assumption of the EEC model is that the two reaction pathways are quasi-independent and take place simultaneously. **Figure 4.5** illustrates the EEC model of HER with the RDE setup, which controls the mass transport conditions. In the series of R_u, there is a parallel connection between the non-Faradaic branch and the Faradaic branches. The non-Faradaic behavior corresponds to the C_{dl}. The Faradaic reactions are attributed to the total HER current mainly from the sum of currents of Volmer-Heyrovsky and Volmer-Tafel reactions.

For the HER in acidic media, the Volmer-Heyrovsky mechanism includes one proton adsorption (Volmer step) and its subsequent reaction with another proton from the solution to form hydrogen gas (Heyrovsky step). In other words, this reaction type is limited by the fractional coverage of the adsorbed hydrogen species at the electrode surface, where the faradaic impedance consists of the charge transfer resistance of the Volmer-Heyrovsky mechanism ($R_{ct,VH}$) in series with the parallel connection between the adsorption resistance (R_a) and capacitance (C_a). The EEC model of the Volmer-Heyrovsky mechanism can be expressed by **Equation 4.1**.

$$\hat{Z}_{VH} = R_{ct,VH} + \frac{1}{j\omega C_a + \frac{1}{R_a}} \qquad \textbf{Equation 4.1}$$

On the other hand, the Volmer-Tafel mechanism is relatively simple and involves the combination of two adsorbed hydrogen atoms to form H_2. At sufficiently high

overpotentials, the Volmer mechanism is regarded as a relatively fast charge transfer step, and the reaction is limited by the hydrogen mass-transport processes.[84,85,277] Since the RDE technique provides a steadily convective flow of electrolytes towards the electrode surfaces, the condition fits the finite-length diffusion with the transmissive boundary. The corresponding Faradaic impedance is equal to the charge-transfer resistance of the Volmer-Tafel mechanism ($R_{ct,VT}$) in a series of the parameter of Ws. The EEC model of the Volmer-Tafel mechanism is written by the mathematical **Equation 4.2**

$$\hat{Z}_{VT} = R_{ct,VT} + \hat{Z}_{W_s} \qquad \textbf{Equation 4.2}$$

The parameter of Ws consists of the two elements of Ws_c and Ws_r, as described in **Equation 4.3**, **Equation 4.4**, **Equation 4.5**, and **Equation 4.6**, respectively.[227]

$$\hat{Z}_{W_s} = \frac{A_W}{\sqrt{j\omega}}\tanh\left(B\sqrt{j\omega}\right) = \frac{\sigma\sqrt{2}}{\sqrt{j\omega}}\tanh\left(\sqrt{\frac{j\omega}{D}}\delta_N\right) \qquad \textbf{Equation 4.3}$$

$$Ws_c = \frac{\delta_N}{\sqrt{D}} \qquad \textbf{Equation 4.4}$$

$$Ws_r = \sigma\sqrt{2} \qquad \textbf{Equation 4.5}$$

$$\sigma = \frac{RT}{n^2F^2A\sqrt{2}}\left(\frac{1}{C_O\sqrt{D_O}} + \frac{1}{C_R\sqrt{D_R}}\right) \qquad \textbf{Equation 4.6}$$

Here, σ is the Warburg coefficient, D is the diffusion coefficient, and δ_N is the Nernst diffusion layer thickness in **Equation 4.4** and **Equation 4.5**. The parameters of Ws_c and Ws_r have the units of $s^{1/2}$ and $\Omega\ s^{-1/2}$, respectively. In **Equation 4.6**,[278] R is the ideal gas constant, T is the temperature, n is the number of electrons involved, F is the Faraday constant, A is the electrode surface area, C_O and C_R are the concentrations of oxidants and reductants, and D_O and D_R are the diffusion coefficients of oxidants and

reductants, respectively.

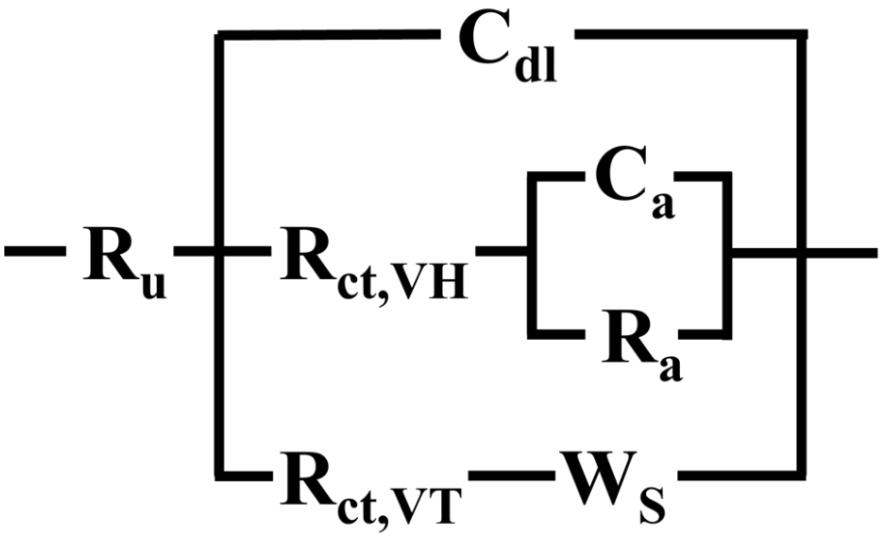

Figure 4.5. The EEC model for HER in acidic and alkaline media under controlled rotation conditions with the RDE setup. The EEC includes the R_u in a series of the parallel non-Faradaic branch of the C_{dl} and the branch of the Faradaic processes of HER, including the Volmer-Heyrovsky and Volmer-Tafel mechanisms. Adapted with permission from reference [276] (own work).

It is pointed out that the common approach to determining the rate-limiting step of the HER mechanisms relies on the calculation of the Tafel slope. The Tafel slopes of approximately 120, 40, and 30 mV dec^{-1} correspond to the rate-limiting Volmer, Heyrovsky, and Tafel steps, respectively.[279,280] However, this method requires precise extraction of the HER kinetics and is dependent on the applied potential. In this work, the study of HER mechanisms is not based on the Tafel slope but rather focuses on the EIS analysis, which can quantitatively differentiate the interfacial parameters based on their frequency domains.

4.2.2. HER for Disc Electrodes in Acidic Media

This work selected Pt(pc) and Pt_5Gd disc electrodes as the model system for investigation and comparison because Pt-based catalysts are known for their high and stable activities in various reaction conditions.[85,153] **Figure 4.6A** shows the Tafel plot of HER for Pt(pc) and Pt_5Gd electrode in H_2-saturated 0.1 M $HClO_4$ at 1600 rpm with a scan rate of 10 mV s^{-1}. The $-j_{kin}$ of Pt_5Gd at -10 mV vs. RHE is higher than that of the Pt(pc) electrode in **Figure 4.6B**. This can be attributed to the compressive strain effect on the Pt_5Gd surface, which reduces the binding energies with reactive intermediates, leading to optimal binding configurations for the HER. Similarly, more promising performance for Pt-based catalysts is observed for the ORR activity in acidic media.[68,251,301]

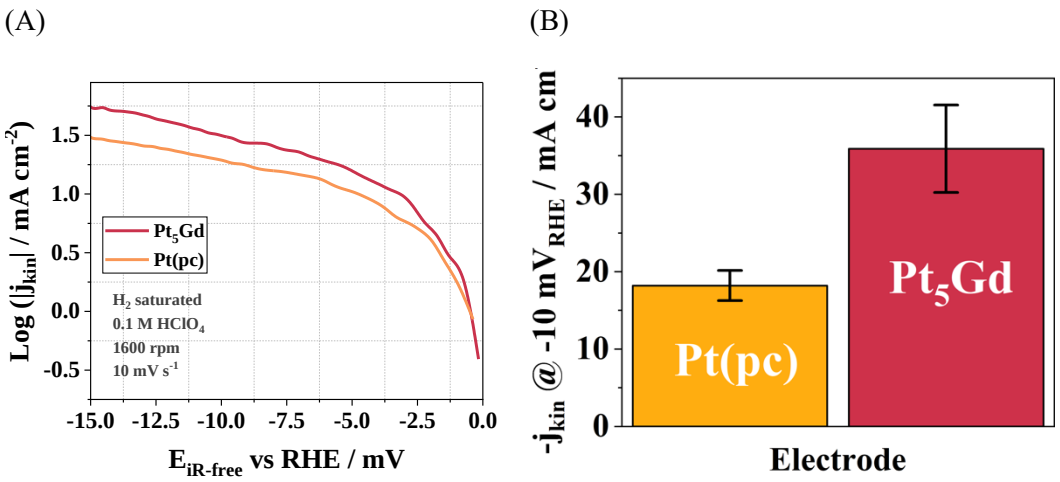

Figure 4.6. (A) The Tafel plot for the HER on the Pt_5Gd and Pt(pc) electrodes measured in H_2-saturated 0.1 $HClO_4$ at 1600 rpm with a scan rate of 10 mV s^{-1}. (B) The bar chart of the negative value of j_{kin} at -10 mV vs RHE for the Pt_5Gd and Pt(pc) electrodes. Adapted with permission from reference [276] (own work).

Besides, **Figures 4.7A** and **4.7B** show the HER/HOR polarization curves for the Pt(pc) and Pt_5Gd electrodes recorded at different rotation rates in H_2-saturated 0.1 M $HClO_4$. As rotation rates increase from 400 rpm to 2500 rpm, the limiting current density of

HOR demonstrates an upward trend. The linear relationship for both electrodes follows the Koutecký-Levich equation at 100 mV vs. RHE, which indicates that the HOR is mainly limited by the mass transport at high overpotentials due to the low solubility of H_2 in aqueous solutions,[281,282,283] as illustrated in the insets of **Figures 4.7A** and **4.7B**.

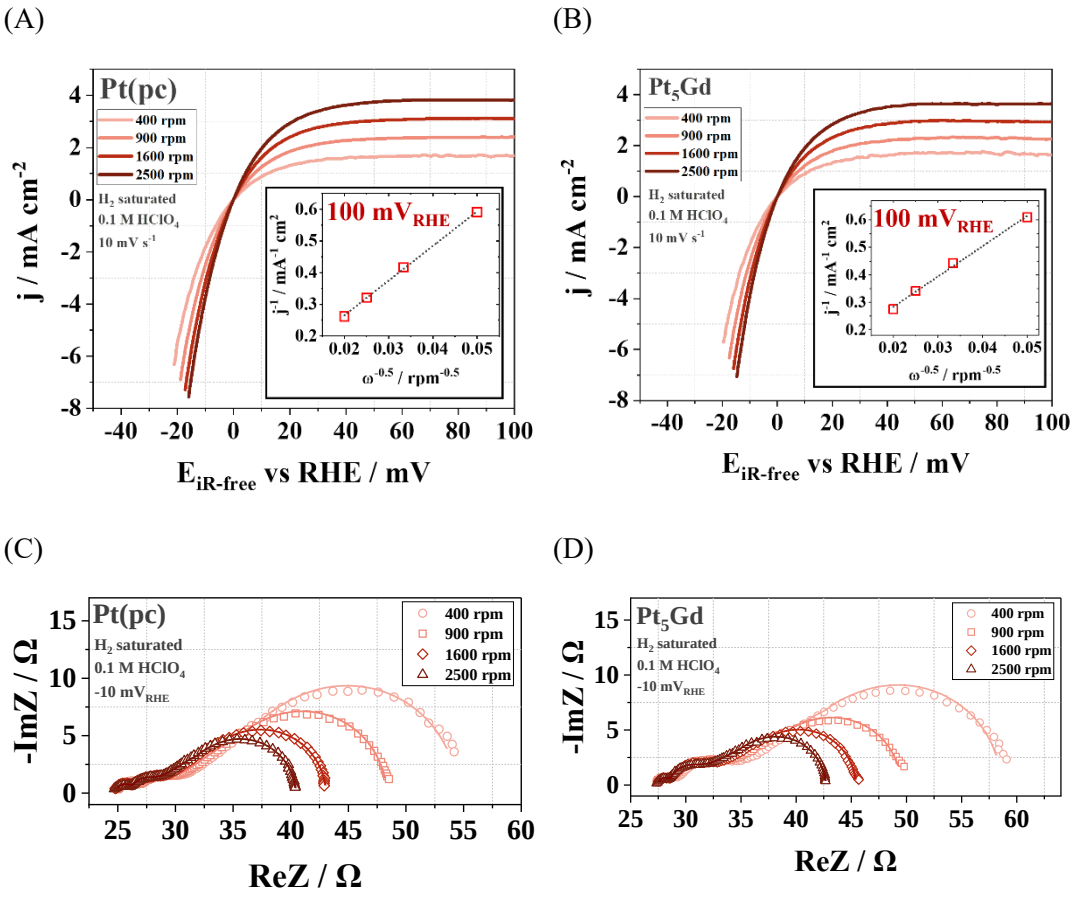

Figure 4.7. The iR-corrected HER/HOR polarization curves (anodic scan) of (A) Pt(pc) and (B) Pt_5Gd electrodes. The inset figures of (A) and (B) illustrate the Koutecký-Levich plot at 100 mV vs RHE. The EIS spectra with the Nyquist presentations of (C) Pt(pc) and (D) Pt_5Gd electrodes at -10 mV vs. RHE. The dotted and the solid lines present the measured and fitted EIS spectra with the EEC model in **Figure 4.5**. The data was recorded in H_2-saturated 0.1 M $HClO_4$ with a scan rate of 10 mV s^{-1} at the chosen rotation rates of 400, 900, 1600, and 2500 rpm, respectively. Adapted with permission from reference [276] (own work).

Similarly, the current density of HER follows the same trend as the HOR and increases

with higher rotation rates for both Pt(pc) and Pt_5Gd electrodes. This indicates that although the HER is assumed to be free of diffusion limitation, the contribution of the overall overpotential from both the charge transfer kinetics and the limiting mass transport needs to be considered for HER in acidic media.[281] **Figures 4.7C** and **4.7D** show the Nyquist plots for the Pt(pc) and Pt_5Gd electrodes, respectively, conducted the HER at -10 mV vs. RHE under different rotation conditions. The Bode plots illustrate added information regarding the total impedance and the phase shift as a function of frequency (see **Appendix**). The EIS data were fitted by the EEC model in **Figure 4.5**, and fitting results provide more quantitative information on the interfacial properties. It is observed that there is a slight alteration of the arcs within the high-frequency region, which is correlated to the Faradaic reactions under different rotation configurations. In contrast, the profound deviations within the lower frequencies mainly relate to the mass transport and adsorption processes. It is worth noting that the chosen potential ranges for the HER/HOR polarization curves and the EIS measurements are relatively low. This ensures that the corresponding current density remains low, thereby preventing the formation of H_2 bubbles on the surface.

Figure 4.8 and **Figure 4.9** show the fitting results of EIS data for the Pt(pc) and Pt_5Gd electrodes, respectively, with each parameter plotting as a function of the square root of the rotation rate. From the Volmer-Heyrovsky reaction pathway in acidic media, the resistance of the Faradaic reaction, the $R_{ct,VH}$, increases with the decrease of the rotation speed for both measured electrodes. This can be related to the concentration variation of the redox species at the electrode/electrolyte interfaces under different rotation configurations and the time shift during the EIS measurements.[284]

Besides, for both Pt(pc) and Pt_5Gd electrodes, the R_a, associated with the resistance response of the adsorption processes, is several factors higher than the $R_{ct,VH}$. The R_a increases significantly, approximately doubling from 2500 rpm to 400 rpm, while the

C_a slightly decreases with the decreasing rotation rate for both electrodes. This clearly demonstrates that the rate-limiting step of the Volmer-Heyrovsky mechanism is rather determined by adsorption processes and closely depends on the coverage fraction of the adsorbed hydrogen species. In other words, as the rotation rate increases, the Volmer-Heyrovsky reaction pathway has a lower adsorption barrier and is preferred to take place at the electrode surfaces.

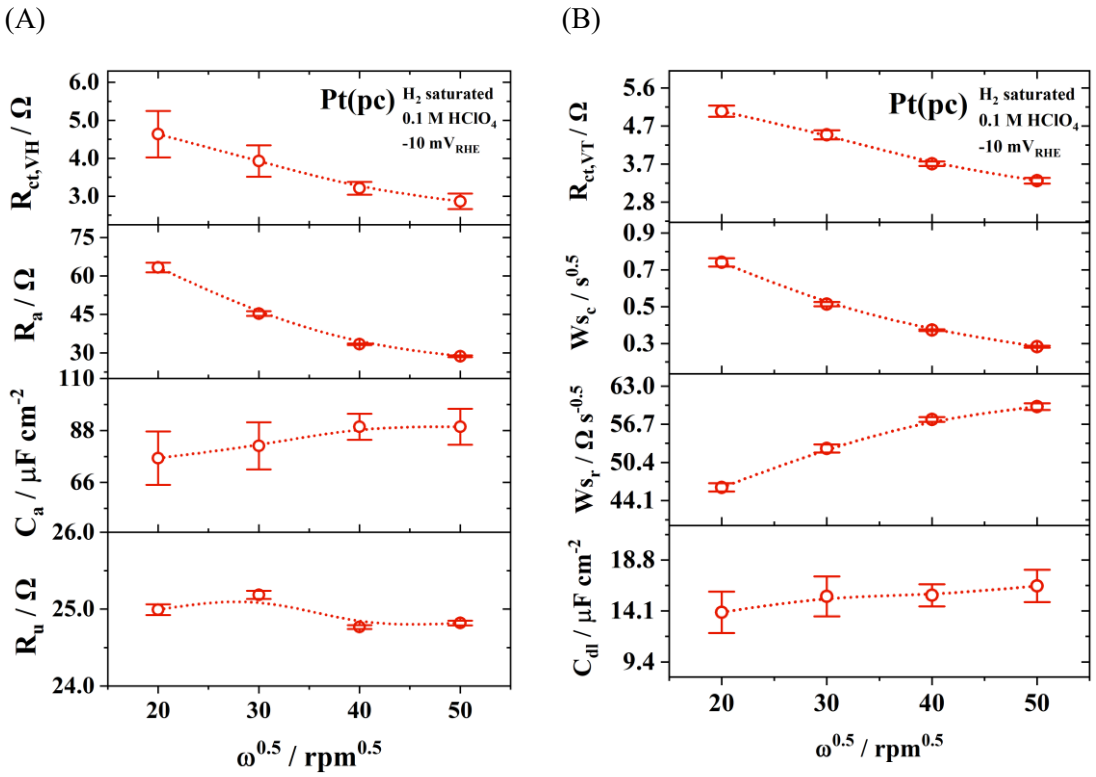

Figure 4.8. The fitting parameters in the EEC model as a function of the square root of the rotation rate for Pt(pc) electrode measured at -10 mV vs. RHE in H_2-saturated $HClO_4$. (A) The parameters include the $R_{ct,VH}$, R_a, and C_a for the Volmer-Heyrovsky mechanism and the R_u. (B) The parameters consist of the $R_{ct,VT}$, and the Ws element (Ws_c and Ws_r) of the Volmer-Tafel mechanism and the non-Faradaic contribution of C_{dl}. Adapted with permission from reference [276] (own work).

On the other hand, the Volmer-Tafel reaction pathway is mainly associated with the charge transfer and diffusion configurations. For the charge transfer processes, the $R_{ct,VT}$ follows a similar trend as the $R_{ct,VH}$, which increases lightly with the decrease of

the rotation rate. It is noted that the values of $R_{ct,VT,}$ and $R_{ct,VH}$ for Pt(pc) are relatively similar; however, the value of $R_{ct,VT}$ is larger than that of $R_{ct,VH}$ for Pt_5Gd electrode. This indicates that the Volmer-Heyrovsky mechanism is preferred to take place for the total HER at -10 mV vs. RHE in 0.1 M $HClO_4$.

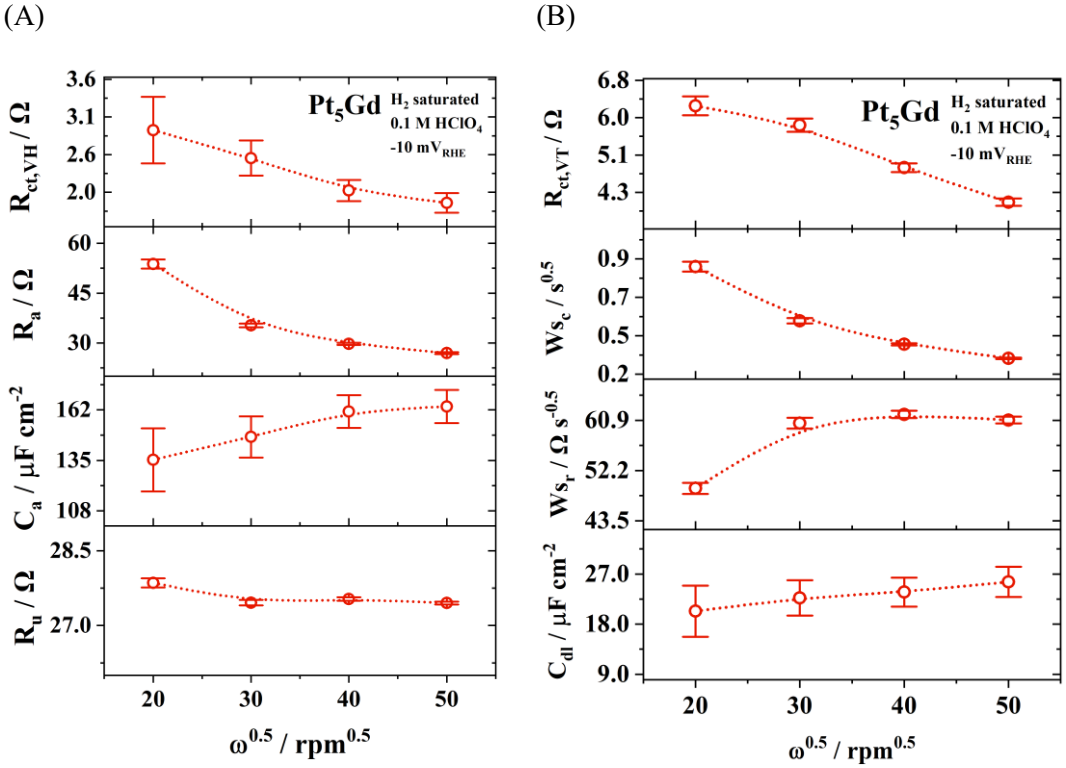

Figure 4.9. The fitting parameters in the EEC model as a function of the square root of the rotation rate for Pt_5Gd electrode recorded at -10 mV vs. RHE in H_2-saturated $HClO_4$. (A) The parameters comprise the $R_{ct,VH}$, R_a, and C_a for the Volmer-Heyrovsky mechanism and the R_u. (B) The parameters include the $R_{ct,VT}$ and the Ws element (Ws_c and Ws_r) of the Volmer-Tafel mechanism and the non-Faradaic contribution of C_{dl}. Adapted with permission from reference [276] (own work).

Besides, the mass-transport properties are precisely illustrated for the RDE setup with the Ws element consisting of Ws_c and Ws_r. The Ws_c is a function of the thickness of the Nernst diffusion layer, and the Ws_r is mainly related to the Warburg coefficient, as shown in **Equation 4.3**, **Equation 4.4**, **Equation 4.5**, and **Equation 4.6**. For both Pt(pc) and Pt_5Gd electrodes, as the rotation rate decreases from 2500 rpm to 400 rpm (i.e., a

slower mass transport), the value of Ws_c increases about two times higher with a broader thickness of the diffusion layer. However, the trend of W_{Sr} shows the opposite as the rotation rate decreases. This can be attributed to the inverse relation between the Warburg coefficient and the species concentrations (see **Equation 4.6**). The larger deviation of both Ws_c and Ws_r with comparable higher impedance compared to the slight difference in the $R_{ct,VT}$ indicates that the HER is rather diffusion limiting instead of the fast Faradaic reactions. In addition, the other two parameters, R_u and C_{dl}, are relatively independent of the rotation rates during the HER, in which the values remain comparably constant at different rotation configurations for both Pt(pc) and Pt_5Gd electrodes.

In order to determine the dominant reaction pathway of HER, the ratio of $R_{ct,VH}/R_{ct,VT}$ is calculated according to the related **Equation 4.7**[151]:

$$\frac{R_{ct,VH}}{R_{ct,VT}} \propto \frac{I_{ct,VT}}{I_{ct,VH}} \qquad \textbf{Equation 4.7}$$

where the $I_{ct,VT}$ and $I_{ct,VH}$ correspond to the partial current of the Volmer-Heyrovsky and Volmer-Tafel reactions towards the total HER current, respectively.

As shown in **Figure 4.10A**, the value demonstrates the relative contribution between the Volmer-Heyrovsky and Volmer-Tefal mechanisms measured at -10 mV vs. RHE in H_2-saturated 0.1 M $HClO_4$ under different rotation conditions. The ratio for both electrodes remains comparably constant under different rotation rates. Besides, the ratios are approximately 0.5 and 0.9 for Pt_5Gd and Pt(pc) electrodes, respectively, which suggest that the Volmer-Heyrovsky is rather dominant in acid for Pt_5Gd compared to Pt(pc) electrode at a certain low overpotential region at different rotation configurations. Furthermore, **Figure 4.10B** displays a clearly linear relationship between the Ws_c and the inverse of the square root of the rotation rate for both electrodes. The trend follows **Equation 4.4** and the following **Equation 4.8**:

$$\delta_N = 1.61 \times D^{1/3}\omega^{-1/2}v^{1/6} \qquad \textbf{Equation 4.8}$$

As mentioned earlier, δ_N is the diffusion-layer thickness, D is the diffusion coefficient, ω is the rotation rate, and v is the solution viscosity, respectively. Consequently, the thickness of the diffusion layer can be quantitatively assessed once all parameters in **Equation 4.8** are known.

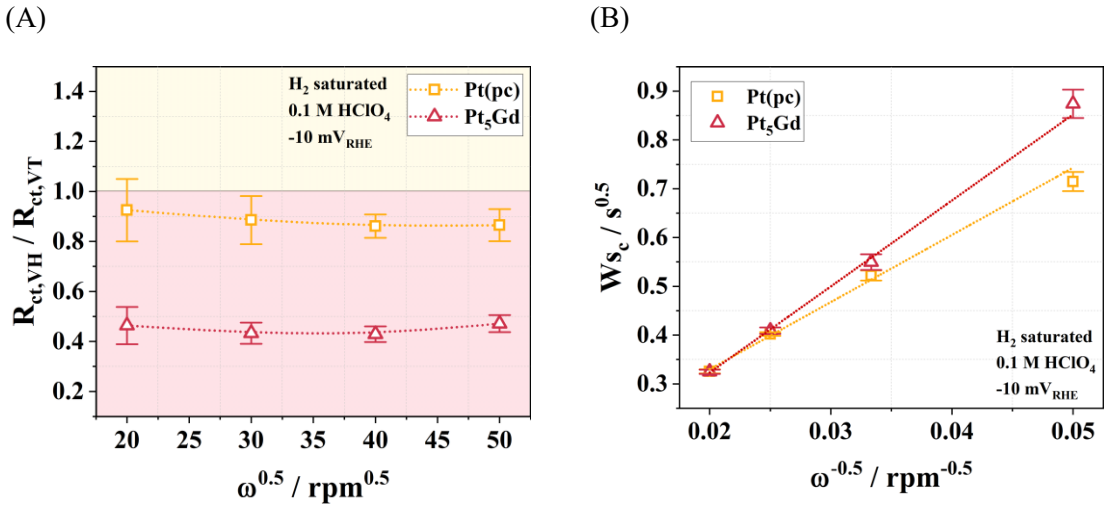

Figure 4.10. (A) The relative contribution between the Volmer-Heyrovsky and Volmer-Tefal mechanisms with the ratio of $R_{ct,VH}/R_{ct,VT}$ as a function of the square root of the rotation rate, and (B) Ws_c as a function of the inverse of the square root of the rotation rate for the Pt(pc) and Pt_5Gd electrodes at -10 mV vs. RHE in H_2-saturated $HClO_4$. The dashed lines in (A) are a guide to the eye, and the lines in (B) are a linear fit of the data, respectively. Adapted with permission from reference [276] (own work).

4.2.3. HER for Disc Electrodes in Alkaline Media

In this subsection, the same set of experiments and approaches was conducted in alkaline media to compare the differences from the measurements in acidic media. The reason for selecting 0.1 M LiOH as the alkaline solution is due to the highest HER activity for the Pt(pc) electrode.[151] Another reason is because of the relatively higher

HER stability compared to other alkaline media (i.e., RbOH and CsOH solutions), for which the formation of irreversible (sub)surface oxidation on Pt electrode for potentials above 0.6 V vs. RHE was reported in the literature.[285,286] It is worth mentioning that because of the instability of Pt-based catalysts in alkaline solutions,[287] the electrodes were conducted by electrochemical cleaning and activation processes before each EIS measurement.

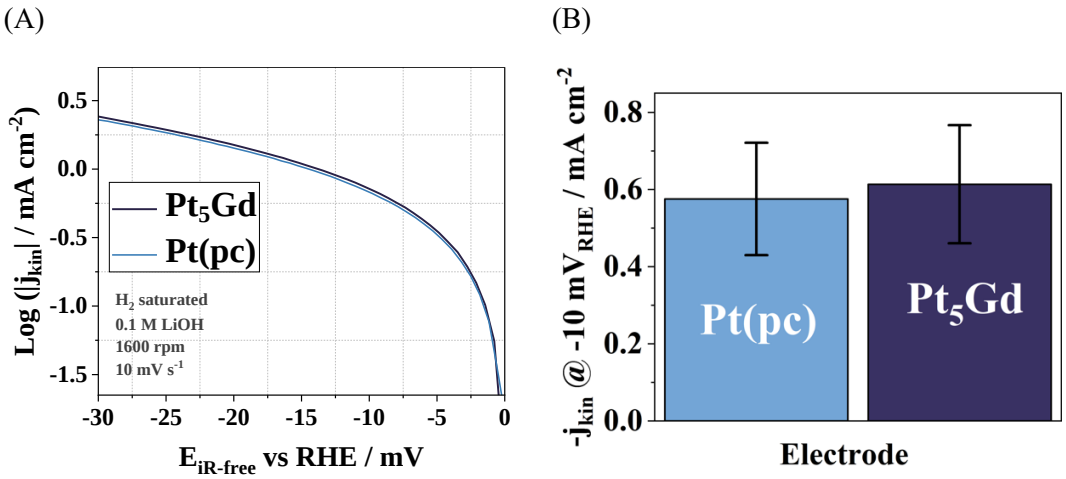

Figure 4.11. (A) The Tafel plot for the HER on the Pt_5Gd and Pt(pc) electrodes measured in H_2-saturated 0.1 LiOH at 1600 rpm with a scan rate of 10 mV s^{-1}. (B) The bar chart of the negative value of j_{kin} at -10 mV vs. RHE for the Pt_5Gd and Pt(pc) electrodes. Adapted with permission from reference [276] (own work).

Figure 4.11 shows the Tafel plots and bar chart of the $-j_{kin}$ at -10 mV vs. RHE for Pt(pc) and Pt_5Gd electrodes recorded in H_2-saturated 0.1 M LiOH at 1600 rpm with a scant rate of 10 mV s^{-1}. The activity of Pt_5Gd is slightly higher than that of the Pt(pc) electrode, which can be attributed to compressive strain effects on the Pt_5Gd surface, showing similar results measured in 0.1 M $HClO_4$, as shown in **Figure 4.6**. Furthermore, it is observed that the $-j_{kin}$ at -10 mV vs. RHE for both electrodes is several orders of magnitude lower in alkaline media than in acidic media, with results comparable to those reported in the literature.[288] This difference in activity can be attributed to the stronger hydrogen binding energy in alkaline media, which results in higher energy

barriers for hydrogen reactions and consequently limits HER activity. It is reported that the hydrogen binding energy depends on the pH of the electrolyte and increases linearly with higher pH values.[274]

Besides, the HER mechanism in alkaline media involves an additional kinetic barrier of the water dissociation process at the Volmer step (**Equation 2.20**), which forms adsorbed H species and is also pH-related.[289,290] Although Pt is located at the peak of the volcano plot in alkaline media compared to the other catalysts,[291] the strategies of decreasing the hydrogen binding energy and reducing the energy barrier of water dissociation are essential to improve the HER performance in alkaline environments.[289]

Moreover, **Figures 4.12A** and **4.12B** show the HER/HOR polarization curves for the Pt(pc) and Pt_5Gd electrodes measured in H_2-saturated 0.1 M LiOH with a scan rate of 10 mV s^{-1} under different rotation conditions. The limiting current density of the HOR for both electrodes increases with the rotation rate. A linear relationship is observed, consistent with the Koutecký-Levich equation at 300 mV vs. RHE, as illustrated in the insets of **Figures 4.12A** and **4.12B**. In contrast, as the rotation rate increases, the HER current density only increases slightly in alkaline media compared to the more pronounced difference observed in acidic media in **Figure 4.7**.

Similar findings are observed in the EIS spectra presented in the Nyquist plots (see **Figures 4.12C** and **4.12D**) and Bode plots (**Appendix**) for both Pt(pc) and Pt_5Gd electrodes. The overall impedance decreases only slightly for both electrodes at -10 mV vs. RHE in H_2-saturated 0.1 M LiOH (**Figures 4.12C** and **4.12D**) compared to the significant change observed in the EIS data in 0.1 M $HClO_4$ (**Figures 4.7C** and **4.7D)**. Additionally, during the HER, the impedance spectra in acidic media consist of two small semicircles at high frequencies and one larger arc in the low-frequency range. However, the EIS spectra in alkaline media show larger semicircles within high frequencies than those in acidic media, indicating that the HER in the alkaline solution

is more dependent on reaction kinetics. This suggests that reaction kinetics become the rate-limiting step in alkaline media, whereas the reaction for the Pt(pc) and Pt_5Gd electrodes is strongly influenced by mass transport and/or adsorption processes in acidic media.

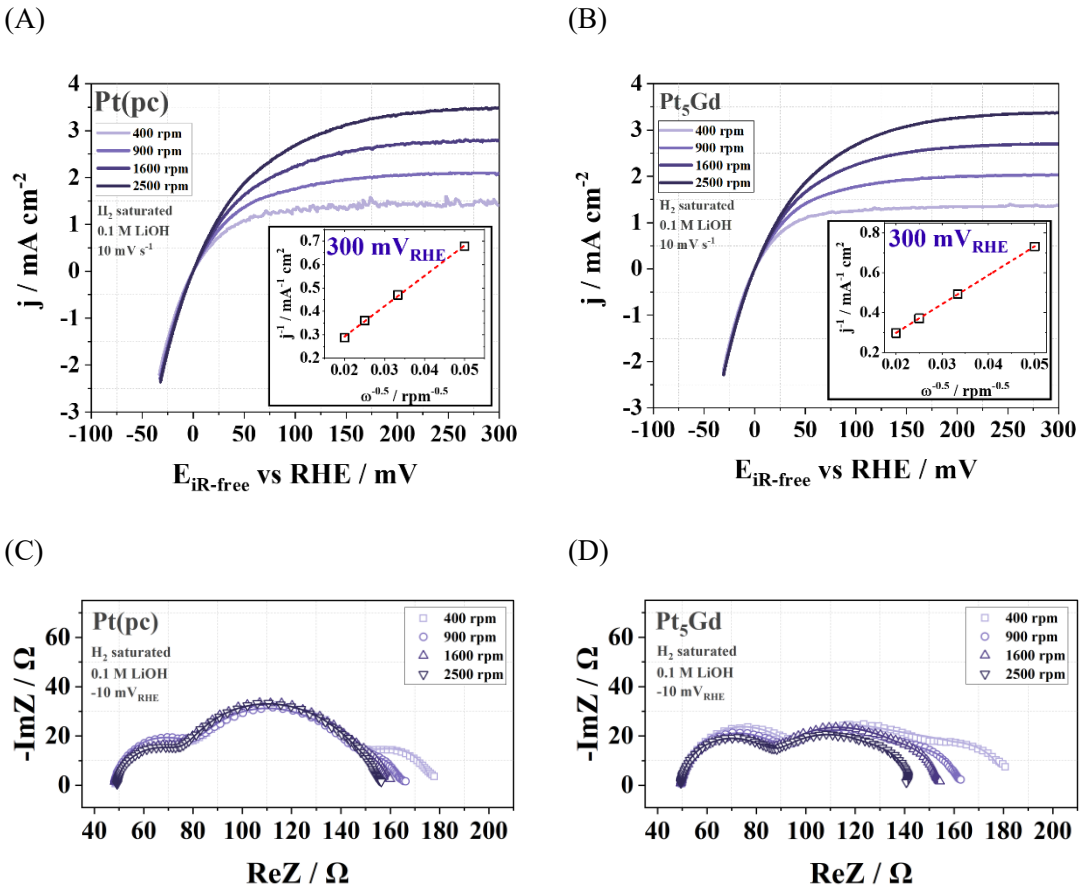

Figure 4.12. The iR-corrected HER/HOR polarization curves (anodic scan) of (A) Pt(pc) and (B) Pt_5Gd electrodes. The inset figures of (A) and (B) illustrate the Koutecký-Levich plot at 300 mV vs. RHE. The EIS data present in the Nyquist plots of (C) Pt(pc) and (D) Pt_5Gd electrodes at -10 mV vs. RHE. The dotted and the solid lines present the measured and fitted EIS spectra with the EEC model in **Figure 4.5**. The data was recorded in H_2-saturated 0.1 M LiOH with a scan rate of 10 mV s^{-1} at the chosen rotation rates of 400, 900, 1600, and 2500 rpm, respectively. Adapted with permission from reference [276] (own work).

Furthermore, **Figure 4.13** and **Figure 4.14** show the fitting results of EIS spectra for the Pt(pc) and Pt_5Gd electrodes, respectively, with each parameter as a function of the

square root of the rotation rate in alkaline media at -10 mV vs. RHE. It is observed that the values of $R_{ct,VH}$, and $R_{ct,VT}$ for both measured electrodes in 0.1 M LiOH are approximately an order of magnitude higher than in 0.1 M $HClO_4$, shown in **Figure 4.8** and **Figure 4.9**. This further implies considerably higher reaction energy barriers, resulting in lower HER kinetics in an alkaline environment.

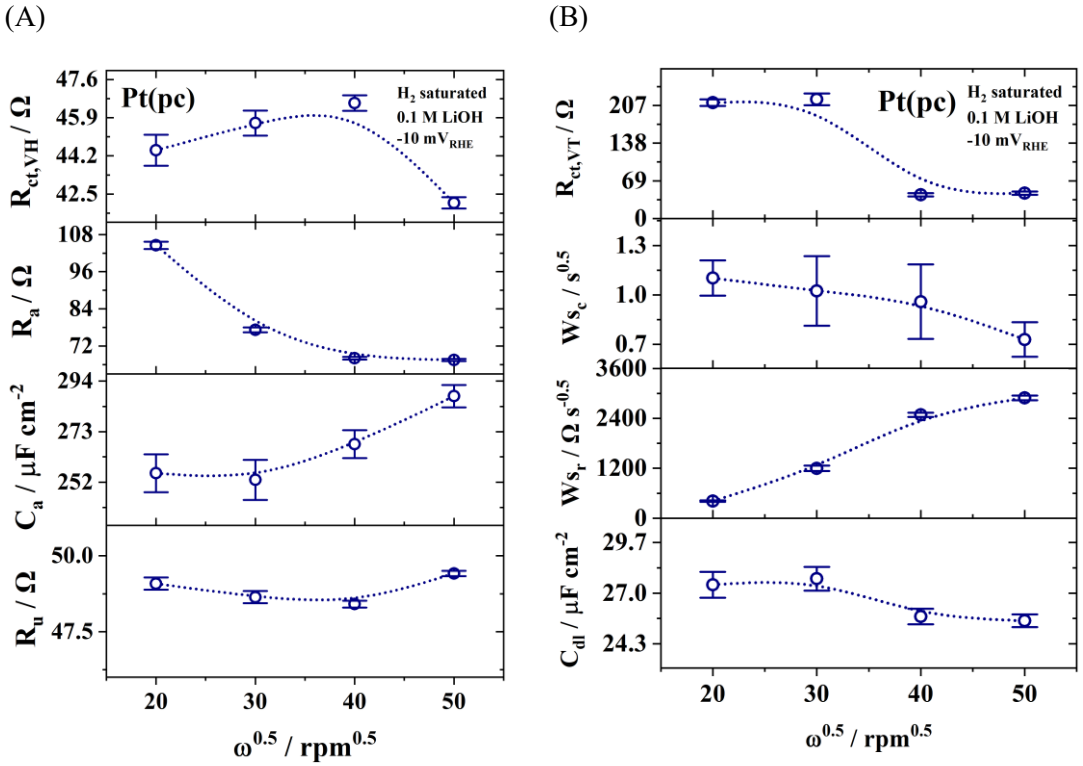

Figure 4.13. The fitting parameters in the EEC model as a function of the square root of the rotation rate for Pt(pc) electrode measured at -10 mV vs. RHE in H_2-saturated LiOH. (A) The parameters consist of the $R_{ct,VH}$, R_a, and C_a for the Volmer-Heyrovsky mechanism, and the R_u. (B) The parameters contain the $R_{ct,VT}$ and the Ws element (Ws_c and Ws_r) of the Volmer-Tafel mechanism, and the non-Faradaic contribution of C_{dl}. Adapted with permission from reference [276] (own work).

Besides, compared to the $R_{ct,VH}$ with relatively small deviations at different rotation rates, the $R_{ct,VT}$ increases more significantly with a higher resistance than that of $R_{ct,VH}$ at 400 rpm, which indicates that the Volmer-Heyrovsky pathway is more dominant at low rotation configurations for the Pt(pc) and Pt_5Gd electrodes. For the adsorption

processes, mainly associated with the Volmer-Heyrovsky reaction pathway in **Equation *4.1***, the variation trend of the R_a and C_a with rotation rate in alkaline media is similar to that observed in acidic media. Specifically, the R_a decreases while the C_a increases as the rotation rate increases from 400 rpm to 2500 rpm. This indicates that HER in alkaline media also occurs more easily under higher rotation conditions, with the proper fractional coverage of the adsorbed species at the electrode surfaces.

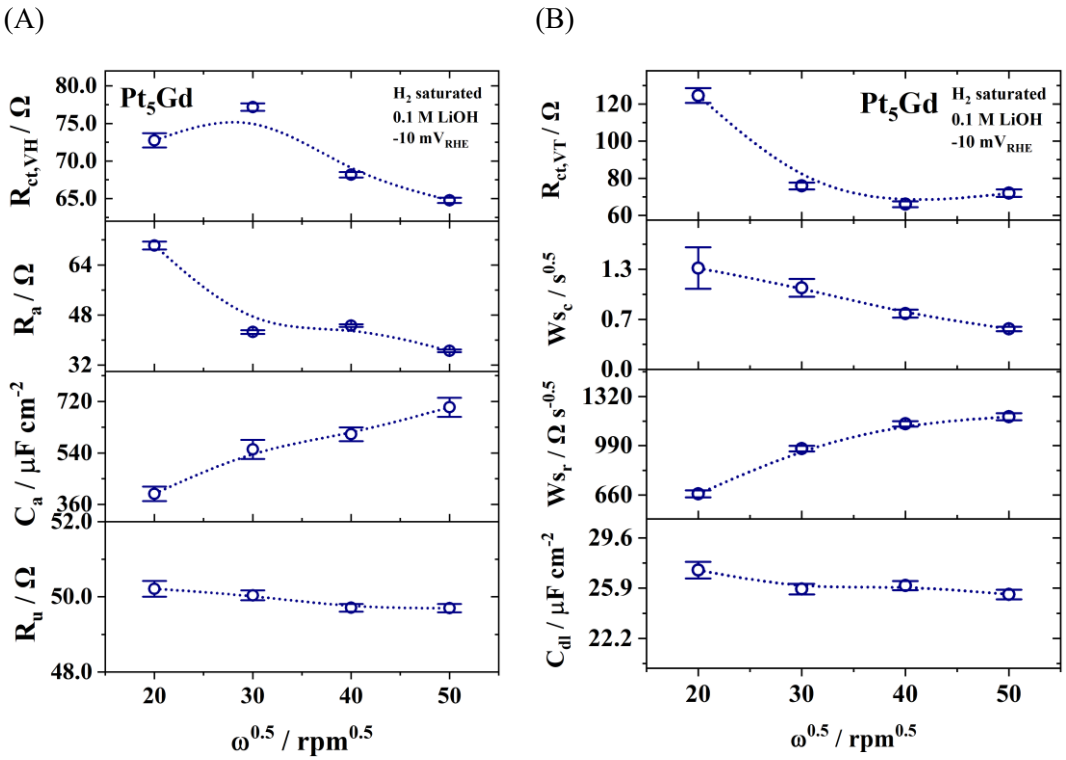

Figure 4.14. The fitting parameters in the EEC model as a function of the square root of the rotation rate for Pt_5Gd electrode recorded at -10 mV vs. RHE in H_2-saturated LiOH. (A) The parameters include the $R_{ct,VH}$, R_a, and C_a for the Volmer-Heyrovsky mechanism, and the R_u. (B) The parameters consist of the $R_{ct,VT}$ and the Ws element (Ws_c and Ws_r) of the Volmer-Tafel mechanism and the non-Faradaic contribution of C_{dl}. Adapted with permission from reference [276] (own work).

In addition, for the Volmer-Tafel reaction pathway, the mass-transport elements (Ws_c and Ws_r) also follow a similar trend as detected in 0.1 M $HClO_4$. For the Pt(pc) and Pt_5Gd electrodes measured in alkaline media, the Ws_c increases slightly, while the Ws_r

decreases significantly, becoming several times lower as the rotation rate drops. This can be associated with the significant increase of the $R_{ct,VT}$ from 2500 rpm to 400 rpm. As the reaction rate decreases dramatically at lower rotation rates, the concentrations of species at the surfaces consequently increase, leading to a decreasing value of Ws_r, as shown in **Equation 4.6**. Meanwhile, as the Ws_c increases, the thickness of the diffuse layer becomes larger for both electrodes in alkaline media (see **Equation 4.4**).

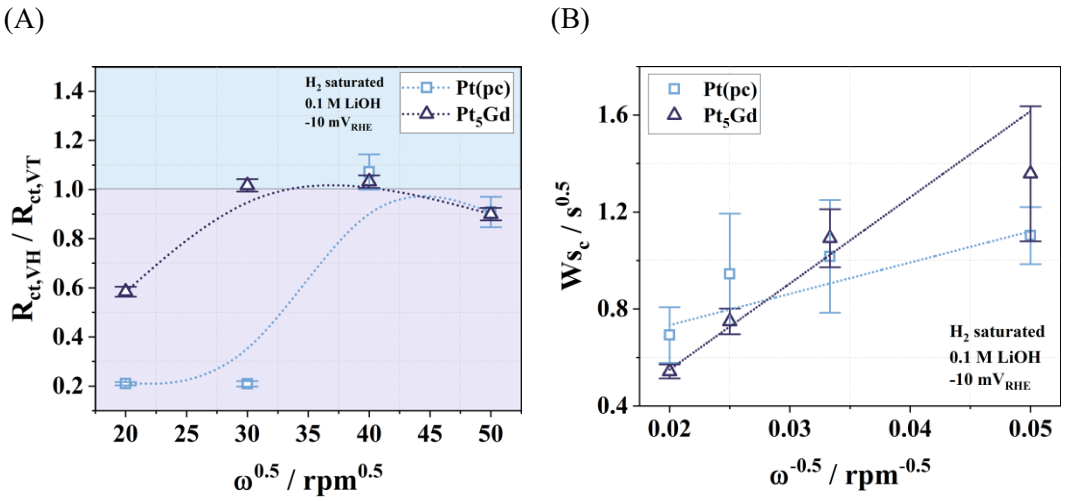

Figure 4.15. (A) The relative contribution between the Volmer-Heyrovsky and Volmer-Tefal mechanisms with the ratio of $R_{ct,VH}/R_{ct,VT}$ as a function of the square root of the rotation rate, and (B) Ws_c as a function of the inverse of the square root of the rotation rate for the Pt(pc) and Pt_5Gd electrodes at -10 mV vs. RHE in H_2-saturated LiOH. The dashed lines in (A) are a guide to the eye and the lines in (B) are a linear fit of the data, respectively. Adapted with permission from reference [276] (own work).

Besides, Pt(pc) and Pt_5Gd electrodes exhibit a higher deviation of Ws_r with different rotation rates in alkaline media, as displayed in **Figures 4.13B** and **4.14B,** than in acid media, shown in **Figures 4.8B** and **4.9B**. This difference can be attributed to the distinct reactants and products of the HER pathways. Since only charge species contribute to the impedance spectra in alkaline media, the diffusion of OH^- species needs to be considered; however, the diffusion of H^+ (H_3O^+) dominates in acidic media.

Furthermore, **Figure 4.15A** shows the relative contribution of the overall HER between

the Volmer-Heyrovsky and Volmer-Tefal mechanisms at different rotation rates in alkaline media based on **Equation 4.7**. The ratio of $R_{ct,VH}/R_{ct,VT}$ is about 1 at 2500 rpm for both electrodes, but the value decreases to approximately 0.6 and 0.2 for the Pt(pc) and Pt_5Gd electrodes, respectively, at 400 rpm. This indicates that the Volmer-Heyrovsky reaction pathway is preferred in alkaline media at lower rotation configurations for both measured electrodes. Additionally, a linear relationship of the Ws_c and the inverse of the square root of the rotation rate is also observed for the Pt(pc) and Pt_5Gd electrodes during the HER in alkaline media (**Figure 4.15B)**. The slopes of both electrodes appear less steep, with higher fitting errors in alkaline media compared to acidic media (**Figure 4.10B**). The reason can be attributed to the different reaction mechanisms and variations in species at the surfaces (see **Section 2.3.1**). For instance, the HER in acidic solutions involves H^+ and/or H_3O^+, and H_2 as the reactants and the products, respectively. In contrast, H_2O molecules are the reactants, and H_2 and OH^- ions are the products of HER in alkaline solutions. The thickness of the diffuse layer for each electrode can also be quantitatively calculated once the parameters in **Equation 4.4** and **Equation 4.8** are known.

4.2.4. HER for Nanostructured Pd/C Catalyst in Acidic Media

In the previous sections, the classical model system involving Pt(pc) and Pt_5Gd disc electrodes for HER in electrolytes of 0.1 M $HClO_4$ and LiOH was discussed by using the combining EIS-RDE approach. Here, we briefly explore the EIS findings in a more complex system, like a nanostructured Pd/C catalyst for HER under different rotation configurations. It is noted that the primary reasons for selecting the Pd/C catalyst for the measurements are its competitively high HER activity, historically lower cost, and its more abundant source.[292] These advantages make it a promising alternative for

HER catalysts in electrolysis. The detailed information, e.g., the top-down approach of producing the nanostructured particles, material characterization, and the ink preparation of catalyst on the RDE, are well illustrated in the publication.[276,293]

Figure 4.16 shows the impedance spectra for about 17.1 wt% Pd/C catalyst measured at -5 mV vs. RHE in H_2-saturated 0.1 M $HClO_4$ under different rotation rates. The Nyquist plots for the Pd/C catalyst exhibit a similar shape to those observed for the Pt(pc) and Pt_5Gd electrodes conducted in acidic media, as shown in **Figure 4.7**.

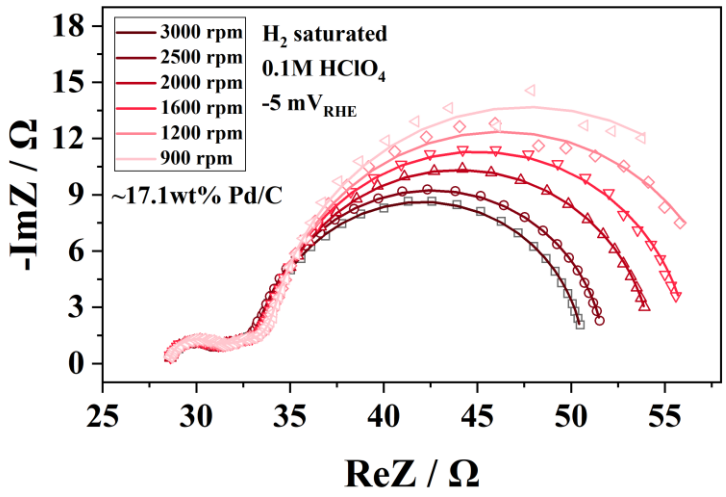

Figure 4.16. The EIS data presented in the Nyquist plots of nanostructured Pd/C catalyst measured at -5 mV vs. RHE in H_2-saturated $HClO_4$ at different rotation rates, including 900, 1200, 1600, 2000, 2500, and 3000 rpm. The dotted and the solid lines present the measured and fitted EIS spectra with the EEC model in **Figure 4.5**. Adapted with permission from reference [276] (own work).

The higher frequency region of the impedance spectra can be mainly associated with the charge transfer process of the Volmer-Heyrovsky and Volmer-Tafel mechanisms, and the lower frequency region can be related to the mass transport and/or the adsorption processes, respectively. At the different rotation configurations, the larger deviation of EIS spectra at the low frequencies is observed, which can also be associated with the facile reaction of HER, which influences the slower processes (e.g., diffusion and adsorption). The Bode plots provide further information in terms of the absolute

value of the impedance and the phase shift as a function of Log frequency (see **Appendix**).

Figure 4.17 shows the fitting results of each parameter in the EEC model for nanostructured Pd/C catalyst from the Nyquist plots in **Figure 4.16**. For the Faradaic reactions, the value of $R_{ct,VH}$ and $R_{ct,VT}$ also change slightly, and the possible explanation is comparable to the disc electrodes in acidic media, as elaborated earlier in **Figure 4.8** and **Figure 4.9**.

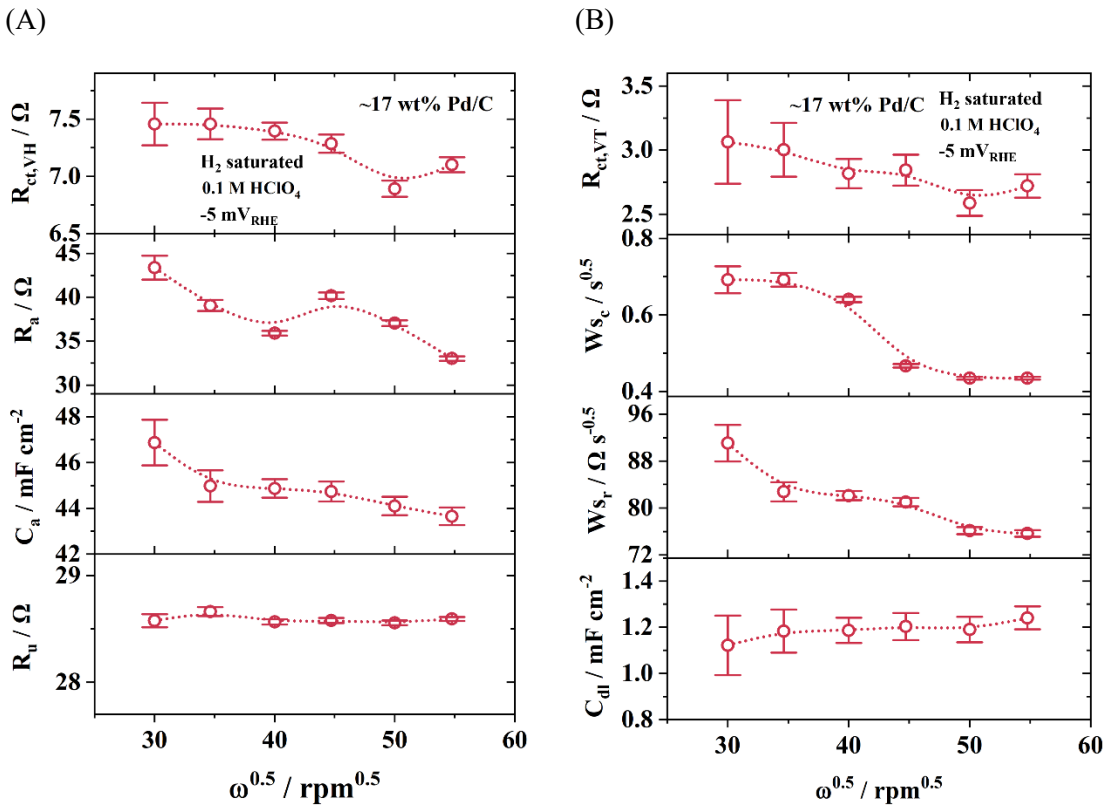

Figure 4.17. The fitting parameters in the EEC model as a function of the square root of the rotation rate for nanostructured Pd/C catalyst measured at -5 mV vs. RHE in H_2-saturated $HClO_4$. (A) The parameters consist of $R_{ct,VH}$, R_a, and C_a for the Volmer-Heyrovsky mechanism, and R_u. (B) The parameters contain $R_{ct,VT,}$ and the Ws element (Ws_c and Ws_r) of the Volmer-Tafel mechanism, and the non-Faradaic contribution of C_{dl}. Adapted with permission from reference [276] (own work).

In contrast, unlike the case of disc electrodes in both acid and alkaline media, all values

of the corresponding adsorption (R_a and C_a) and diffusion (Ws_c and Ws_r) processes increase as the rotation rate decreases. In particular, the trend of C_a and Ws_r shows the opposite compared to the disc electrodes with decreasing rotation configurations. These can be associated with the more complex Pd/C catalyst involving the nanostructured reaction interfaces and the phenomenon of hydrogen absorption during the HER.[293] The systematical properties of R_u and C_{dl} remain constant with different rotation rates.

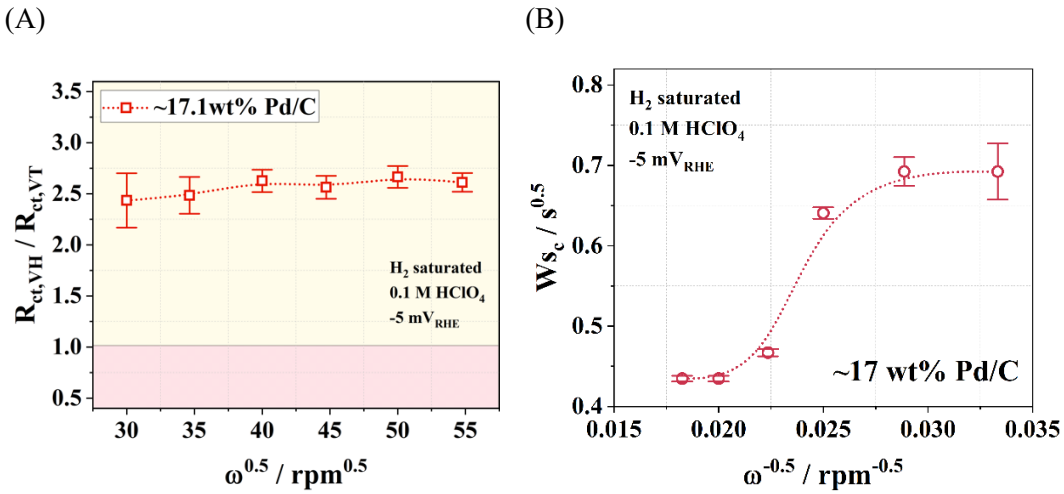

Figure 4.18. (A) The fitting parameters of $R_{ct,VH}$, and $R_{ct,VT}$ as a function of the square root of the rotation rate for nanostructured Pd/C catalyst, and (B) Ws_c as a function of the inverse of the square root of the rotation rate at -5 mV vs. RHE in H_2-saturated $HClO_4$. The dotted lines in (A) and (B) are a guide to the eye. Adapted with permission from reference [276] (own work).

Besides, compared to the Pt_5Gd electrode with the dominating Volmer-Heyrovsky mechanism of HER (see **Figure 4.10A**), the results of the Pd/C catalyst in **Figure 4.18A** show the opposite. The value of $R_{ct,VH}$ is about twice as high as that of $R_{ct,VT}$ in acidic solutions within the selected rotation rates, which indicates the Volmer-Tafel reaction pathway is preferred to take place at the surfaces. Last but not least, while the spectra at lower frequencies decrease significantly, the expected linear relationship between Ws_r and the inverse of the square root of the rotation rate is not observed for the nanostructured Pd/C catalyst in **Figure 4.18B**, in contrast to the disc-electrode systems

depicted in **Figure 4.10B**. This deviation is likely attributable to the complex surface structure of the nanostructured catalyst, resulting in localized variations in diffusion properties compared to the flat disc electrode.

4.3. Influence of Alkali Metal Cations on the ORR of Pt_5Y and Pt_5Gd Alloys

In this section, we chose polycrystalline Pt_5Gd and Pt_5Y electrodes as model systems for Pt-based alloys. First, we investigated their ORR activities in acidic solutions, comparing them with the Pt(pc) electrode. Then, we further elucidated the effect of alkali metal cations on the ORR kinetic current for the measured disc electrodes in alkaline media. To investigate the experimental findings of Pt and Pt alloys more profoundly, we conducted theoretical DFT calculations that systematically correlated the influences of the surface strains from lattice mismatch of bulk alloys and the presence of alkali cations in the electrolyte on the ORR activities.

The major part of the work is based on the published manuscript with the agreement of the listed co-authors:

Song, K.-T.; Zagalskaya, A.; Schott, C. M.; Schneider, P. M.; Garlyyev, B.; Alexandrov, V.; Bandarenka, A. S. Influence of Alkali Metal Cations on the Oxygen Reduction Activity of Pt_5Y and Pt_5Gd Alloys. J. Phys. Chem. C **2024**, 128 (12), 4969–4977.[294]

4.3.1. ORR in Acidic Media

It is worth noting that the main reason for selecting polycrystalline Pt_5Gd and Pt_5Y as the model system of Pt-based alloys is due to their high thermodynamic stability. Although there are various bimetallic Pt alloys with late transition metals (e.g., Cu, Ni, and Co) demonstrating outstanding ORR activities, the critical durability issue remains due to the segregation and continuous dissolution of atoms of the secondary elements into acidic solutions.[295,296,297,298] In comparison, the Pt alloys with Gd and Y atoms as the minor elements have negative heat formation properties, which can prevent the continuous dealloying process through the entire bulk and offer a relatively stable

condition during electrochemical reactions.[68,251,299,300,301]

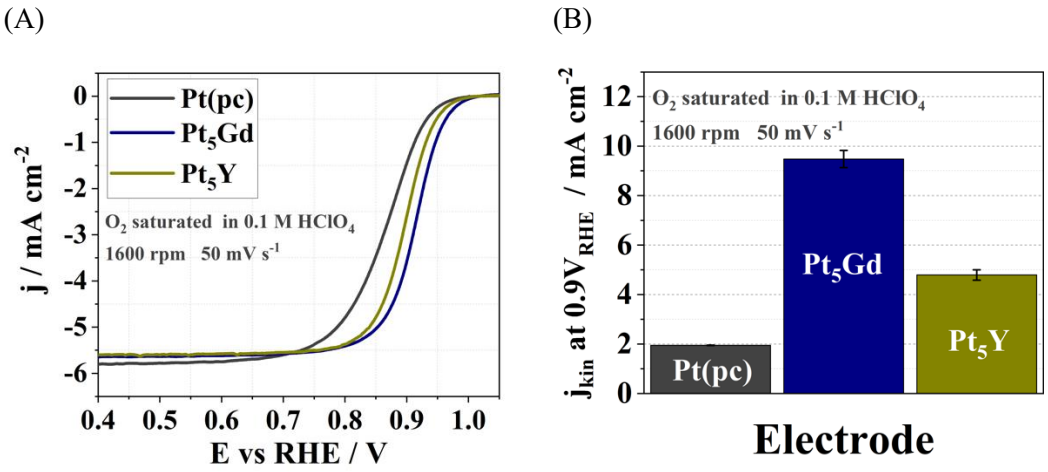

Figure 4.19. (A) The iR-corrected ORR polarization curves (anodic scans) and (B) the bar chart of the j_{kin} at 0.9 V vs. RHE of the Pt(pc), Pt_5Gd, and Pt_5Y electrodes in O_2-saturated 0.1 M $HClO_4$ with the scan rate of 50 mV s^{-1} at 1600 rpm. Adapted with permission from reference [294] (own work).

Figure 4.19A demonstrates the typical ORR polarization curves of Pt_5Gd, Pt_5Y, and Pt(pc) electrodes in O_2-saturated 0.1 M $HClO_4$ at 1600 rpm with a scan rate of 50 mV s^{-1}. The extracted ORR kinetic current densities at 0.9 V vs. RHE exhibit the following trend: Pt_5Gd > Pt_5Y > Pt(pc), as shown in **Figure 4.19B**. The resulting current densities are comparable to the reported literature.[68,251,301,302] The 2-4 times improved ORR activities of the Pt alloys compared with pure Pt electrodes mainly due to the compressive strain effects within the Pt overlayer on the surface, in which the Pt-Pt interatomic distances are shorter than in bulk Pt alloys, as also indicated by the XRD analysis (see **Section 4.1.1**) and the literature.[68,251,301] The d-band theory further strengthens the observed enhancement of ORR activities for Pt alloys.[303,304] The energy levels of metal d-band centers shift downwards for a Pt-overlayer under the compressive strain conditions, which leads to lower binding energies of adsorbed intermediates such as *O, *OH, and *OOH on the electrodes.

4.3.2. ORR in Alkaline Media

Before delving into the ORR activities in various alkaline solutions, it's important to note that potential issues arising from contaminations of alkaline media with glass cells[257,258,259,260,261] have been addressed.

(A) (B)

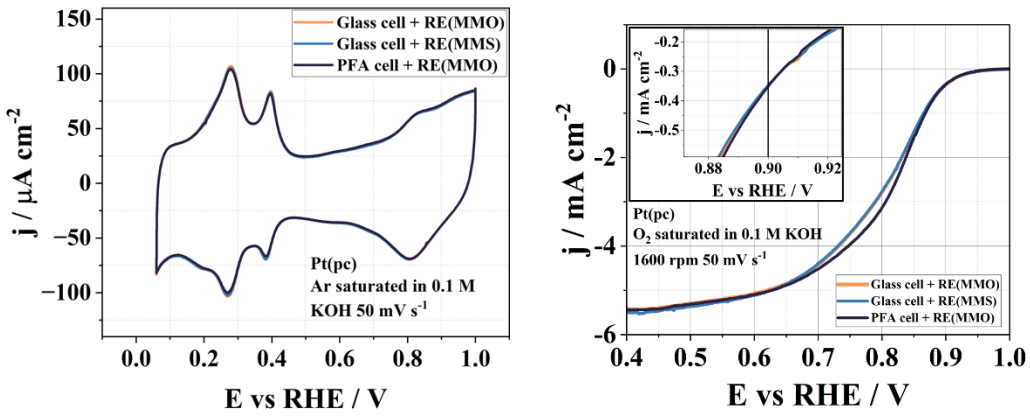

Figure 4.20. (A) The CVs for Pt(pc) in Ar-saturated 0.1 M KOH and (B) the iR-corrected ORR polarization curves (anodic sweeps) for Pt(pc) in O_2-saturated 0.1 M KOH with a scan rate of 50 mV s^{-1} by using MMS and MMO as the REs and with the glass cell and the perfluoroalkoxy (PFA) cell. The inset in (B) presents the enlarged scale of measured current density at potentials near 0.9 V vs. RHE. Adapted with permission from reference [294] (own work).

Figure 4.20 shows the CVs and the ORR polarization curves obtained under three conditions of experimental cell and RE (i.e., the glass cell with the MMS, the glass cell with the MMO, and the PFA cell with the MMO) in Ar-saturated and O_2-saturated 0.1 M KOH, respectively. The results show negligible differences, indicating good agreement with short-term measurements conducted in alkaline media using glass cells. However, it is still highly recommended to use highly chemically inert materials (e.g., PFA) for long-term measurements in alkaline solutions.

Prior to the ORR measurements, CVs for Pt(pc) in Ar-saturated metal hydroxide electrolytes, AM-OH (AM^+ = Li^+, Na^+, K^+, Rb^+, and Cs^+), have been conducted to check the surface quality (see **Figure 4.21**). As mentioned previously, the CV comprises three primary regions: hydrogen adsorption/desorption, double layer, and oxide formation/reduction. The presence of various alkali metal cations in the solution causes shifts in the characteristic peaks in their CVs.

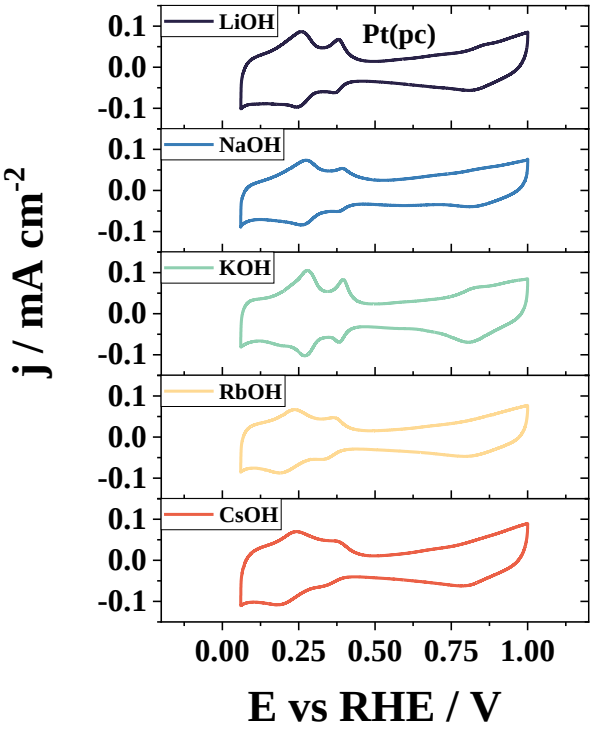

Figure 4.21. The CVs for Pt(pc) in Ar-saturated 0.1 M AM−OH (AM = Li^+, Na^+, K^+, Rb^+, and Cs^+) electrolytes with a scan rate of 50 mV s^{-1}. Adapted with permission from reference [294] (own work).

Furthermore, to understand the influence of the alkali metal cations on the ORR activity, we compare the results of Pt alloys with the reference model system of Pt(pc). **Figure 4.22A** shows the ORR polarization curves for the Pt(pc) electrode in different O_2-saturated 0.1 M alkaline media. The set of measurements is the same as that in acidic media (see **Figure 4.19**). To further evaluate the ORR kinetics in the presence of

different alkali cations in the electrolyte, **Figure 4.22B** shows the corresponding bar charts of the calculated ORR kinetic current densities of Pt(pc) at 0.9 V vs. RHE.

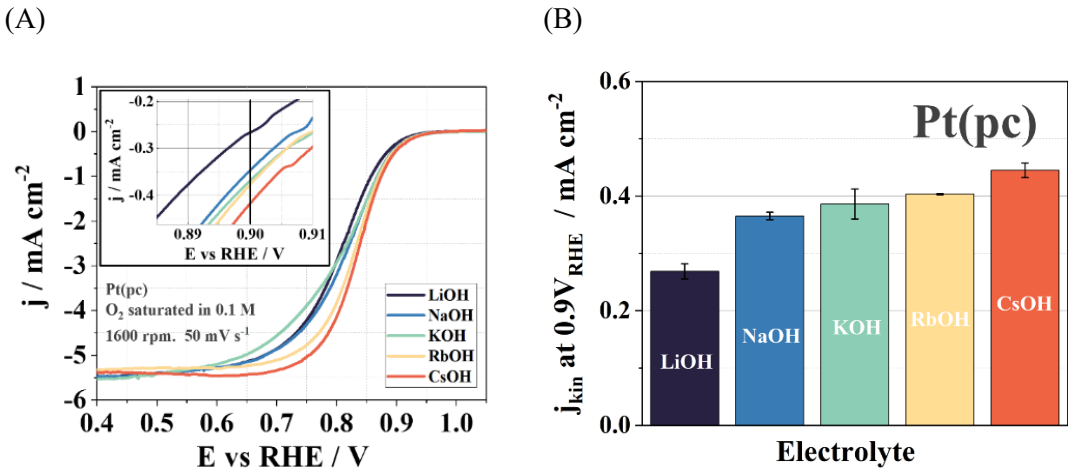

Figure 4.22. (A) The iR-corrected ORR polarization curves (anodic scans) and (B) the bar chart of j_{kin} at 0.9 V vs. RHE for Pt(pc) electrode, recorded in O_2-saturated 0.1 M AM−OH ($AM^+ = Li^+$, Na^+, K^+, Rb^+, and Cs^+) electrolytes with the scan rate of 50 mV s^{-1} at 1600 rpm. The inset figure of (A) represents the enlarged scale of measured current density at potentials near 0.9 V vs. RHE. Adapted with permission from reference [294] (own work).

The ORR activity of Pt(pc) follows in the order of $Li^+ < Na^+ < K^+ < Rb^+ < Cs^+$, which follows the same order as Pt(111) in the literature.[81] The results can be associated with the non-covalent interactions at electrode/electrolyte interfaces, where these interactions involve stabilization and bond energies of less than 85 kJ mol^{-1}, including hydrogen bonding, cation-OH bonding, and cation-water bonding.[81,305,306,307] Here, we highlight the interactions at the electrode/electrolyte interface during the ORR between the adsorbed species in the IHP and the hydrated alkali metal cations ($AM^+(H_2O)_x$) in the OHP, as schematically illustrated in **Figure 4.25A**. The charge density of alkali cations correlates with the cation hydration energy and increases with stronger interactions. In alkaline electrolytes, the structure-making cations (i.e., Li^+ and Na^+) demonstrate higher charge densities as well as a higher stabilizing effect on chemisorbed species on pure Pt surfaces. Consequently, along with the slightly stronger intrinsic binding energy between Pt and reaction intermediates (e.g., Pt-OH), the cations

possessing higher solvation energy hinder the mobility of reactive species and decrease the kinetics of the ORR. However, the structure-breaking cations (e.g., Rb^+ and Cs^+) have the opposite influence, in which the weaker interactions promote the movement of the intermediates and thus increase the ORR activities.

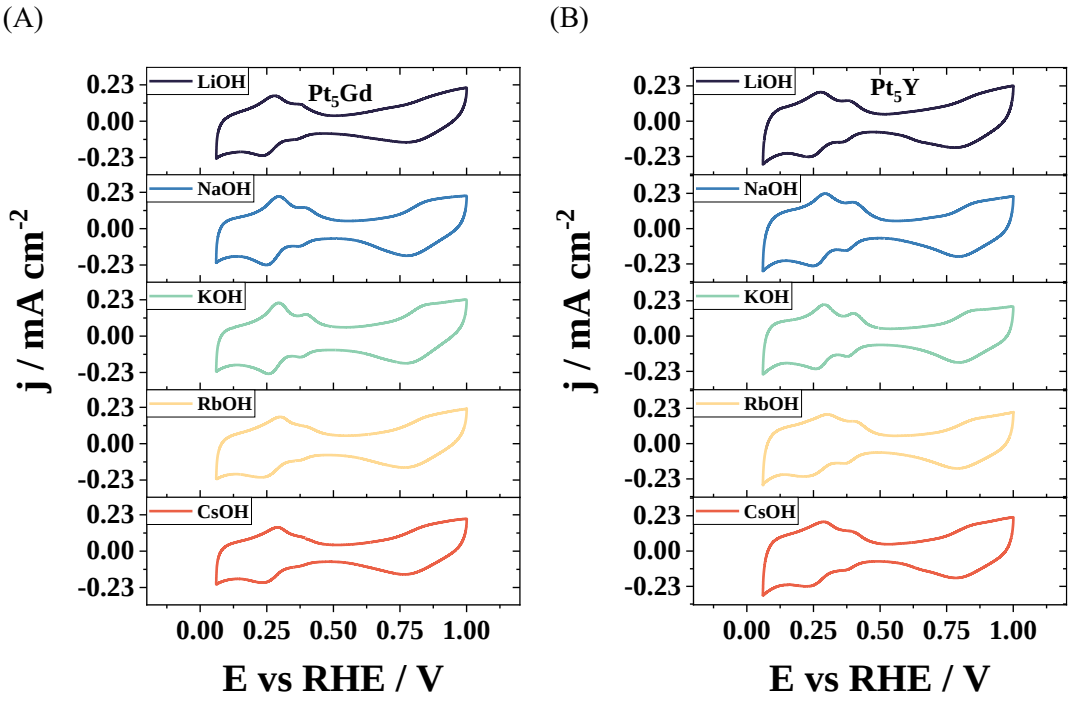

Figure 4.23. The CVs for (A) Pt_5Gd and (B) Pt_5Y in Ar-saturated 0.1 M AM−OH (AM = Li^+, Na^+, K^+, Rb^+, and Cs^+) electrolytes with a scan rate of 50 mV s^{-1}. Adapted with permission from reference [294] (own work).

Figure 4.23 shows the CVs for Pt_5Gd and Pt_5Y in different Ar-saturated 0.1 M alkaline solutions before ORR measurements to check the quality of the electrode surface conditions. In contrast, the ORR polarization curves and activities in **Figures 4.24A** and **4.24B** for both Pt_5Gd and Pt_5Y electrodes show a different trend compared to the Pt(pc) electrode in alkaline media in **Figure 4.22**. The order of the ORR kinetic current density at 0.9 V vs. RHE of both alloys follows the opposite order (i.e., $Li^+ > Na^+ > K^+ > Rb^+ > Cs^+$), and the value measured in LiOH is more than twice as high as that in CsOH for each electrode (see **Figure 4.24C** and **Figure 4.24D**). This can be attributed to both non-covalent interactions and surface strain effects at the electrode/electrolyte interface.

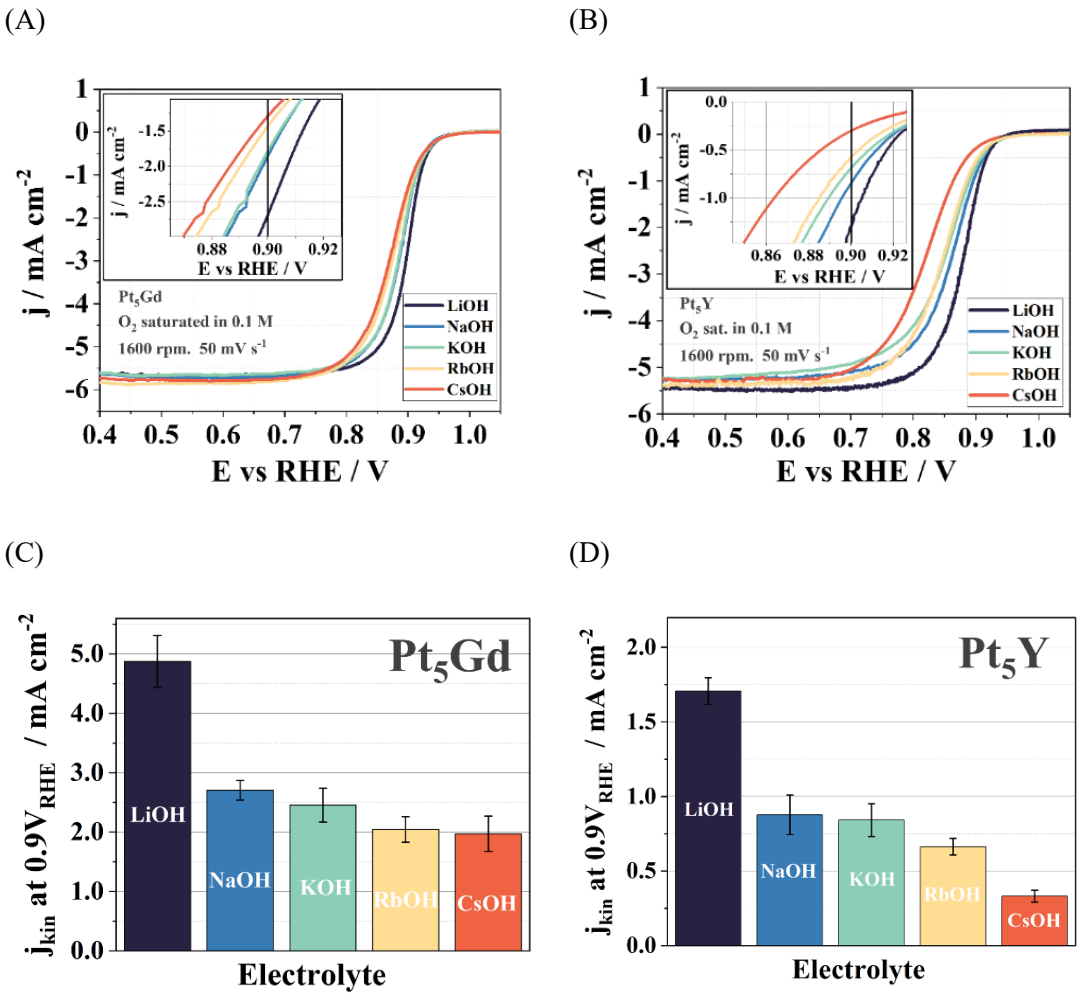

Figure 4.24. The iR-corrected ORR polarization curves (anodic scans) of (A) Pt_5Gd and (B) Pt_5Y, and the bar charts of j_{kin} at 0.9 V vs. RHE for (C) Pt_5Gd and (D) Pt_5Y, respectively, measured in O_2-saturated 0.1 M AM−OH (AM^+ = Li^+, Na^+, K^+, Rb^+, and Cs^+) electrolytes with the scan rate of 50 mV s^{-1} at 1600 rpm. The inset figures of (A) and (B) represent the enlarged scale of measured current density at potentials near 0.9 V vs. RHE. Adapted with permission from reference [294] (own work).

Compared to a pure Pt surface under no strain conditions, the compressive strains are introduced on the Pt-overlayer of Pt alloys after acid leaching, lowering the adsorbed species' binding energy and demonstrating higher intrinsic ORR activity of Pt alloys. The existence of the stronger solvation shells optimizes and stabilizes the molecular interactions within the outer and inner Helmholtz layers and causes enhanced ORR activity. However, the weaker hydrated alkali cations, which decrease the interaction

strength between the reaction intermediates and hydrated shells, further destabilize the binding of Pt-OH on the compressively strained surface and hinder the reaction kinetics of the ORR.

(A) (B)

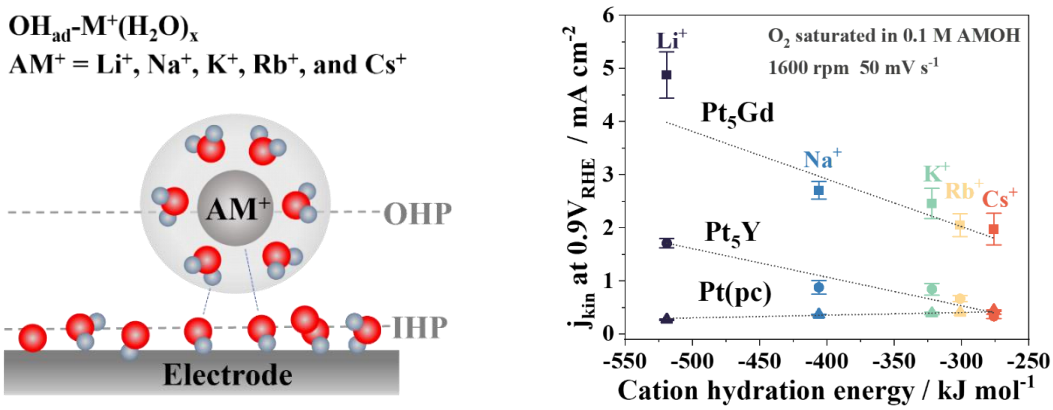

Figure 4.25. (A) The schematic of electrode/electrolyte interface during the ORR in alkaline media with the interactions between the hydrated cation in the OHP and the adsorbed species (e.g., *O, *H_2O,*OH, and *OOH) in the IHP. (B) The j_{kin} at 0.9 V vs. RHE for Pt_5Gd, Pt_5Y, and Pt(pc) electrodes, extracted from **Figure 4.22** and **Figure 2.24**, as a function of cation hydration energy with the dotted lines as linear fits. Adapted with permission from reference [294] (own work).

Furthermore, **Figure 4.25B** combines the results of the ORR kinetic current densities at 0.9 V vs. RHE as a function of cation hydration energy for all measured electrodes in 0.1 M alkaline solutions. It has been found that the ORR activities of both Pt_5Gd and Pt_5Y electrodes are higher than those of Pt(pc) except for Pt_5Y in CsOH, mainly due to the compressive strain effects on the Pt surface of Pt alloys. In addition, the ORR activity for Pt alloys increases linearly with the increase in the hydration energy (i.e., the ORR reaction rate shows the highest and worst in 0.1 M LiOH and CsOH, respectively). On the contrary, Pt(pc) demonstrates the opposite activity trend.

It is noted that the ORR activities recorded in alkaline media are several factors lower than in 0.1 M $HClO_4$ in **Figure 4.19** for all measured electrodes. The results are

comparable to the literature with Pt-based electrocatalysts.[288,308,309,310] One reason for the lower activities in alkaline media could be the formation of the undesired HOO^- species on the electrode surface, which involves the two-electron transfer of reaction pathway in the outer sphere process[311,312,313] (see **Figure 2.9**). Another possible explanation could be the existence of various reaction mechanisms of the ORR in alkaline media, where excessively strong Pt-OH bonding energy may lead to undesirable blockages of the active sites on the Pt surface and, therefore, decrease the reaction rate of the ORR.[311]

4.3.3. Density Functional Theory Calculations of Alkali Cation and Strain Effects on the ORR

Our collaborators at UNL conducted DFT calculations to investigate the different ORR trends for Pt-based electrocatalysts in alkaline electrolytes further. The computational details are reported in the **Appendix** and the published paper.[294] This work uses the Pt(111) surface as a standard model for Pt-based electrodes because of the favorable low surface energy and its common presence in polycrystalline structures. The electrocatalytic system is modeled under the conditions of Pt(111) surface with the adsorbed OH species.[68,314] The applied strain associated with the Pt-Pt distance on the surface is presented in **Appendix**. According to the results of XRD analysis (see **Figure 4.1** and **Table 4.1**), the computational strain corresponding to the experimental data is about -2% on the Pt surface.

Figure 4.26A depicts the adsorption energy of *OH species for the system containing different alkali metal cations, plotted against the Pt-Pt distance, along with the corresponding surface strain. Additionally, it includes a schematic representation of

structures and cell dimensions for the case at 0% strain on the right-hand side. It is observed that as the compressive strain (i.e., negative % strain) increases, the *OH adsorption energy increases, causing the destabilization of *OH on the pristine Pt surface[68, 315] as well as in the presence of different alkali metal cations. This destabilization has been previously demonstrated to enhance the ORR activity of Pt-based catalysts by shifting the ΔG_{*OH} closer to the peak of the volcano plot. The observed slope of -0.03 eV/% for pure Pt agrees with previous computational studies.[68]

Compared to the destabilization effect of compressive strain on the adsorption energy of *OH species, the presence of alkali cations provides the opposite impact, stabilizing the Pt-OH interaction at the electrode/electrolyte interface. This stabilizing effect increases with the higher hydration energy of the alkali cations. For instance, the highly hydrated Li^+ cation stabilizes *OH by 0.75 eV, whereas the least hydrated cation (e.g., Cs^+) merely stabilizes *OH by 0.37 eV for Pt at 0 % of strain (see **Appendix**).

Figure 4.26B shows the theoretical volcano plot with the correlation between the ORR overpotential (η_{ORR}) and the adsorbed energy of *OH. To obtain the optimal binding condition with the lowest η_{ORR}, it is essential to consider both the effects of surface strain and the specific nature of alkali cation. In particular, the pure Pt surface has too strong *OH adsorption energy under less compressive and no-strain conditions. The existence of Cs^+ exhibits lower theoretical ORR overpotentials compared to Li^+ due to the larger stabilization effect. For example, for the Pt surface strain at -2 % (i.e., corresponding to the Pt(pc) electrode), the η_{ORR} of Li^+ is 0.57 V, while the η_{ORR} of Cs^+ is 0.37 V. However, as larger compressive strains are applied (i.e., corresponding to the Pt overlayer on bulk alloys), the value of η_{ORR} decreases in the presence of Li^+ while increasing for Cs^+. This is because under such significant compressive strains, the interaction of Pt-OH becomes too destabilized, and the strong stabilizing effect of Li^+ brings it closer to the volcano peak with optimal ORR activity. Therefore, the

computational findings strongly support and help to elucidate the experimental observations, which illustrate the opposite trends of the ORR activity under the influence of alkali cations on the Pt(pc) and Pt alloys (see **Figure 4.25B**).

(A)

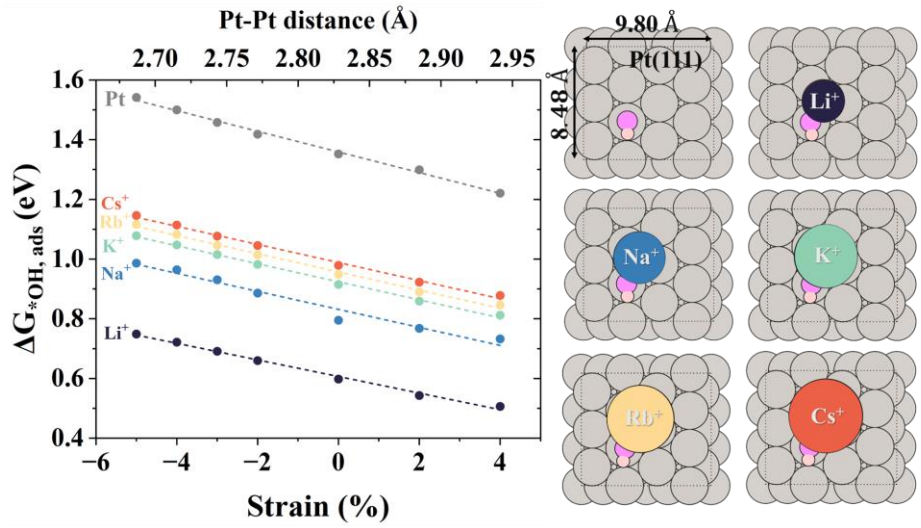

(B)

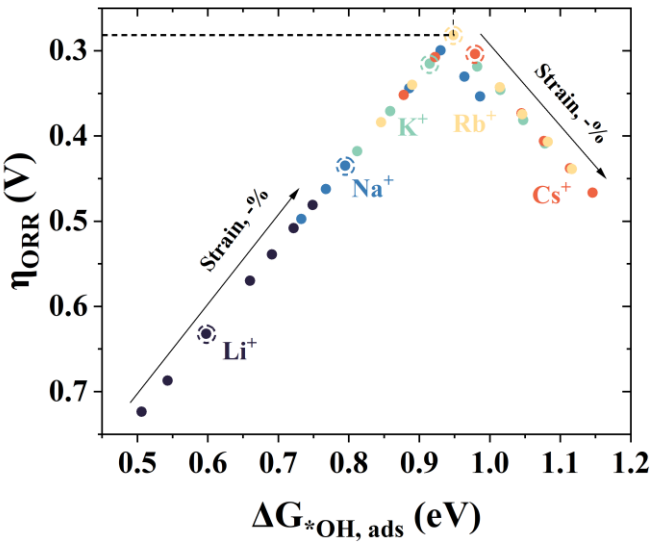

Figure 4.26. (A) The adsorption energy of *OH on Pt(111) as a function of strain from -5% (compression) to +4% (expansion) (left), and the schematic structures and cell dimensions corresponding to 0% strain (right). (B) The theoretical volcano plot with the correlation between the η_{ORR} and the computed *OH adsorption energy on the pure Pt(111) surface with alkali cations. The arrows demonstrate the direction of the strain (from tensile to compressive), and the encircled dots relate to 0% strain, respectively. Adapted with permission from reference [294] (own work).

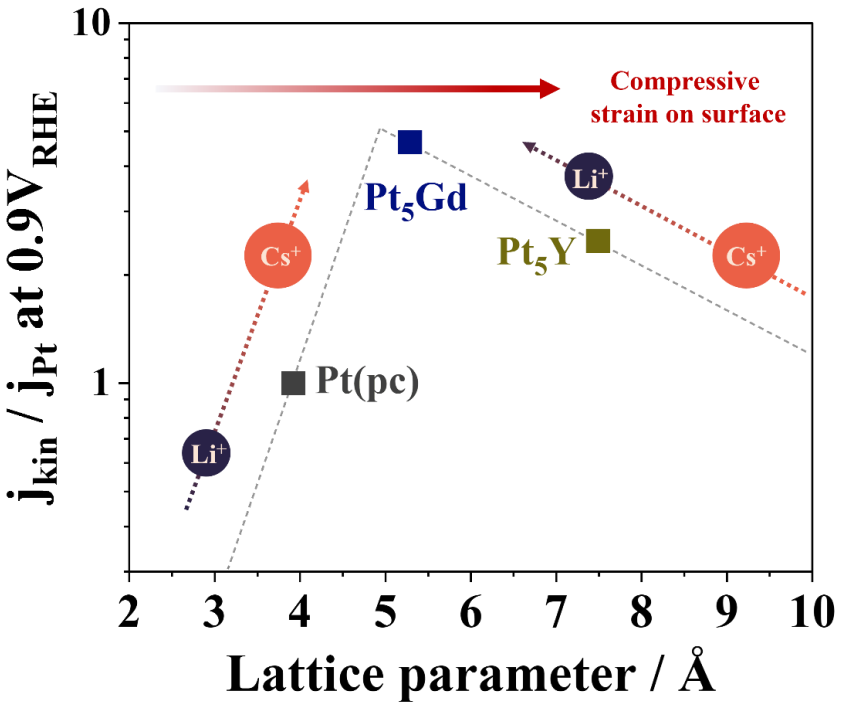

Figure 4.27. The relative ORR activity at 0.9 V vs. RHE as a function of lattice parameter in O_2-saturated 0.1 M $HClO_4$ for Pt_5Gd, Pt_5Y, and Pt(pc) electrodes and the ORR activity-trend recorded in 0.1 M O_2-saturated alkaline solutions with the dotted arrows. The induced compressive strain on the surface increases with a larger lattice parameter a. It is worth mentioning that the dashed lines of the pseudo volcano plot only represent the guides to the eyes, and the lattice parameter a of each electrode referred to the experimental XRD data in **Section 4.1.1**, which is comparable to the literature [68,251,301]. Adapted with permission from reference [294] (own work).

Figure 4.27 briefly summarizes the investigation of the ORR performance in this work with the correlation between the influences of surface strains and alkali cations at the electrode/electrolyte interface. The (pseudo-)volcano plot demonstrates the relative ORR activities at 0.9 V vs. RHE in 0.1 M $HClO_4$ for the Pt(pc), Pt_5Gd, and Pt_5Y electrodes as a function of lattice parameters a, according to the fitting XRD patterns (**Section 4.1.1**). The plot empirically explains that as the lattice parameter a increases, the compressed surface strain increases from Pt to Pt overlayers of bulk alloys. Based on the experimental and computational results, compressive strain and stronger

hydrated alkali cations have opposite impacts on the ORR activity. It is observed that the Pt(pc) has slightly too strong binding energy with the *OH species, and the ORR activity increases as the cation hydration energy decreases by destabilizing the non-covalent interactions in 0.1 M alkaline media. However, in the case of Pt_5Gd and Pt_5Y electrodes, which have larger lattice parameters and weaker bound energies, the ORR activities increase with the presence of higher hydrated alkali cations.

5. Conclusions and Outlook

Improving renewable energy conversion is increasingly important to build the so-called hydrogen economy for sustainable development. Electrocatalysis plays a crucial role in energy devices like electrolyzers and fuel cells. Pt-based catalysts are the state-of-the-art cathode materials commonly used for the HER for water splitting and the ORR in fuel cells. However, due to the slightly stronger binding energies of the reaction intermediates for Pt, the corresponding kinetics do not reach the optimum. The effects of surface structure and electrolyte composition are crucial for rationalizing electrocatalytic performance. To achieve this goal, we investigated the cathodic reactions of HER and ORR by utilizing Pt(pc), Pt_5Gd, and Pt_5Y bulk electrodes in both acidic and alkaline media under controlled hydrodynamic conditions via RDE techniques.

Firstly, the combined study of RDE and EIS provides informative information on interfacial properties during the HER. Fitting the EEC model of EIS spectra comprehensively elucidates the HER mechanisms (i.e., the Volmer-Heyrovsky and Volmer-Tafel mechanisms) in 0.1 M $HClO_4$ and LiOH solutions under different rotation configurations. Overall, due to the faster reaction kinetics in acidic than in alkaline media, the HER polarization curves in acidic media are more mass diffusion limiting than in alkaline media. The HER activity of Pt_5Gd is higher than that of Pt(pc), mainly attributed to the induced compressive strain on the Pt overlayer of the bulk alloy surface after the so-called acid leaching process. Through EIS analysis in an acidic environment, the Volmer-Heyrovsky mechanism is more preferred for Pt_5Gd than for Pt(pc), and the rotation rates do not affect the relative contributions of the two reaction pathways for either electrode. However, the Volmer-Heyrovsky mechanism dominates at lower rotation rates in alkaline media. Besides the charge transfer process, the adsorption and

diffusion properties during the HER are also well elucidated by EIS. For instance, the finite diffusion behavior with RDE adequately fits with the Ws element in the EEC. In addition to the model system of disc electrodes, the more complex system of a nanostructured Pd/C electrocatalyst in acid was also successfully described by the EEC model, with the Volmer-Tafel mechanism dominating under the controlled rotation configurations.

Secondly, the study of the influence of alkali metal cations on ORR activities for Pt(pc), Pt_5Gd, and Pt_5Y electrodes has been demonstrated. Due to compressive strain effects, it has been verified that the ORR kinetic current densities of Pt alloys are several times higher than that of Pt(pc) in 0.1 M $HClO_4$, in the order of Pt_5Gd > Pt_5Y > Pt(pc). In alkaline media, it has been confirmed that the ORR kinetic current density for Pt alloys decreases linearly with decreasing hydration energy of the alkali cation in the order of $Li^+ > Na^+ > K^+ > Rb^+ > Cs^+$. In contrast, the opposite trend is observed for Pt(pc). The reasons have been identified by the non-covalent interactions between reactive intermediates and hydrated alkali cations that affect the ORR kinetics at the electrode/electrolyte interface. For pure Pt, the existence of structure-breaking alkali cations with lower hydration energies, such as Rb^+ and Cs^+, optimizes the originally too-strong binding energies towards ORR; however, on the compressively strained surface, the presence of alkali cations with higher hydration energy, such as Li^+ and Na^+, enhances the ORR performance for the Pt_5Gd and Pt_5Y electrodes. The DFT computational results have further supported the elucidation of the experimental observations of the different ORR trends under the influence of alkali metal cations on Pt surfaces with different strain conditions.

In summary, the electrolyte components and electrode structure profoundly impact electrocatalytic efficiency. This thesis has successfully demonstrated the HER and ORR activities for Pt and Pt alloys in acid and alkaline media. The way of investigating the

HER pathways for well-defined model systems, like disc electrodes, by combining the EIS and RDE techniques can be applied to different electrocatalysts and other essential reaction mechanisms. Studying the impact of alkali metal cations on ORR activities provides a promising way to correlate the nature of alkali cations and the surface strains to reach the optimal binding energy and to rationalize the design of next-generation electrocatalysts for energy-conversion devices in the future.

6. Appendix

6.1. Bode Plots

(A)

(B)

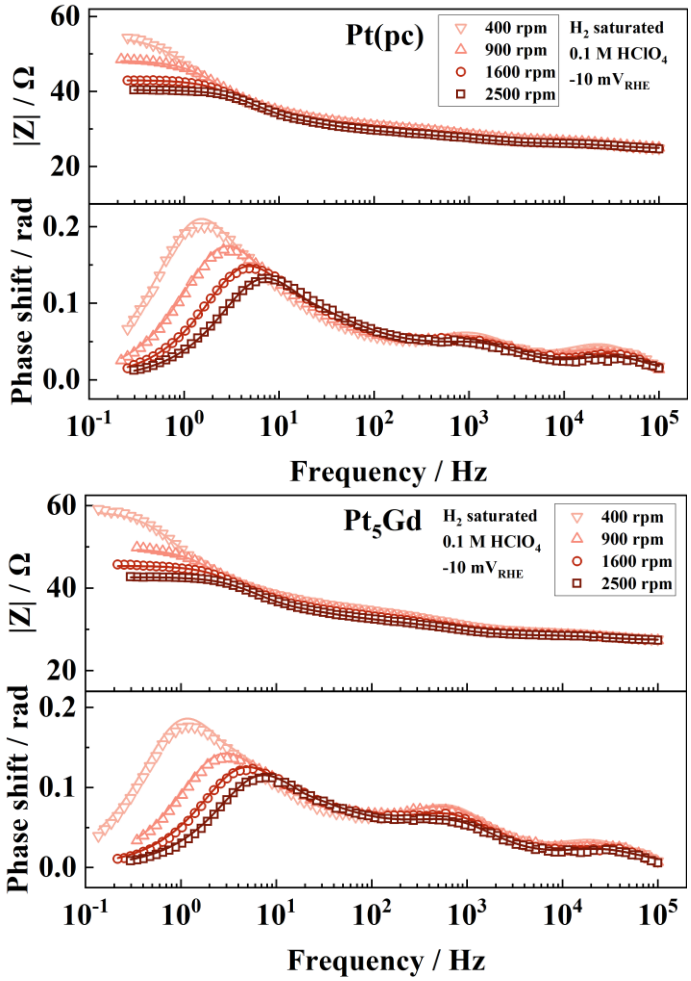

Figure 6.1. EIS data presented in the Bode plots for the (A) Pt(pc) and (B) Pt_5Gd electrodes in H_2-saturated 0.1 M $HClO_4$ at -10 mV vs. RHE at different rotation rates of 400 rpm, 900 rpm, 1600 rpm, and 2500 rpm. The solid lines represent the fitting lines with the EEC model in **Figure 4.5**. Adapted with permission from reference [276].

(A)

(B)

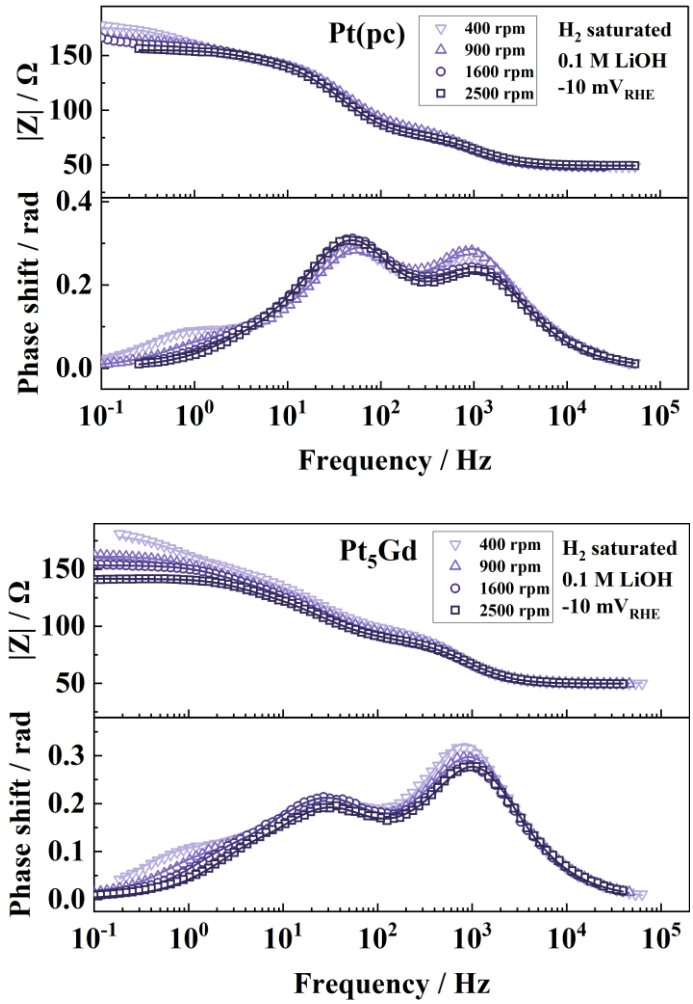

Figure 6.2. EIS data presented in the Bode plots for the (A) Pt(pc) and (B) Pt_5Gd electrodes in H_2-saturated 0.1 M LiOH at -10 mV vs. RHE at different rotation rates of 400 rpm, 900 rpm, 1600 rpm, and 2500 rpm. The solid lines represent the fitting lines with the EEC model in **Figure 4.5**. Adapted with permission from reference [276].

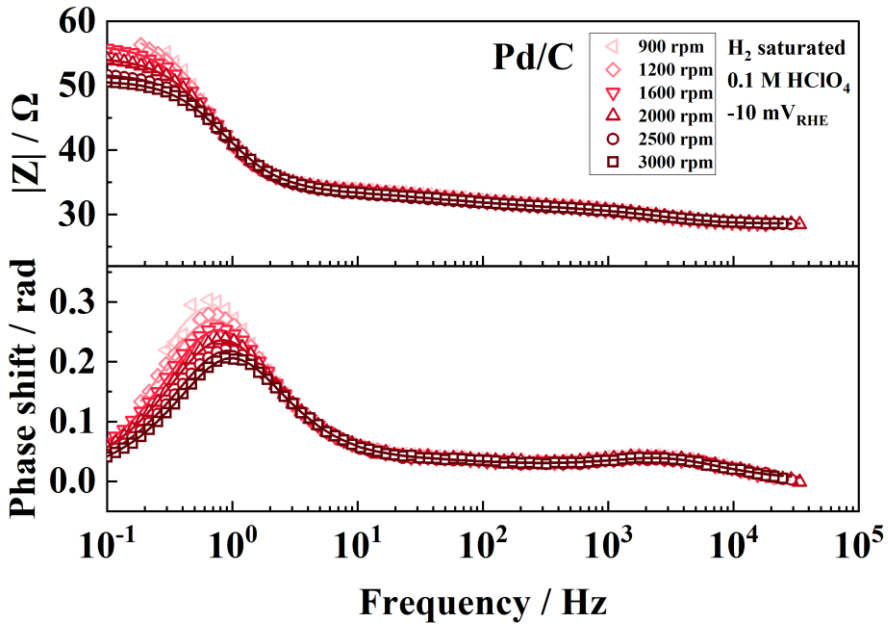

Figure 6.3. EIS data presented in the Bode plots for the nanostructured Pd/C catalyst in H_2-saturated 0.1 M $HClO_4$ at -5 mV vs. RHE at different rotation rates of 900 rpm, 1200 rpm, 1600 rpm, 2000 rpm, 2500 rpm, and 3000 rpm. The solid lines represent the fitting lines with the EEC model in **Figure 4.5**. Adapted with permission from reference [276].

6.2. Computational Details

Table 6.1. The Pt-Pt distance in the slabs relating to the applied strain. The table is reproduced with permission from reference [294].

Strain	-5.00%	-4.00%	-3.00%	-2.00%	0%	2%	4.00%
Pt-Pt distance, Å	2.687	2.715	2.743	2.772	2.828	2.885	2.941

Table 6.2. Calculated adsorption energies and corresponding ORR overpotentials on the pristine Pt(111). The table is reproduced with permission from reference [294].

Strain	**ΔG(OH)-ΔG(OH)Pt@0%**	**ΔGads(O), eV**	**ΔGads(OH), eV**	**ΔGads(OOH), eV**	**ΔG1, eV**	**ΔG2, eV**	**ΔG3, eV**	**ΔG4, eV**	**η, V**
Pristine Pt(111)									
-5%	0.19	3.04	1.54	4.56	-0.36	-1.52	-1.50	-1.54	**0.87**
-4%	0.15	2.98	1.50	4.52	-0.40	-1.54	-1.48	-1.50	**0.83**
-3%	0.11	2.92	1.46	4.47	-0.45	-1.55	-1.46	-1.46	**0.78**
-2%	0.07	2.12	1.42	4.43	-0.49	-2.31	-0.70	-1.42	**0.74**
0%	0.00	2.75	1.35	4.35	-0.57	-1.59	-1.40	-1.35	**0.66**
2%	-0.05	2.65	1.30	4.30	-0.62	-1.65	-1.35	-1.30	**0.61**
4%	-0.13	2.55	1.22	4.21	-0.71	-1.65	-1.33	-1.22	**0.52**

Table 6.3. Calculated adsorption energies and corresponding ORR overpotentials on Pt(111) in the presence of alkali metal cations. The table is reproduced with permission from reference [294].

Strain	**ΔG(OH)-ΔG(OH)Pt@0%**	**ΔGads(O), eV**	**ΔGads(OH), eV**	**ΔGads(OOH), eV**	**ΔG1, eV**	**ΔG2, eV**	**ΔG3, eV**	**ΔG4, eV**	**η, V**
Li^+@Pt(111)									
-5%	0.15	2.18	0.75	3.86	-1.06	-1.68	-1.43	-0.75	**0.48**

-4%	0.12	2.14	0.72	3.83	-1.09	-1.68	-1.42	-0.72	**0.51**
-3%	0.09	2.11	0.69	3.80	-1.12	-1.70	-1.42	-0.69	**0.54**
-2%	0.06	1.67	0.66	3.77	-1.15	-2.10	-1.01	-0.66	**0.57**
0%	0.00	1.99	0.60	3.70	-1.22	-1.71	-1.40	-0.60	**0.63**
2%	-0.05	1.90	0.54	3.65	-1.27	-1.76	-1.35	-0.54	**0.69**
4%	-0.09	1.86	0.51	3.61	-1.31	-1.75	-1.36	-0.51	**0.72**
Na^+@Pt(111)									
-5%	0.19	2.40	0.99	4.04	-0.88	-1.64	-1.42	-0.99	**0.35**
-4%	0.17	2.36	0.96	4.02	-0.90	-1.66	-1.40	-0.96	**0.33**
-3%	0.14	2.32	0.93	3.99	-0.93	-1.66	-1.39	-0.93	**0.30**
-2%	0.09	2.06	0.89	3.94	-0.98	-1.89	-1.17	-0.89	**0.34**
0%	0.00	2.18	0.79	3.86	-1.06	-1.68	-1.38	-0.79	**0.44**
2%	-0.03	2.09	0.77	3.82	-1.10	-1.72	-1.32	-0.77	**0.46**
4%	-0.06	2.07	0.73	3.78	-1.14	-1.70	-1.34	-0.73	**0.50**
K^+@Pt(111)									
-5%	0.16	2.46	1.08	4.10	-0.82	-1.64	-1.38	-1.08	**0.41**
-4%	0.13	2.42	1.05	4.07	-0.85	-1.65	-1.37	-1.05	**0.38**
-3%	0.10	2.38	1.02	4.04	-0.88	-1.66	-1.36	-1.02	**0.35**
-2%	0.07	2.03	0.98	4.01	-0.91	-1.98	-1.04	-0.98	**0.32**
0%	0.00	2.25	0.91	3.93	-0.99	-1.68	-1.34	-0.91	**0.32**
2%	-0.06	2.15	0.86	3.88	-1.04	-1.73	-1.29	-0.86	**0.37**
4%	-0.10	2.10	0.81	3.82	-1.10	-1.71	-1.29	-0.81	**0.42**
Rb^+@Pt(111)									
-5%	0.17	2.48	1.12	4.13	-0.79	-1.65	-1.37	-1.12	**0.44**
-4%	0.13	2.44	1.08	4.10	-0.82	-1.65	-1.36	-1.08	**0.41**
-3%	0.10	2.40	1.05	4.06	-0.86	-1.66	-1.36	-1.05	**0.37**
-2%	0.07	2.36	1.01	4.03	-0.89	-1.67	-1.35	-1.01	**0.34**
0%	0.00	2.28	0.95	3.96	-0.96	-1.68	-1.33	-0.95	**0.28**
2%	-0.06	2.17	0.89	3.90	-1.02	-1.73	-1.28	-0.89	**0.34**
4%	-0.10	2.12	0.85	3.84	-1.08	-1.72	-1.28	-0.85	**0.38**
Cs^+@Pt(111)									
-5%	0.17	2.49	1.15	4.16	-0.76	-1.67	-1.34	-1.15	**0.47**

-4%	0.13	2.45	1.11	4.13	-0.79	-1.68	-1.33	-1.11	**0.44**
-3%	0.10	2.41	1.08	4.10	-0.82	-1.68	-1.34	-1.08	**0.41**
-2%	0.07	2.03	1.05	4.06	-0.86	-2.03	-0.99	-1.05	**0.37**
0%	0.00	2.29	0.98	3.99	-0.93	-1.71	-1.31	-0.98	**0.30**
2%	-0.06	2.18	0.92	3.94	-0.98	-1.75	-1.26	-0.92	**0.31**
4%	-0.10	2.14	0.88	3.88	-1.04	-1.74	-1.26	-0.88	**0.35**

6.3. Abbreviations

AC	alternating current
AR-XPS	angle-resolved X-ray photoelectron spectroscopy
BEVs	battery electric vehicles
C_{dl}	double-layer capacitance
CE	counter electrode
$\overline{CN}$	generalized coordination number
CPE	constant phase element
Cu_{UPD}	copper underpotential deposition
CV	cyclic voltammogram
DFT	density functional theory
ECSA	electrochemical active surface area
EDL	electrical double layer
EEC	electrical equivalent circuit
EIS	electrochemical impedance spectroscopy
FCVs	fuel cell vehicles
GDL	gas diffusion layer
GEIS	galvanostatic electrochemical impedance spectroscopy
HEMFCs	hydroxide exchange membrane fuel cells
HER	hydrogen evolution reaction
HOR	hydrogen oxidation reaction
H_{UPD}	underpotentially deposited hydrogen
IHP	inner Helmholtz plane
ImZ	imaginary part of the impedance

IPCC	Intergovernmental Panel on Climate Change
KK	Kramers-Kronig
MEA	membrane electrode assembly
MMO	mercury-mercuric oxide
MMS	mercury-mercurous sulfate
OER	oxygen evolution reaction
OHP	outer Helmholtz plane
ORR	oxygen reduction reaction
PDF	powder diffraction file
PEIS	potentiostatic electrochemical impedance spectroscopy
PEM	proton-exchange membrane
PEMFC	proton-exchange membrane fuel cell
PHEVs	plug-in hybrid electric vehicles
RDE	rotating disc electrode
RRDE	rotating ring-disc electrode
RE	reference electrode
ReZ	real part of the impedance
RHE	reversible hydrogen electrode
rpm	revolutions per minute
RSF	relative sensitivity factor
SHE	standard hydrogen electrode
UPD	underpotentially deposited
WE	working electrode
XPS	X-ray photoelectron spectroscopy
XRD	X-ray diffraction

6.4. Main Publications

IOP Publishing J. Phys. Energy 5 (2023) 014016 https://doi.org/10.1088/2515-7655/acabe5

Journal of Physics: Energy

PAPER

OPEN ACCESS

RECEIVED
10 September 2022

REVISED
5 December 2022

ACCEPTED FOR PUBLICATION
15 December 2022

PUBLISHED
10 January 2023

Combining impedance and hydrodynamic methods in electrocatalysis. Characterization of Pt(pc), Pt_5Gd, and nanostructured Pd for the hydrogen evolution reaction

Kun-Ting Song[1,3], **Christian M Schott**[1,3], **Peter M Schneider**[1], **Sebastian A Watzele**[1], **Regina M Kluge**[1], **Elena L Gubanova**[1,*] **and Aliaksandr S Bandarenka**[1,2,*]

[1] Department of Physics, Physics of Energy Conversion and Storage, Technical University of Munich, James-Franck-Str. 1, 85748 Garching bei München, Germany
[2] Catalysis Research Center, Technical University of Munich, Ernst-Otto-Fischer-Straße 1, 85748 Garching bei München, Germany
[3] These authors contributed equally to this work.
[*] Authors to whom any correspondence should be addressed.

E-mail: elena.gubanova@tum.de and bandarenka@ph.tum.de

Keywords: hydrogen evolution reaction, impedance spectroscopy, hydrodynamic methods, electrocatalysis, electrochemical interface

Supplementary material for this article is available online

Abstract

Electrochemical hydrodynamic techniques typically involve electrodes that move relative to the solution. Historically, approaches involving rotating disc electrode (RDE) configurations have become very popular, as one can easily control the electroactive species' mass transport in those cases. The combination of cyclic voltammetry and RDE is nowadays one of the standard characterization protocols in electrocatalysis. On the other hand, impedance spectroscopy is one of the most informative electrochemistry techniques, enabling the acquisition of information on the processes taking place simultaneously at the electrode/electrolyte interface. In this work, we investigated the hydrogen evolution reaction (HER) catalyzed by polycrystalline Pt (Pt(pc)) and Pt_5Gd disc electrodes and characterized them using RDE and electrochemical impedance spectroscopy techniques simultaneously. Pt_5Gd shows higher HER activities than Pt in acidic and alkaline media due to strain and ligand effects. The mechanistic study of the reaction showed that the rotation rates in acidic media do not affect the contribution of the Volmer–Heyrovsky and Volmer–Tafel pathways. However, the Volmer–Heyrovsky pathway dominates at lower rotation rates in alkaline media. Besides, the HER in acidic solutions depends more strongly on mass diffusion than in alkaline media. In addition to simple and clearly defined systems, the combined method of both techniques is applicable for systems with greater complexity, such as Pd/C nanostructured catalysts. Applying the above-presented approach, we found that the Volmer–Tafel pathway is the dominating mechanism of the HER for this catalytic system.

1. Introduction

The concept of combining several electrochemical or non-electrochemical techniques in one dedicated experiment is relatively common [1–3]. However, in the case of rotating disc electrode (RDE) measurements, its combination with electrochemical impedance spectroscopy (EIS) needs more exploration (see, e.g. [4–9]) to provide a more informative methodology for electrocatalysis. A specific power of EIS is that it helps to elucidate the mechanism of electrocatalytic reactions and estimate physicochemical parameters related to the interfacial processes taking place simultaneously. EIS has been combined with various techniques under different conditions demonstrating a great increase in the informative power of experiments [10–13]. However, despite the frequent positive synergistic effect while using such different combinations of techniques, their application methodology needs to be sufficiently elaborated. This is especially true in the case of electrocatalysis.

The particular combination of EIS measurements performed under hydrodynamic conditions should be especially beneficial. The RDE configuration is standard in electrocatalysis: it facilitates the control over the

mass transport and helps to benchmark the electrode activity [14–16]. On the other hand, one can envisage that this option will also be helpful in the identification, testing, and verification of the physical impedance models. Therefore, accurate activity information, the reaction mechanism, and physicochemical parameters like the double layer capacitance or the uncompensated resistance should be available in one experiment and valid for the same conditions.

In this work, polycrystalline Pt (Pt(pc)), as a reliable and well-studied system in electrocatalysis (see, e.g. [17–20]), is used to establish the methodology for the combination of hydrodynamic RDE techniques and EIS measurements. The hydrogen evolution reaction (HER) was investigated due to its importance and key role in a sustainable energy transition [21]. While RDE measurements typically deliver only a change in current densities, i.e. activities, upon changing hydrodynamic conditions, such as rotation speeds, they lack further information about the reaction mechanisms. However, additional EIS measurements at different rotation speeds can give further insights into the change of parameters, such as charge transfer resistance or Warburg diffusion behavior for the RDE setup, which help to elucidate the different reaction mechanisms of the HER in acidic and alkaline media. Furthermore, Pt_5Gd, as a novel electrocatalyst material with high activity toward the oxygen reduction reaction (ORR), was chosen to test the methodology developed above and identify the connection between induced ligand and strain effects and increased electrocatalytic activity toward the HER in acidic and alkaline media compared to pure Pt (see, e.g. [22–26]). Finally, we used Pd nanoparticles supported on high surface area carbon (Pd/C) as a promising hydrogen evolution electrocatalyst to demonstrate the informative power of the EIS-RDE approach for a more complex system [27, 28]. To harvest results with profound physical meaning, a suitable equivalent electric circuit (EEC) model for the EIS data is used in this work [19]. Subsequently, the EIS parameters were elucidated and verified in the RDE configuration on Pt(pc), Pt_5Gd, and Pd/C. As a result, the EIS-RDE approach can address the role of the Volmer–Heyrovsky and Volmer–Tafel pathways in these different systems, motivating the combined study as a new and valid approach for the complete characterization of electrocatalyst materials.

2. Experimental

Pt(pc) and Pt_5Gd disc electrodes (MaTeck, Germany) with a 5 mm diameter were applied as working electrodes (WEs). For the production of the Pd/C nanostructured catalyst, a surfactant-free top-down approach was used [29–32]. The Pd nanoparticle formation mechanism relies on the electrochemical erosion of bulk Pd wires ($\varnothing = 0.25$ mm, 99.95%, MaTecK, Germany), which were immersed in a 1 M $NaNO_3$ (ACS, ISO, Reag, Ph Eur, Merck, Germany) synthesis electrolyte containing a H_2O_2 (30% H_2O_2, p.a., ISO, Carl Roth, Germany) pretreated Vulcan® XC72R carbon support (Cabot, USA). For their electrochemical characterization, a catalyst ink consisting of 10 mg synthesized Pd/C powder, 3600 μl ultrapure water (18.2 MΩcm, Merck Millipore, USA), 1446 μl isopropanol (puriss. p.a., ACS reagent, $\geqslant$ 99.8%, Sigma Aldrich, USA), and 30 μl Nafion® dispersion (5 wt% in lower aliphatic alcohols and water, Sigma Aldrich, USA) was prepared. To ensure homogeneity, the ink was ultrasonicated for 10 min, and subsequently, drop-casted on a glassy carbon disc electrode ($\varnothing = 5$ mm). Similar to standard protocols, 10 μl ink coatings served as a WE for RDE measurements. In order to record reasonable EIS spectra, the ink amounts for the coating were decreased to 5 μl to suppress the noise arising from hydrogen evolution.

For the electrochemical measurements, a three-electrode set-up was used with a mercury − mercurous sulfate electrode (MMS) (SI Analytics, Germany) as the reference electrode (RE) and a platinum wire (99.9% purity, MaTecK, Germany) as the counter electrode. EIS and RDE techniques were performed using a VSP-300 potentiostat (Bio-Logic, France). Since the EIS measurements were performed at high frequencies, measurement artifacts caused by the impedance of the RE were suppressed by a shunt capacitor placed between the RE and a Pt wire, which was immersed into the electrolyte close to the Luggin capillary [27, 33]. This is also how to make the iR compensation for the HER/HOR polarization curves. Prior to the measurements, the cells and all glassware were cleaned with a 3:1 mixture of H_2SO_4 (96% H_2SO_4, p.a., ISO, Carl Roth, Germany) and H_2O_2, and then rinsed several times alternately with ultrapure water.

As the acidic and alkaline electrolytes, perchloric acid (70% $HClO_4$, extra pure, Acros, Germany) and lithium hydroxide (LiOH, anhydrous, 99.995% (metals basis), Sigma-Aldrich, USA) solutions, respectively, were chosen and diluted to 0.1 M concentration with ultrapure water. The alkaline medium was chosen as 0.1 M LiOH due to the better HER stability and activity values compared to other alkaline solutions reported previously [20, 34].

For the electrochemical measurements on the Pt(pc) and Pt_5Gd disc electrodes, the acidic or alkaline solution was first purged with H_2 (5.0, Westfalen, Germany) for 30 min. Subsequently, cyclic voltammograms (CVs) were recorded within a potential range of about −0.13 V to 0.32 V and −0.05 V to 0.39 V vs reversible hydrogen electrode (RHE) for acidic and alkaline electrolyte solutions, respectively, at a scan rate of 10 mV s^{-1} until reaching steady current densities. This step also ensured the calibration versus

the RHE [35] avoiding the potential shift in the Nernst equation due to a liquid junction potential between the inner electrolyte of the MMS electrode and the operating electrolyte [36]. The measurements of the Pd/C catalyst were only performed in 0.1 M $HClO_4$. To activate the Pd/C catalyst, CVs at a scan rate of 50 mV s^{-1} were performed in an Ar-saturated environment (5.0, Westfalen, Germany) in the potential range of 0.06 to 1.2 V vs RHE, until establishing a relatively stable state. Similar to the Pt-based disc electrodes, the electrolyte was purged with H_2 for 30 min, and HER/ hydrogen oxidation reaction (HOR) polarization curves were subsequently recorded in a potential range from −0.13 to 0.82 V at 1600 rpm. All potentials in this work are referenced to the RHE scale. The measured current densities are normalized to the geometrical surface area of the disc electrodes (0.196 cm^2).

In the case of the Pd/C catalyst, posterior evaluations of the iR-corrected HER/HOR polarization curves at −5 mV vs RHE determines the mass and specific activity. The former depends on the mass loading, the latter on the electrochemically active surface area (ECSA) of the Pd/C catalyst. Due to the carbon-based support material, thermogravimetric analysis quantifies the Pd/C mass loading reliably using a Mettler Toledo instrument. Consequently, the relative Pd loading to total mass of the catalyst corresponds to ∼17 wt%.

Arguably one of the essential components for the characterization of nanostructured catalysts corresponds to the specific surface area (SSA). For its estimation, the ECSA needs to be detected and normalized to the Pd mass, which can be calculated considering the Pd/C mass loading. Next to the hydrogen underpotential deposition (H_{upd}) technique, CO stripping belongs to the most well-known techniques for ECSA determination [16, 37]. The first technique introduces a non-neglectable error in the ECSA for Pd-based systems, presumably owing to hydride formation. With these considerations in mind, CO stripping was used in the following work by assuming entire adsorbed CO monolayers on the Pd nanoparticles and a CO oxidation charge per unit area of 420 $\mu C\ cm^{-2}$. For the experiment, the 0.1 M $HClO_4$ electrolyte was initially purged with CO (1000 ppm CO in Ar, 4.7/5.0, Westfalen, Germany) for 15 min. Subsequent polarization of the WE at 0.1 V vs RHE for 50 min under persistent rotation of 400 rpm ensures that an entire monolayer of adsorbed CO forms on the catalytic surface. Then, the electrolyte is purged with Ar for 15 min, and afterward, two CV cycles are executed with a scan rate of 10 mV s^{-1} within the potential range of 0.06 to 1.2 V vs RHE.

It should be noticed that the HER activity in alkaline media was not stable and decreased gradually, which is already a known phenomenon in the literature [38]. Therefore, the disc electrodes were electrochemically cleaned and activated before each EIS measurement was performed. The EIS measurements were performed within the AC-probing frequency range from 100 kHz to 0.1 Hz at different rotation rates. For Pt(pc) and Pt_5Gd, −10 mV vs RHE potential was applied during the EIS measurements with a 10 mV perturbation amplitude. For the nanostructured Pd/C catalyst, a lower potential of −5 mV vs RHE was selected to avoid excessive H_2 formation on the electrode surface. The impedance data were analyzed via the EIS Spectrum Analyzer 1.3 software [39, 40] and checked by Kramers–Kronig Relations.

For material characterization, scanning electron microscopy (SEM) techniques visualized the structure of the elucidated Pd/C catalyst with nanometric resolution. The used ZEISS Gemini Nvision 40 accelerates electrons with a 5 kV voltage for the performed measurements. For a deeper fundamental understanding of the nanostructured system, x-ray diffraction (XRD) elucidates crystallographic and structural properties. The diffractometer of the used Rigaku MiniFlex 600-C produces monochromatic x-ray beams with a Cu-Kα source and a Ni-based filter. The angle of 2Θ in the diffraction patterns changed with 5° min^{-1} step velocity in the range from 5° to 90°. Subsequently, the Scherrer equation can be used to estimate the average crystallite sizes of the Pd/C nanoparticles [41]. In the case of Pt(pc) and Pt_5Gd, the XRD patterns were measured by X'Pert Pro PANanalytical instrument with Cu-Kα source and a Ni-based filter. The scanning 2Θ angle varied from 5° to 90° with ∼4 and ∼0.78° min^{-1} step velocity for Pt(pc) and Pt_5Gd, respectively.

3. Results and discussion

Before electrochemical measurements, the polycrystalline structure of the Pt(pc) and Pt_5Gd disc electrodes in figure S1 are shown by XRD measurements. In order to fully characterize the HER on the chosen model systems, Pt(pc), Pt_5Gd, and Pd/C, we combine the classical methodology of RDE with EIS. The RDE experiment determines the HER activity and controls the mass diffusion in a standardized way. The EIS method quantitatively provides the relevant physicochemical parameters to describe the electrochemical interface and to distinguish the relevant reaction pathways. As an overview, the overall and elementary pathways of the HER in acidic and alkaline media are illustrated in table 1. In acidic media, the hydrogen ions (H^+) are adsorbed at the electrode surface (H_{ads}) and produce H_2 in the overall reaction; however, in alkaline media, water molecules are reduced and form H_2 and hydroxides (OH^-). The elemental reaction processes of the HER mechanisms can be separated into the Volmer−Heyrovsky and the Volmer−Tafel

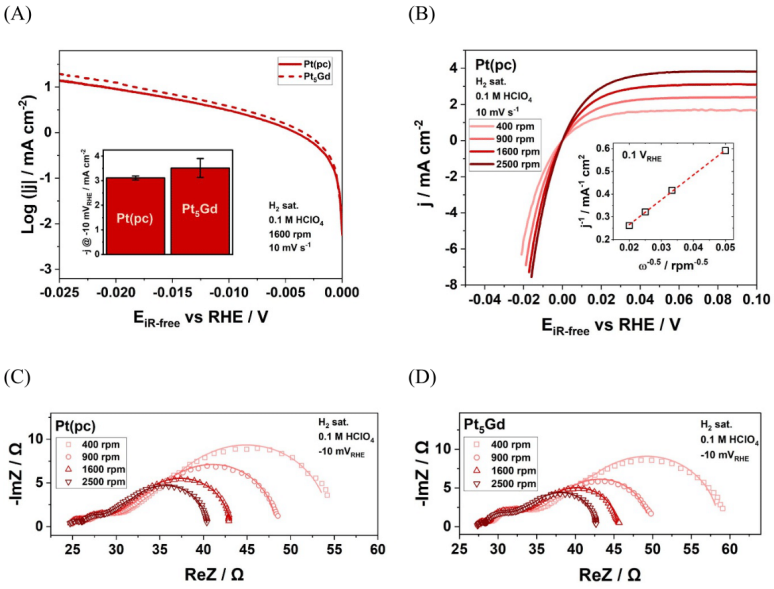

Figure 2. In acidic media, (A) Tafel plots for the HER on the Pt(pc) and Pt_5Gd electrodes at 1600 rpm with the inserted bar chart of the current densities at −10 mV vs RHE. (B) iR-corrected HER/HOR polarization curves (anodic scan) at different rotation speeds of Pt(pc) electrode with a scan rate of 10 mV s^{-1}. The inset shows the Koutecky–Levich plot at 0.1 V vs RHE. (C) and (D) EIS data presented in the Nyquist plots of Pt(pc) and Pt_5Gd electrodes, respectively, at different rotation rates at −10 mV vs RHE. The solid lines in (C) and (D) illustrate the fitting to the EEC model given in figure 1. The data was recorded in H_2-saturated 0.1 M $HClO_4$ at the selected rotation rates of 400, 900, 1600, and 2500 rpm.

Further, the relative contributions of the Volmer–Heyrovsky and the Volmer–Tafel pathways on the Pt(pc) and Pt_5Gd electrodes in 0.1 M $HClO_4$, $R_{ct,1}$ and $R_{ct,2}$ are shown as a function of the square root of the rotation rate in figures 3(A) and (B), respectively. For the Pt(pc) electrode, $R_{ct,1}$ and $R_{ct,2}$ slightly decrease with increasing rotation rate, as displayed in figure 3(A). Correspondingly, the charge transfer reaction on the Pt_5Gd electrode indicates a similar trend as for the Pt(pc) electrode with the change in the rotation rate, as shown in figure 3(B). Compared to the Pt(pc) electrode, $R_{ct,2}$ is considerably higher than $R_{ct,1}$ at different rotation rates on the Pt_5Gd electrode, indicating that the Volmer–Heyrovsky pathway is the preferred mechanism. The increase of the charge transfer resistance can be associated with a change in the concentration of the redox species at the electrode surface due to rotation rate variations and a time shift [47] in the EIS measurements.

Moreover, figures 3(C) and (D) show the Ws_c, which corresponds to the controlled finite length diffusion with transmissive boundary by the RDE setup versus the inverse of the square root of the rotation rate. In the case of Pt(pc), Ws_c linearly decreases with increasing rotation rate, while the Warburg coefficient (Ws_r) increases, as shown in figures 3(C) and S3, respectively. Similar results were obtained for the Pt_5Gd electrode, as presented in figures 3(D) and S4. Therefore, the observations indicate that Ws_c is inversely proportional to the square root of the rotation rate. The thickness of the diffusion layer depends on the rotation rate and can be quantitatively calculated. Other essential parameters obtained by the fit of the EIS data, shown in the EEC, as a function of the square root of the rotation rate on Pt(pc) and Pt_5Gd electrodes in 0.1 M $HClO_4$ are shown in figures S3 and S4, respectively.

In the second step, the same set of experiments was conducted in the alkaline media for comparison and to underline the analytical strength of the approach. Here, the activities of the Pt(pc) and Pt_5Gd electrodes toward the HER at −10 mV vs RHE at 1600 rpm are approximately six times smaller in 0.1 M LiOH than in 0.1 M $HClO_4$, as shown in figures 2(A) and 4(A), respectively. The activity of Pt_5Gd is slightly higher than that of Pt(pc) in alkaline media, which could again be ascribed to the ligand and strain effects of the alloy. The polarization curves of the HER/HOR with different rotation rates on Pt(pc) in H_2-saturated 0.1 M LiOH

Table 1. Overall and elementary steps of the HER in acidic and alkaline media [44].

	Acidic media	Alkaline media
Overall reaction	$2H^{+}_{(aq)} + 2e^{-} \rightarrow H_{2(g)}$	$2H_2O_{(l)} + 2e^{-} \rightarrow H_{2(g)} + 2OH^{-}_{(aq)}$
Volmer step	$H^{+} + e^{-} \rightarrow H_{ads}$	$H_2O + e^{-} \rightarrow H_{ads} + OH^{-}$
Heyrovsky step	$H_{ads} + H^{+} + e^{-} \rightarrow H_2$	$H_2O + H_{ads} + e^{-} \rightarrow H_2 + OH^{-}$
Tafel step	$2H_{ads} \rightarrow H_2$	$2H_{ads} \rightarrow H_2$

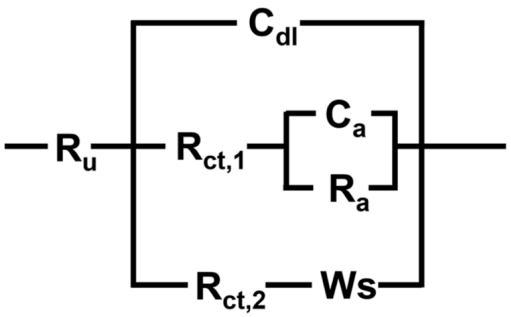

Figure 1. The EEC model used in this work to fit the EIS data of the hydrogen reactions in 0.1 M $HClO_4$ and 0.1 M LiOH solutions.

pathway. In a previous study on a Pt(pc) microelectrode [19], an EEC model was developed to evaluate the impedance data corresponding to the hydrogen reactions and to extract the involved physicochemical properties. As shown in figure 1, the EEC model includes the uncompensated resistance (R_u), which accounts for the resistance of the electrolyte and electronic resistances. In series to the uncompensated resistance, there is a parallel connection of the double layer capacitance (C_{dl}), the Volmer–Heyrovsky, and Volmer–Tafel pathways. The non-Faradaic branch corresponds to the electrochemical double layer. The Volmer–Heyrovsky pathway comprises a charge transfer resistance ($R_{ct,1}$), an adsorption capacitance (C_a), and an adsorption resistance (R_a). The Volmer–Tafel pathway is described by a charge transfer resistance ($R_{ct,2}$) and a Warburg short element (Ws) due to the finite length transmissive diffusion with the RDE setup. Ws consists of two parameters, namely the Warburg coefficient Ws_r and the time constant parameter Ws_c, which is related to the Nernst diffusion layer thickness [42, 43]. Further information is provided in the SI.

The Pt(pc) and Pt_5Gd systems are probed and compared in the acidic media. Initially, RDE experiments are applied to classically measure the HER activity at 1600 rpm in H_2-saturated 0.1 M $HClO_4$ with a scan rate of 10 mV s^{-1}. As shown in figure 2(A), the HER activity of Pt_5Gd is higher than for Pt(pc). This can be associated with the ligand and strain effects on the Pt_5Gd surface, weakening the binding energy of the reaction intermediates to reach optimal binding conditions. The promising activity improvement on the Pt-based alloys can also be observed for the ORR activities in acidic media [23, 24, 45].

Additionally, the polarization curves of the HER/HOR at different rotation rates on the Pt(pc) electrode in 0.1 M $HClO_4$ are shown in figure 2(B). The HOR limiting current density increases with increasing rotation rates from 400 to 2500 rpm, which agrees with the linear behavior of the Koutecky–Levich equation at 0.1 V vs RHE, as shown in the inset of figure 2(B), mainly because of the limited mass transport. Similarly, the measured current densities of the HER show the same trend as the HOR current densities. This indicates that the HER current density is associated with the charge transfer reactions and limiting diffusion [46], which will be further investigated in the EIS data discussion. A comparable trend was obtained for the Pt_5Gd electrode and is given in figure S2. In addition, EIS spectra were measured at different rotation rates at −10 mV vs RHE on the Pt(pc) and Pt_5Gd electrodes to quantitatively analyze the relationship between the rotation rate and the HER performance. The results are displayed in figures 2(C) and (D), along with the fits according to the EEC in figure 1. At different rotation speeds, the slight deviations of the arcs in the high-frequency regime can be associated with the changes in charge transfer reactions. More importantly, the profound differences in the low-frequency region correspond primarily to the change in mass diffusion. The Bode plots provide additional information on the phase shift and the total impedance as a function of frequency in figure S11.

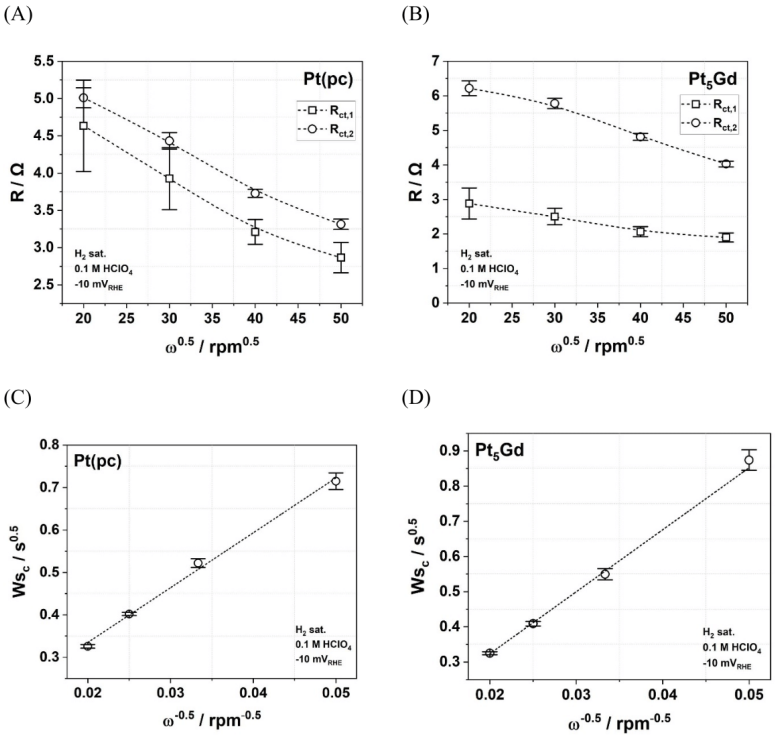

Figure 3. In acidic media, $R_{ct,1}$ and $R_{ct,2}$ as a function of the square root of the rotation rate on (A) Pt(pc) and (B) Pt_5Gd electrodes. W_{S_C} as a function of the inverse of the square root of the rotation rate on (C) Pt(pc) and (D) Pt_5Gd electrodes. The dotted lines in (A) and (B) are a guide to the eye and the lines in (C) and (D) are a linear fit of the data.

at a scan rate of 10 mV s^{-1} are given in figure 4(B). The HOR current densities are rising with increasing rotation rate, which follows the Koutecky–Levich equation with a linear relationship at 0.3 V vs RHE, as shown in the inset of figure 4(B). However, the current densities toward the HER increase slightly with higher rotation rates in alkaline media compared to the more pronounced increase in acidic media in figure 2(B). This indicates that the HER in alkaline media is rather limited by kinetics than diffusion compared to the mainly limiting diffusion in acidic media [46]. The polarization curves of HER/HOR with different rotation rates on Pt_5Gd in 0.1 M LiOH are shown in figure S2, illustrating a similar behavior as for Pt(pc) in figure 4(B). The detailed interpretation of the HER current densities influenced by different rotation rates can be given with the help of the impedance data shown in figures 4(C) and (D) for Pt(pc) and Pt_5Gd electrodes, respectively. The EIS spectra presented in the Nyquist plots decrease slightly with the increase of the rotation rate for Pt(pc) and Pt_5Gd electrodes, at −10 mV vs RHE in H_2-saturated 0.1 M LiOH compared to the dramatic change of the EIS data in acidic media shown in figures 2(C) and (D). While the Nyquist plots consist of two small semicircles at high frequencies and one larger arc at low frequencies in acidic media, as shown in figures 2(C) and (D), the Nyquist plots in figures 4(C) and (D) in alkaline media illustrate different shapes. The EIS toward HER in alkaline media includes two larger arcs within the high-frequency region and one small arc within the lower-frequency region. The Bode plots in figure S11 display further details of the influence of rotational rate on the phase shift and total impedance within different frequencies.

In the following, the fit parameters obtained from the EIS spectra for the Pt(pc) and Pt_5Gd electrodes in the alkaline media are discussed and interpreted. In figure 5(A), the values of $R_{ct,1}$ and $R_{ct,2}$ on Pt(pc) in alkaline media are more pronounced than those in acidic media, which are shown in figure 3(A). This

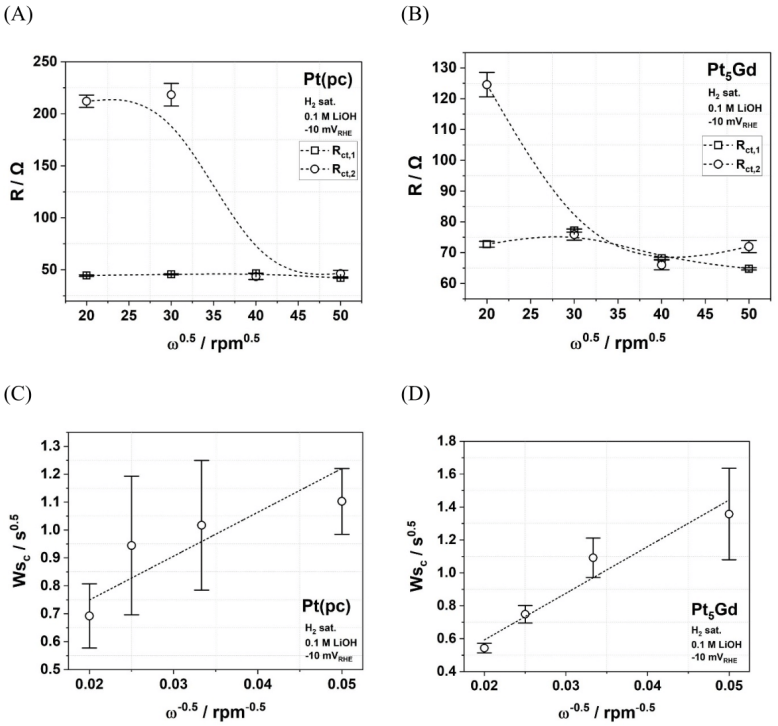

Figure 5. In alkaline media, $R_{ct,1}$ and $R_{ct,2}$ as a function of the square root of rotation rate on (A) Pt(pc) and (B) Pt_5Gd electrodes. Ws_c as a function of the inverse of the square root of the rotation rate on (C) Pt(pc) and (D) Pt_5Gd electrodes. The dotted lines in (A) and (B) and the dotted straight lines in (C) and (D) present guidelines and linear fits, respectively.

provide a general characterization of the synthesized nanoparticles. The XRD measurement is displayed in figure S8 and its subsequent analysis reveals an average Pd crystallite size of (6.6 ± 2.3) nm. Additionally, the SEM image of the Pd/C catalyst shows homogeneously distributed Pd nanoparticles on the carbon-based support. The small nanoparticle size and their proper distribution results in a large SSA of (67.3 ± 0.2) m^2 g^{-1}.

With this characteristic knowledge of the Pd/C catalyst, the mass and specific HER activity can be investigated via RDE techniques. Figure S9 illustrates the HER/HOR polarization curve at 1600 rpm in 0.1 M $HClO_4$. Evaluating the activity at −5 mV vs RHE determines the geometric, mass, and specific activity of (1.23 ± 0.37) mA $cm_{geo}{}^{-2}$, (71.4 ± 21.5) mA mg^{-1} and (0.11 ± 0.03) mA $cm_{ECSA}{}^{-2}$, respectively. Furthermore, the following EIS analysis provides insights into the dominating hydrogen reaction mechanism. As known from the literature [48], stability problems related to agglomeration and dissolution of the nanoparticles arise for the Pd/C system under cycling voltammetry operations in 0.1 M $HClO_4$. In order to guarantee an active state and relatively stable structural conditions of the Pd/C catalyst prior to the RE calibration and EIS measurements, 68 cycles in the aforementioned potential area were performed, as shown in figure S9. Figure 6(A) displays the EIS spectra as Nyquist plots for the Pd/C catalyst with different rotation rates. In the high-frequency regime, minor deviations occur, which can be attributed to a small change in the charge transfer resistance of the Volmer–Heyrovsky and Volmer–Tafel steps. Accordingly, $R_{ct,1}$ and $R_{ct,2}$ vary only slightly with different rotation rates, as shown in figure 6(B). The explanation for the change is similar to the disc electrodes in acidic media, as mentioned above. Since $R_{ct,2}$ is considerably smaller than $R_{ct,1}$ for all selected rotation rates, the Volmer–Tafel pathway is the dominating mechanism in hydrogen reactions for the Pd/C catalyst. In contrast, in the low-frequency range of the impedance spectra,

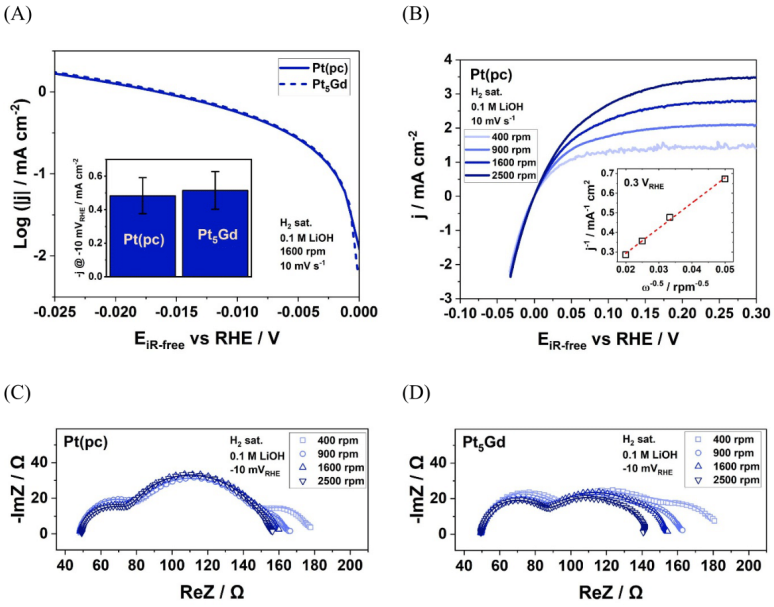

Figure 4. In alkaline media, (A) Tafel plots for the HER on Pt(pc) and Pt_5Gd electrodes at 1600 rpm. The inserted bar chart shows the current densities at −10 mV vs RHE. (B) iR-corrected HER/HOR polarization curves (anodic scan) at different rotation speeds of the Pt(pc) electrode at a scan rate of 10 mV s^{-1}. The inset presents the Koutecky–Levich plot at 0.3 V vs RHE. (C) and (D) EIS data presented in the Nyquist plots of the Pt(pc) and Pt_5Gd electrodes, respectively, at different rotation rates at −10 mV vs RHE. The solid lines in (C) and (D) fit the EEC model in figure 1. The data was collected in H_2-saturated 0.1 M LiOH at the selected rotation rates of 400, 900, 1600, and 2500 rpm.

explains the slower HER kinetics on Pt(pc) in 0.1 M LiOH compared to those in 0.1 M $HClO_4$ under the same experimental conditions. Furthermore, $R_{ct,1}$ and $R_{ct,2}$ show similar values at higher rotation rates. At lower rotation rates, $R_{ct,2}$ increases dramatically, while $R_{ct,1}$ remains constant, as illustrated in figure 5(A). This implies that the contribution of the Volmer–Tafel and Volmer–Heyrovsky pathways are comparable at higher rotation speeds, but at lower rotation speeds, the Volmer–Heyrovsky pathway dominates in alkaline media. A similar trend is shown in figure 5(B) for the Pt_5Gd electrode in 0.1 M LiOH. In addition, Ws_c decreases while Ws_r increases with increasing rotation rates for Pt(pc), as shown in figures 5(C) and S5, respectively. The trend of the finite length transmissive diffusion with the RDE setup in alkaline media is comparable to that in acidic media; however, in alkaline media, the values of Ws_c are about two times larger, and the values of Ws_r are more than ten times larger than in acidic media, as shown in figures 3(C) and S3, respectively. The difference in the mass transport between the acidic and alkaline solutions can be explained due to the dissimilar reactants toward HER shown in table 1. The behavior of mass diffusion on Pt_5Gd follows a similar trend as for Pt(pc) in 0.1 M LiOH, as presented in figures 5(D) and S6. The additional critical parameters in the EEC as a function of the square root of the rotation rate for Pt(pc) and Pt_5Gd electrodes in 0.1 M LiOH are given in figures S5 and S6, respectively. To further investigate the dominating reaction pathway toward HER in acidic and alkaline media, the ratio of $R_{ct,1}/R_{ct,2}$ is calculated for different rotation speeds, as shown in figure S7, respectively. The relative contributions of the Volmer–Heyrovsky and Volmer–Tafel pathways toward the overall HER in acidic media remain comparably stable at different rotation rates. The Volmer–Heyrovsky mechanism is more preferred for Pt_5Gd than for Pt(pc), according to the results. On the other hand, both reaction pathways contributed more or less equally at higher rotation rates, while the Volmer–Heyrovsky mechanism dominates only at lower rotation rates for both Pt(pc) and Pt_5Gd electrodes in alkaline media.

The combination of EIS and RDE is applicable not only for model systems like Pt(pc) and Pt_5Gd disc electrodes but also for more complex nanostructured catalysts. In the case of the ∼17 wt% Pd/C catalyst, we

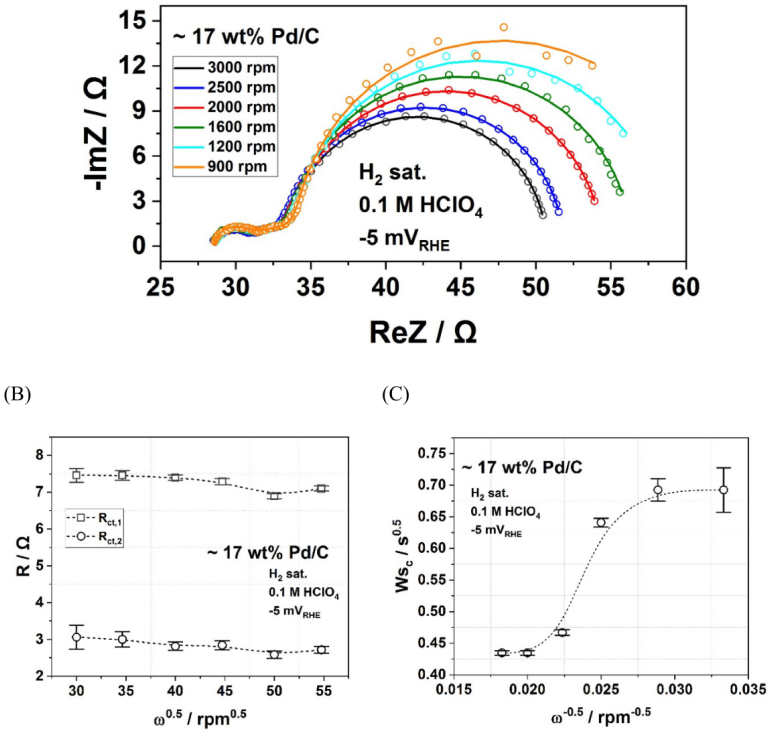

Figure 6. (A) Impedance data presented in the Nyquist plots of nanostructured Pd/C catalyst, at −5 mV vs RHE. The solid lines demonstrate the fitting to the EEC model. The data was collected in H_2-saturated 0.1 M $HClO_4$ at the selected rotation rates of 900, 1200, 1600, 2000, 2500, and 3000 rpm. (B) $R_{ct,1}$ and $R_{ct,2}$ as a function of the square root of the rotation rate of the Pd/C catalyst. (C) Ws_c as a function of the inverse of the square root of the rotation rate of Pd/C. The dotted lines in (B) and (C) illustrate the guides to the eye.

significant differences occur due to the change in diffusion via different rotation rates. This is illustrated by the change in Ws_c, as shown in figure 6(C). The Bode plots present further information in figure S11. As elucidated earlier in the discussion for the disc electrodes, an inversely linear dependency with the square root of the rotation rate is expected (see figures 3(C) and 5(C) for Pt(pc) and 3(D) and 5(D) for Pt_5Gd). For the Pd/C catalyst, this linear trend is not observed. One possible explanation can be the complex structure of the nanostructured catalyst leading to different diffusion properties compared to disc electrodes. In addition, figure S10 provides further essential parameters in the EEC as a function of the square root of the rotation rate for the Pd/C catalyst in 0.1 M $HClO_4$.

4. Summary and conclusions

In this work, the EIS combined with the hydrodynamic RDE technique provides an essential approach to investigating the different reaction mechanisms of hydrogen evolution in acidic and alkaline media under reaction conditions. The power of the strategy is demonstrated for Pt(pc) and Pt_5Gd model systems. In general, Pt_5Gd shows higher HER activities than Pt(pc), which could be ascribed to strain and ligand effects in both media. For both Pt(pc) and Pt_5Gd electrodes, the activity increases with an increasing rotation speed of the electrodes. The EIS data recorded in 0.1 M $HClO_4$ varies stronger with the rotation rate than in 0.1 M LiOH. These findings indicate that the HER in acidic media depends more strongly on mass diffusion than

in alkaline media. From a physical model of the EIS data, we can conclude that the reaction ratio of Volmer–Heyrovsky and Volmer–Tafel mechanisms are independent of the rotation rate in acidic media. However, the Volmer–Heyrovsky pathway becomes the dominating mechanism at lower rotation rates in alkaline media. The finite diffusion in the electrolytes is properly demonstrated by the Warburg short element with the RDE setup. In addition to the well-defined model systems of the disc electrodes, the more complex system of nanostructured Pd catalyst is investigated for hydrogen reactions, revealing the Volmer–Tafel pathway as the dominating mechanism. The combined study of impedance and RDE measurements provides a powerful tool for further investigations of electrolyte effects and other critical reactions for electrocatalysis in the future.

Data availability statement

The data that support the findings of this study are available upon reasonable request from the authors.

Acknowledgments

This Project has received funding from the European Union's Horizon 2020 research and innovation program under Grant Agreement HERMES No. 952184. Funding from the German Research Foundation (DFG) under Germany's excellence strategy—EXC 2089/1–390776260, Germany's excellence cluster 'e-conversion', under DFG Project Nos. BA 5795/6-1, and TUM IGSSE, Project 11.01 is gratefully acknowledged. The authors would like to thank Batyr Garlyyev for his assistance with the performed SEM experiments.

ORCID iD

Aliaksandr S Bandarenka https://orcid.org/0000-0002-5970-4315

References

[1] Andersen S Z *et al* 2019 *Nature* **570** 504
[2] Berkes B B, Jozwiuk A, Vracar M, Sommer H, Brezesinski T and Janek J 2015 *Anal. Chem.* **87** 5878
[3] Berkes B B, Maljusch A, Schuhmann W and Bondarenko A S 2011 *J. Phys. Chem.* C **115** 9122–30
[4] Barber J, Morin S and Conway B E 1998 *J. Electroanal. Chem.* **446** 125
[5] Pfeifer R, Martinhon P T, Sousa C, Moreira J C, Nascimento M A C, Barek J and Vyskočil V 2019 *J. Electroanal. Chem.* **838** 129
[6] Thomberg T, Nerut J, Lust K, Jäger R and Lust E 2008 *Electrochim. Acta* **53** 3337
[7] Láng G G, Sas N S, Ujvári M and Horányi G 2008 *Electrochim. Acta* **53** 7436
[8] Park S Y, Lee J W, Jang S H, Kim L H, Choi D K and Joe Y I 1999 *J. Power Sources* **83** 217
[9] Fushimi K, Neelakantan L, Eggeler G and Hassel A W 2018 *Phys. Status Solidi* a **215** 1800011
[10] Lasia A 2018 *Impedance Spectroscopy Applied to the Study of Electrocatalytic Processes* (Amsterdam: Elsevier) (https://doi.org/10.1016/B978-0-12-409547-2.13361-X)
[11] Bandarenka A S 2013 *Analyst* **138** 5540
[12] Haimerl F, Sabawa J P, Dao T A and Bandarenka A S 2022 *ChemElectroChem* **9** e202200069
[13] Bandarenka A S, Eckhard K, Maljusch A and Schuhmann W 2013 *Anal. Chem.* **85** 2443
[14] Kocha S S, Shinozaki K, Zack J W, Myers D J, Kariuki N N, Nowicki T, Stamenkovic V, Kang Y, Li D and Papageorgopoulos D 2017 *Electrocatalysis* **8** 366
[15] Shinozaki K, Zack J W, Pylypenko S, Richards R M, Pivovar B S and Kocha S S 2015 *Int. J. Hydrog. Energy* **40** 16820
[16] Wei C, Rao R R, Peng J, Huang B, Stephens I E L, Risch M, Xu Z J and Shao-Horn Y 2019 *Adv. Mater.* **31** 1806296
[17] Mayrhofer K J J, Strmcnik D, Blizanac B B, Stamenkovic V, Arenz M and Markovic N M 2008 *Electrochim. Acta* **53** 3181
[18] Gasteiger H A, Kocha S S, Sompalli B and Wagner F T 2005 *Appl. Catal.* B **56** 9
[19] Watzele S, Fichtner J, Garlyyev B, Schwämmlein J N and Bandarenka A S 2018 *ACS Catal.* **8** 9456
[20] Xue S, Garlyyev B, Watzele S, Liang Y, Fichtner J, Pohl M D and Bandarenka A S 2018 *ChemElectroChem* **5** 2326
[21] Zhu J, Hu L, Zhao P, Lee L Y and Wong K Y 2020 *Chem. Rev.* **120** 851
[22] Kluge R M, Psaltis E, Haid R W, Hou S, Schmidt T O, Schneider O, Garlyyev B, Calle-Vallejo F and Bandarenka A S 2022 *ACS Appl. Mater. Interfaces* **14** 19604
[23] Escudero-Escribano M, Verdaguer-Casadevall A, Malacrida P, Grønbjerg U, Knudsen B P, Jepsen A K, Rossmeisl J, Stephens I E L and Chorkendorff I 2012 *J. Am. Chem. Soc.* **134** 16476
[24] Escudero-Escribano M, Malacrida P, Hansen M H, Vej-Hansen U G, Velázquez-Palenzuela A, Tripkovic V, Schiøtz J, Rossmeisl J, Stephens I E L and Chorkendorff I 2016 *Science* **352** 73
[25] Qin J, Li Z, Ye K, Zhang Y, Liu Q and Yin F 2021 *Energy Fuels* **35** 14868
[26] Campos-Roldán C A, Pailloux F, Blanchard P Y, Jones D I, Rozière J and Cavaliere S 2021 *ACS Catal.* **11** 13519
[27] Schmidt T O *et al* 2022 *Small* **18** 2202410
[28] Zheng J, Zhou S, Gu S, Xu B and Yan Y 2016 *J. Electrochem. Soc.* **163** 499
[29] Yanson A I, Rodriguez P, Garcia-Araez N, Mom R V, Tichelaar F D and Koper M T M 2011 *Angew. Chem., Int. Ed.* **50** 6346
[30] Fichtner J *et al* 2020 *ACS Catal.* **10** 3131
[31] Fichtner J *et al* 2019 *ACS Appl. Mater. Interfaces* **11** 5129
[32] Hersbach T J P and Koper M T M 2021 *Curr. Opin. Electrochem.* **26** 100653
[33] Čolić V, Tymoczko J, Maljusch A, Ganassin A, Schuhmann W and Bandarenka A S 2014 *ChemElectroChem* **2** 143
[34] Huang B *et al* 2021 *J. Am. Chem. Soc.* **1** 1674

[35] Sheng W, Gasteiger H A and Shao-Horn Y 2010 *J. Electrochem. Soc.* **157** B1529
[36] Niu S, Li S S, Du Y, Han X and Xu P 2020 *ACS Energy Lett.* **5** 1083
[37] Rudi S, Cui C, Gan L and Strasser P 2014 *Electrocatalysis* **5** 408
[38] Zadick A, Dubau L, Sergent N, Berthomé G and Chatenet M 2015 *ACS Catal.* **5** 4819
[39] Bondarenko A S 2012 *Anal. Chim. Acta* **743** 41
[40] Bandarenka A S 2022 *Energy Materials A Short Introduction to Functional Materials for Energy Conversion and Storage* (Boca Raton, FL: CRC Press) (https://doi.org/10.1201/9781003025498)
[41] Holder C F and Schaak R E 2019 *ACS Nano* **13** 7359
[42] Lasia A 2014 *Electrochemical Impedance Spectroscopy and Its Applications* (Berlin: Springer) (https://doi.org/10.1007/978-1-4614-8933-7)
[43] Leuaa P, Priyadarshani D, Tripathi A K and Neergat M 2019 *J. Phys. Chem.* C **123** 21440
[44] Jayabal S, Saranya G, Wu J, Liu Y, Geng D and Meng X 2017 *J. Mater. Chem.* A **5** 24540
[45] Garlyyev B, Pohl M D, Čolić V, Liang Y, Butt F K, Holleitner A and Bandarenka A S 2018 *Electrochem. Commun.* **88** 10
[46] Jie Zheng J, Yan Y and Xu B 2015 *J. Electrochem. Soc.* **162** F1470
[47] Leuaaa P, Priyadarshanib D, Choudhurya D, Mauryaa R and Neergat M 2020 *RSC Adv.* **10** 30887
[48] Smiljanić M, Bele M, Moriau L, Ruiz-Zepeda F, Šala M and Hodnik N 2021 *J. Phys. Chem.* C **125** 27534

THE JOURNAL OF PHYSICAL CHEMISTRY C
A JOURNAL OF THE AMERICAN CHEMICAL SOCIETY
pubs.acs.org/JPCC

Article

Influence of Alkali Metal Cations on the Oxygen Reduction Activity of Pt_5Y and Pt_5Gd Alloys

Kun-Ting Song, Alexandra Zagalskaya, Christian M. Schott, Peter M. Schneider, Batyr Garlyyev, Vitaly Alexandrov,* and Aliaksandr S. Bandarenka*

Cite This: J. Phys. Chem. C 2024, 128, 4969−4977

ABSTRACT: Electrolyte species can significantly influence the electrocatalytic performance. In this work, we investigate the impact of alkali metal cations on the oxygen reduction reaction (ORR) on active Pt_5Gd and Pt_5Y polycrystalline electrodes. Due to the strain effects, Pt alloys exhibit a higher kinetic current density of ORR than pure Pt electrodes in acidic media. In alkaline solutions, the kinetic current density of ORR for Pt alloys decreases linearly with the decreasing hydration energy in the order of $Li^+ > Na^+ > K^+ > Rb^+ > Cs^+$, whereas Pt shows the opposite trend. To gain further insights into these experimental results, we conduct complementary density functional theory calculations considering the effects of both electrode surface strain and electrolyte chemistry. The computational results reveal that the different trends in the ORR activity in alkaline media can be explained by the change in the adsorption energy of reaction intermediates with applied surface strain in the presence of alkali metal cations. Our findings provide important insights into the effects of the electrolyte and the strain conditions on the electrocatalytic performance and thus offer valuable guidelines for optimizing Pt-based electrocatalysts.

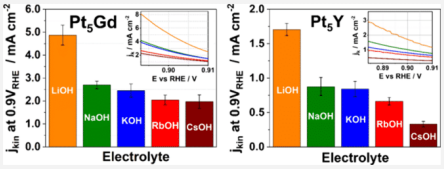

INTRODUCTION

The role of renewable energy in developing sustainable economies is increasingly important.[1,2] Energy storage and conversion devices such as metal-air batteries and polymer electrolyte membrane fuel cells (PEMFCs) are necessary to achieve this goal.[3−8] However, several critical problems must be solved to efficiently employ these devices. For example, in the case of the oxygen reduction reaction (ORR) in fuel cells, sluggish reaction kinetics increase the cathode mass loading and limit the overall performance of PEMFCs.[9,10] Thus, finding more efficient electrocatalysts to enhance the ORR performance is critical. Platinum (Pt) is commonly used as an ORR catalyst. Still, it does not reach optimal catalytic activity on the Sabatier volcano plot due to the non-optimum binding of key reaction intermediates such as *OOH, *O, and *OH at the electrode/electrolyte interface according to density functional theory (DFT) calculations.[11−14] Additionally, the scarcity and high cost of raw materials make commercial use of Pt as a catalyst problematic.[15−18] Therefore, strategies to decrease the mass loading and enhance the catalytic performance of Pt-based catalysts are crucial for commercializing PEMFCs.[19−21]

Efforts to develop higher-performance PEMFCs have been largely focused on the optimization and tailoring of the shape, size, and surface structure of Pt-based electrocatalysts.[22−25] Electrochemical scanning tunneling microscopy (EC-STM) has often been used to identify the nature of active sites that provide optimal binding energy for reaction intermediates during ORR.[26−28] This allows one to explore the correlation between the coordination and the adsorption energies of intermediate species on active sites and maximize their number in nanostructured electrocatalysts.[25] Furthermore, alloying Pt with lanthanide materials and transition metals is a common approach to modify surface chemical properties generally referred to as strain and/or ligand effects.[29−31] Such an alloying may also improve ORR activity in polycrystalline and nanoparticulate catalysts.[10,28,29,32−38] The Pt-enriched overlayer forms on the bulk of Pt alloys after the so-called acid-leaching process.[10] The consequent lattice mismatch between the acid-leached Pt overlayer and the bimetallic bulk alloy causes in the overlayer. The ligand effects are attributed to the dissimilar surrounding atoms, which influence the electronic structure as well as the surface chemical properties.[30] The combination of strain and ligand effects results in weaking of the binding energy of intermediates and improves the ORR activity.

Received: January 25, 2024
Revised: February 28, 2024
Accepted: February 28, 2024
Published: March 18, 2024

https://doi.org/10.1021/acs.jpcc.4c00531
J. Phys. Chem. C 2024, 128, 4969−4977

Furthermore, electrolyte effects in electrocatalytic systems have become an active area of research in recent years. The anion and cation species from supporting electrolytes are regarded as "spectators", which can effectively affect the electrode/electrolyte interfacial properties and electrocatalytic performance.[39−44] Frumkin initially demonstrated the correlation between cation adsorption and reaction kinetics within the double-layer region.[45] Strmcnik et al. illustrated that the noncovalent interactions between reaction intermediates and hydrated alkali metal cations alter the reaction kinetics at the electrode/electrolyte interface.[43] In the case of Pt(111) electrodes, the ORR activity in alkaline media has been examined,[43] and the catalytic trend is CsOH > KOH> NaOH > LiOH. Moreover, Huang et al. reported an opposite trend for Pt polycrystalline (Pt(pc)) toward hydrogen evolution and oxidation reactions (HER/HOR) in alkaline media,[46] which further highlighted the fact that cation-dependent interfacial hydrogen-bonding network can strongly affect reorganization energy and reaction entropy.

Herein, the main objective of this work is to investigate the role of alkali metal cations in the ORR activity of Pt-based alloys in the presence of induced strain on the surface. Here, we select Pt_5Gd and Pt_5Y polycrystalline alloys as the model electrodes for Pt-based alloys due to their high thermodynamic stability with negative heat formation to prevent the continuous dealloying process and provide a relatively steady system during reactions.[32,35,47,48] We measured the strain effects on the ORR activity of Pt alloys and further investigated the cation effect on the activities under strain conditions in different alkaline media. Besides the experimental findings, we employed DFT calculations for the corresponding model systems to study the correlation between the ORR theoretical overpotential and the adsorption energies of the intermediates accounting for both strain and cation effects.

METHODS

Experimental Section. The electrodes of Pt(pc), Pt_5Gd, and Pt_5Y (MaTeck, Germany) with a diameter of about 5 mm were utilized as working electrodes (WEs) in this work. For the electrochemical measurements, the diluted perchloric acid solution (70% $HClO_4$, Suprapur, Merck, and extra pure, Acros, Germany) is selected for the acidic media. The diluted alkaline solutions are synthesized by lithium hydroxide (LiOH, anhydrous, 99.995% (metals basis), Thermo Fisher Scientific, USA), sodium hydroxide (NaOH, 99.99% (metals basis), Thermo Fisher Scientific, USA), potassium hydroxide (KOH, 99.98% (metals basis), Alfa Aesar, USA), rubidium hydroxide (RbOH solution, 50 wt % in H_2O, 99.9% trace metals basis, Sigma-Aldrich, USA), and cesium hydroxide (CsOH solution, 50 wt % in H_2O, 99.9% trace metals basis, Sigma-Aldrich, USA). Ultrapure water (18.2 MΩ·cm, Merck Millipore, Germany) was used to prepare all diluted solutions.

Besides, X-ray diffraction (XRD) was used to investigate the structural and crystallographic properties of electrodes. The XRD measurements were conducted by X'Pert pro PAN-analytical, including a Cu-Ka source and a Ni-based filter. The scanning range (2θ) was from 5° to 90° with a scan rate of approximately 0.78° min^{-1}. The crystal structure for the electrodes, Pt(pc), Pt_5Gd, and Pt_5Y, were fitted with the powder diffraction files corresponding to the literature.[10,32,35] X-ray photoelectron spectroscopy (XPS) was conducted to analyze the surface composition of the Pt alloys after electrochemical measurements by Thermo Scientific K-Alpha$^+$. The XPS spectra were fitted by the CasaXPS software.

Prior to the electrochemical measurements, the cells were cleaned with the so-called "Piranha solution", a 3:1 mixture of sulfuric acid (96% H_2SO_4, p.a., ISO, Carl Roth, Germany) and hydrogen peroxide (30% H_2O_2, p.a., ISO, Carl Roth, Germany), and rinsed with hot ultrapure water several times. The electrochemical cell was composed of a WE, a Pt wire (99.9% purity, MaTeck, Germany) as a counter electrode (CE), and a mercury-mercurous sulfate (MMS) (SI Analytics, Germany) electrode or a mercury-mercuric oxide (MMO) (BAS Inc., Japan) as a reference electrode (RE). For the activity measurements of the ORR in acidic and alkaline media, the cyclic voltammograms (CVs) were first recorded in Ar-saturated conditions as the background CVs for the ORR polarization curves with a scan rate of 50 mV s^{-1} for the Pt_5Gd, Pt_5Y, and Pt(pc) electrodes. After reaching stable CVs, the ORR measurements were then collected in the O_2-saturated condition at the rotation speed rate of 1600 rpm with a scan rate of 50 mV s^{-1}. In this work, all voltammograms of ORR are presented with the *iR*-correction potential due to the ohmic drop losses, and the current is subtracted from the background current in Ar-saturated CVs. The ORR kinetic current density is determined from the following Koutecký−Levich equation.[49]

$$\frac{1}{j_m} = \frac{1}{j_{kin}} + \frac{1}{j_{lim}}$$

where j_m, j_{kin}, and j_{lim} represent the measured, the kinetic, and the diffusion-limited current density, respectively.

The ohmic drop, mainly due to the solution and electric resistance of the three-electrode setup, was measured via electrochemical impedance spectroscopy (EIS) with a shunt capacitor connected between RE and CE to filter out the error signal from the high-frequency range.[50] All electrochemical measurements were conducted via a VSP-300 potentiostat (Bio-Logic, France).

It is noted that all measured potentials with the REs of MMS or MMO were converted to the reversible hydrogen electrode (RHE) scale by the potential calibration in the H_2-saturated condition to avoid the potential shift due to the liquid junction potential appearing between the inner electrolyte and the operating electrolyte.[51,52] The solutions were purged with H_2 for about 30 min, and the CVs were recorded with a scan rate of 10 mV s^{-1} at 1600 rpm to find the intersection potentials of zero current and to obtain the average potential for the measured acidic and alkaline solutions. It is worth emphasizing that the calibration process is necessary to estimate the ORR performance in different solutions precisely. Furthermore, to make sure that the DURAN borosilicate glass cell used for the ORR measurements in alkaline solutions has no impact on the activities due to undesired contamination issues from the glass in alkaline media,[53,54] all measurements were conducted in short-term periods in diluted alkaline solutions. The self-constructed perfluoroalkoxy (PFA) electrochemical cell was used to compare with a typical glass cell.

Finally, to precisely estimate the electrochemical active surface area (ECSA) for the Pt_5Gd, Pt_5Y, and Pt(pc) electrodes, the Cu underpotential deposition measurements were carried out according to the method illustrated by Green and Kucernak[55] and Stephens et al.,[35] which are suitable for determining the ECSA of Pt-based alloys. Before the Cu underpotential deposition measurements, the electrode surface

https://doi.org/10.1021/acs.jpcc.4c00531
J. Phys. Chem. C 2024, 128, 4969−4977

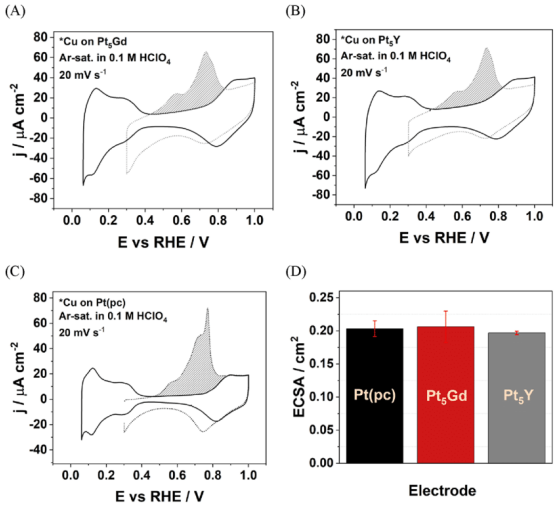

Figure 1. Typical CVs of (A) Pt_5Gd, (B) Pt_5Y, and (C) Pt(pc) electrodes in Ar-saturated 0.1 M $HClO_4$ with the scan rate of 20 mV s^{-1}. The solid and dashed lines represent the typical CVs and the first cycle of Cu stripping, respectively, with the estimated electrochemical active surface areas noted in gray. (D) The bar chart represents the ECSAs of Pt_5Gd, Pt_5Y, and Pt(pc) electrodes determined by Cu underpotential deposition/monolayer stripping.

was first cleaned electrochemically in Ar-saturated 0.1 M $HClO_4$ until stable CVs were reached. The electrode was then measured in an Ar-saturated mixture solution of 0.1 M $HClO_4$ and 2 mM CuO in the hanging meniscus configuration. The WEs were polarized at 1.0 V vs RHE for 160 s to remove Cu before being polarized at 0.3 V vs RHE for 100 s to form a Cu monolayer on the surface. The CVs were recorded in the potential range from 0.06 to 1.0 V vs RHE and from 0.3 to 1.0 V vs RHE with the scan rate of 20 mV s^{-1}, before and during the Cu underpotential deposition process, respectively. All of the detailed results are shown in the Supporting Information.

Computational Section. DFT calculations were performed using the revised Perdew–Burke–Ernzerhof (RPBE) functional[56,57] in Vienna Ab Initio Simulation Package (VASP).[58,59] The projector-augmented wave (PAW) potentials were taken from the VASP library (Pt, O, H, Li_sv, Na_sv, K_sv, Rb_sv, and Cs_sv). The unit cell of bulk Pt was optimized with a 9 × 9 × 9 Monkhorst–Pack mesh to sample the *k*-space and cutoff energy of 700 eV. The convergence criteria for the total energy and atomic forces were set to 10^{-8} eV and 0.01 eV/$Å^{-1}$, respectively. The computed Pt lattice parameter of 3.9974 Å differs from the experimental value of 3.9237 Å[35] by 2%, which is related to overbinding in RPBE but allows one to obtain more accurate binding energies.[32,60] In this paper, we refer our results to the computed values, and therefore, experimental data correspond to the strain of −2%.

The six-layer Pt(111) slab was constructed in VESTA[61] with a vacuum gap of at least 20 Å applying tensile and compressive strain. When applying tensile and compressive strains, the coordinates of all Pt atoms were fixed to avoid surface reconstruction leading to the local strain that would not correspond to the targeted strain value.

All alkali cations were placed on the most favorable fcc site, while the top position was considered for all of the ORR intermediates. The computational hydrogen electrode (CHE) approach[11,62] was employed to calculate the free energies of *O, *OH, and *OOH intermediates, including zero-point energy (ZPE) and vibrational entropy S_{vib} contributions taken at T = 300 K as $\Delta G_{*X} = E_{*X,\,DFT}$ + ZPE − TS_{vib}, where *X stands for the above-mentioned reaction intermediates. The following corrections of 0.36, 0.07, and 0.40 eV were taken to include the zero-point energy and vibrational entropy contributions for *OH, *O, and *OOH. Adsorption energies of the reaction intermediates were computed as $\Delta G_{*OH,\,ads} = \Delta G_{*OH} - \Delta G_{*} - \Delta G_{H2O} - 1/2\Delta G_{H2}$; $\Delta G_{*O,\,ads} = \Delta G_{*O} - \Delta G_{*} - \Delta G_{H2O} - \Delta G_{H2}$; $\Delta G_{*OOH,\,ads} = \Delta G_{*OH} - \Delta G_{*} - 3/2\Delta G_{H2O} - 2\Delta G_{H2}$.

The theoretical overpotential of the ORR was computed as $\eta = 1.23 + \max\{\Delta G_1, \Delta G_2, \Delta G_3, \text{and } \Delta G_4\}/e$, where $\Delta G_1 = \Delta G_{*OOH} - 4.92$, $\Delta G_2 = \Delta G_{*O} - \Delta G_{*OOH}$, $\Delta G_3 = \Delta G_{*OH} - \Delta G_{*O}$, and $\Delta G_4 = -\Delta G_{*OH}$.

A plane-wave cutoff energy of 450 eV and a 3 × 3 × 1 Monkhorst–Pack sampling of the reciprocal space were adopted in all slab calculations. The convergence criteria for the total energy and atomic forces were set to 10^{-4} eV and 0.05 eV/Å, respectively.

RESULTS AND DISCUSSION

The Pt-based electrocatalysts, including Pt_5Gd, Pt_5Y, and Pt(pc) electrodes, were first characterized by XRD measurements. As shown in Figure S1 and Table S1, all XRD patterns show typical polycrystalline structures of all measured electrodes, and the patterns are comparable to the literature with the corresponding crystalline structures and lattice

https://doi.org/10.1021/acs.jpcc.4c00531
J. Phys. Chem. C 2024, 128, 4969−4977

parameters.[10,32,35] Moreover, the XPS results in Figure S2 prove the formation of a Pt overlayer on the surface of bulk Pt_5Gd and Pt_5Y electrodes after the electrochemical measurements. The surface compressive strain is introduced on the Pt overlayer of bulk Pt alloys after the acid leaching process due to the different lattice constants between the surface and bulk crystal.

To study electrochemical properties, CVs of bulk Pt_5Gd, Pt_5Y, and Pt(pc) electrodes were recorded in Ar-saturated 0.1 M $HClO_4$ within the potential range between 0.06 and 1.0 V vs RHE in Figure 1A–C, respectively. Furthermore, the ECSA was estimated by the Cu underpotential deposition and subsequent monolayer stripping method. It is noted that this approach has some advantages for bimetallic electrocatalysts because it can precisely distinguish the contribution sites of deposited Cu atoms from Pt sites with no possible contribution of the solute atoms with different adsorption energies at the surface.[28,55] Figure 1D shows that the average ECSA of each bulk electrode is approximately 0.2 cm^2, similar to their geometric surface area (for an approximately 5 mm diameter disk). Evaluation of the anodic peaks between the Cu underpotential deposition and the background CVs (area with gray color) yields an integrated charge density of about 420 μC cm^{-2}, which is close to the ideal assumption of a monolayer of *Cu on a pure Pt surface and further verifies the formation of a Pt overlayer on bulk Pt alloys (where "*" is noted as the adsorption site of an atom). As the ECSA of each measured electrode is comparable to the geometric surface area, all recorded currents in this work are normalized to the geometric surface area.

To assess the ORR performance in an acidic environment, the standard ORR polarization curves in an O_2-saturated 0.1 M $HClO_4$ solution at 1600 rpm were recorded (see Figure 2A).

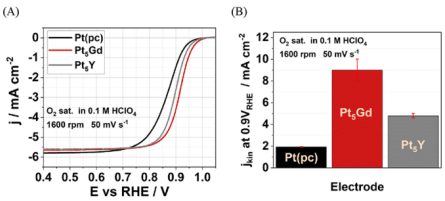

Figure 2. (A) *i*R-corrected voltammograms with anodic scan and (B) bar chart of the j_{kin} at 0.9 V vs RHE of the Pt(pc), Pt_5Gd, and Pt_5Y electrodes in O_2-saturated 0.1 M $HClO_4$ with the scan rate of 50 mV s^{-1} at 1600 rpm.

The trend of the extracted ORR kinetic current densities at 0.9 V vs RHE shown in Figure 2B is as follows: Pt_5Gd > Pt_5Y > Pt(pc). The measured ORR activities for each system are found to be comparable to the literature data.[10,32,35,56] The 2–4 times enhanced ORR activities of Pt alloys compared to pure Pt electrodes are attributed to the effect of compressive strain in the Pt overlayer on the surface, where the surface Pt–Pt interatomic distances decrease compared to the bulk Pt alloys as seen from XRD measurements in Figure S1 and Table S1 and from the literature.[10,32,35] The results of increased ORR activities for Pt alloys are also supported by the d-band theory.[48,63] For Pt-overlayers under compressive strains, the metal d-band center energies shift downward. The binding energy of adsorbed intermediates, including *O, *OH, and *OOH, on the Pt overlayer becomes lower due to the compressive strains. The ORR performance improves to reach the optimal state, where the binding energy is approximately 0.2 eV lower than on pure Pt.[63,64]

To understand the influence of alkali metal cations on the ORR performance, the bar charts and the inset polarization curves shown in Figure 3A–C illustrate the ORR kinetic

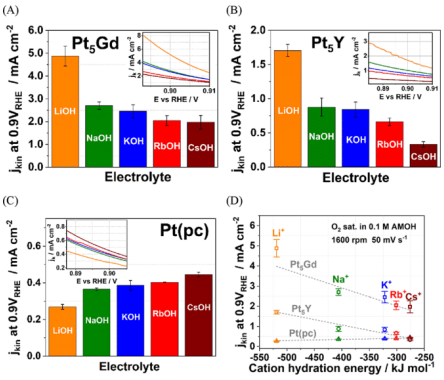

Figure 3. *i*R-corrected voltammograms with anodic scan of (A) Pt_5Gd, (B) Pt_5Y, and (C) Pt(pc) electrodes in O_2-saturated 0.1 M AM–OH (AM^+ = Li^+, Na^+, K^+, Rb^+, and Cs^+) electrolytes with the scan rate of 50 mV s^{-1} at 1600 rpm. The insets in panels (A–C) represent exemplary j_{kin} versus potential curves. (D) The j_{kin} at 0.9 V vs RHE of the Pt(pc), Pt_5Gd, and Pt_5Y electrodes was determined from the insets as a function of cation hydration energy with the dashed lines of the linear fit.

current densities at 0.9 V vs RHE measured in the O_2-saturated 0.1 M metal hydroxide electrolytes, AM–OH (AM^+ = Li^+, Na^+, K^+, Rb^+, and Cs^+) for all electrodes under the same experimental conditions as in acid shown in Figure 2A. The ORR activities measured in alkaline media are several factors lower than in acid for all electrodes, and the results are comparable to the previous studies of Pt-based catalysts.[65–67] One of the reasons for lower ORR activities in alkaline media may be due to the unwarranted hydroperoxyl (HOO^-) species formed on the electrode surface with the undesired $2e^-$ reaction pathway.[68,69] Another explanation is that the different reaction mechanisms of ORR in an alkaline solution with too strong Pt–OH bonding energy are possible, which undesirably blocks the Pt active surface.[68]

Moreover, we determine for the Pt_5Gd and Pt_5Y systems in alkaline solutions (see Figure 3A,B) that the largest ORR kinetic current densities correspond to LiOH, which is more than twice greater than those measured in CsOH. However, the trend is reversed for Pt(pc), for which the highest ORR activity is observed in the case of CsOH, as seen in Figure 3C. These observations can be correlated with the noncovalent interactions between the hydrated alkali metal cations in the outer Helmholtz plane (OHP), as well as the adsorbed and reactive oxygen species in the inner Helmholtz plane (IHP) at the solid/liquid interface as reported in ref 43. The greater structure-making cations (Li^+ and Na^+) strongly bind and interact with the chemisorbed species on pure Pt surfaces with

https://doi.org/10.1021/acs.jpcc.4c00531
J. Phys. Chem. C 2024, 128, 4969–4977

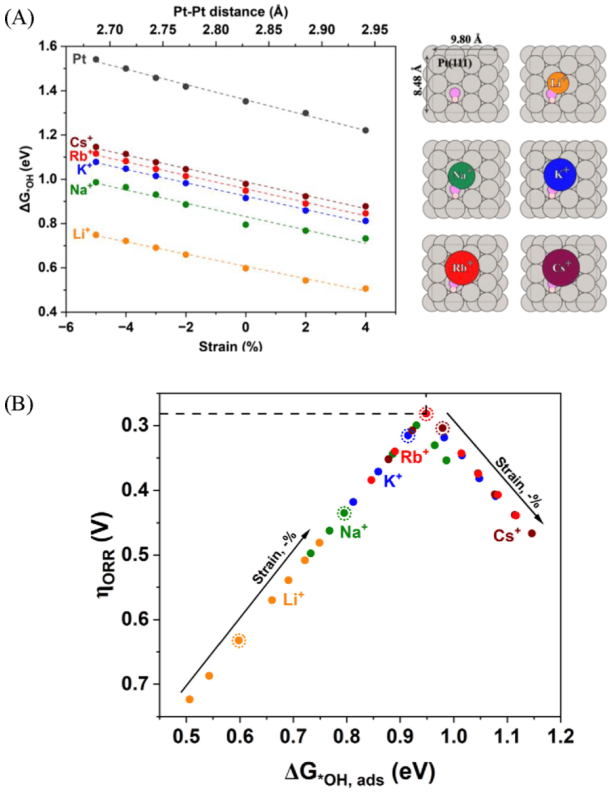

Figure 4. (A) The adsorption energy of *OH on Pt(111) as a function of strain ranged from −5% (compression) to +4% (expansion). The schematic structures and cell dimensions corresponding to 0% strain are shown on the right. (B) The theoretical volcano plot represents the relationship between ORR activity and computed *OH adsorption energy on the pristine Pt(111) surface and in the presence of alkali metal cations. The arrows show the direction of the strain (from tensile to compressive), and the encircled dots correspond to 0% strain. Dashed lines depict the minimum calculated overpotential of 0.28 V corresponding to Rb^+-Pt@0%. Details of the performed calculations can be found in the Supporting Information.

no strain. As a result, besides the intrinsic stronger binding energy like Pt−OH, the extrinsic alkali cations with higher solvation energy inhibit the movement of reactive species and impede the ORR reaction kinetics. By contrast, the compressed-strain surface may have weaker binding energy with the adsorbed species for the Pt overlayer on bulk alloys. Stronger solvation shells optimize and stabilize the Helmholtz plane's molecular interaction energy and promote the ORR process than weaker solvated cations (Rb^+ and Cs^+). Figure 3D shows the ORR kinetic densities at 0.9 V versus RHE as a function of cation hydration energy for the studied electrodes. The ORR activities of Pt alloys decline linearly with the decrease of the hydration energy for alkali cations in the order of $Li^+ > Na^+ > K^+ > Rb^+ > Cs^+$. Conversely, Pt(pc) electrodes display the opposite trend.

The observed opposite ORR trends for the Pt catalysts in alkaline electrolytes are further investigated using DFT calculations. Here, we consider the Pt(111) surface slab with an adsorbed *OH species as the model ORR electrocatalytic system. The Pt(111) surface is commonly taken as a model for Pt electrodes due to its low surface energy and the common existence within the crystalline structures of metals.[32,70] The applied strain corresponding to the surface Pt−Pt distance is illustrated in Table S3. Figure 4A shows the difference between the *OH adsorption energy for the system under applied strain and the value obtained for the case with 0% strain. It is seen that compressive strain leads to the destabilization of *OH on the pristine Pt surface,[32,71] as well as in the presence of alkali metal cations. This was previously demonstrated to improve the ORR activity as the destabilization of *OH on pure Pt(111) moves ΔG_{*OH} closer to the volcano peak. The

https://doi.org/10.1021/acs.jpcc.4c00531
J. Phys. Chem. C 2024, 128, 4969−4977

obtained slope of −0.03 eV/% for pure Pt fully agrees with previous computational results.[32] Contrary to the destabilizing effect of the compressive strain on *OH binding, alkali cations stabilize *OH adsorption. However, different alkali cations stabilize *OH on the surface differently, with Li^+ having the strongest stabilizing effect. For example, Li^+ stabilizes *OH by 0.75 eV, while Cs^+ stabilizes *OH by 0.37 eV relative to the pristine Pt surface (see Tables S4 and S5).

As seen in Figure 4B, to achieve the minimum of the ORR theoretical overpotential (η_{ORR}), the effects of both strain and the nature of the alkali cation should be considered. Specifically, along with the smaller compressive and nonstrain region (i.e., pure Pt surface, where *OH adsorption is too strong), Cs^+ is characterized by lower computed ORR overpotentials than Li^+ as Li leads to larger stabilization of *OH. For example, for the pristine Pt@0%, η_{ORR} (Li^+) = 0.63 V > η_{ORR} (Cs^+) = 0.30 V. When applying larger compressive strains (i.e., corresponding to the Pt overlayer on bulk alloys), the ORR overpotential in the presence of Li^+ decreases. In contrast, the opposite trend is observed for Cs^+. This is because under such large compressive strains *OH becomes too destabilized, and the strong stabilizing effect of Li^+ will bring it closer to the volcano peak with optimal ORR activity. Thus, our computational results support experimental findings on the reverse trend of alkali cations, shown in Figure 3D.

Figure 5 schematically illustrates the obtained results on relative ORR activities for the Pt alloys in acidic and alkaline media as a function of lattice parameters. It is noted that the pseudo volcano plot depicted with dashed lines only supports the conceptional relationship between the ORR performance and the Pt lattice constant relating strain effect and the influence of alkali cations at the electrode/electrolyte interface. The larger lattice parameter of bulk electrodes represents higher compressive strains on the surfaces of Pt or Pt-overlayers. Pt(pc) has slightly too strong binding energy between the Pt surface and the reaction intermediates. The existence of the alkali cations at the interface influences the ORR activities, which increase with the lower cation hydration energy. However, in the case of Pt_5Gd and Pt_5Y electrodes, which have larger lattice parameters and slightly weaker binding energies, the presence of alkali cations with higher solvation energy optimizes the binding energies on the compressed surfaces. Consequently, the ORR activity increases with increasing hydration energy for Pt_5Gd and Pt_5Y electrodes. In the future outlook, the different ORR trends between the Pt-alloys and Pt(pc) electrodes due to the existence of different cations at interfaces can be further investigated by combining in situ EIS and Raman spectroscopy to identify the double-layer capacitance, the adsorption processes, and the surface chemical speciation, and to provide more comprehensive insights into the rational design of electrocatalysts.

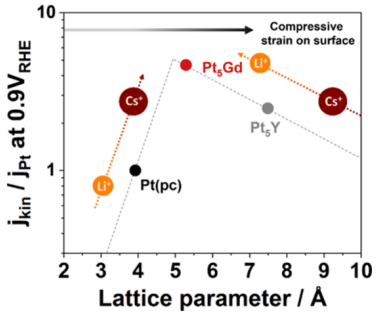

Figure 5. Relative ORR activity at 0.9 V vs RHE as a function of lattice parameter in O_2-saturated 0.1 M $HClO_4$ for Pt(pc), Pt_5Gd, and Pt_5Y electrodes (corresponding to black, red, and gray circles, respectively) and their ORR activity-trend measured in 0.1 M O_2-saturated alkaline solutions with dashed arrows. The induced strain (compression) on the surface increases with a larger lattice parameter. It is noted that the dashed lines of the pseudo volcano plot only represent the guides to the eyes, and the lattice parameters of measured electrodes are referred to the experimental XRD patterns in the Supporting Information in agreement with refs 10, 32, and 35.

CONCLUSIONS

In summary, this work explored the effect of electrolyte cation on the electrochemical ORR under different surface strains of Pt-based electrocatalysts in alkaline solutions. It is revealed that the ORR activities of the studied electrodes follow the order of P_5Gd > Pt_5Y > Pt(pc) in acidic media. Compressive strains allow one to achieve more optimal binding energies for reaction intermediates than for the pure Pt surface, leading to enhanced ORR kinetics. Moreover, the ORR performance of the Pt alloys improves with the increase of cation hydration energy in the order of Li^+> Na^+ > K^+ > Rb^+ > Cs^+; however, the pure Pt electrodes demonstrate the opposite trend in alkaline media. Our computational results support the experimental findings that the noncovalent interactions between the solvated cations and intermediates and the strain effects on the surfaces strongly influence the ORR overpotential. For a pure Pt surface, slightly too strong adsorption of reaction intermediates and the presence of structure-making alkali cations result in increased ORR overpotentials. In comparison, the presence of cations with a higher hydration energy optimizes the binding conditions of adsorbed species on the compressively strained surface, thus enhancing the ORR activities.

ASSOCIATED CONTENT

Supporting Information

The Supporting Information is available free of charge at https://pubs.acs.org/doi/10.1021/acs.jpcc.4c00531.

The X-ray diffraction (XRD) patterns of Pt_5Gd, Pt_5Y, and Pt polycrystalline electrodes; the XRD fitting results with the corresponding literature; X-ray photoelectron spectroscopy data; the typical cyclic voltammograms; the *iR*-corrected voltammograms of the electrodes in O_2-saturated electrolytes; HER calibration data; calculated adsorption energies and corresponding oxygen reduction reaction overpotentials on the pristine Pt(111); calculated adsorption energies and corresponding ORR overpotentials on Pt(111) in the presence of alkali metal cations (PDF)

AUTHOR INFORMATION

Corresponding Authors

Aliaksandr S. Bandarenka − *Physik-Department ECS, Technische Universität München, Garching D-85748, Germany; Catalysis Research Center TUM, Garching bei*

https://doi.org/10.1021/acs.jpcc.4c00531
J. Phys. Chem. C 2024, 128, 4969−4977

München 85748, Germany; orcid.org/0000-0002-5970-4315; Phone: +49 (0) 89 289 12531; Email: bandarenka@ph.tum.de

Vitaly Alexandrov − *Department of Chemical and Biomolecular Engineering and Nebraska Center for Materials and Nanoscience, University of Nebraska-Lincoln, Lincoln, Nebraska 68588, United States;* orcid.org/0000-0003-2063-6914; Email: valexandrov2@unl.edu

Authors

Kun-Ting Song − *Physik-Department ECS, Technische Universität München, Garching D-85748, Germany*

Alexandra Zagalskaya − *Department of Chemical and Biomolecular Engineering, University of Nebraska-Lincoln, Lincoln, Nebraska 68588, United States; Quantum Simulations Group, Materials Science Division, Lawrence Livermore National Laboratory, Livermore, California 94550, United States*

Christian M. Schott − *Physik-Department ECS, Technische Universität München, Garching D-85748, Germany*

Peter M. Schneider − *Physik-Department ECS, Technische Universität München, Garching D-85748, Germany*

Batyr Garlyyev − *Physik-Department ECS, Technische Universität München, Garching D-85748, Germany;* orcid.org/0000-0002-2756-2105

Complete contact information is available at: https://pubs.acs.org/10.1021/acs.jpcc.4c00531

Notes

The authors declare no competing financial interest.

■ ACKNOWLEDGMENTS

This project is supported by funding from the German Research Foundation (DFG) under Germany's excellence strategy − EXC 2089/1-390776260, Germany's excellence cluster "e-conversion" and under DFG Project no. BA 5795/6-1. P.M.S. and A.S.B. acknowledge financial support via the Excellence Strategy of the Federal Government and the Länder in the context of the TUM Innovation Network for Artificial Intelligence-powered Multifunctional Material Design (ARTEMIS). V.A. acknowledges funding support from the National Science Foundation (NSF) through the NSF CAREER award (grant no. CBET-1941204). This research used resources of the National Energy Research Scientific Computing Center, a DOE Office of Science User Facility supported by the Office of Science of the US Department of Energy under contract no. DE-AC02-05CH11231. We also gratefully acknowledge the XPS measurements supported by Dr. Cindy Tseng from the group of Prof. Dr. Ifan E. L. Stephens at the Department of Materials at Imperial College London.

■ REFERENCES

(1) Sen, S.; Ganguly, S. Opportunities, Barriers and Issues with Renewable Energy Development − A Discussion. *Renewable Sustainable Energy Rev.* **2017**, *69*, 1170−1181.

(2) Xu, X.; Wei, Z.; Ji, Q.; Wang, C.; Gao, G. Global Renewable Energy Development: Influencing Factors, Trend Predictions and Countermeasures. *Resour. Policy* **2019**, *63*, No. 101470.

(3) Chandan, A.; Hattenberger, M.; El-kharouf, A.; Du, S.; Dhir, A.; Self, V.; Pollet, B. G.; Ingram, A.; Bujalski, W. High Temperature (HT) Polymer Electrolyte Membrane Fuel Cells (PEMFC) − A Review. *J. Power Sources* **2013**, *231*, 264−278.

(4) Wang, Y.-J.; Long, W.; Wang, L.; Yuan, R.; Ignaszak, A.; Fang, B.; Wilkinson, D. P. Unlocking the Door to Highly Active ORR Catalysts for PEMFC Applications: Polyhedron-Engineered Pt-Based Nanocrystals. *Energy Environ. Sci.* **2018**, *11* (2), 258−275.

(5) Costamagna, P.; Srinivasan, S. Quantum Jumps in the PEMFC Science and Technology from the 1960s to the Year 2000: Part II. Engineering, Technology Development and Application Aspects. *J. Power Sources* **2001**, *102* (1), 253−269.

(6) Gasteiger, H. A.; Kocha, S. S.; Sompalli, B.; Wagner, F. T. Activity Benchmarks and Requirements for Pt, Pt-Alloy, and Non-Pt Oxygen Reduction Catalysts for PEMFCs. *Appl. Catal., B* **2005**, *56* (1), 9−35.

(7) Blurton, K. F.; Sammells, A. F. Metal/air Batteries: Their Status and Potential — a Review. *J. Power Sources* **1979**, *4* (4), 263−279.

(8) Rahman, M. A.; Wang, X.; Wen, C. High Energy Density Metal-Air Batteries: A Review. *J. Electrochem. Soc.* **2013**, *160* (10), A1759.

(9) Wang, J.; Zhao, C.-X.; Liu, J.-N.; Ren, D.; Li, B.-Q.; Huang, J.-Q.; Zhang, Q. Quantitative Kinetic Analysis on Oxygen Reduction Reaction: A Perspective. *Nano Materials Science* **2021**, 3 (3), 313−318.

(10) Escudero-Escribano, M.; Verdaguer-Casadevall, A.; Malacrida, P.; Grønbjerg, U.; Knudsen, B. P.; Jepsen, A. K.; Rossmeisl, J.; Stephens, I. E. L.; Chorkendorff, I. Pt_3Gd as a Highly Active and Stable Catalyst for Oxygen Electroreduction. *J. Am. Chem. Soc.* **2012**, *134* (40), 16476−16479.

(11) Nørskov, J. K.; Rossmeisl, J.; Logadottir, A.; Lindqvist, L.; Kitchin, J. R.; Bligaard, T.; Jónsson, H. Origin of the Overpotential for Oxygen Reduction at a Fuel-Cell Cathode. *J. Phys. Chem. B* **2004**, *108* (46), 17886−17892.

(12) Kulkarni, A.; Siahrostami, S.; Patel, A.; Nørskov, J. K. Understanding Catalytic Activity Trends in the Oxygen Reduction Reaction. *Chem. Rev.* **2018**, *118* (5), 2302−2312.

(13) Hansen, H. A.; Rossmeisl, J.; Nørskov, J. K. Surface Pourbaix Diagrams and Oxygen Reduction Activity of Pt, Ag and Ni(111) Surfaces Studied by DFT. *Phys. Chem. Chem. Phys.* **2008**, *10* (25), 3722−3730.

(14) Karlberg, G. S.; Rossmeisl, J.; Nørskov, J. K. Estimations of Electric Field Effects on the Oxygen Reduction Reaction Based on the Density Functional Theory. *Phys. Chem. Chem. Phys.* **2007**, *9* (37), 5158−5161.

(15) Guo, S.; Zhang, S.; Sun, S. Tuning Nanoparticle Catalysis for the Oxygen Reduction Reaction. *Angew. Chem., Int. Ed. Engl.* **2013**, *52* (33), 8526−8544.

(16) Jung, N.; Chung, D. Y.; Ryu, J.; Yoo, S. J.; Sung, Y.-E. Pt-Based Nanoarchitecture and Catalyst Design for Fuel Cell Applications. *Nano Today* **2014**, *9* (4), 433−456.

(17) Bashyam, R.; Zelenay, P. A Class of Non-Precious Metal Composite Catalysts for Fuel Cells. *Nature* **2006**, *443* (7107), 63−66.

(18) Nikoloski, A. N.; Ang, K.-L. Review of the Application of Ion Exchange Resins for the Recovery of Platinum-Group Metals From Hydrochloric Acid Solutions. *Miner. Process. Extr. Metall. Rev.* **2014**, *35* (6), 369−389.

(19) Sharma, S.; Pollet, B. G. Support Materials for PEMFC and DMFC electrocatalysts—A Review. *J. Power Sources* **2012**, *208*, 96−119.

(20) Liu, S.; Li, S.; Wang, R.; Rao, Y.; Zhong, Q.; Hong, K.; Pan, M. Preparation of High Performance and Ultra-Low Platinum Loading Membrane Electrode Assembly for PEMFC Commercial Application. *J. Electrochem. Soc.* **2019**, *166* (16), F1308.

(21) Kongkanand, A.; Mathias, M. F. The Priority and Challenge of High-Power Performance of Low-Platinum Proton-Exchange Membrane Fuel Cells. *J. Phys. Chem. Lett.* **2016**, *7* (7), 1127−1137.

(22) Garlyyev, B.; Watzele, S.; Fichtner, J.; Michalička, J.; Schökel, A.; Senyshyn, A.; Perego, A.; Pan, D.; El-Sayed, H. A.; Macak, J. M.; et al. Electrochemical Top-down Synthesis of C-Supported Pt Nano-Particles with Controllable Shape and Size: Mechanistic Insights and Application. *Nano Res.* **2021**, *14* (8), 2762−2769.

(23) Garlyyev, B.; Kratzl, K.; Rück, M.; Michalička, J.; Fichtner, J.; Macak, J. M.; Kratky, T.; Günther, S.; Cokoja, M.; Bandarenka, A. S.; et al. Optimizing the Size of Platinum Nanoparticles for Enhanced

Mass Activity in the Electrochemical Oxygen Reduction Reaction. *Angew. Chem., Int. Ed. Engl.* **2019**, *58* (28), 9596−9600.
(24) Fichtner, J.; Watzele, S.; Garlyyev, B.; Kluge, R. M.; Haimerl, F.; El-Sayed, H. A.; Li, W.-J.; Maillard, F. M.; Dubau, L.; Chattot, R.; et al. Tailoring the Oxygen Reduction Activity of Pt Nanoparticles through Surface Defects: A Simple Top-Down Approach. *ACS Catal.* **2020**, *10* (5), 3131−3142.
(25) Calle-Vallejo, F.; Pohl, M. D.; Reinisch, D.; Loffreda, D.; Sautet, P.; Bandarenka, A. S. Why Conclusions from Platinum Model Surfaces Do Not Necessarily Lead to Enhanced Nanoparticle Catalysts for the Oxygen Reduction Reaction. *Chem. Sci.* **2017**, *8* (3), 2283−2289.
(26) Pfisterer, J. H. K.; Liang, Y.; Schneider, O.; Bandarenka, A. S. Direct Instrumental Identification of Catalytically Active Surface Sites. *Nature* **2017**, *549* (7670), 74−77.
(27) Haid, R. W.; Kluge, R. M.; Liang, Y.; Bandarenka, A. S. In Situ Quantification of the Local Electrocatalytic Activity via Electrochemical Scanning Tunneling Microscopy. *Small Methods* **2021**, *5* (2), No. e2000710.
(28) Kluge, R. M.; Haid, R. W.; Riss, A.; Bao, Y.; Seufert, K.; Schmidt, T. O.; Watzele, S. A.; Barth, J. V.; Allegretti, F.; Auwärter, W.; et al. A Trade-off between Ligand and Strain Effects Optimizes the Oxygen Reduction Activity of Pt Alloys. *Energy Environ. Sci.* **2022**, *15* (12), 5181−5191.
(29) Strasser, P.; Koh, S.; Anniyev, T.; Greeley, J.; More, K.; Yu, C.; Liu, Z.; Kaya, S.; Nordlund, D.; Ogasawara, H.; et al. Lattice-Strain Control of the Activity in Dealloyed Core−shell Fuel Cell Catalysts. *Nat. Chem.* **2010**, *2* (6), 454−460.
(30) Kitchin, J. R.; Nørskov, J. K.; Barteau, M. A.; Chen, J. G. Role of Strain and Ligand Effects in the Modification of the Electronic and Chemical Properties of Bimetallic Surfaces. *Phys. Rev. Lett.* **2004**, *93* (15), No. 156801.
(31) Čolić, V.; Bandarenka, A. S. Pt Alloy Electrocatalysts for the Oxygen Reduction Reaction: From Model Surfaces to Nanostructured Systems. *ACS Catal.* **2016**, *6* (8), 5378−5385.
(32) Escudero-Escribano, M.; Malacrida, P.; Hansen, M. H.; Vej-Hansen, U. G.; Velázquez-Palenzuela, A.; Tripkovic, V.; Schiøtz, J.; Rossmeisl, J.; Stephens, I. E. L.; Chorkendorff, I. Tuning the Activity of Pt Alloy Electrocatalysts by Means of the Lanthanide Contraction. *Science* **2016**, *352* (6281), 73−76.
(33) Fichtner, J.; Garlyyev, B.; Watzele, S.; El-Sayed, H. A.; Schwämmlein, J. N.; Li, W.-J.; Maillard, F. M.; Dubau, L.; Michalička, J.; Macak, J. M.; et al. Top-Down Synthesis of Nanostructured Platinum−Lanthanide Alloy Oxygen Reduction Reaction Catalysts: Pt_5Pr/C as an Example. *ACS Appl. Mater. Interfaces* **2019**, *11* (5), 5129−5135.
(34) Malacrida, P.; Escudero-Escribano, M.; Verdaguer-Casadevall, A.; Stephens, I. E. L.; Chorkendorff, I. Enhanced Activity and Stability of Pt−La and Pt−Ce Alloys for Oxygen Electroreduction: The Elucidation of the Active Surface Phase. *J. Mater. Chem. A Mater. Energy Sustain.* **2014**, *2* (12), 4234−4243.
(35) Stephens, I. E. L.; Bondarenko, A. S.; Bech, L.; Chorkendorff, I. Oxygen Electroreduction Activity and X-ray Photoelectron Spectroscopy of Platinum and Early Transition Metal Alloys. *ChemCatChem.* **2012**, *4* (3), 341−349.
(36) Garlyyev, B.; Pohl, M. D.; Čolić, V.; Liang, Y.; Butt, F. K.; Holleitner, A.; Bandarenka, A. S. High Oxygen Reduction Reaction Activity of Pt_5Pr Electrodes in Acidic Media. *Electrochem. Commun.* **2018**, *88*, 10−14.
(37) Kluge, R. M.; Psaltis, E.; Haid, R. W.; Hou, S.; Schmidt, T. O.; Schneider, O.; Garlyyev, B.; Calle-Vallejo, F.; Bandarenka, A. S. Revealing the Nature of Active Sites on Pt−Gd and Pt−Pr Alloys during the Oxygen Reduction Reaction. *ACS Appl. Mater. Interfaces* **2022**, *14* (17), 19604−19613.
(38) Stamenkovic, V. R.; Fowler, B.; Mun, B. S.; Wang, G.; Ross, P. N.; Lucas, C. A.; Marković, N. M. Improved Oxygen Reduction Activity on Pt_3Ni(111) via Increased Surface Site Availability. *Science* **2007**, *315* (5811), 493−497.
(39) Berkes, B. B.; Inzelt, G.; Schuhmann, W.; Bondarenko, A. S. Influence of Cs^+ and Na^+ on Specific Adsorption of *OH, *O, and *H at Platinum in Acidic Sulfuric Media. *J. Phys. Chem. C Nanomater. Interfaces* **2012**, *116* (20), 10995−11003.
(40) Garlyyev, B.; Xue, S.; Watzele, S.; Scieszka, D.; Bandarenka, A. S. Influence of the Nature of the Alkali Metal Cations on the Electrical Double-Layer Capacitance of Model Pt(111) and Au(111) Electrodes. *J. Phys. Chem. Lett.* **2018**, *9* (8), 1927−1930.
(41) Garlyyev, B.; Xue, S.; Pohl, M. D.; Reinisch, D.; Bandarenka, A. S. Oxygen Electroreduction at High-Index Pt Electrodes in Alkaline Electrolytes: A Decisive Role of the Alkali Metal Cations. *ACS Omega* **2018**, *3* (11), 15325−15331.
(42) Xue, S.; Garlyyev, B.; Auer, A.; Kunze-Liebhäuser, J.; Bandarenka, A. S. How the Nature of the Alkali Metal Cations Influences the Double-Layer Capacitance of Cu, Au, and Pt Single-Crystal Electrodes. *J. Phys. Chem. C* **2020**, *124* (23), 12442−12447.
(43) Strmcnik, D.; Kodama, K.; van der Vliet, D.; Greeley, J.; Stamenkovic, V. R.; Marković, N. M. The Role of Non-Covalent Interactions in Electrocatalytic Fuel-Cell Reactions on Platinum. *Nat. Chem.* **2009**, *1* (6), 466−472.
(44) Xue, S.; Garlyyev, B.; Watzele, S.; Liang, Y.; Fichtner, J.; Pohl, M. D.; Bandarenka, A. S. Influence of Alkali Metal Cations on the Hydrogen Evolution Reaction Activity of Pt, Ir, Au, and Ag Electrodes in Alkaline Electrolytes. *ChemElectroChem.* **2018**, *5* (17), 2326−2329.
(45) Frumkin, A. N. Influence of Cation Adsorption on the Kinetics of Electrode Processes. *Trans. Faraday Soc.* **1959**, *55*, 156−167.
(46) Huang, B.; Rao, R. R.; You, S.; Hpone Myint, K.; Song, Y.; Wang, Y.; Ding, W.; Giordano, L.; Zhang, Y.; Wang, T.; et al. Cation- and pH-Dependent Hydrogen Evolution and Oxidation Reaction Kinetics. *JACS Au* **2021**, *1* (10), 1674−1687.
(47) Jacob, K. T.; Waseda, Y. Thermodynamic Properties of Platinum-Rich Intermetallics in the Pt−Gd System. *Mater. Trans., JIM* **1990**, *31* (2), 135−140.
(48) Jóhannesson, G. H.; Bligaard, T.; Ruban, A. V.; Skriver, H. L.; Jacobsen, K. W.; Nørskov, J. K. Combined Electronic Structure and Evolutionary Search Approach to Materials Design. *Phys. Rev. Lett.* **2002**, *88* (25 Pt 1), No. 255506.
(49) Liu, M.; Zhao, Z.; Duan, X.; Huang, Y. Nanoscale Structure Design for High-Performance Pt-Based ORR Catalysts. *Adv. Mater.* **2019**, *31* (6), No. e1802234.
(50) Čolić, V.; Tymoczko, J.; Maljusch, A.; Ganassin, A.; Schuhmann, W.; Bandarenka, A. S. Experimental Aspects in Benchmarking of the Electrocatalytic Activity. *ChemElectroChem.* **2015**, *2* (1), 143−149.
(51) Niu, S.; Li, S.; Du, Y.; Han, X.; Xu, P. How to Reliably Report the Overpotential of an Electrocatalyst. *ACS Energy Lett.* **2020**, *5* (4), 1083−1087.
(52) Song, K.-T.; Schott, C. M.; Schneider, P. M.; Watzele, S. A.; Kluge, R. M.; Gubanova, E. L.; Bandarenka, A. S. Combining Impedance and Hydrodynamic Methods in Electrocatalysis. Characterization of Pt(pc), Pt5Gd, and Nanostructured Pd for the Hydrogen Evolution Reaction. *J. Phys. Energy* **2023**, *5* (1), No. 014016.
(53) Mayrhofer, K. J. J.; Crampton, A. S.; Wiberg, G. K. H.; Arenz, M. Analysis of the Impact of Individual Glass Constituents on Electrocatalysis on Pt Electrodes in Alkaline Solution. *J. Electrochem. Soc.* **2008**, *155* (6), P78.
(54) Sebastián-Pascual, P.; Sarabia, F. J.; Climent, V.; Feliu, J. M.; Escudero-Escribano, M. Elucidating the Structure of the Cu-Alkaline Electrochemical Interface with the Laser-Induced Temperature Jump Method. *J. Phys. Chem. C* **2020**, *124* (42), 23253−23259.
(55) Green, C. L.; Kucernak, A. Determination of the Platinum and Ruthenium Surface Areas in Platinum−Ruthenium Alloy Electrocatalysts by Underpotential Deposition of Copper. I. Unsupported Catalysts. *J. Phys. Chem. B* **2002**, *106* (5), 1036−1047.
(56) Perdew, J. P.; Burke, K.; Ernzerhof, M. Generalized Gradient Approximation Made Simple. *Phys. Rev. Lett.* **1996**, *77* (18), 3865−3868.
(57) Zhang, Y.; Yang, W. Comment on Generalized Gradient Approximation Made Simple. *Phys. Rev. Lett.* **1998**, *80* (4), 890−890.

https://doi.org/10.1021/acs.jpcc.4c00531
J. Phys. Chem. C 2024, 128, 4969−4977

(58) Kresse, G.; Furthmüller, J. Efficient Iterative Schemes for Ab Initio Total-Energy Calculations Using a Plane-Wave Basis Set. *Phys. Rev. B Condens. Matter* **1996**, *54* (16), 11169−11186.
(59) Kresse, G.; Furthmüller, J. Efficiency of Ab-Initio Total Energy Calculations for Metals and Semiconductors Using a Plane-Wave Basis Set. *Comput. Mater. Sci.* **1996**, *6* (1), 15−50.
(60) Hammer, B.; Hansen, L. B.; Nørskov, J. K. Improved Adsorption Energetics within Density-Functional Theory Using Revised Perdew-Burke-Ernzerhof Functionals. *Phys. Rev. B Condens. Matter* **1999**, *59* (11), 7413−7421.
(61) Momma, K.; Izumi, F. VESTA 3 for Three-Dimensional Visualization of Crystal, Volumetric and Morphology Data. *J. Appl. Crystallogr.* **2011**, *44* (6), 1272−1276.
(62) Man, I. C.; Su, H.; Calle-Vallejo, F.; Hansen, H. A.; Martínez, J. I.; Inoglu, N. G.; Kitchin, J.; Jaramillo, T. F.; Nørskov, J. K.; Rossmeisl, J. Universality in Oxygen Evolution Electrocatalysis on Oxide Surfaces. *ChemCatChem.* **2011**, *3* (7), 1159−1165.
(63) Stamenkovic, V.; Mun, B. S.; Mayrhofer, K. J. J.; Ross, P. N.; Markovic, N. M.; Rossmeisl, J.; Greeley, J.; Nørskov, J. K. Changing the Activity of Electrocatalysts for Oxygen Reduction by Tuning the Surface Electronic Structure. *Angew. Chem., Int. Ed. Engl.* **2006**, *45* (18), 2897−2901.
(64) Greeley, J.; Stephens, I. E. L.; Bondarenko, A. S.; Johansson, T. P.; Hansen, H. A.; Jaramillo, T. F.; Rossmeisl, J.; Chorkendorff, I.; Nørskov, J. K. Alloys of Platinum and Early Transition Metals as Oxygen Reduction Electrocatalysts. *Nat. Chem.* **2009**, *1* (7), 552−556.
(65) Nesselberger, M.; Ashton, S.; Meier, J. C.; Katsounaros, I.; Mayrhofer, K. J. J.; Arenz, M. The Particle Size Effect on the Oxygen Reduction Reaction Activity of Pt Catalysts: Influence of Electrolyte and Relation to Single Crystal Models. *J. Am. Chem. Soc.* **2011**, *133* (43), 17428−17433.
(66) You, G.; Zhu, W.; Zhuang, Z. Impacts of Anions on the Electrochemical Oxygen Reduction Reaction Activity and Stability of Pt/C in Alkaline Electrolyte. *Int. J. Hydrogen Energy* **2019**, *44* (26), 13373−13382.
(67) Sheng, W.; Gasteiger, H. A.; Shao-Horn, Y. Hydrogen Oxidation and Evolution Reaction Kinetics on Platinum: Acid vs Alkaline Electrolytes. *J. Electrochem. Soc.* **2010**, *157* (11), B1529.
(68) Liu, S.; White, M. G.; Liu, P. Mechanism of Oxygen Reduction Reaction on Pt(111) in Alkaline Solution: Importance of Chemisorbed Water on Surface. *J. Phys. Chem. C* **2016**, *120* (28), 15288−15298.
(69) Ge, X.; Sumboja, A.; Wuu, D.; An, T.; Li, B.; Goh, F. W. T.; Hor, T. S. A.; Zong, Y.; Liu, Z. Oxygen Reduction in Alkaline Media: From Mechanisms to Recent Advances of Catalysts. *ACS Catal.* **2015**, *5* (8), 4643−4667.
(70) Vitos, L.; Ruban, A. V.; Skriver, H. L.; Kollár, J. The Surface Energy of Metals. *Surf. Sci.* **1998**, *411* (1), 186−202.
(71) Kattel, S.; Wang, G. Beneficial Compressive Strain for Oxygen Reduction Reaction on Pt (111) Surface. *J. Chem. Phys.* **2014**, *141* (12), No. 124713.

https://doi.org/10.1021/acs.jpcc.4c00531
J. Phys. Chem. C 2024, 128, 4969−4977

References

[1] Houghton, J. Global Warming. *Rep. Prog. Phys.* **2005**, *68* (6), 1343.

[2] Kerr, R. A. Climate Change. Global Warming Is Changing the World. *Science* **2007**, *316* (5822), 188–190.

[3] Noll, K. E. *Adsorption Technology for Air and Water Pollution Control*; CRC Press, **1991**.

[4] Greenstone, M.; Hanna, R. Environmental Regulations, Air and Water Pollution, and Infant Mortality in India. *Am. Econ. Rev.* **2014**, *104* (10), 3038–3072.

[5] Züttel, A.; Remhof, A.; Borgschulte, A.; Friedrichs, O. Hydrogen: The Future Energy Carrier. *Philos. Trans. A Math. Phys. Eng. Sci.* **2010**, *368* (1923), 3329–3342.

[6] Schleussner, C.-F.; Rogelj, J.; Schaeffer, M.; Lissner, T.; Licker, R.; Fischer, E. M.; Knutti, R.; Levermann, A.; Frieler, K.; Hare, W. Science and Policy Characteristics of the Paris Agreement Temperature Goal. *Nat. Clim. Chang.* **2016**, *6* (9), 827–835.

[7] Horowitz, C. A. Paris Agreement. *Int. Leg. Mater.* **2016**, *55* (4), 740–755.

[8] Hanley, E. S.; Deane, J. P.; Gallachóir, B. P. Ó. The Role of Hydrogen in Low Carbon Energy futures–A Review of Existing Perspectives. *Renew. Sustain. Energy Rev.* **2018**, *82*, 3027–3045.

[9] Environmental; Energy Study Institute (EESI). *Behind the 2 degree scenario presented at COP21*. https://www.eesi.org/articles/view/behind-the-2-degree-scenario-presented-at-cop21 (accessed 2024-03-07).

[10] Huang, Z.-F.; Song, J.; Dou, S.; Li, X.; Wang, J.; Wang, X. Strategies to Break the Scaling Relation toward Enhanced Oxygen Electrocatalysis. *Matter* **2019**, *1* (6), 1494–1518.

[11] Crabtree, G. W.; Dresselhaus, M. S.; Buchanan, M. V. The Hydrogen Economy. *Phys. Today* **2004**, *57* (12), 39–44.

[12] Barreto, L.; Makihira, A.; Riahi, K. The Hydrogen Economy in the 21st Century: A Sustainable Development Scenario. *Int. J. Hydrogen Energy* **2003**, *28* (3), 267–284.

[13] Dawood, F.; Anda, M.; Shafiullah, G. M. Hydrogen Production for Energy: An Overview. *Int. J. Hydrogen Energy* **2020**, *45* (7), 3847–3869.

[14] El-Shafie, M.; Kambara, S.; Hayakawa, Y. Hydrogen Production Technologies Overview. *Proc. Inst. Mech. Eng. A: J. Power Energy* **2019**, *07* (01), 107–154.

[15] Satyapal, S.; Petrovic, J.; Read, C.; Thomas, G.; Ordaz, G. The U.S. Department of Energy's National Hydrogen Storage Project: Progress towards Meeting Hydrogen-Powered Vehicle Requirements. *Catal. Today* **2007**, *120* (3), 246–256.

[16] Pareek, A.; Dom, R.; Gupta, J.; Chandran, J.; Adepu, V.; Borse, P. H. Insights into Renewable Hydrogen Energy: Recent Advances and Prospects. *Mater. Sci. Energy Technol.* **2020**, *3*, 319–327.

[17] Kalamaras, C. M.; Efstathiou, A. M. Hydrogen Production Technologies: Current State and Future Developments. *Conf. Pap. Energy* **2013**, *2013*, 1–9.

[18] Osman, A. I.; Mehta, N.; Elgarahy, A. M.; Hefny, M.; Al-Hinai, A.; Al-Muhtaseb, A. H.; Rooney, D. W. Hydrogen Production, Storage, Utilisation and Environmental Impacts: A Review. *Environ. Chem. Lett.* **2022**, *20* (1), 153–188.

[19] Ratnakar, R. R.; Gupta, N.; Zhang, K.; van Doorne, C.; Fesmire, J.; Dindoruk, B.; Balakotaiah, V. Hydrogen Supply Chain and Challenges in Large-Scale LH2 Storage and Transportation. *Int. J. Hydrogen Energy* **2021**, *46* (47), 24149–24168.

[20] Li, S.; Kang, Q.; Baeyens, J.; Zhang, H. L.; Deng, Y. M. Hydrogen Production: State of Technology. *IOP Conf. Ser.: Earth Environ. Sci.* **2020**, *544* (1), 012011.

[21] Abdin, Z.; Zafaranloo, A.; Rafiee, A.; Mérida, W.; Lipiński, W.; Khalilpour, K. R. Hydrogen as an Energy Vector. *Renew. Sustain. Energy Rev.* **2020**, *120*, 109620.

[22] Maestre, V. M.; Ortiz, A.; Ortiz, I. Challenges and Prospects of Renewable Hydrogen-Based Strategies for Full Decarbonization of Stationary Power Applications. *Renew. Sustain. Energy Rev.* **2021**, *152*, 111628.

[23] Ariizumi, R. *Renewable hydrogen: Key to a new civilization - our world*. https://ourworld.unu.edu/en/renewable-hydrogen-key-to-a-new-civilization (accessed 2023-12-07).

[24] Shiva Kumar, S.; Lim, H. An Overview of Water Electrolysis Technologies for Green Hydrogen Production. *Energy Reports* **2022**, *8*, 13793–13813.

[25] Nikolaidis, P.; Poullikkas, A. A Comparative Overview of Hydrogen Production Processes. *Renew. Sustain. Energy Rev.* **2017**, *67*, 597–611.

[26] Ishaq, H.; Dincer, I.; Crawford, C. A Review on Hydrogen Production and Utilization: Challenges and

Opportunities. *Int. J. Hydrogen Energy* **2022**, *47* (62), 26238–26264.

[27] Ritchie, H. Cars, Planes, Trains: Where Do CO_2 Emissions from Transport Come From? *Our World in Data* **2020**.

[28] *Parliament pushes for cleaner cars on EU roads by 2030*. https://www.europarl.europa.eu/news/en/press-room/20180925IPR14306/parliament-pushes-for-cleaner-cars-on-eu-roads-by-2030 (accessed 2024-03-07).

[29] König, A.; Nicoletti, L.; Schröder, D.; Wolff, S.; Waclaw, A.; Lienkamp, M. An Overview of Parameter and Cost for Battery Electric Vehicles. *World Electr. Veh. J.* **2021**, *12* (1), 21.

[30] Cuma, M. U.; Koroglu, T. A Comprehensive Review on Estimation Strategies Used in Hybrid and Battery Electric Vehicles. *Renew. Sustain. Energy Rev.* **2015**, *42*, 517–531.

[31] Green, R. C.; Wang, L.; Alam, M. The Impact of Plug-in Hybrid Electric Vehicles on Distribution Networks: A Review and Outlook. *Renew. Sustain. Energy Rev.* **2011**, *15* (1), 544–553.

[32] Amjad, S.; Neelakrishnan, S.; Rudramoorthy, R. Review of Design Considerations and Technological Challenges for Successful Development and Deployment of Plug-in Hybrid Electric Vehicles. *Renew. Sustain. Energy Rev.* **2010**, *14* (3), 1104–1110.

[33] Manoharan, Y.; Hosseini, S. E.; Butler, B.; Alzhahrani, H.; Senior, B. T. F.; Ashuri, T.; Krohn, J. Hydrogen Fuel Cell Vehicles; Current Status and Future Prospect. *Appl. Sci.* **2019**, *9* (11), 2296.

[34] Aminudin, M. A.; Kamarudin, S. K.; Lim, B. H.; Majilan, E. H.; Masdar, M. S.; Shaari, N. An Overview: Current Progress on Hydrogen Fuel Cell Vehicles. *Int. J. Hydrogen Energy* **2023**, *48* (11), 4371–4388.

[35] *Global EV market share*. Statista. https://www.statista.com/statistics/1371599/global-ev-market-share/ (accessed 2024-03-07).

[36] Deng, J.; Bae, C.; Denlinger, A.; Miller, T. Electric Vehicles Batteries: Requirements and Challenges. *Joule* **2020**, *4* (3), 511–515.

[37] Manzetti, S.; Mariasiu, F. Electric Vehicle Battery Technologies: From Present State to Future Systems. *Renew. Sustain. Energy Rev.* **2015**, *51*, 1004–1012.

[38] *2024 Toyota Mirai*. https://www.toyota.com/mirai/ (accessed 2024-03-07).

[39] *Hydrogen Business*. https://global.honda/en/hydrogen/ (accessed 2024-03-07).

[40] *Hyundai hydrogen mobility*. Hyundai Hydrogen Mobility. https://hyundai-hm.com/en/ (accessed 2024-03-07).

[41] BMW. *Hydrogen fuel cell cars: what you need to know*. BMW. https://www.bmw.com/en/innovation/how-hydrogen-fuel-cell-cars-work.html (accessed 2024-03-07).

[42] Wang, Y.; Pang, Y.; Xu, H.; Martinez, A.; Chen, K. S. PEM Fuel Cell and Electrolysis Cell Technologies and Hydrogen Infrastructure Development – a Review. *Energy Environ. Sci.* **2022**, *15* (6), 2288–2328.

[43] Yang, B.; Zhang, R.; Shao, Z.; Zhang, C. The Economic Analysis for Hydrogen Production Cost towards Electrolyzer Technologies: Current and Future Competitiveness. *Int. J. Hydrogen Energy* **2023**, *48* (37), 13767–13779.

[44] Mayyas, A.; Mann, M. Emerging Manufacturing Technologies for Fuel Cells and Electrolyzers. *Procedia Manufacturing* **2019**, *33*, 508–515.

[45] İnci, M.; Büyük, M.; Demir, M. H.; İlbey, G. A Review and Research on Fuel Cell Electric Vehicles: Topologies, Power Electronic Converters, Energy Management Methods, Technical Challenges, Marketing and Future Aspects. *Renew. Sustain. Energy Rev.* **2021**, *137*, 110648.

[46] Luo, Y.; Wu, Y.; Li, B.; Mo, T.; Li, Y.; Feng, S.-P.; Qu, J.; Chu, P. K. Development and Application of Fuel Cells in the Automobile Industry. *J. Energy Storage* **2021**, *42*, 103124.

[47] *NEXO*. HYUNDAI MOTORS. https://www.hyundai.com/worldwide/en/eco/nexo/because-of-you (accessed 2024-03-07).

[48] *Hydrogen, green oil for heavy duty transport*. https://www.sia-partners.com/en/insights/publications/hydrogen-green-oil-heavy-duty-transport (accessed 2024-03-07).

[49] Kunz, E. *Hydrogen Buses Market Size to reach $49.2 billion globally by 2030: Latest report by vantage market research*. EIN Presswire. https://www.einnews.com/pr_news/683815396/hydrogen-buses-market-size-to-reach-49-2-billion-globally-by-2030-latest-report-by-vantage-market-research (accessed 2024-03-07).

[50] *Hydrogen aircraft market size worldwide*. Statista. https://www.statista.com/statistics/1366788/hydrogen-aircraft-worldwide-market-size/ (accessed 2024-03-07).

[51] Bandarenka, A. S.; Koper, M. T. M. Structural and Electronic Effects in Heterogeneous

Electrocatalysis: Toward a Rational Design of Electrocatalysts. *J. Catal.* **2013**, *308*, 11–24.

[52] Arán-Ais, R. M.; Gao, D.; Roldan Cuenya, B. Structure- and Electrolyte-Sensitivity in CO2 Electroreduction. *Acc. Chem. Res.* **2018**, *51* (11), 2906–2917.

[53] Colic, V.; Pohl, M. D.; Scieszka, D.; Bandarenka, A. S. Influence of the Electrolyte Composition on the Activity and Selectivity of Electrocatalytic Centers. *Catal. Today* **2016**, *262*, 24–35.

[54] Stamenkovic, V. R.; Mun, B. S.; Mayrhofer, K. J. J.; Ross, P. N.; Markovic, N. M. Effect of Surface Composition on Electronic Structure, Stability, and Electrocatalytic Properties of Pt-Transition Metal Alloys: Pt-Skin versus Pt-Skeleton Surfaces. *J. Am. Chem. Soc.* **2006**, *128* (27), 8813–8819.

[55] Elnagar, M. M.; Hermann, J. M.; Jacob, T.; Kibler, L. A. Tailoring the Electrode Surface Structure by Cathodic Corrosion in Alkali Metal Hydroxide Solution: Nanostructuring and Faceting of Au. *Curr. Opin. Electrochem.* **2021**, *27*, 100696.

[56] Antolini, E. Carbon Supports for Low-Temperature Fuel Cell Catalysts. *Appl. Catal. B* **2009**, *88* (1), 1–24.

[57] Lu, W.; Chung, D. D. L. Preparation of Conductive Carbons with High Surface Area. *Carbon* **2001**, *39* (1), 39–44.

[58] Wang, J. N.; Zhao, Y. Z.; Niu, J. J. Preparation of Graphitic Carbon with High Surface Area and Its Application as an Electrode Material for Fuel Cells. *J. Mater. Chem.* **2007**, *17* (21), 2251–2256.

[59] Lebedeva, N. P.; Koper, M. T. M.; Feliu, J. M.; Van Santen, R. A. Role of Crystalline Defects in Electrocatalysis: Mechanism and Kinetics of CO Adlayer Oxidation on Stepped Platinum Electrodes. *J. Phys. Chem. B* **2002**, *106* (50), 12938–12947.

[60] Jacob, T.; Muller, R. P.; Goddard, W. A. Chemisorption of Atomic Oxygen on Pt(111) from DFT Studies of Pt-Clusters. *J. Phys. Chem. B* **2003**, *107* (35), 9465–9476.

[61] Koper, M. T. M. Structure Sensitivity and Nanoscale Effects in Electrocatalysis. *Nanoscale* **2011**, *3* (5), 2054–2073.

[62] Madey, T. E.; Chen, W.; Wang, H.; Kaghazchi, P.; Jacob, T. Nanoscale Surface Chemistry over Faceted Substrates: Structure, Reactivity and Nanotemplates. *Chem. Soc. Rev.* **2008**, *37* (10), 2310–2327.

[63] Zagalskaya, A.; Alexandrov, V. Role of Defects in the Interplay between Adsorbate Evolving and Lattice Oxygen Mechanisms of the Oxygen Evolution Reaction in RuO2 and IrO2. *ACS Catal.* **2020**, *10* (6), 3650–3657.

[64] Calle-Vallejo, F.; Martínez, J. I.; García-Lastra, J. M.; Sautet, P.; Loffreda, D. Fast Prediction of Adsorption Properties for Platinum Nanocatalysts with Generalized Coordination Numbers. *Angew. Chem. Int. Ed Engl.* **2014**, *53* (32), 8316–8319.

[65] Fichtner, J.; Watzele, S.; Garlyyev, B.; Kluge, R. M.; Haimerl, F.; El-Sayed, H. A.; Li, W.-J.; Maillard, F. M.; Dubau, L.; Chattot, R.; Michalička, J.; Macak, J. M.; Wang, W.; Wang, D.; Gigl, T.; Hugenschmidt, C.; Bandarenka, A. S. Tailoring the Oxygen Reduction Activity of Pt Nanoparticles through Surface Defects: A Simple Top-Down Approach. *ACS Catal.* **2020**, *10* (5), 3131–3142.

[66] Wang, Y.-J.; Zhao, N.; Fang, B.; Li, H.; Bi, X. T.; Wang, H. Carbon-Supported Pt-Based Alloy Electrocatalysts for the Oxygen Reduction Reaction in Polymer Electrolyte Membrane Fuel Cells: Particle Size, Shape, and Composition Manipulation and Their Impact to Activity. *Chem. Rev.* **2015**, *115* (9), 3433–3467.

[67] Kirchhoff, B.; Jung, C.; Jónsson, H.; Fantauzzi, D.; Jacob, T. Simulations of the Electrochemical Oxidation of Pt Nanoparticles of Various Shapes. *J. Phys. Chem. C* **2022**, *126* (15), 6773–6781.

[68] Escudero-Escribano, M.; Malacrida, P.; Hansen, M. H.; Vej-Hansen, U. G.; Velázquez-Palenzuela, A.; Tripkovic, V.; Schiøtz, J.; Rossmeisl, J.; Stephens, I. E. L.; Chorkendorff, I. Tuning the Activity of Pt Alloy Electrocatalysts by Means of the Lanthanide Contraction. *Science* **2016**, *352* (6281), 73–76.

[69] Fichtner, J.; Garlyyev, B.; Watzele, S.; El-Sayed, H. A.; Schwämmlein, J. N.; Li, W.-J.; Maillard, F. M.; Dubau, L.; Michalička, J.; Macak, J. M.; Holleitner, A.; Bandarenka, A. S. Top-Down Synthesis of Nanostructured Platinum–Lanthanide Alloy Oxygen Reduction Reaction Catalysts: PtxPr/C as an Example. *ACS Appl. Mater. Interfaces* **2019**, *11* (5), 5129–5135.

[70] Ma, M.; Hansen, H. A.; Valenti, M.; Wang, Z.; Cao, A.; Dong, M.; Smith, W. A. Electrochemical Reduction of CO2 on Compositionally Variant Au-Pt Bimetallic Thin Films. *Nano Energy* **2017**, *42*, 51–57.

[71] Stamenkovic, V. R.; Mun, B. S.; Arenz, M.; Mayrhofer, K. J. J.; Lucas, C. A.; Wang, G.; Ross, P. N.; Markovic, N. M. Trends in Electrocatalysis on Extended and Nanoscale Pt-Bimetallic Alloy Surfaces. *Nat. Mater.* **2007**, *6* (3), 241–247.

[72] Jacob, T.; Goddard, W. A. Adsorption of Atomic H and O on the (111) Surface of Pt3Ni Alloys. *J. Phys. Chem. B* **2004**, *108* (24), 8311–8323.

[73] Jacob, T.; Goddard, W. A., 3rd. Water Formation on Pt and Pt-Based Alloys: A Theoretical Description of a Catalytic Reaction. *ChemPhysChem* **2006**, *7* (5), 992–1005.

[74] Nørskov, J. K.; Rossmeisl, J.; Logadottir, A.; Lindqvist, L.; Kitchin, J. R.; Bligaard, T.; Jónsson, H.

Origin of the Overpotential for Oxygen Reduction at a Fuel-Cell Cathode. *J. Phys. Chem. B* **2004**, *108* (46), 17886–17892.

[75] Kulkarni, A.; Siahrostami, S.; Patel, A.; Nørskov, J. K. Understanding Catalytic Activity Trends in the Oxygen Reduction Reaction. *Chem. Rev.* **2018**, *118* (5), 2302–2312.

[76] Hansen, H. A.; Rossmeisl, J.; Nørskov, J. K. Surface Pourbaix Diagrams and Oxygen Reduction Activity of Pt, Ag and Ni(111) Surfaces Studied by DFT. *Phys. Chem. Chem. Phys.* **2008**, *10* (25), 3722–3730.

[77] Karlberg, G. S.; Rossmeisl, J.; Nørskov, J. K. Estimations of Electric Field Effects on the Oxygen Reduction Reaction Based on the Density Functional Theory. *Phys. Chem. Chem. Phys.* **2007**, *9* (37), 5158–5161.

[78] Greeley, J.; Stephens, I. E. L.; Bondarenko, A. S.; Johansson, T. P.; Hansen, H. A.; Jaramillo, T. F.; Rossmeisl, J.; Chorkendorff, I.; Nørskov, J. K. Alloys of Platinum and Early Transition Metals as Oxygen Reduction Electrocatalysts. *Nat. Chem.* **2009**, *1* (7), 552–556.

[79] Jacob, T. The Mechanism of Forming H2O from H2 and O2 over a Pt Catalyst via Direct Oxygen Reduction. *Fuel Cells* **2006**, *6* (3-4), 159–181.

[80] Gao, W.; Keith, J. A.; Anton, J.; Jacob, T. Theoretical Elucidation of the Competitive Electro-Oxidation Mechanisms of Formic Acid on Pt(111). *J. Am. Chem. Soc.* **2010**, *132* (51), 18377–18385.

[81] Strmcnik, D.; Kodama, K.; van der Vliet, D.; Greeley, J.; Stamenkovic, V. R.; Marković, N. M. The Role of Non-Covalent Interactions in Electrocatalytic Fuel-Cell Reactions on Platinum. *Nat. Chem.* **2009**, *1* (6), 466–472.

[82] Rojas-Carbonell, S.; Artyushkova, K.; Serov, A.; Santoro, C.; Matanovic, I.; Atanassov, P. Effect of pH on the Activity of Platinum Group Metal-Free Catalysts in Oxygen Reduction Reaction. *ACS Catal.* **2018**, *8* (4), 3041–3053.

[83] Zamora Zeledón, J. A.; Kamat, G. A.; Gunasooriya, G. T. K. K.; Nørskov, J. K.; Stevens, M. B.; Jaramillo, T. F. Probing the Effects of Acid Electrolyte Anions on Electrocatalyst Activity and Selectivity for the Oxygen Reduction Reaction. *ChemElectroChem* **2021**, *8* (13), 2467–2478.

[84] Watzele, S. A. Methodological Aspects of In-Depth Electrochemical Characterization of Metal and Metal Oxide Electrocatalysts, Technische Universität München, **2020**.

[85] Watzele, S.; Fichtner, J.; Garlyyev, B.; Schwämmlein, J. N.; Bandarenka, A. S. On the Dominating Mechanism of the Hydrogen Evolution Reaction at Polycrystalline Pt Electrodes in Acidic Media. *ACS*

Catal. **2018**, *8* (10), 9456–9462.

[86] Garlyyev, B.; Xue, S.; Pohl, M. D.; Reinisch, D.; Bandarenka, A. S. Oxygen Electroreduction at High-Index Pt Electrodes in Alkaline Electrolytes: A Decisive Role of the Alkali Metal Cations. *ACS Omega* **2018**, *3* (11), 15325–15331.

[87] Suntivich, J.; Perry, E. E.; Gasteiger, H. A.; Shao-Horn, Y. The Influence of the Cation on the Oxygen Reduction and Evolution Activities of Oxide Surfaces in Alkaline Electrolyte. *Electrocatalysis* **2013**, *4* (1), 49–55.

[88] Kamat, G. A.; Zamora Zeledón, J. A.; Gunasooriya, G. T. K. K.; Dull, S. M.; Perryman, J. T.; Nørskov, J. K.; Stevens, M. B.; Jaramillo, T. F. Acid Anion Electrolyte Effects on Platinum for Oxygen and Hydrogen Electrocatalysis. *Commun Chem* **2022**, *5* (1), 20.

[89] Jin, W.; Du, H.; Zheng, S.; Xu, H.; Zhang, Y. Comparison of the Oxygen Reduction Reaction between NaOH and KOH Solutions on a Pt Electrode: The Electrolyte-Dependent Effect. *J. Phys. Chem. B* **2010**, *114* (19), 6542–6548.

[90] Huang, K.; Song, T.; Morales-Collazo, O.; Jia, H.; Brennecke, J. F. Enhancing Pt/C Catalysts for the Oxygen Reduction Reaction with Protic Ionic Liquids: The Effect of Anion Structure. *J. Electrochem. Soc.* **2017**, *164* (13), F1448.

[91] Ostwald, W. Catalysis. *Phys. Z.* **1901**, *3*, 313–322.

[92] Lu, G.-Q.; Wieckowski, A. Heterogeneous Electrocatalysis: A Core Field of Interfacial Science. *Curr. Opin. Colloid Interface Sci.* **2000**, *5* (1), 95–100.

[93] Ooka, H.; Huang, J.; Exner, K. S. The Sabatier Principle in Electrocatalysis: Basics, Limitations, and Extensions. *Front. Energy Res.* **2021**, *9*. https://doi.org/10.3389/fenrg.2021.654460.

[94] Hong, W. T.; Risch, M.; Stoerzinger, K. A.; Grimaud, A.; Suntivich, J.; Shao-Horn, Y. Toward the Rational Design of Non-Precious Transition Metal Oxides for Oxygen Electrocatalysis. *Energy Environ. Sci.* **2015**, *8* (5), 1404–1427.

[95] Neyerlin, K. C.; Gu, W.; Jorne, J.; Gasteiger, H. A. Study of the Exchange Current Density for the Hydrogen Oxidation and Evolution Reactions. *J. Electrochem. Soc.* **2007**, *154* (7), B631.

[96] Fukumoto, T.; Endo, N.; Natsukoshi, K.; Tachikawa, Y.; Harrington, G. F.; Lyth, S. M.; Matsuda, J.; Sasaki, K. Exchange Current Density of Reversible Solid Oxide Cell Electrodes. *Int. J. Hydrogen Energy* **2022**, *47* (37), 16626–16639.

[97] Jung, S.; McCrory, C. C. L.; Ferrer, I. M.; Peters, J. C.; Jaramillo, T. F. Benchmarking Nanoparticulate Metal Oxide Electrocatalysts for the Alkaline Water Oxidation Reaction. *J. Mater. Chem. A Mater. Energy Sustain.* **2016**, *4* (8), 3068–3076.

[98] McCrory, C. C. L.; Jung, S.; Peters, J. C.; Jaramillo, T. F. Benchmarking Heterogeneous Electrocatalysts for the Oxygen Evolution Reaction. *J. Am. Chem. Soc.* **2013**, *135* (45), 16977–16987.

[99] Anantharaj, S.; Kundu, S. Do the Evaluation Parameters Reflect Intrinsic Activity of Electrocatalysts in Electrochemical Water Splitting? *ACS Energy Lett.* **2019**, *4* (6), 1260–1264.

[100] Klingan, K.; Ringleb, F.; Zaharieva, I.; Heidkamp, J.; Chernev, P.; Gonzalez-Flores, D.; Risch, M.; Fischer, A.; Dau, H. Water Oxidation by Amorphous Cobalt-Based Oxides: Volume Activity and Proton Transfer to Electrolyte Bases. *ChemSusChem* **2014**, *7* (5), 1301–1310.

[101] Anantharaj, S.; Karthik, P. E.; Noda, S. The Significance of Properly Reporting Turnover Frequency in Electrocatalysis Research. *Angew. Chem. Int. Ed Engl.* **2021**, *60* (43), 23051–23067.

[102] Kozuch, S.; Martin, J. M. L. "Turning Over" Definitions in Catalytic Cycles. *ACS Catal.* **2012**, *2* (12), 2787–2794.

[103] De Vylder, A.; Lauwaert, J.; Van Auwenis, S.; De Clercq, J.; Thybaut, J. W. Catalyst Stability Assessment in a Lab-Scale Liquid-Solid $(LS)^2$ Plug-Flow Reactor. *Catalysts* **2019**, *9* (9), 755.

[104] Sachtler, W. M. H. The Second Rideal Lecture. What Makes a Catalyst Selective ? *Faraday Discuss. Chem. Soc.* **1981**, *72* (0), 7–31.

[105] Vogt, C.; Weckhuysen, B. M. The Concept of Active Site in Heterogeneous Catalysis. *Nat. Rev. Chem.* **2022**, *6* (2), 89–111.

[106] Langmuir, I. Part II.—"Heterogeneous Reactions". Chemical Reactions on Surfaces. *Trans. Faraday Soc.* **1922**, *17* (0), 607–620.

[107] Taylor, H. S. A Theory of the Catalytic Surface. *Proc. R. Soc. Lond. A Math. Phys. Sci.* **1925**, *108* (745), 105–111.

[108] Védrine, J. C. Revisiting Active Sites in Heterogeneous Catalysis: Their Structure and Their Dynamic Behaviour. *Appl. Catal. A* **2014**, *474*, 40–50.

[109] Sabatier, P. Hydrogénations and Déshydrogénations by Catalysis. *Ber. Dtsch. Chem. Ges.* **1911**, *44(3)*, 1984–2001.

[110] Calle-Vallejo, F.; Koper, M. T. M.; Bandarenka, A. S. Tailoring the Catalytic Activity of Electrodes

with Monolayer Amounts of Foreign Metals. *Chem. Soc. Rev.* **2013**, *42* (12), 5210–5230.

[111] Balandin, A. A. Modern State of the Multiplet Theor of Heterogeneous Catalysis. *Adv. Catal.* **1969**, *19*, 1–210.

[112] Jaksic, M. M. Volcano Plots along the Periodic Table, Their Causes and Consequences on Electrocatalysis for Hydrogen Electrode Reactions. *J. New Mater. Electrochem. Syst.* **2000**, *3* (2), 153–168.

[113] Zhang, M.; Zhang, K.; Ai, X.; Liang, X.; Zhang, Q.; Chen, H.; Zou, X. Theory-Guided Electrocatalyst Engineering: From Mechanism Analysis to Structural Design. *Chin. J. Catal.* **2022**, *43* (12), 2987–3018.

[114] Montoya, J. H.; Seitz, L. C.; Chakthranont, P.; Vojvodic, A.; Jaramillo, T. F.; Nørskov, J. K. Materials for Solar Fuels and Chemicals. *Nat. Mater.* **2016**, *16* (1), 70–81.

[115] Dourado, A. H. B. Electric Double Layer: The Good, the Bad, and the Beauty. *Electrochemistry* **2022**, *3* (4), 789–808.

[116] Schmickler, W. Double Layer Theory. *J. Solid State Electrochem.* **2020**, *24* (9), 2175–2176.

[117] Shin, S.-J.; Kim, D. H.; Bae, G.; Ringe, S.; Choi, H.; Lim, H.-K.; Choi, C. H.; Kim, H. On the Importance of the Electric Double Layer Structure in Aqueous Electrocatalysis. *Nat. Commun.* **2022**, *13* (1), 174.

[118] Helmholtz, H. Ueber Einige Gesetze Der Vertheilung Elektrischer Ströme in Körperlichen Leitern Mit Anwendung Auf Die Thierisch-elektrischen Versuche. *Ann. Phys.* **1853**, *165* (6), 211–233.

[119] Gouy, M. Sur La Constitution de La Charge électrique à La Surface D'un électrolyte. *J. Phys. Théor. Appl.* **1910**, *9* (1), 457–468.

[120] Chapman, D. L. LI. A Contribution to the Theory of Electrocapillarity. *The London, Edinburgh, and Dublin Philosophical Magazine and Journal of Science* **1913**, *25* (148), 475–481.

[121] Stern, O. Zur Theorie Der Elektrolytischen Doppelschicht. *Z. Elektrochem. Angew. Phys. Chem.* **1924**, *30* (21-22), 508–516.

[122] Grahame, D. C. The Electrical Double Layer and the Theory of Electrocapillarity. *Chem. Rev.* **1947**, *41* (3), 441–501.

[123] Haid, R. W. Methodology and Applications of Electrochemical Scanning Tunneling Microscopy for the Evaluation of Electrocatalysts under Reaction Conditions, Technische Universität München, **2022**.

[124] Bohra, D.; Chaudhry, J. H.; Burdyny, T.; Pidko, E. A.; Smith, W. A. Modeling the Electrical Double Layer to Understand the Reaction Environment in a CO 2 Electrocatalytic System. *Energy Environ. Sci.* **2019**, *12* (11), 3380–3389.

[125] Ji, H.; Zhao, X.; Qiao, Z.; Jung, J.; Zhu, Y.; Lu, Y.; Zhang, L. L.; MacDonald, A. H.; Ruoff, R. S. Capacitance of Carbon-Based Electrical Double-Layer Capacitors. *Nat. Commun.* **2014**, *5*, 3317.

[126] Memet, J. B.; Girault, P.; Sabot, R.; Compère, C.; Deslouis, C. Electrochemical Impedance Spectroscopy of a Free-Standing Oxide Film. *Electrochim. Acta* **2002**, *47* (7), 1043–1053.

[127] Braunwarth, L.; Jung, C.; Jacob, T. Potential-Dependent Pt(111)/Water Interface: Tackling the Challenge of a Consistent Treatment of Electrochemical Interfaces. *ChemPhysChem* **2023**, *24* (1), e202200336.

[128] Watzele, S. A.; Katzenmeier, L.; Sabawa, J. P.; Garlyyev, B.; Bandarenka, A. S. Temperature Dependences of the Double Layer Capacitance of Some Solid/liquid and Solid/solid Electrified Interfaces. An Experimental Study. *Electrochim. Acta* **2021**, *391*, 138969.

[129] Compton, R. G.; Banks, C. E. *Understanding Voltammetry (Third Edition)*; World Scientific, **2018**.

[130] Lasia, A. Advanced Electrochemistry. *Interfaces, thermodynamics, and electrochemical techniques* **2019**.

[131] Jerkiewicz, G. Standard and Reversible Hydrogen Electrodes: Theory, Design, Operation, and Applications. *ACS Catal.* **2020**, *10* (15), 8409–8417.

[132] Ranjandish, R.; Jang, T.; Schmid, A. An Active Charge Balancing Method Suitable for Integration in the Output-Stage of Electrical Neural Stimulators. *Analog Integr. Circuits Signal Process.* **2022**, *111* (1), 89–102.

[133] Bard, Allen J.; Faulkner, Larry R. Fundamentals and Applications. *Electrochem. Methods* **2001**, *2* (482), 580–632.

[134] Abd El Monem, A. A.; Azmy, A. M.; Mahmoud, S. A. Effect of Process Parameters on the Dynamic Behavior of Polymer Electrolyte Membrane Fuel Cells for Electric Vehicle Applications. *Ain Shams Eng. J.* **2014**, *5* (1), 75–84.

[135] Olabi, A. G.; Wilberforce, T.; Alanazi, A.; Vichare, P.; Sayed, E. T.; Maghrabie, H. M.; Elsaid, K.; Abdelkareem, M. A. Novel Trends in Proton Exchange Membrane Fuel Cells. *Energies* **2022**, *15* (14), 4949.

[136] Kühl, S.; Strasser, P. Oxygen Electrocatalysis on Dealloyed Pt Nanocatalysts. *Top. Catal.* **2016**, *59* (17), 1628–1637.

[137] Chanpeng, W.; Khunatorn, Y. The Effect of the Input Load Current Changed to a 1.2kW PEMFC Performance. *Energy Procedia* **2011**, *9*, 316–325.

[138] Shiva Kumar, S.; Himabindu, V. Hydrogen Production by PEM Water Electrolysis – A Review. *Mater. Sci. Energy Technol.* **2019**, *2* (3), 442–454.

[139] Hren, M.; Božič, M.; Fakin, D.; Kleinschek, K. S.; Gorgieva, S. Alkaline Membrane Fuel Cells: Anion Exchange Membranes and Fuels. *Sustain. Energy Fuels* **2021**, *5* (3), 604–637.

[140] Carmo, M.; Fritz, D. L.; Mergel, J.; Stolten, D. A Comprehensive Review on PEM Water Electrolysis. *Int. J. Hydrogen Energy* **2013**, *38* (12), 4901–4934.

[141] Exner, K. S. On the Optimum Binding Energy for the Hydrogen Evolution Reaction: How Do Experiments Contribute? *Electrochem. Sci. Adv.* **2022**, *2* (4). e2100111.

[142] Bao, F.; Kemppainen, E.; Dorbandt, I.; Bors, R.; Xi, F.; Schlatmann, R.; Krol, R.; Calnan, S. Understanding the Hydrogen Evolution Reaction Kinetics of Electrodeposited Nickel-molybdenum in Acidic, Near-neutral, and Alkaline Conditions. *ChemElectroChem* **2021**, *8* (1), 195–208.

[143] Cheng, T.; Wang, L.; Merinov, B. V.; Goddard, W. A., 3rd. Explanation of Dramatic pH-Dependence of Hydrogen Binding on Noble Metal Electrode: Greatly Weakened Water Adsorption at High pH. *J. Am. Chem. Soc.* **2018**, *140* (25), 7787–7790.

[144] Ďurovič, M.; Hnát, J.; Bouzek, K. Electrocatalysts for the Hydrogen Evolution Reaction in Alkaline and Neutral Media. A Comparative Review. *J. Power Sources* **2021**, *493*, 229708.

[145] Wendt, H.; Spinacé, E. V.; Oliveira Neto, A.; Linardi, M. Electrocatalysis and Electrocatalysts for Low Temperature Fuel Cells: Fundamentals, State of the Art, Research and Development. *Quím. Nova* **2005**, *28* (6), 1066–1075.

[146] Wei, C.; Rao, R. R.; Peng, J.; Huang, B.; Stephens, I. E. L.; Risch, M.; Xu, Z. J.; Shao-Horn, Y. Recommended Practices and Benchmark Activity for Hydrogen and Oxygen Electrocatalysis in Water Splitting and Fuel Cells. *Adv. Mater.* **2019**, *31* (31), e1806296.

[147] Yin, Y.; Han, J.; Zhang, Y.; Zhang, X.; Xu, P.; Yuan, Q.; Samad, L.; Wang, X.; Wang, Y.; Zhang, Z.; Zhang, P.; Cao, X.; Song, B.; Jin, S. Contributions of Phase, Sulfur Vacancies, and Edges to the Hydrogen Evolution Reaction Catalytic Activity of Porous Molybdenum Disulfide Nanosheets. *J. Am. Chem. Soc.*

2016, *138* (25), 7965–7972.

[148] Jaramillo, T. F.; Jørgensen, K. P.; Bonde, J.; Nielsen, J. H.; Horch, S.; Chorkendorff, I. Identification of Active Edge Sites for Electrochemical H_2 Evolution from MoS_2 Nanocatalysts. *Science* **2007**, *317* (5834), 100–102.

[149] Kibsgaard, J.; Tsai, C.; Chan, K.; Benck, J. D.; Nørskov, J. K.; Abild-Pedersen, F.; Jaramillo, T. F. Designing an Improved Transition Metal Phosphide Catalyst for Hydrogen Evolution Using Experimental and Theoretical Trends. *Energy Environ. Sci.* **2015**, *8* (10), 3022–3029.

[150] Xue, S.; Garlyyev, B.; Watzele, S.; Liang, Y.; Fichtner, J.; Pohl, M. D.; Bandarenka, A. S. Influence of Alkali Metal Cations on the Hydrogen Evolution Reaction Activity of Pt, Ir, Au, and Ag Electrodes in Alkaline Electrolytes. *ChemElectroChem* **2018**, *5* (17), 2326–2329.

[151] Taji, Y.; Zagalskaya, A.; Evazzade, I.; Watzele, S.; Song, K.-T.; Xue, S.; Schott, C.; Garlyyev, B.; Alexandrov, V.; Gubanova, E.; Bandarenka, A. S. Alkali Metal Cations Change the Hydrogen Evolution Reaction Mechanisms at Pt Electrodes in Alkaline Media. *Nano Mater. Sci.* **2022**. https://doi.org/10.1016/j.nanoms.2022.09.003

[152] Zheng, J.; Zhou, S.; Gu, S.; Xu, B.; Yan, Y. Size-Dependent Hydrogen Oxidation and Evolution Activities on Supported Palladium Nanoparticles in Acid and Base. *J. Electrochem. Soc.* **2016**, *163* (6), F499.

[153] Gasteiger, H. A.; Kocha, S. S.; Sompalli, B.; Wagner, F. T. Activity Benchmarks and Requirements for Pt, Pt-Alloy, and Non-Pt Oxygen Reduction Catalysts for PEMFCs. *Appl. Catal. B* **2005**, *56* (1), 9–35.

[154] Neyerlin, K. C.; Gu, W.; Jorne, J.; Gasteiger, H. A. Study of the Exchange Current Density for the Hydrogen Oxidation and Evolution Reactions. *J. Electrochem. Soc.* **2007**, *154* (7), B631.

[155] Wee, J.-H.; Lee, K.-Y. Overview of the Development of CO-Tolerant Anode Electrocatalysts for Proton-Exchange Membrane Fuel Cells. *J. Power Sources* **2006**, *157* (1), 128–135.

[156] Liu, Y.; Duan, Z.; Henkelman, G. Computational Design of CO-Tolerant Pt3M Anode Electrocatalysts for Proton-Exchange Membrane Fuel Cells. *Phys. Chem. Chem. Phys.* **2019**, *21* (7), 4046–4052.

[157] Liu, P.; Nørskov, J. K. Kinetics of the Anode Processes in PEM Fuel Cells - the Promoting Effect of Ru in PtRu Anodes. *Fuel Cells* **2001**, *1* (3-4), 192–201.

[158] Gasteiger, H. A.; Markovic, N. M.; Ross, P. N., Jr. H2 and CO Electrooxidation on Well-Characterized Pt, Ru, and Pt-Ru. 2. Rotating Disk Electrode Studies of CO/H2 Mixtures at 62.degree.C. *J. Phys. Chem.*

1995, *99* (45), 16757–16767.

[159] Mukerjee, S.; Urian, R. C.; Lee, S. J.; Ticianelli, E. A.; McBreen, J. Electrocatalysis of CO Tolerance by Carbon-Supported PtMo Electrocatalysts in PEMFCs. *J. Electrochem. Soc.* **2004**, *151* (7), A1094.

[160] Stamenković, V. R.; Arenz, M.; Lucas, C. A.; Gallagher, M. E.; Ross, P. N.; Marković, N. M. Surface Chemistry on Bimetallic Alloy Surfaces: Adsorption of Anions and Oxidation of CO on Pt3Sn(111). *J. Am. Chem. Soc.* **2003**, *125* (9), 2736–2745.

[161] Su, L.; Gong, D.; Jin, Y.; Wu, D.; Luo, W. Recent Advances in Alkaline Hydrogen Oxidation Reaction. *J. Energy Chem.* **2022**, *66*, 107–122.

[162] Durst, J.; Siebel, A.; Simon, C.; Hasché, F.; Herranz, J.; Gasteiger, H. A. New Insights into the Electrochemical Hydrogen Oxidation and Evolution Reaction Mechanism. *Energy Environ. Sci.* **2014**, *7* (7), 2255–2260.

[163] Wagner, F. T.; Lakshmanan, B.; Mathias, M. F. Electrochemistry and the Future of the Automobile. *J. Phys. Chem. Lett.* **2010**, *1* (14), 2204–2219.

[164] Zhao, J.; Lian, J.; Zhao, Z.; Wang, X.; Zhang, J. A Review of In-Situ Techniques for Probing Active Sites and Mechanisms of Electrocatalytic Oxygen Reduction Reactions. *Nano-Micro Lett.* **2022**, *15* (1), 19.

[165] Borup, R.; Meyers, J.; Pivovar, B.; Kim, Y. S.; Mukundan, R.; Garland, N.; Myers, D.; Wilson, M.; Garzon, F.; Wood, D.; Zelenay, P.; More, K.; Stroh, K.; Zawodzinski, T.; Boncella, J.; McGrath, J. E.; Inaba, M.; Miyatake, K.; Hori, M.; Ota, K.; Ogumi, Z.; Miyata, S.; Nishikata, A.; Siroma, Z.; Uchimoto, Y.; Yasuda, K.; Kimijima, K.-I.; Iwashita, N. Scientific Aspects of Polymer Electrolyte Fuel Cell Durability and Degradation. *Chem. Rev.* **2007**, *107* (10), 3904–3951.

[166] Siahrostami, S.; Verdaguer-Casadevall, A.; Karamad, M.; Deiana, D.; Malacrida, P.; Wickman, B.; Escudero-Escribano, M.; Paoli, E. A.; Frydendal, R.; Hansen, T. W.; Chorkendorff, I.; Stephens, I. E. L. S.; Rossmeisl, J. Enabling Direct H2O2 Production through Rational Electrocatalyst Design. *Nat. Mater.* **2013**, *12* (12), 1137–1143.

[167] Ramaswamy, N.; Mukerjee, S. Fundamental Mechanistic Understanding of Electrocatalysis of Oxygen Reduction on Pt and Non-Pt Surfaces: Acid versus Alkaline Media. *Adv. Phys. Chem.* **2012**, *2012* (1), 491604.

[168] Keith, J. A.; Jerkiewicz, G.; Jacob, T. Theoretical Investigations of the Oxygen Reduction Reaction on Pt(111). *ChemPhysChem* **2010**, 11 (13), 2779–2794.

[169] Keith, J. A.; Jacob, T. Theoretical Studies of Potential-Dependent and Competing Mechanisms of the Electrocatalytic Oxygen Reduction Reaction on Pt(111). *Angew. Chem. Int. Ed Engl.* **2010**, *49* (49), 9521–9525.

[170] Fantauzzi, D.; Calderón, S. K.; Mueller, J.; Grabau, M.; Papp, C.; Steinrück, H.; Senftle, T.; van Duin, A. V.; Jacob, T. Growth of Stable Surface Oxides on Pt(111) at near-Ambient Pressures. *Angew. Chem. Int. Ed Engl.* **2017**, *56* (10), 2594–2598.

[171] Kirchhoff, B.; Braunwarth, L.; Jung, C.; Jónsson, H.; Fantauzzi, D.; Jacob, T. Simulations of the Oxidation and Degradation of Platinum Electrocatalysts. *Small* **2020**, *16* (5), 1905159.

[172] Jacob, T. Theoretical Investigations on the Potential-Induced Formation of Pt-Oxide Surfaces. *J. Electroanal. Chem.* **2007**, *607* (1), 158–166.

[173] Calle-Vallejo, F. The ABC of Generalized Coordination Numbers and Their Use as a Descriptor in Electrocatalysis. *Adv. Sci.* **2023**, *10* (20), e2207644.

[174] Calle-Vallejo, F.; Pohl, M. D.; Reinisch, D.; Loffreda, D.; Sautet, P.; Bandarenka, A. S. Why Conclusions from Platinum Model Surfaces Do Not Necessarily Lead to Enhanced Nanoparticle Catalysts for the Oxygen Reduction Reaction. *Chem. Sci.* **2017**, *8* (3), 2283–2289.

[175] Yan, Z.; Wang, M.; Liu, J.; Liu, R.; Zhao, J. Glycerol-Stabilized NaBH4 Reduction at Room-Temperature for the Synthesis of a Carbon-Supported PtxFe Alloy with Superior Oxygen Reduction Activity for a Microbial Fuel Cell. *Electrochim. Acta* **2014**, *141*, 331–339.

[176] Kluge, R. M.; Haid, R. W.; Riss, A.; Bao, Y.; Seufert, K.; Schmidt, T. O.; Watzele, S. A.; Barth, J. V.; Allegretti, F.; Auwärter, W.; Calle-Vallejo, F.; Bandarenka, A. S. A Trade-off between Ligand and Strain Effects Optimizes the Oxygen Reduction Activity of Pt Alloys. *Energy Environ. Sci.* **2022**, *15* (12), 5181–5191.

[177] Liu, M.; Zhao, Z.; Duan, X.; Huang, Y. Nanoscale Structure Design for High-Performance Pt-Based ORR Catalysts. *Adv. Mater.* **2019**, *31* (6), 1802234.

[178] Favry, E.; Wang, D.; Fantauzzi, D.; Anton, J.; Su, D. S.; Jacob, T.; Alonso-Vante, N. Synthesis, Electrochemical Characterization and Molecular Dynamics Studies of Surface Segregation of Platinum Nano-Alloy Electrocatalysts. *Phys. Chem. Chem. Phys.* **2011**, *13* (20), 9201–9208.

[179] Čolić, V.; Bandarenka, A. S. Pt Alloy Electrocatalysts for the Oxygen Reduction Reaction: From Model Surfaces to Nanostructured Systems. *ACS Catal.* **2016**, *6* (8), 5378–5385.

[180] Kitchin, J. R.; Nørskov, J. K.; Barteau, M. A.; Chen, J. G. Role of Strain and Ligand Effects in the

Modification of the Electronic and Chemical Properties of Bimetallic Surfaces. *Phys. Rev. Lett.* **2004**, *93* (15), 156801.

[181] Deng, Z.; Pang, W.; Gong, M.; Jin, Z.; Wang, X. Revealing the Role of Mo Doping in Promoting Oxygen Reduction Reaction Performance of Pt3Co Nanowires. *J. Energy Chem.* **2022**, *66*, 16–23.

[182] Mueller, J. E.; Krtil, P.; Kibler, L. A.; Jacob, T. Bimetallic Alloys in Action: Dynamic Atomistic Motifs for Electrochemistry and Catalysis. *Phys. Chem. Chem. Phys.* **2014**, *16* (29), 15029–15042.

[183] Suen, N.-T.; Hung, S.-F.; Quan, Q.; Zhang, N.; Xu, Y.-J.; Chen, H. M. Electrocatalysis for the Oxygen Evolution Reaction: Recent Development and Future Perspectives. *Chem. Soc. Rev.* **2017**, *46* (2), 337–365.

[184] Seh, Z. W.; Kibsgaard, J.; Dickens, C. F.; Chorkendorff, I.; Nørskov, J. K.; Jaramillo, T. F. Combining Theory and Experiment in Electrocatalysis: Insights into Materials Design. *Science* **2017**, *355* (6321).

[185] Damjanović, A.; Birss, V.; Boudreaux, D. Electron Transfer through Thin Anodic Oxide Films during the Oxygen Evolution Reactions at Pt Electrodes I. Acid Solutions. *J. Electrochem. Soc.* **1991**, *138*, 2549–2555.

[186] Reier, T.; Nong, H. N.; Teschner, D.; Schlögl, R.; Strasser, P. Electrocatalytic Oxygen Evolution Reaction in Acidic Environments - Reaction Mechanisms and Catalysts. *Adv. Energy Mater.* **2017**, *7* (1), 1601275.

[187] Sun, H.; Xu, X.; Song, Y.; Zhou, W.; Shao, Z. Designing High-valence Metal Sites for Electrochemical Water Splitting. *Adv. Funct. Mater.* **2021**, *31* (16), 2009779.

[188] Guerrini, E.; Chen, H.; Trasatti, S. Oxygen Evolution on Aged IrOx/Ti Electrodes in Alkaline Solutions. *J. Solid State Electrochem.* **2007**, *11* (7), 939–945.

[189] McCrory, C. C. L.; Jung, S.; Ferrer, I. M.; Chatman, S. M.; Peters, J. C.; Jaramillo, T. F. Benchmarking Hydrogen Evolving Reaction and Oxygen Evolving Reaction Electrocatalysts for Solar Water Splitting Devices. *J. Am. Chem. Soc.* **2015**, *137* (13), 4347–4357.

[190] Zhang, B.; Zheng, X.; Voznyy, O.; Comin, R.; Bajdich, M.; García-Melchor, M.; Han, L.; Xu, J.; Liu, M.; Zheng, L.; García de Arquer, F. P.; Dinh, C. T.; Fan, F.; Yuan, M.; Yassitepe, E.; Chen, N.; Regier, T.; Liu, P.; Li, Y.; De Luna, P.; Janmohamed, A.; Xin, H. L.; Yang, H.; Vojvodic, A.; Sargent, E. H. Homogeneously Dispersed Multimetal Oxygen-Evolving Catalysts. *Science* **2016**, *352* (6283), 333–337.

[191] Ashok, A.; Kumar, A.; Bhosale, R. R.; Almomani, F.; Malik, S. S.; Suslov, S.; Tarlochan, F. Combustion Synthesis of Bifunctional LaMO3 (M=Cr, Mn, Fe, Co, Ni) Perovskites for Oxygen

Reduction and Oxygen Evolution Reaction in Alkaline Media. *J. Electroanal. Chem.* **2018**, *809*, 22–30.

[192] Pandey, A.; Dalal, S.; Dutta, S.; Dixit, A. Structural Characterization of Polycrystalline Thin Films by X-Ray Diffraction Techniques. *J. Mater. Sci.: Mater. Electron.* **2021**, *32* (2), 1341–1368.

[193] Dolabella, S.; Borzì, A.; Dommann, A.; Neels, A. Lattice Strain and Defects Analysis in Nanostructured Semiconductor Materials and Devices by High-Resolution X-Ray Diffraction: Theoretical and Practical Aspects. *Small Methods* **2022**, *6* (2), 2100932.

[194] Bunaciu, A. A.; Udriştioiu, E. G.; Aboul-Enein, H. Y. X-Ray Diffraction: Instrumentation and Applications. *Crit. Rev. Anal. Chem.* **2015**, *45* (4), 289–299.

[195] Sharma, R.; Bisen, D. P.; Shukla, U.; Sharma, B. G. X-Ray Diffraction: A Powerful Method of Characterizing Nanomaterials. *Recent Res. Sci. Technol.* **2012**, *4* (8), 77–79.

[196] Ali, A.; Chiang, Y. W.; Santos, R. M. X-Ray Diffraction Techniques for Mineral Characterization: A Review for Engineers of the Fundamentals, Applications, and Research Directions. *Minerals* **2022**, *12* (2), 205.

[197] Andrade, J. D. X-Ray Photoelectron Spectroscopy (XPS). *Surface and Interfacial Aspects of Biomedical Polymers: Volume 1 Surface Chemistry and Physics* **1985**, 105–195.

[198] Krishna, D. N. G.; Philip, J. Review on Surface-Characterization Applications of X-Ray Photoelectron Spectroscopy (XPS): Recent Developments and Challenges. *Appl. Surf. Sci. Adv.* **2022**, *12*, 100332.

[199] Teterin, Y. A.; Teterin, A. Y. Structure of X-Ray Photoelectron Spectra of Lanthanide Compounds. *Russ. Chem. Rev.* **2002**, *71* (5), 347–381.

[200] Lefebvre, J.; Galli, F.; Bianchi, C. L.; Patience, G. S.; Boffito, D. C. Experimental Methods in Chemical Engineering: X-ray Photoelectron spectroscopy-XPS. *Can. J. Chem. Eng.* **2019**, *97* (10), 2588–2593.

[201] Greczynski, G.; Hultman, L. X-Ray Photoelectron Spectroscopy: Towards Reliable Binding Energy Referencing. *Prog. Mater Sci.* **2020**, *107*, 100591.

[202] Palmberg, P. W. Quantitative Auger Electron Spectroscopy Using Elemental Sensitivity Factors. *J. Vac. Sci. Technol.* **1976**, *13* (1), 214–218.

[203] Greczynski, G.; Hultman, L. A Step-by-Step Guide to Perform X-Ray Photoelectron Spectroscopy. *J. Appl. Phys.* **2022**, *132* (1), 011101.

[204] Elgrishi, N.; Rountree, K. J.; McCarthy, B. D.; Rountree, E. S.; Eisenhart, T. T.; Dempsey, J. L. A Practical Beginner's Guide to Cyclic Voltammetry. *J. Chem. Educ.* **2018**, *95* (2), 197–206.

[205] Costentin, C.; Fortage, J.; Collomb, M.-N. Electrophotocatalysis: Cyclic Voltammetry as an Analytical Tool. *J. Phys. Chem. Lett.* **2020**, *11* (15), 6097–6104.

[206] Heinze, J. Cyclic Voltammetry—"electrochemical Spectroscopy". New Analytical Methods (25). *Angew. Chem. Int. Ed Engl.* **1984**, *23* (11), 831–847.

[207] Wang, H.; Pilon, L. Physical Interpretation of Cyclic Voltammetry for Measuring Electric Double Layer Capacitances. *Electrochim. Acta* **2012**, *64*, 130–139.

[208] Morales, D. M.; Risch, M. Seven Steps to Reliable Cyclic Voltammetry Measurements for the Determination of Double Layer Capacitance. *J. Phys. Energy* **2021**, *3* (3), 034013.

[209] Gharbi, O.; Tran, M. T. T.; Tribollet, B.; Turmine, M.; Vivier, V. Revisiting Cyclic Voltammetry and Electrochemical Impedance Spectroscopy Analysis for Capacitance Measurements. *Electrochim. Acta* **2020**, *343*, 136109.

[210] Li, W.; Lane, A. M. Resolving the HUPD and HOPD by DEMS to Determine the ECSA of Pt Electrodes in PEM Fuel Cells. *Electrochem. Commun.* **2011**, *13* (9), 913–916.

[211] Lohmann-Richters, F. P.; Abel, B.; Varga, Á. In Situ Determination of the Electrochemically Active Platinum Surface Area: Key to Improvement of Solid Acid Fuel Cells. *J. Mater. Chem. A* **2018**, *6* (6), 2700–2707.

[212] Rudi, S.; Cui, C.; Gan, L.; Strasser, P. Comparative Study of the Electrocatalytically Active Surface Areas (ECSAs) of Pt Alloy Nanoparticles Evaluated by Hupd and CO-Stripping Voltammetry. *Electrocatalysis* **2014**, *5* (4), 408–418.

[213] Bandarenka, A. S. Exploring the Interfaces between Metal Electrodes and Aqueous Electrolytes with Electrochemical Impedance Spectroscopy. *Analyst* **2013**, *138* (19), 5540–5554.

[214] Magar, H. S.; Hassan, R. Y. A.; Mulchandani, A. Electrochemical Impedance Spectroscopy (EIS): Principles, Construction, and Biosensing Applications. *Sensors* **2021**, *21* (19), 6578.

[215] Lazanas, A. C.; Prodromidis, M. I. Electrochemical Impedance Spectroscopy-A Tutorial. *ACS Meas. Sci. Au* **2023**, *3* (3), 162–193.

[216] Bandarenka, A. S.; Eckhard, K.; Maljusch, A.; Schuhmann, W. Localized Electrochemical Impedance Spectroscopy: Visualization of Spatial Distributions of the Key Parameters Describing Solid/liquid

Interfaces. *Anal. Chem.* **2013**, *85* (4), 2443–2448.

[217] Chang, B.-Y.; Park, S.-M. Electrochemical Impedance Spectroscopy. *Annu. Rev. Anal. Chem.* **2010**, *3*, 207–229.

[218] Wang, S.; Zhang, J.; Gharbi, O.; Vivier, V.; Gao, M.; Orazem, M. E. Electrochemical Impedance Spectroscopy. *Nat. Rev. Methods Primers* **2021**, *1* (1), 1–21.

[219] Vadhva, P.; Hu, J.; Johnson, M. J.; Stocker, R.; Braglia, M.; Brett, D. J. L.; Rettie, A. J. E. Electrochemical Impedance Spectroscopy for All-solid-state Batteries: Theory, Methods and Future Outlook. *ChemElectroChem* **2021**, *8* (11), 1930–1947.

[220] Mei, B.-A.; Lau, J.; Lin, T.; Tolbert, S. H.; Dunn, B. S.; Pilon, L. Physical Interpretations of Electrochemical Impedance Spectroscopy of Redox Active Electrodes for Electrical Energy Storage. *J. Phys. Chem. C* **2018**, *122* (43), 24499–24511.

[221] Padha, B.; Verma, S.; Mahajan, P.; Arya, S. Electrochemical Impedance Spectroscopy (EIS) Performance Analysis and Challenges in Fuel Cell Applications. *J. Electrochem. Sci. Technol.* **2022**, *13* (2), 167–176.

[222] Wang, H.; Gaillard, A.; Hissel, D. A Review of DC/DC Converter-Based Electrochemical Impedance Spectroscopy for Fuel Cell Electric Vehicles. *Renew. Energy* **2019**, *141*, 124–138.

[223] Leever, B. J.; Bailey, C. A.; Marks, T. J.; Hersam, M. C.; Durstock, M. F. In Situ Characterization of Lifetime and Morphology in Operating Bulk Heterojunction Organic Photovoltaic Devices by Impedance Spectroscopy. *Adv. Energy Mater.* **2012**, *2* (1), 120–128.

[224] Haimerl, F.; Sabawa, J. P.; Dao, T. A.; Bandarenka, A. S. Spatially Resolved Electrochemical Impedance Spectroscopy of Automotive PEM Fuel Cells. *ChemElectroChem* **2022**, *9* (10), e202200069.

[225] Gaddam, R. R.; Katzenmeier, L.; Lamprecht, X.; Bandarenka, A. S. Review on Physical Impedance Models in Modern Battery Research. *Phys. Chem. Chem. Phys.* **2021**, *23* (23), 12926–12944.

[226] Lazanas, A. C.; Prodromidis, M. I. Electrochemical Impedance Spectroscopy-A Tutorial. *ACS Meas. Sci. Au* **2023**, *3* (3), 162–193.

[227] Lasia, A. Electrochemical Impedance Spectroscopy and Its Applications. In *Modern Aspects of Electrochemistry*; Conway, B. E., Bockris, J. O., White, R. E., Eds.; Springer US: Boston, MA, **2002**; pp 143–248.

[228] Macdonald, J. R. Impedance Spectroscopy: Emphasizing Solid Materials and Systems. *Appl. Opt.*

1989, *28* (6), 1083.

[229] Agarwal, P.; Orazem, M. E.; Garcia-Rubio, L. H. Measurement Models for Electrochemical Impedance Spectroscopy: I. Demonstration of Applicability. *J. Electrochem. Soc.* **1992**, *139* (7), 1917.

[230] Urquidi-Macdonald, M.; Real, S.; Macdonald, D. D. Applications of Kramers—Kronig Transforms in the Analysis of Electrochemical Impedance data—III. Stability and Linearity. *Electrochim. Acta* **1990**, *35* (10), 1559–1566.

[231] Orazem, M. E.; Esteban, J. M.; Moghissi, O. C. Practical Applications of the Kramers-Kronig Relations. *Corrosion* **1991**, *47* (4), 248–259.

[232] Bayer, M. H.; Schneider, I. A. Application of the Kramers Kronig Relations to Locally Resolved Impedance Data of Polymer Electrolyte Fuel Cells. *J. Electroanal. Chem.* **2013**, *689*, 42–45.

[233] Urquidi-Macdonald, M.; Real, S.; Macdonald, D. D. Application of Kramers-Kronig Transforms in the Analysis of Electrochemical Impedance Data: II. Transformations in the Complex Plane. *J. Electrochem. Soc.* **1986**, *133* (10), 2018.

[234] VanderNoot, T. J. Hilbert Transformation of Immittance Data Using the Fast Fourier Transform. *J. Electroanal. Chem.* **1992**, *322* (1), 9–24.

[235] Boukamp, B. A. Electrochemical Impedance Spectroscopy in Solid State Ionics: Recent Advances. *Solid State Ionics* **2004**, *169* (1), 65–73.

[236] Boukamp, B. A. A Linear Kronig-Kramers Transform Test for Immittance Data Validation. *J. Electrochem. Soc.* **1995**, *142* (6), 1885.

[237] Sadkowski, A. Unusual Electrochemical Immittance Spectra with Negative Resistance and Their Validation by Kramers–Kronig Transformation. *Solid State Ionics* **2005**, *176* (25), 1987–1996.

[238] Berkes, B. B.; Bandarenka, A. S.; Inzelt, G. Electropolymerization: Further Insight into the Formation of Conducting Polyindole Thin Films. *J. Phys. Chem. C* **2015**, *119* (4), 1996–2003.

[239] Dolin, P.; Ershler, B. The Kinetics of Discharge and Ionization of Hydrogen Adsorbed at Pt-Electrode. *Acta Physicochim. URSS* **1940**, *13*, 747.

[240] Randles, J. E. B. Kinetics of Rapid Electrode Reactions. *Discuss. Faraday Soc.* **1947**, *1*, 11.

[241] Jomori, S.; Nonoyama, N.; Yoshida, T. Analysis and Modeling of PEMFC Degradation: Effect on Oxygen Transport. *J. Power Sources* **2012**, *215*, 18–27.

[242] Moniri, S.; Van Cleve, T.; Linic, S. Pitfalls and Best Practices in Measurements of the Electrochemical Surface Area of Platinum-Based Nanostructured Electro-Catalysts. *J. Catal.* **2017**, *345*, 1–10.

[243] Reid, O. 'rian; Saleh, F. S.; Easton, E. B. Determining Electrochemically Active Surface Area in PEM Fuel Cell Electrodes with Electrochemical Impedance Spectroscopy and Its Application to Catalyst Durability. *Electrochim. Acta* **2013**, *114*, 278–284.

[244] Schenk, A.; Grimmer, C.; Perchthaler, M.; Weinberger, S.; Pichler, B.; Heinzl, C.; Scheu, C.; Mautner, F.-A.; Bitschnau, B.; Hacker, V. Platinum–cobalt Catalysts for the Oxygen Reduction Reaction in High Temperature Proton Exchange Membrane Fuel Cells – Long Term Behavior under Ex-Situ and in-Situ Conditions. *J. Power Sources* **2014**, *266*, 313–322.

[245] Zhao, S.; Yu, H.; Maric, R.; Danilovic, N.; Capuano, C. B.; Ayers, K. E.; Mustain, W. E. Calculating the Electrochemically Active Surface Area of Iridium Oxide in Operating Proton Exchange Membrane Electrolyzers. *J. Electrochem. Soc.* **2015**, *162* (12), F1292.

[246] Zhao, S.; Yu, H.; Maric, R.; Danilovic, N.; Capuano, C.; Ayers, K. E.; Mustain, W. E. Determining the Electrochemically Active Area of IrO_x Powder Catalysts in an Operating Proton Exchange Membrane Electrolyzer. *ECS Trans.* **2015**, *69* (17), 877.

[247] Mayrhofer, K. J. J.; Strmcnik, D.; Blizanac, B. B.; Stamenkovic, V.; Arenz, M.; Markovic, N. M. Measurement of Oxygen Reduction Activities via the Rotating Disc Electrode Method: From Pt Model Surfaces to Carbon-Supported High Surface Area Catalysts. *Electrochim. Acta* **2008**, *53* (7), 3181–3188.

[248] Shao, M.; Odell, J. H.; Choi, S.-I.; Xia, Y. Electrochemical Surface Area Measurements of Platinum- and Palladium-Based Nanoparticles. *Electrochem. Commun.* **2013**, *31*, 46–48.

[249] Wei, C.; Sun, S.; Mandler, D.; Wang, X.; Qiao, S. Z.; Xu, Z. J. Approaches for Measuring the Surface Areas of Metal Oxide Electrocatalysts for Determining Their Intrinsic Electrocatalytic Activity. *Chem. Soc. Rev.* **2019**, *48* (9), 2518–2534.

[250] Kim, C.; Dionigi, F.; Beermann, V.; Wang, X.; Möller, T.; Strasser, P. Alloy Nanocatalysts for the Electrochemical Oxygen Reduction (ORR) and the Direct Electrochemical Carbon Dioxide Reduction Reaction (CO2 RR). *Adv. Mater.* **2019**, *31* (31), e1805617.

[251] Stephens, I. E. L.; Bondarenko, A. S.; Bech, L.; Chorkendorff, I. Oxygen Electroreduction Activity and X-ray Photoelectron Spectroscopy of Platinum and Early Transition Metal Alloys. *ChemCatChem* **2012**, *4* (3), 341–349.

[252] Green, C. L.; Kucernak, A. Determination of the Platinum and Ruthenium Surface Areas in Platinum−Ruthenium Alloy Electrocatalysts by Underpotential Deposition of Copper. I. Unsupported

Catalysts. *J. Phys. Chem. B* **2002**, *106* (5), 1036–1047.

[253] Zamora Zeledón, J. A.; Jackson, A.; Stevens, M. B.; Kamat, G. A.; Jaramillo, T. F. Methods—A Practical Approach to the Reversible Hydrogen Electrode Scale. *J. Electrochem. Soc.* **2022**, *169* (6), 066505.

[254] Inzelt, G.; Lewenstam, A.; Scholz, F. *Handbook of Reference Electrodes*; Springer, **2013**; Vol. 541.

[255] Niu, S.; Li, S.; Du, Y.; Han, X.; Xu, P. How to Reliably Report the Overpotential of an Electrocatalyst. *ACS Energy Lett.* **2020**, *5* (4), 1083–1087.

[256] Zoski, C. G. *Handbook of Electrochemistry*; Elsevier, **2007**.

[257] Mayrhofer, K. J. J.; Crampton, A. S.; Wiberg, G. K. H.; Arenz, M. Analysis of the Impact of Individual Glass Constituents on Electrocatalysis on Pt Electrodes in Alkaline Solution. *J. Electrochem. Soc.* **2008**, *155* (6), P78.

[258] Sebastián-Pascual, P.; Sarabia, F. J.; Climent, V.; Feliu, J. M.; Escudero-Escribano, M. Elucidating the Structure of the Cu-Alkaline Electrochemical Interface with the Laser-Induced Temperature Jump Method. *J. Phys. Chem. C* **2020**, *124* (42), 23253–23259.

[259] Mayrhofer, K. J. J.; Wiberg, G. K. H.; Arenz, M. Impact of Glass Corrosion on the Electrocatalysis on Pt Electrodes in Alkaline Electrolyte. *J. Electrochem. Soc.* **2007**, *155* (1), P1.

[260] Weber, D. J.; Dosche, C.; Oezaslan, M. Fundamental Aspects of Contamination during the Hydrogen Evolution/Oxidation Reaction in Alkaline Media. *J. Electrochem. Soc.* **2020**, *167* (2), 024506.

[261] Campos-Roldán, C. A.; González-Huerta, R. G.; Alonso-Vante, N. Experimental Protocol for HOR and ORR in Alkaline Electrochemical Measurements. *J. Electrochem. Soc.* **2018**, *165* (15), J3001.

[262] Opekar, F.; Beran, P. Rotating Disk Electrodes. *J. Electroanal. Chem. Interfacial Electrochem.* **1976**, *69* (1), 1–105.

[263] Treimer, S.; Tang, A.; Johnson, D. C. A Consideration of the Application of Koutecký-Levich Plots in the Diagnoses of Charge-Transfer Mechanisms at Rotated Disk Electrodes. *Electroanalysis* **2002**, *14* (3), 165-171.

[264] Bruckenstein, S.; Miller, B. Unraveling Reactions with Rotating Electrodes. *Acc. Chem. Res.* **1977**, *10* (2), 54–61.

[265] Kocha, S. S.; Shinozaki, K.; Zack, J. W.; Myers, D. J.; Kariuki, N. N.; Nowicki, T.; Stamenkovic, V.; Kang, Y.; Li, D.; Papageorgopoulos, D. Best Practices and Testing Protocols for Benchmarking ORR

Activities of Fuel Cell Electrocatalysts Using Rotating Disk Electrode. *Electrocatalysis* **2017**, *8* (4), 366–374.

[266] Zamburlini, E.; Jensen, K. D.; Stephens, I. E. L.; Chorkendorff, I.; Escudero-Escribano, M. Benchmarking Pt and Pt-Lanthanide Sputtered Thin Films for Oxygen Electroreduction: Fabrication and Rotating Disk Electrode Measurements. *Electrochim. Acta* **2017**, *247*, 708–721.

[267] Shinozaki, K.; Zack, J. W.; Pylypenko, S.; Richards, R. M.; Pivovar, B. S.; Kocha, S. S. Benchmarking the Oxygen Reduction Reaction Activity of Pt-Based Catalysts Using Standardized Rotating Disk Electrode Methods. *Int. J. Hydrogen Energy* **2015**, *40* (46), 16820–16830.

[268] Bard, A. J.; Faulkner, L. R.; White, H. S. *Electrochemical Methods: Fundamentals and Applications*; John Wiley & Sons, **2022**.

[269] Čolić, V.; Tymoczko, J.; Maljusch, A.; Ganassin, A.; Schuhmann, W.; Bandarenka, A. S. Experimental Aspects in Benchmarking of the Electrocatalytic Activity. *ChemElectroChem* **2015**, *2* (1), 143–149.

[270] Arulmozhi, N.; Esau, D.; van Drunen, J.; Jerkiewicz, G. Design and Development of Instrumentations for the Preparation of Platinum Single Crystals for Electrochemistry and Electrocatalysis Research Part 3: Final Treatment, Electrochemical Measurements, and Recommended Laboratory Practices. *Electrocatalysis* **2018**, *9* (1), 113–123.

[271] Dutta, G.; Jo, K.; Lee, H.; Kim, B.; Woo, H. Y.; Yang, H. Time-Dependent Decrease in the Enhanced Electrocatalytic Activities Observed after Three Different Pretreatments of Gold Electrodes. *J. Electroanal. Chem.* **2012**, *675*, 41–46.

[272] Watzele, S.; Hauenstein, P.; Liang, Y.; Xue, S.; Fichtner, J.; Garlyyev, B.; Scieszka, D.; Claudel, F.; Maillard, F.; Bandarenka, A. S. Determination of Electroactive Surface Area of Ni-, Co-, Fe-, and Ir-Based Oxide Electrocatalysts. *ACS Catal.* **2019**, *9* (10), 9222–9230.

[273] Markovic, N.; Gasteiger, H.; Ross, P. N. Kinetics of Oxygen Reduction on Pt(hkl) Electrodes: Implications for the Crystallite Size Effect with Supported Pt Electrocatalysts. *J. Electrochem. Soc.* **1997**, *144* (5), 1591.

[274] Sheng, W.; Zhuang, Z.; Gao, M.; Zheng, J.; Chen, J. G.; Yan, Y. Correlating Hydrogen Oxidation and Evolution Activity on Platinum at Different pH with Measured Hydrogen Binding Energy. *Nat. Commun.* **2015**, *6*, 5848.

[275] Garcia-Araez, N.; Climent, V.; Feliu, J. M. Analysis of Temperature Effects on Hydrogen and OH Adsorption on Pt(111), Pt(100) and Pt(110) by Means of Gibbs Thermodynamics. *J. Electroanal. Chem.*

2010, *649* (1), 69–82.

[276] Song, K.-T.; Schott, C. M.; Schneider, P. M.; Watzele, S. A.; Kluge, R. M.; Gubanova, E. L.; Bandarenka, A. S. Combining Impedance and Hydrodynamic Methods in Electrocatalysis. Characterization of Pt(pc), Pt5Gd, and Nanostructured Pd for the Hydrogen Evolution Reaction. *J. Phys. Energy* **2023**, *5* (1), 014016.

[277] Kucernak, A. R.; Zalitis, C. General Models for the Electrochemical Hydrogen Oxidation and Hydrogen Evolution Reactions: Theoretical Derivation and Experimental Results under near Mass-Transport Free Conditions. *J. Phys. Chem. C Nanomater. Interfaces* **2016**, *120* (20), 10721–10745.

[278] Vedalakshmi, R.; Saraswathy, V.; Song, H.-W.; Palaniswamy, N. Determination of Diffusion Coefficient of Chloride in Concrete Using Warburg Diffusion Coefficient. *Corros. Sci.* **2009**, *51* (6), 1299–1307.

[279] McAllister, J.; Bandeira, N. A. G.; McGlynn, J. C.; Ganin, A. Y.; Song, Y.-F.; Bo, C.; Miras, H. N. Tuning and Mechanistic Insights of Metal Chalcogenide Molecular Catalysts for the Hydrogen-Evolution Reaction. *Nat. Commun.* **2019**, *10* (1), 370.

[280] Shinagawa, T.; Garcia-Esparza, A. T.; Takanabe, K. Insight on Tafel Slopes from a Microkinetic Analysis of Aqueous Electrocatalysis for Energy Conversion. *Sci. Rep.* **2015**, *5*, 13801.

[281] Zheng, J.; Yan, Y.; Xu, B. Correcting the Hydrogen Diffusion Limitation in Rotating Disk Electrode Measurements of Hydrogen Evolution Reaction Kinetics. *J. Electrochem. Soc.* **2015**, *162* (14), F1470.

[282] Zenyuk, I. V.; Litster, S. Spatially Resolved Modeling of Electric Double Layers and Surface Chemistry for the Hydrogen Oxidation Reaction in Water-Filled Platinum–Carbon Electrodes. *J. Phys. Chem. C* **2012**, *116* (18), 9862–9875.

[283] Mann, R. F.; Amphlett, J. C.; Peppley, B. A.; Thurgood, C. P. Henry's Law and the Solubilities of Reactant Gases in the Modelling of PEM Fuel Cells. *J. Power Sources* **2006**, *161* (2), 768–774.

[284] Leuaa, P.; Priyadarshani, D.; Choudhury, D.; Maurya, R.; Neergat, M. Resolving Charge-Transfer and Mass-Transfer Processes of VO2+/VO2 + Redox Species across the Electrode/electrolyte Interface Using Electrochemical Impedance Spectroscopy for Vanadium Redox Flow Battery. *RSC Adv.* **2020**, *10* (51), 30887–30895.

[285] Nakamura, M.; Nakajima, Y.; Hoshi, N.; Tajiri, H.; Sakata, O. Effect of Non-Specifically Adsorbed Ions on the Surface Oxidation of Pt(111). *ChemPhysChem* **2013**, *14* (11), 2426–2431.

[286] Huang, B.; Rao, R. R.; You, S.; Hpone Myint, K.; Song, Y.; Wang, Y.; Ding, W.; Giordano, L.; Zhang,

Y.; Wang, T.; Muy, S.; Katayama, Y.; Grossman, J. C.; Willard, A. P.; Xu, K.; Jiang, Y.; Shao-Horn, Y. Cation- and pH-Dependent Hydrogen Evolution and Oxidation Reaction Kinetics. *JACS Au* **2021**, *1* (10), 1674–1687.

[287] Zadick, A.; Dubau, L.; Sergent, N.; Berthomé, G.; Chatenet, M. Huge Instability of Pt/C Catalysts in Alkaline Medium. *ACS Catal.* **2015**, *5* (8), 4819–4824.

[288] Sheng, W.; Gasteiger, H. A.; Shao-Horn, Y. Hydrogen Oxidation and Evolution Reaction Kinetics on Platinum: Acid vs Alkaline Electrolytes. *J. Electrochem. Soc.* **2010**, *157* (11), B1529.

[289] Zheng, Y.; Jiao, Y.; Vasileff, A.; Qiao, S.-Z. The Hydrogen Evolution Reaction in Alkaline Solution: From Theory, Single Crystal Models, to Practical Electrocatalysts. *Angew. Chem. Int. Ed Engl.* **2018**, *57* (26), 7568–7579.

[290] Zheng, Y.; Jiao, Y.; Zhu, Y.; Li, L. H.; Han, Y.; Chen, Y.; Jaroniec, M.; Qiao, S.-Z. High Electrocatalytic Hydrogen Evolution Activity of an Anomalous Ruthenium Catalyst. *J. Am. Chem. Soc.* **2016**, *138* (49), 16174–16181.

[291] Sheng, W.; Myint, M.; Chen, J. G.; Yan, Y. Correlating the Hydrogen Evolution Reaction Activity in Alkaline Electrolytes with the Hydrogen Binding Energy on Monometallic Surfaces. *Energy Environ. Sci.* **2013**, *6* (5), 1509–1512.

[292] Zhang, L.; Chang, Q.; Chen, H.; Shao, M. Recent Advances in Palladium-Based Electrocatalysts for Fuel Cell Reactions and Hydrogen Evolution Reaction. *Nano Energy* **2016**, *29*, 198–219.

[293] Schott, C. M.; Schneider, P. M.; Sadraoui, K.; Song, K.-T.; Garlyyev, B.; Watzele, S. A.; Michalička, J.; Macak, J. M.; Viola, A.; Maillard, F.; Others. Top-down Surfactant-Free Synthesis of Supported Palladium-Nanostructured Catalysts. *Small Sci.* **2024**, *4* (3), 2300241.

[294] Song, K.-T.; Zagalskaya, A.; Schott, C. M.; Schneider, P. M.; Garlyyev, B.; Alexandrov, V.; Bandarenka, A. S. Influence of Alkali Metal Cations on the Oxygen Reduction Activity of Pt_5Y and Pt_5Gd Alloys. *J. Phys. Chem. C* **2024**, *128* (12), 4969–4977.

[295] Campos-Roldán, C. A.; Jones, D. J.; Rozière, J.; Cavaliere, S. Platinum-Rare Earth Alloy Electrocatalysts for the Oxygen Reduction Reaction: A Brief Overview. *ChemCatChem* **2022**, *14* (19), e202200334.

[296] Wu, D.; Shen, X.; Pan, Y.; Yao, L.; Peng, Z. Platinum Alloy Catalysts for Oxygen Reduction Reaction: Advances, Challenges and Perspectives. *ChemNanoMat* **2020**, *6* (1), 32–41.

[297] Strasser, P.; Kühl, S. Dealloyed Pt-Based Core-Shell Oxygen Reduction Electrocatalysts. *Nano*

Energy **2016**, *29*, 166–177.

[298] Stephens, I. E. L.; Bondarenko, A. S.; Grønbjerg, U.; Rossmeisl, J.; Chorkendorff, I. Understanding the Electrocatalysis of Oxygen Reduction on Platinum and Its Alloys. *Energy Environ. Sci.* **2012**, *5* (5), 6744–6762.

[299] Hernandez-Fernandez, P.; Masini, F.; McCarthy, D. N.; Strebel, C. E.; Friebel, D.; Deiana, D.; Malacrida, P.; Nierhoff, A.; Bodin, A.; Wise, A. M.; Nielsen, J. H.; Hansen, T. W.; Nilsson, A.; Stephens, I. E. L.; Chorkendorff, I. Mass-Selected Nanoparticles of PtxY as Model Catalysts for Oxygen Electroreduction. *Nat. Chem.* **2014**, *6* (8), 732–738.

[300] Velázquez-Palenzuela, A.; Masini, F.; Pedersen, A. F.; Escudero-Escribano, M.; Deiana, D.; Malacrida, P.; Hansen, T. W.; Friebel, D.; Nilsson, A.; Stephens, I. E. L.; Chorkendorff, I. The Enhanced Activity of Mass-Selected PtxGd Nanoparticles for Oxygen Electroreduction. *J. Catal.* **2015**, *328*, 297–307.

[301] Escudero-Escribano, M.; Verdaguer-Casadevall, A.; Malacrida, P.; Grønbjerg, U.; Knudsen, B. P.; Jepsen, A. K.; Rossmeisl, J.; Stephens, I. E. L.; Chorkendorff, I. Pt5Gd as a Highly Active and Stable Catalyst for Oxygen Electroreduction. *J. Am. Chem. Soc.* **2012**, *134* (40), 16476–16479.

[302] Garlyyev, B.; Pohl, M. D.; Čolić, V.; Liang, Y.; Butt, F.; Holleitner, A.; Bandarenka, A. High Oxygen Reduction Reaction Activity of Pt5Pr Electrodes in Acidic Media. *Electrochem. Commun.* **2018**, *88*, 10–14.

[303] Jóhannesson, G. H.; Bligaard, T.; Ruban, A. V.; Skriver, H. L.; Jacobsen, K. W.; Nørskov, J. K. Combined Electronic Structure and Evolutionary Search Approach to Materials Design. *Phys. Rev. Lett.* **2002**, *88* (25), 255506.

[304] Stamenkovic, V.; Mun, B. S.; Mayrhofer, K. J. J.; Ross, P. N.; Markovic, N. M.; Rossmeisl, J.; Greeley, J.; Nørskov, J. K. Changing the Activity of Electrocatalysts for Oxygen Reduction by Tuning the Surface Electronic Structure. *Angew. Chem. Int. Ed Engl.* **2006**, *45* (18), 2897–2901.

[305] Müller-Dethlefs, K.; Hobza, P. Noncovalent Interactions: A Challenge for Experiment and Theory. *Chem. Rev.* **2000**, *100* (1), 143–168.

[306] Miller, D. J.; Lisy, J. M. Hydrated Alkali-Metal Cations: Infrared Spectroscopy and Ab Initio Calculations of M+(H2O)x=2−5Ar Cluster Ions for M = Li, Na, K, and Cs. *J. Am. Chem. Soc.* **2008**, *130* (46), 15381–15392.

[307] Miller, D. J.; Lisy, J. M. Entropic Effects on Hydrated Alkali-Metal Cations: Infrared Spectroscopy and Ab Initio Calculations of M+(H2O)x=2−5 Cluster Ions for M = Li, Na, K, and Cs. *J. Am. Chem. Soc.*

2008, *130* (46), 15393–15404.

[308] Lima, F. H. B.; Zhang, J.; Shao, M. H.; Sasaki, K.; Vukmirovic, M. B.; Ticianelli, E. A.; Adzic, R. R. Catalytic Activity−d-Band Center Correlation for the O2 Reduction Reaction on Platinum in Alkaline Solutions. *J. Phys. Chem. C* **2007**, *111* (1), 404–410.

[309] Nesselberger, M.; Ashton, S.; Meier, J. C.; Katsounaros, I.; Mayrhofer, K. J. J.; Arenz, M. The Particle Size Effect on the Oxygen Reduction Reaction Activity of Pt Catalysts: Influence of Electrolyte and Relation to Single Crystal Models. *J. Am. Chem. Soc.* **2011**, *133* (43), 17428–17433.

[310] You, G.; Zhu, W.; Zhuang, Z. Impacts of Anions on the Electrochemical Oxygen Reduction Reaction Activity and Stability of Pt/C in Alkaline Electrolyte. *Int. J. Hydrogen Energy* **2019**, *44* (26), 13373–13382.

[311] Liu, S.; White, M. G.; Liu, P. Mechanism of Oxygen Reduction Reaction on Pt(111) in Alkaline Solution: Importance of Chemisorbed Water on Surface. *J. Phys. Chem. C* **2016**, *120* (28), 15288–15298.

[312] Ge, X.; Sumboja, A.; Wuu, D.; An, T.; Li, B.; Goh, F. W. T.; Hor, T. S. A.; Zong, Y.; Liu, Z. Oxygen Reduction in Alkaline Media: From Mechanisms to Recent Advances of Catalysts. *ACS Catal.* **2015**, *5* (8), 4643–4667.

[313] Ramaswamy, N.; Mukerjee, S. Influence of Inner- and Outer-Sphere Electron Transfer Mechanisms during Electrocatalysis of Oxygen Reduction in Alkaline Media. *J. Phys. Chem. C* **2011**, *115* (36), 18015–18026.

[314] Vitos, L.; Ruban, A. V.; Skriver, H. L.; Kollár, J. The Surface Energy of Metals. *Surf. Sci.* **1998**, *411* (1), 186–202.

[315] Kattel, S.; Wang, G. Beneficial Compressive Strain for Oxygen Reduction Reaction on Pt (111) Surface. *J. Chem. Phys.* **2014**, *141* (12), 124713.